

University of Crete, Department of Physics
Fo.R.T.H., Institute of Electronic Structure and Lasers

Doctor of Philosophy Dissertation

Spin Noise, Decoherence and Magnetic effects in Alkali Atoms and Biomolecules

by

Katsoprinakis Yiorgos

Supervisor: Dimitris Charalambides, Iannis Kominis

Iraklion, 2010

To Mika, to Katia, to my undaunted family...

Contents

Contents	i
Acknowledgements	1
Abstract	3
I Spin Noise	5
I:1 Alkali metals	7
i:1.1 General physical properties	7
i:1.2 Atomic properties	8
i:1.3 Mathematical formalism: Spherical tensors	9
i:1.3.1 Spherical tensor basis	9
a:/Definitions and properties	9
b:/Coupled (F) to uncoupled (I, J) relations	10
i:1.3.2 Spherical tensor basis expansions	11
a:/General formalism	11
b:/Angular momentum operators	12
c:/Wigner-Eckart theorem; dipole operator reduction	14
d:/The Density Matrix	16
e:/Eigenobservables	18
i:1.4 Interactions and system evolution	20
i:1.4.1 Master equation	20
i:1.4.2 Hamiltonian	21
a:/Hyperfine interaction	21
b:/Interaction with static magnetic fields	22
c:/Interaction with static electric fields	23
i:1.4.3 Relaxation	24
a:/Binary Collisions and van der Waals molecule formation	24

	b:/Wall collisions and Diffusion	27
	c:/Inhomogeneous magnetic fields	29
	d:/Radiation trapping, coherence narrowing and quenching	30
I:1.4.4	Spin exchange: a special mention	30
	a:/Origins	30
	b:/Mathematical treatment	31
	c:/Case of $\langle S \rangle = 0$	33
	d:/Case of $\langle S \rangle \neq 0$ and the Spin-temperature limit	33
	e:/Effects of rapid spin exchange	34
I:1.5	Light propagation	37
I:1.5.1	Polarizability and susceptibility	37
I:1.5.2	Polarizability of the alkali atoms	40
	a:/In terms of the dipole moment expectation value	40
	b:/In terms of eigenobservables	42
	c:/Faraday rotation	46
I:2	Laboratory	49
I:2.1	The “patient”: Alkali metal vapors	49
I:2.2	The “operating theater”	51
I:2.2.1	Magnetic shield	51
I:2.2.2	Cell heating and ovens	52
I:2.2.3	Optical tables	54
I:2.3	The “surgical instruments”: lasers and optics	55
I:2.3.1	Diode lasers	55
I:2.3.2	Optics	57
I:2.4	The “life support”: measurement and power	57
I:2.4.1	Wavelength-Frequency meters	57
	a:/Thorlabs Fabry-Perot resonator	57
	b:/Ocean Optics spectrometer	58
	c:/HighFinesse wavelength meter	58
I:2.4.2	Lock-In amplifier	59
I:2.4.3	Spectrum analyzer	60
I:2.4.4	Flux gate magnetometer	62
I:2.4.5	LabView virtual instruments	62
I:2.4.6	Rest of supporting equipment	62
I:3	Experimental work	65
I:3.1	Measurement of Transverse Spin Relaxation rate	65
I:3.1.1	Spin noise	65
I:3.1.2	Stochastic system evolution	66
	a:/The QSD evolution equation	66
	b:/Spin noise evolution in the QSD scheme	67

c:/The power spectrum of spin noise	70
d:/Stochastic evolution of the Faraday rotation angle	71
i:3.1.3 Experiment	72
i:3.1.4 Data analysis	74
i:3.2 A Quantum Random Number Generator	78
i:3.2.1 Random number generators	78
a:/Why random numbers?	78
b:/Computational generators and pseudo-randomness	78
c:/Physical generators and true randomness	78
d:/Verification of randomness	81
i:3.2.2 The spin-noise QRNG	85
a:/Method and experiment: Spin noise transient signals	85
b:/Testing randomness	90

Bibliography @ Spin Noise 93

II Quantum Biology 99

II:1 Spin Chemistry 101

ii:1.1 Introduction	101
ii:1.2 Radical Ion Pairs	102
ii:1.3 MFEs in RIPs: a roundup of experimental observations	103
ii:1.3.1 The Normal or High Field Effect	103
ii:1.3.2 The Low Field Effect	105
ii:1.3.3 Other effects	107
a:/ Δg mechanism	107
b:/Spin exchange	107
c:/Dipolar interaction	108
ii:1.4 Magnetoreception: the avian compass	109
ii:1.4.1 Earth's magnetic field and compass types	109
ii:1.4.2 Experimental observations	111
a:/Magnetic field for orientation: the avian compass	111
b:/Non-compass uses of the magnetic field	113
c:/Electromagnetic characteristics of the avian compass	113
ii:1.4.3 Proposed mechanisms for magnetoreception	114
a:/The magnetite hypothesis	114
b:/The radical pair hypothesis	115

II:2 Quantum Mechanical Description of RIPs 123

ii:2.1 Definition of states	123
ii:2.2 Master equation	124
ii:2.2.1 The Phenomenological Master Equation (PME)	125

II:2.2.2	The Jones-Hore Master Equation (JHME)	126
II:2.2.3	The Quantum Measurement Master Equation (QMME)	127
II:2.2.4	The Hamiltonian	128
II:2.2.5	Effects not accounted for in the Master Equations	136
II:2.3	Product Yields and Sensitivity	138
II:3	The QMME	141
II:3.1	Explanation of MFEs	141
II:3.2	Working in the Zeno regime	144
II:3.3	Coherent Triplet excitation	146
II:3.3.1	An intuitive interaction representation	147
II:3.3.2	Anisotropic effects in isotropic material	149
a:/	Sensitivity to the alignment of the field	149
b:/	Sensitivity to the orientation of the field	152
II:3.3.3	Effects in anisotropic materials	153
a:/	Explanation of the effect	156
b:/	Influence of real-life effects	158
	Bibliography @ Quantum Biology	161
A	Table of alkali constants & D1 and D2 transitions	169
B	Shot noise and polarimetry	177
B.1	Photodiode shot noise	177
B.2	Polarimetry	178
B.2.1	One photodiode: crossed and 45° geometries	179
B.2.2	Two photodiodes: balanced polarimetry	181
C	Alkali vapor density measurements	183
D	Vector models in radical pairs	189
a:/	The semi-classical vector model	189
b:/	The qualitative spin vector model	190
c:/	The home-bred vector model	191
	List of Symbols and Abbreviations	195
	List of Figures	196
	List of Tables	199

Acknowledgements

I would like to acknowledge prof. Iannis Kominis for supervising this work. We've had our ups and downs with Iannis and, then, well we've had some more ups and downs. No one can deny he is brilliant, though, and the times when we were actually able to work together as a group, were good times.

I would also like to thank prof. Dimitris Charalambidis for being there, with his positive aura and humorous attitude; and, ehm, for the financial support.

I am obliged to the rest of my PhD committee, D. Anglos, P. Tzanetakis, P. Tzallas, W. von Klitzing and P. Rakitzis, for responding to my plead to participate at a rather short notice. Thank you.

Special thanks go to all the friends I've made, who turned Fo.R.T.H. into a pleasant working environment: Argyris, Lykourgos, Melina, Manolis, Grigoris, Marina, Alexandros and so many more.

Last, but certainly not least, I would like to acknowledge my family for the unyielding support all these years. To my wife, who gave birth to our lovely daughter last year and who has been babysitting unassisted for the tedious past months; to my father and mother, who would give away anything for their children and who belong to the few romantic figures left, placing so much more weight on education than what education actually bears in Greece in the new millennium.

Thank you all.



Abstract

This PhD dissertation contains work done by the author between the years 2007 and 2010, under the supervision of professors I. Kominis and D. Charalambidis. It comprises two parts.

The first part is about spin polarization noise in thermal alkali vapors. Spin noise is a fundamental source of noise, imposing the, so called, *fundamental quantum limits* to precision measurements employing spin polarized targets. However, being, as it is, of magnetic origin, spin noise can be manipulated to reveal system specific information and in this, first part of the thesis, we use it to extract such parts of information, experimentally. Part I is organized as follows. In the first chapter, the general properties of alkali metals and their atomic structure are discussed. We build the formalism used to attack calculations in alkali systems, a formalism based on spherical tensor algebra, and present the various interactions and relaxation processes relevant to the description of a thermal vapor. Finally, since light beams are used to probe the properties of the medium, the impact of these properties on the characteristics of passing light are analyzed. It is important to note at this point that the chapter has been written out rather exhaustively, with an eye on it serving as a textbook reference for spherical tensor algebra calculations in the context of alkali metals. In the second chapter, a description of our laboratory is given; quoting suppliers, equipment and such. In the third, and final, chapter of this part, the experimental work performed is presented. This involved extracting the *transverse relaxation rate* of an alkali vapor, which is the main decoherence rate in the system, and providing a proof of principle on the ability of spin noise measurements to serve as a *Quantum Random Number Generator*.

The second part is about *quantum biology*. The incentive for this work has been the magnetoreception ability of certain species of plants and animals and, particularly, the proposed explanation of the avian compass by means of *magnetic field effects* in *radical ion pairs* (RIPs). RIPs are formed in spin correlated states, by a charge transfer process between two free radicals. This correlated state evolves coherently between the singlet and triplet subspaces, an evolution which

can be influenced by magnetic fields before charge recombination occurs, thus making the RIP act as a magnetic sensor. The author's work on the subject was to theorize on the implications of initially exciting RIPs in coherent triplet states, rather than in the singlet state. Part II is organized as follows. In the first chapter, a round-up of experimental observations on magnetic field effects on radical ion pairs is presented and magnetoreception, being the incentive for this work, is discussed. This chapter, like the first chapter of part I, is written as a general reference/introduction to the field of spin chemistry. In the second chapter, the mathematical formalism traditionally pertaining to the description of RIP reactions is given and a new, conceptually different, master equation by I. Kominis is introduced. In the final chapter, the excitation of RIPs in triplet, rather than singlet, states is discussed. Specifically, we analyze how a coherent triplet state can provide not only alignment, but also orientational, information for an external magnetic field in a radical pair which demonstrates isotropic hyperfine interaction; an impossibility for singlet-born pairs. We also discuss the case of a triplet excited state in a pair with anisotropic hyperfine interaction and show how the angular sensitivity, in the context of the new theory and in specific ranges of parameters, demonstrates radically different behavior than expected from the traditional, phenomenological approach.



Part I

Spin Noise

Chapter I:1

Alkali metals

I.1.1 General physical properties

Alkali metals form Group 1 of the periodic table*. The alkali metals are lithium (Li), sodium (Na), potassium (K), rubidium (Rb), cesium (Cs), and francium (Fr), they are silver-colored (cesium has a golden tinge), soft, low-density metals, with low melting and boiling temperatures. They all have one electron in their outermost shell, so the energetically preferred state of achieving a filled electron shell is to lose this electron to form a singly charged positive ion. Owing to their single outer shell electron, they are highly reactive, making it impossible to exist in elemental form in nature. They react readily with halogens to form ionic salts, and with water to form strongly alkaline (basic) hydroxides. The latter reaction is indicative of the increasing reactivity on descending the Group. Li reacts steadily with water, with effervescence; Na reacts more violently and can burn with an orange flame; K ignites on contact with water and burns with a lilac flame; Cs sinks in water, and the rapid generation of hydrogen gas under water produces a shock wave that can shatter a glass container. Important physical properties of the alkali metals are summarized in Table A#1.

Of particular interest in our work was rubidium and cesium. Rubidium naturally occurs at a 2.6:1 ratio of the stable ^{85}Rb (72.2%) to - mildly - radioactive ^{87}Rb (27.8%). Although isotopically pure rubidium could be sourced, we used samples at natural abundances. Cesium on the other hand naturally occurs in the form of the stable isotope ^{133}Cs , with only very small traces of ^{135}Cs and ^{137}Cs .

*Hydrogen, which is the first member of Group 1, does not exhibit similar behavior to the rest of the group elements and is not considered an alkali metal. This is no longer the case at unusually high pressures and low temperatures where, indeed, hydrogen becomes metallic in terms of physical behavior.

1.1.2 Atomic properties

Alkali metals occupy a central position in the experimental study of atomic physics. A combination of two facts has contributed to this state of affairs. On one hand, their simple, hydrogen-like atomic structure with a single electron in an s orbital provides an easy to handle model for qualitative predictions and for - more or less - tractable mathematical calculations. The existence of non-zero nuclear spin and the resulting hyperfine structure definitely complicates the situation, but this is rarely an undesired complication. On the other hand, it has been long known that alkali metals, when heated in a flame, color the flame with characteristic, well defined colors. This obviously implies that easily accessible optical transitions exist in alkali metals, making their optical probing with cheap light sources trivial. With the advent of diode lasers, available light sources were no longer just “cheap”, but also became tunable, stable, monochromatic, with well defined polarization and of an overall high quality. Today, state-of-art atomic clocks, magnetometers, BECs and more rely on diode laser mediated, pump-probe or quantum non-demolition techniques applied on alkali metals [KAKR03, Leg01, NIS, SVR10].

In the context of atomic physics, alkali atoms are characterized by their fine and hyperfine structure. Fine structure arises from spin-orbit coupling, yielding a total electronic angular momentum $\mathbf{J} = \mathbf{L} + \mathbf{S}$, with $J = |L - S|, \dots, L + S = |L \pm \frac{1}{2}|$. Alkali metals have one electron in an s outer shell, making $n^2S_{1/2}$ their ground state, where n is the principal quantum number and the spectroscopic notation, $^{2S+1}L_J$, is used for the designation of states. The most prominent optical transitions of alkalis are from the ground to the first excited states $n^2P_{1/2}$ and $n^2P_{3/2}$. These are the D-line transitions, hereafter referred to as D1 ($n^2S_{1/2} \rightarrow n^2P_{1/2}$) and D2 ($n^2S_{1/2} \rightarrow n^2P_{3/2}$). D1 and D2 lines are resolvable by lasers for most alkalis and are, thus, treated separately.

Hyperfine structure arises from the interaction of the electronic and nuclear spins of the alkali, yielding the total angular momentum $\mathbf{F} = \mathbf{I} + \mathbf{J}$, with $F = |I - J|, \dots, I + J$. For the heavier alkalis, the hyperfine splittings are large enough to be resolved by narrow-band lasers, while for the lighter ones the temperature has to be decreased significantly. Velocity class selective techniques, such as saturation spectroscopy, can also be used to take advantage of the hyperfine structure in Doppler broadened media. The Hamiltonian describing the hyperfine interaction and the resulting energy level splittings are given in the following sections.

1.1.3 Mathematical formalism: Spherical tensors

In the context of our work, where the outcome of the experiments is heavily influenced by the relative orientation of the quantum and macroscopic physical quantities involved, separating dynamics from geometry greatly facilitates both the theoretical predictions, as well as the analysis of the results. We present here the mathematical tools to accomplish this task. The bulk of the following description is based on [Sob92, Hap72, HM67a, MTH70, ABE⁺98, KWH88], with the first four being the dominant references.

1.1.3.1 Spherical tensor basis

▷ a./ *Definitions and properties*

For small magnetic fields, the hyperfine structure of the alkali metals is well resolved, particularly in the ground state. We, thus, define the spherical basis tensors in the $|F, m\rangle$ basis as:

$$T_{L,M}(F, F') = \sum_{m=-F}^F (-1)^{m-M-F'} \mathbb{C}_{m(M-m)M}^{FF'L} |F, m\rangle \langle F', m-M| \quad (1.1.1)$$

$$= \sum_{m=-F}^F (-1)^{m+F-2F'} \sqrt{2L+1} \begin{pmatrix} F & F' & L \\ m & M-m & -M \end{pmatrix} |F, m\rangle \langle F', m-M| \quad (1.1.2)$$

where the - yet another - notation used for the Clebsch-Gordan[†] coefficients is chosen so as to relate as a mnemonic rule to the more frequently used Wigner 3J symbols[‡]:

$$\mathbb{C}_{mm'M}^{FF'L} = (-1)^{m+F-F'} \sqrt{2L+1} \begin{pmatrix} F & F' & L \\ m & m' & -M \end{pmatrix} \quad (1.1.3)$$

The inverse relation quickly becomes very important for calculations involving sequences of operator applications on atomic states and is given by:

$$|F, \mu\rangle \langle F', \nu| = \sum_L (-1)^{\nu-F'} \mathbb{C}_{\mu(-\nu)(\mu-\nu)}^{FF'L} T_{L,\mu-\nu}(F, F') \quad (1.1.4)$$

$$= \sum_L (-1)^{2\nu-F-\mu} \sqrt{2L+1} \begin{pmatrix} F & F' & L \\ \mu & -\nu & -\mu+\nu \end{pmatrix} T_{L,\mu-\nu}(F, F') \quad (1.1.5)$$

[†]Other notations: $\mathbb{C}_{mm'M}^{FF'L} = \langle LM | FF'mm' \rangle = (LM | FmF'm') = C(FF'L; mm')$ etc.

[‡]The Racah V-coefficients also express the same symmetries as the Clebsch-Gordan and 3J, but are not used here. For the record though: $\mathbb{V}(FF'L; mm'M) = (-1)^{-F+F'+L} \begin{pmatrix} F & F' & F \\ m' & m & m' \end{pmatrix}$

The spherical basis tensors are orthonormal in the sense:

$$\text{Tr} \left([T_{L,M}(F, F')]^\dagger T_{l,m}(f, f') \right) = \delta_{Ll} \delta_{Mm} \delta_{Ff} \delta_{F'f'} \quad (1.1.6)$$

with Hermitian conjugation being obtained through:

$$[T_{L,M}(F, F')]^\dagger = (-1)^{F-F'+M} T_{L,-M}(F', F) \quad (1.1.7)$$

▷ *b:/ Coupled (F) to uncoupled (I, J) relations*

It is sometimes useful to transform from the coupled, total angular momentum representation (F) to the constituent, uncoupled representation (I, J), or vice versa. Since the multipole operators $T_{L,M}(F, F')$ essentially correspond to four angular momenta (two instances of I and J) being coupled to a total L with an M \hat{z} -projection, the transformation will involve a 9J symbol:

$$T_{L,M}(F, F') = \sum_{j,j'} \sqrt{[F][F'][j][j']} \begin{Bmatrix} I & I & j \\ J & J & j' \\ F & F' & L \end{Bmatrix} [T_{,j}(II)T_{,j'}(JJ)]_{L,M} \quad (1.1.8)$$

where $[A] = 2A + 1$ and $[\dots j \dots j']_{L,M}$ implies that j and j' have been coupled to a total angular momentum L with \hat{z} -projection M . The inverse relation is a consequence of the 9J symbol orthogonality properties and is given by:

$$[T_{,j}(II)T_{,j'}(JJ)]_{L,M} = \sum_{F,F'} \sqrt{[F][F'][j][j']} \begin{Bmatrix} I & I & j \\ J & J & j' \\ F & F' & L \end{Bmatrix} T_{L,M}(F, F') \quad (1.1.9)$$

Two very important special cases are the following:

$$T_{L,M}(II) = \sum_{F,F'} \sqrt{[F][F']} \mathbb{W}(F' J L I; I F) T_{L,M}(F, F') \quad (1.1.10)$$

$$T_{L,M}(JJ) = \sum_{F,F'} \sqrt{[F][F']} \mathbb{W}(I F J L; J F') T_{L,M}(F, F') \quad (1.1.11)$$

where the Racah coefficient, \mathbb{W} , is related to the 6J symbols through[§]:

$$\mathbb{W}(i \ n \ s \ e ; \ c \ t) = (-1)^{-(s+i+n+e)} \begin{Bmatrix} i & n & c \\ e & s & t \end{Bmatrix} \quad (1.1.12)$$

[§]The symbols used as arguments may serve as a mnemonic rule. Note, also, that the other commonly cited definition $\mathbb{W}(abcd; ef) = (-1)^{-(a+b+c+d)} \begin{Bmatrix} a & b & c \\ d & e & f \end{Bmatrix}$ yields different results.

1.1.3.2 Spherical tensor basis expansions

▷ a:/ General formalism

Any operator acting on a particular $F = f(I, J)$ hyperfine multiplet can be written down in the spherical tensor basis as:

$$\hat{O} = \sum_{\substack{L,M \\ F,F'}} O_{L,M}(F, F') T_{L,M}(F, F') \quad (1.1.13)$$

where $O_{L,M}(F, F') = \text{Tr} \left(\hat{O} \cdot [T_{L,M}(F, F')]^\dagger \right)$. Spatial vectors are expressed in terms of spherical coordinate unit vectors as:

$$\mathbf{A} = \sum_q (-1)^q A_q \hat{\mathbf{u}}_{-q}, \quad \text{where } A_q = \mathbf{A} \cdot \hat{\mathbf{u}}_q \quad (1.1.14)$$

$$\left. \begin{aligned} \hat{\mathbf{u}}_{+1} &\equiv \hat{\mathbf{u}}_+ = -\frac{\hat{\mathbf{x}} + i\hat{\mathbf{y}}}{\sqrt{2}} \\ \hat{\mathbf{u}}_0 &= \hat{\mathbf{z}} \\ \hat{\mathbf{u}}_{-1} &\equiv \hat{\mathbf{u}}_- = \frac{\hat{\mathbf{x}} - i\hat{\mathbf{y}}}{\sqrt{2}} \end{aligned} \right\} \text{Spherical unit vectors} \quad (1.1.15)$$

with $(\hat{\mathbf{u}}_q)^* = (-1)^q \hat{\mathbf{u}}_{-q}$ and orthogonality satisfied by $(\hat{\mathbf{u}}_q)^* \cdot \hat{\mathbf{u}}_p = \delta_{q,p}$. Spatial tensors, such as the vapor dielectric susceptibility tensor or the light polarization tensor, are analogously expressed in terms of basis dyadics defined as:

$$\ddot{\mathbf{Q}}_{L,M} = \sum_q \hat{\mathbf{u}}_q (\hat{\mathbf{u}}_{q-M})^* (-1)^{q-M-1} \mathbb{C}_{q, M-q, M}^{1,1,L} \quad (1.1.16)$$

with the inverse relationship being:

$$\hat{\mathbf{u}}_p \hat{\mathbf{u}}_q = - \sum_L \ddot{\mathbf{Q}}_{L, p+q} \mathbb{C}_{p, q, p+q}^{1,1,L} \quad (1.1.17)$$

The unit dyadic is:

$$\ddot{\mathbf{i}} = \sum_q \hat{\mathbf{q}} \hat{\mathbf{q}}^* = \sqrt{3} \ddot{\mathbf{Q}}_{0,0} \quad (1.1.18)$$

Basis dyadics are orthogonal, as it is readily shown:

$$\ddot{\mathbf{Q}}_{L,M} : \ddot{\mathbf{Q}}_{L',M'} \equiv \sum_{p,q} \hat{\mathbf{u}}_p^* \cdot \ddot{\mathbf{Q}}_{L,M} \cdot \hat{\mathbf{u}}_q \hat{\mathbf{u}}_q^* \cdot \ddot{\mathbf{Q}}_{L',M'} \cdot \hat{\mathbf{u}}_p = (-1)^M \delta_{L,L'} \delta_{M,M'} \quad (1.1.19)$$

and complex conjugation is defined as $[\ddot{\mathbf{Q}}_{L,M}]^* = (-1)^{L+M} \ddot{\mathbf{Q}}_{L,-M}$. Finally, the cross product between two vectors can be written as:

$$\mathbf{A} \times \mathbf{B} = -i\sqrt{2} \sum_q (-1)^q A_{-q} \ddot{\mathbf{Q}}_{1,q} \cdot \mathbf{B} \quad (1.1.20)$$

▷ b:/ *Angular momentum operators*

The total angular momentum operator vector is decomposed according to Eqs. (1.1.13) and (1.1.14) as:

$$\hat{\mathbf{F}} = \hbar \sum_{q,f} (-1)^q \hat{\mathbf{u}}_{-q} \sqrt{\frac{f(f+1)(2f+1)}{3}} T_{1,q}(f, f) \quad (1.1.21)$$

which implies

$$\hat{F}_q = \hbar \sum_f \sqrt{\frac{f(f+1)(2f+1)}{3}} T_{1,q}(f, f) \quad (1.1.22)$$

The relation to the corresponding Cartesian operators is given by[¶]:

$$\hat{F}_{\pm 1} \equiv \hat{F}_{\pm} = \mp \frac{1}{\sqrt{2}} (\hat{F}_x \pm i\hat{F}_y) \quad \text{and} \quad \hat{F}_0 = \hat{F}_z \quad (1.1.23)$$

Action of the operators above on the $|F, m\rangle$ states results in:

$$\hat{F}_0 |F, m\rangle = m \hbar |F, m\rangle \quad (1.1.24)$$

$$\hat{F}_{\pm} |F, m\rangle = \mp \frac{1}{\sqrt{2}} \sqrt{F(F+1) - m(m \pm 1)} \hbar |F, m \pm 1\rangle \quad (1.1.25)$$

$$= \mp \frac{1}{\sqrt{2}} \sqrt{(F \mp m)(F \pm m + 1)} \hbar |F, m \pm 1\rangle \quad (1.1.26)$$

In all of the above \hbar has been grayed out as a reminder that it is commonly omitted in the course of calculations ($\hbar = 1$), but is necessary in order to restore the correct units. Using the above along with a significant part of the full battery of Clebsch-Gordan coefficients and 3J, 6J and 9J symbol identities and relations, we have calculated the spherical basis expansion of the interaction of two spherical basis tensors:

$$T_{K,N}(F, F') T_{L,M}(F', F'') = (-1)^{F-2F'-F''-N-M} \sum_{Q=|L-K|}^{L+K} \sqrt{(2K+1)(2L+1)(2Q+1)} \times \\ \times \begin{pmatrix} L & K & Q \\ M & N & -(M+N) \end{pmatrix} \begin{Bmatrix} L & K & Q \\ F & F'' & F' \end{Bmatrix} T_{Q,M+N}(F, F'') \quad (1.1.27)$$

Note that the resulting expansion couples the hyperfine multiplet upon which the rightmost input spherical tensor acts, to the multiplet on which the leftmost

[¶]Another form of these relations is routinely used, with $\hat{F}_{\pm} = \hat{F}_x \pm i\hat{F}_y$, but we prefer the ones above as they are more symmetric.

tensor projects, while the intermediate multiplet must be common for both. Also note that the resulting expansion involves only components of the same projection, which is the sum of the projections of the initial tensors, but these components span all possible ranks which can result from the ranks of the input tensors, provided they are allowed by geometry. This expression, although difficult to describe and not really usable in this most general form, quickly becomes an invaluable tool when targeted to specific situations, considerably speeding up calculations and highlighting structural symmetries.

Sometimes it is preferable or sufficient to work with the fine structure, rather than the hyperfine. In this case, $\hat{\mathbf{J}}$ is the angular momentum operator of choice, which is decomposed exactly as in Eqs.(1.1.21) and (1.1.22), by substitution of F 's with J 's. For the ground state electronic spin in particular, we set $J = \frac{1}{2}$ to get:

$$\hat{S}_q = \frac{\hbar}{\sqrt{2}} T_{1,q}(\frac{1}{2}, \frac{1}{2}) \quad (1.1.28)$$

The \hat{J} operators can be connected back to hyperfine operators by expressing the $T_{1,q}(J, J)$ in terms of $T_{1,q}(F, F')$, according to Eq.(1.1.11). In the general case this results in:

$$\hat{\mathbf{J}} = \hbar \sum_{\substack{q \\ F, F'}} (-1)^q \sqrt{\frac{J(J+1)(2J+1)}{3}} \sqrt{(2F+1)(2F'+1)} \mathbb{W}(1JFI; JF') T_{1,q}(F, F') \quad (1.1.29)$$

where $F, F' = |I - J|, \dots, I + J$. Note that the \hat{J} operators can couple different hyperfine multiplets (different F 's), whereas the \hat{F} operators, by definition, do not. Specifically for the ground state electronic spin operator components, the above yields:

$$\hat{S}_q = \frac{\hbar}{\sqrt{2}} \sum_{F, F'} \sqrt{(2F+1)(2F'+1)} \mathbb{W}(IF\frac{1}{2}1; \frac{1}{2}F') T_{1,q}(F, F') \quad (1.1.30)$$

and the link to Cartesian coordinates is forged via:

$$\hat{S}_x = -\frac{\hat{S}_+ - \hat{S}_-}{\sqrt{2}}, \quad \hat{S}_y = i \frac{\hat{S}_+ + \hat{S}_-}{\sqrt{2}}, \quad \hat{S}_z = \hat{S}_0 \quad (1.1.31)$$

to yield:

$$\begin{aligned}
\hat{S}_x &= -\frac{\hbar}{2} \sum_{F,F'} \sqrt{(2F+1)(2F'+1)} \mathbb{W}(IF\frac{1}{2}1;\frac{1}{2}F') (T_{1,1}(F,F') - T_{1,-1}(F,F')) \\
\hat{S}_y &= \frac{i\hbar}{2} \sum_{F,F'} \sqrt{(2F+1)(2F'+1)} \mathbb{W}(IF\frac{1}{2}1;\frac{1}{2}F') (T_{1,1}(F,F') + T_{1,-1}(F,F')) \\
\hat{S}_z &= \frac{\hbar}{\sqrt{2}} \sum_{F,F'} \sqrt{(2F+1)(2F'+1)} \mathbb{W}(IF\frac{1}{2}1;\frac{1}{2}F') T_{1,0}(F,F') \quad (1:1.32)
\end{aligned}$$

where $F, F' = \alpha, \beta$, with the common symbolization for the ground state hyperfine multiplets, $\alpha = I + \frac{1}{2}$ and $\beta = I - \frac{1}{2}$, being used.

▷ c:/ *Wigner-Eckart theorem; dipole operator reduction*

Angular momenta are at home when expressed in the spherical tensor basis in terms of a simple numerical constant describing the magnitude of the angular momentum vector and a Clebsch-Gordan factor characterizing angular dependence. The Wigner-Eckart theorem states that all vectors can be decomposed in the spherical tensor basis as products of a *reduced* matrix element independent of geometrical features and characterizing the isotropic dynamics of the vector-system interaction times a Clebsch-Gordan geometrical factor. The theorem can be generalized to tensors of arbitrary rank. The reduced matrix element has to be explicitly calculated for the specific operator-system configuration; usually as an expectation value of the operator. The Wigner-Eckart theorem provides no hints as to how to go about this task. Its real strength is in providing the means to predict all angular behavior of the operator, independently of its reduced value and, consequently, in relating the behavior of the operator along different directions. In doing so, the Wigner-Eckart theorem also produces the selection rules governing the interaction between the physical process described by the operator and the system at hand. To better understand how the Wigner-Eckart theorem is implemented, we use as an example the reduction of the dipole operator; probably the most important operator in light-atom interactions.

The strength of the interaction between an atomic system and near resonant electromagnetic radiation is characterized by the dipole matrix elements coupling states of the system. Denoting ground and excited states with unprimed and primed letters, respectively, the Wigner-Eckart theorem yields:

$$\begin{aligned}
\langle F, m | d_q | F', m' \rangle &= \langle F || \mathbf{d} || F' \rangle \mathbb{C}_{m',q,m}^{F',1,F} \quad (1:1.33) \\
&= \langle F || \mathbf{d} || F' \rangle (-1)^{F'-1+m} \sqrt{2F+1} \begin{pmatrix} F' & 1 & F \\ m' & q & -m \end{pmatrix}
\end{aligned}$$

with $\mathbf{d} = e\mathbf{r}$ being the dipole operator and $\langle \dots \parallel \dots \parallel \dots \rangle$ denoting the m -independent, reduced matrix element. Using the symmetry properties of 3J symbols and the definition (1.1.2) of the spherical tensors, after some algebraic manipulation we conclude that the components of the dipole operator are given, as expected, by:

$$d_q = \sum_{F, F'} \langle F \parallel \mathbf{d} \parallel F' \rangle \sqrt{\frac{2F+1}{3}} T_{1,q}(F, F') \quad (1.1.34)$$

Note from the above equation that, if instead of the dipole operator we had the total angular momentum operator, $\hat{\mathbf{F}}$, then the reduced matrix element would be just $\langle F \parallel \hat{\mathbf{F}} \parallel F' \rangle = \delta_{F, F'} \hbar \sqrt{F(F+1)}$, and Eq.(1.1.34) would lead to Eq.(1.1.22).

The reduced matrix element, $\langle F \parallel \mathbf{d} \parallel F' \rangle$, can be further reduced in the decoupled (I, J) picture, according to [Ste09]:

$$\langle F \parallel \mathbf{d} \parallel F' \rangle = \langle J \parallel \mathbf{d} \parallel J' \rangle (-1)^{F'+J+1+I} \sqrt{(2F'+1)(2J+1)} \begin{Bmatrix} J & J' & 1 \\ F' & F & I \end{Bmatrix} \quad (1.1.35)$$

and further still, $\langle J \parallel \mathbf{d} \parallel J' \rangle$ can be decomposed in the (L, S) picture through the substitution $F \rightarrow J$, $J \rightarrow L$, $I \rightarrow S$ in (1.1.35) :

$$\langle J \parallel \mathbf{d} \parallel J' \rangle = \langle L \parallel \mathbf{d} \parallel L' \rangle (-1)^{J'+L+1+S} \sqrt{(2J'+1)(2L+1)} \begin{Bmatrix} L & L' & 1 \\ J' & J & S \end{Bmatrix} \quad (1.1.36)$$

The particularly important values of the D1 and D2 reduced matrix elements, $\langle J = 1/2 \parallel \mathbf{d} \parallel J' = 1/2 \rangle$ and $\langle J = 1/2 \parallel \mathbf{d} \parallel J' = 3/2 \rangle$, respectively, which are related to the observed lifetimes of these transitions via:

$$\frac{1}{\tau} = \frac{\omega_o^3}{3\pi\epsilon_o\hbar c^3} \frac{2J+1}{2J'+1} |\langle J \parallel \mathbf{d} \parallel J' \rangle|^2 \quad (1.1.37)$$

are given in Table A#1. For the sake of completeness we also write down the formulas relating the reduced matrix elements to another commonly cited parameter characterizing the strength of a transition, namely the *oscillator strength*, f^{\parallel} . The oscillator strength is related to the lifetime through:

$$\frac{1}{\tau} = \frac{e^2\omega_o^2}{2\pi\epsilon_o m_e c^3} \frac{2J+1}{2J'+1} f \quad (1.1.38)$$

and, thus:

$$f = \frac{2}{3} \frac{m_e \omega_o}{\hbar e^2} |\langle J \parallel \mathbf{d} \parallel J' \rangle|^2 \quad (1.1.39)$$

^{||}We refer here to the *absorption* oscillator strength, related to its *emission* counterpart through $(2J+1)f_{\text{abs}} = (2J'+1)f_{\text{em}}$

The oscillator strengths for the D1 and D2 transitions of alkali metals are also listed in Table A#1.

From the Wigner-Eckart reduction equations and through the symmetries of Clebsch-Gordan coefficients and 3J and 6J symbols, the selection rules for electric dipole transitions can be deduced. For example, since the upper row in a 6J symbol has to satisfy triangle conditions, from Eq. (1.1.36) we immediately conclude that $\Delta L = L - L' = \pm 1$ for a transition to be allowed. Also, from Eq. (1.1.33) we see that only transitions with $\Delta m = m - m' = 0, \pm 1$ are allowed and this only by appropriately polarized light; π -polarized light ($q = 0$) induces $m = m'$ transitions, while σ^\pm -polarized light ($q = \pm 1$) induces $m = m' \pm 1$ transitions. Analogous conclusions can be drawn by applying the Wigner-Eckart theorem to other operators.

▷ d:/ The Density Matrix

The benefits of describing incoherent ensembles of atoms via density matrices, rather than with multi-particle wavefunctions, are well known and documented (see for example [Fan57, Blu96]). The density matrix is generally defined as:

$$\rho = \frac{1}{N} \sum_{i=1}^N |\psi_i\rangle \langle \psi_i| \quad (1.1.40)$$

where $|\psi_i\rangle$ is the wavefunction of the i^{th} atom, in a total population of N atoms. With the aid of the density matrix, the expectation value of an observable O may be calculated through:

$$\langle O \rangle \equiv \frac{1}{N} \sum_{i=1}^N \langle \psi_i | \hat{O} | \psi_i \rangle = \text{Tr}[\rho \cdot O] \quad (1.1.41)$$

Expressing the density matrix in terms of spherical tensor multipoles fully justifies the introduction of this particular tensor algebra to the description of our physical system. We first give the various expansions and then a limited discussion of their significance. Within a given fine structure multiplet, the density matrix is expanded as:

$$\rho = \sum_{\substack{L,M \\ F,F'}} \text{Tr}[\rho T_{L,M}(F, F')] T_{L,M}(F, F')^\dagger = \sum_{\substack{L,M \\ F,F'}} (-1)^{F-F'+M} \rho_{L,M}(F, F') T_{L,-M}(F', F) \quad (1.1.42)$$

where one must stretch the difference between the above equation describing the decomposition of a state matrix and Eq.(1.1.13) describing the corresponding decomposition for a generic operator acting *on* the states of the system. This is the *coupled* expansion of the density matrix. An *uncoupled* expansion is obtained

by expressing the density matrix in terms of the J and I spherical components, as:

$$\rho = \sum_{\substack{K,L \\ M,N}} (-1)^{M+N} \rho_{KN;LM} T_{K,-N}(I, I) T_{L,-M}(J, J) \quad (1.1.43)$$

where again $\rho_{KN;LM} = \text{Tr}[\rho T_{K,N}(I, I) T_{L,M}(J, J)]$. The formulas in Eq.(1.1.8) to (1.1.11) come in handy when transforming between the coupled and uncoupled expansions. A particularly useful form of the ground state density matrix of alkali atoms is the one separating the electronic from the nuclear spin [ABE⁺98, Hap72]:

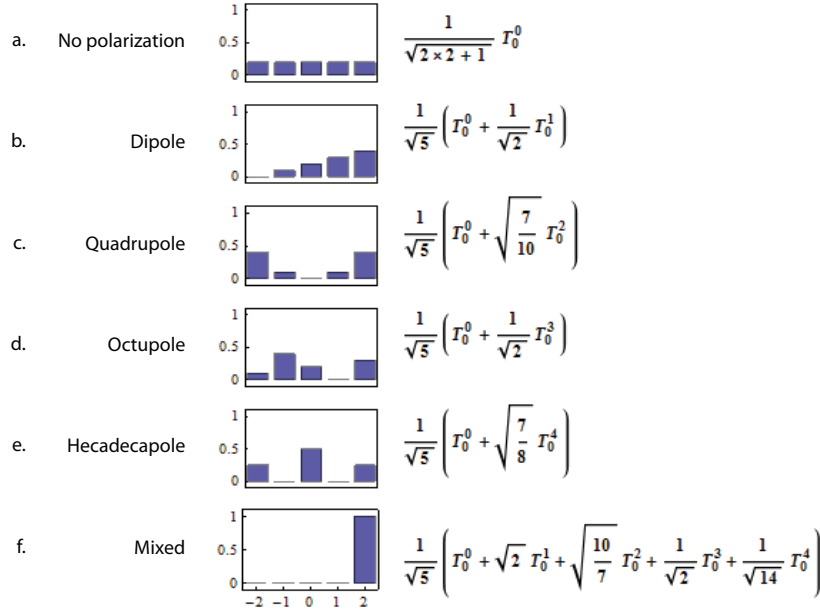
$$\rho = \varphi + \Theta \cdot \mathbf{S} \quad (1.1.44)$$

where \mathbf{S} is the electronic spin and φ and Θ are purely nuclear operators. Since, as described earlier, $S_q = \frac{1}{\sqrt{2}} T_{1,q}(\frac{1}{2}, \frac{1}{2})$, the above is a version of the uncoupled expansion, with:

$$\varphi = \frac{1}{\sqrt{2}} \sum_{L,M} (-1)^M \rho_{LM;00} T_{L,-M}(II) \quad (1.1.45)$$

$$\Theta_q = \sqrt{2} \sum_{L,M} (-1)^M \rho_{LM;1q} T_{L,-M}(II) \quad (1.1.46)$$

An example can help put the formalism into perspective and facilitate the understanding of the significance of the multipole representation. In Fig.1:1-1 we depict various multipole population distributions in an $F = 2$ multiplet. The corresponding density matrix, normalized to unity, is written next to each distribution. The theoretical advantage provided by this type of expansion is many-sided. First of all, in each case only the corresponding magnetic moment is non-zero, e.g. in (b) it is the magnetic dipole moment, in (c) the quadrupole moment and so on. Static or oscillating magnetic fields can only rotate, but can not change the multipolarity of a distribution. A rotated dipole distribution is still a dipole distribution. Also, when atoms are allowed to relax toward a random distribution, each multipole is decoupled from the rest and relaxes at a, possibly different and characteristic, rate. Finally, absorption or emission (spontaneous or otherwise) of light is affected only by the dipole and quadrupole configuration of the atom and is insensitive to higher order multipoles. That is to say, the octupole (d) or hexadecapole (e) distributions absorb and emit light in exactly the same manner as the random distribution (a). This can obviously lead to great simplification for atoms with large spins, as one will only have to deal with the simplest two moments.

**Figure 1:1-1**

Various population distributions in an $F = 2$ state multiplet and the corresponding multipole representations of the density matrix. Full polarization is a mixture of multipole components.

▷ e:/ *Eigenobservables*

Strong atom-light interactions, collisions, magnetic and electric fields and other perturbative processes can result in a rather complicated density matrix. Then, although a calculation of the complete list of populations (ρ_{mm}) and coherences (ρ_{mn}) fully determines the state of the system, it may be counter-intuitive and/or counter-productive to pursue such knowledge. As described earlier, each multipole in the expansion of the density matrix may evolve in a rather simple manner and at a characteristic time frame. It is, thus, possible to express the density matrix in terms of a certain set of observables, each of which will depend in specific ways on the multipoles and evolve as a mono-exponential damped oscillation. These observables are called *eigenobservables*.

In many cases an orthonormal set of eigenobservables can be chosen and the density matrix will be:

$$\rho = \sum_l \langle \hat{Q}^l \rangle \hat{Q}^l \quad (1:1.47)$$

where \hat{Q}^l are the eigenobservable operators and $\langle \hat{Q}^l \rangle = \sum_{mn} q_{mn}^l \rho_{mn}$, with q_{mn}^l being numerical coefficients defining the matrix elements of \hat{Q}^l . The contribution from the observable Q^l to the population of sublevel m is easily seen to be

Eigen Observable Q^l	1	$\bar{I} \cdot \bar{S}$	\bar{I}_z	Q_e
Distribution of Q^l_{mm}				
Relaxation Rate	0	$\frac{1}{T}$	$\frac{1}{8T}$	$\frac{1}{T}$

Eigen Observable Q^l	$\bar{T}_{20}(II)$	Q_{2e}	$T_{30}(aa)$	$T_{40}(aa)$
Distribution of Q^l_{mm}				
Relaxation Rate	$\frac{3}{8T}$	$\frac{1}{T}$	$\frac{3}{4T}$	$\frac{1}{T}$

Figure I:1-2

Ground state eigenobservables for a $I = \frac{3}{2}$ nuclear spin under the influence of electron randomization collisions. Relaxation rates are expressed as a numerical factor times the electron randomization rate, $1/T$. Barred operators do not couple different hyperfine multiplets, i.e. they are defined as $\bar{O} = \sum_{f,m,m'} |fm\rangle \langle fm| \hat{O} |fm'\rangle |fm'\rangle$ (Figure taken from [KWH88]).

$\langle \hat{Q}^l \rangle q^l_{mm}$. In the general case, however, the chosen set of eigenobservables is not necessarily orthogonal.

As an example we consider an atom with a nuclear spin $I = \frac{3}{2}$ undergoing electron randomization collisions; i.e. collisions which completely destroy the electronic part of the density matrix, reducing $\rho_{\text{before}} = \varphi + \Theta \cdot \mathbf{S}$ to $\rho_{\text{after}} = \varphi$. The eigenobservables of the atomic state are depicted in Fig. I:1-2, along with their characteristic relaxation rates as functions of the electron randomization collision rate, $\frac{1}{T}$.

1.1.4 Interactions and system evolution

1.1.4.1 Master equation

The master equation governing the evolution of the alkali vapor density matrix is of the form:

$$\frac{d\rho}{dt} = -\frac{i}{\hbar}[\mathcal{H}, \rho] + \mathcal{L}[\rho] \quad (1.1.48)$$

where the first part on the right hand side is the *Liouville part*, with \mathcal{H} the Hamiltonian of the system and $[A, B] = A \cdot B - B \cdot A$ denoting operator commutation, and the second part expresses decoherence, with \mathcal{L} being a superoperator describing all incoherent processes affecting evolution, such as radiative and non-radiative decay, collisions, diffusion and so on and so forth. Some processes may comprise a coherent part (included in the Hamiltonian) and an incoherent part (included in the decoherence superoperator). In such cases, it is usually the dominant of the two parts which ultimately determines how will this process be treated and is dependent on whether the potential from which it originates creates coherence at a faster or slower rate than it destroys it; one such process is the spin exchange relaxation, another is optical pumping.

In most cases of interest, the decoherence part can be put in the, so called, *Lindblad form*. This corresponds to \mathcal{L} on the right hand side of Eq.(1.1.48) being replaced by a sum of Lindblad superoperators, involving operators from an arbitrary orthonormal operator basis on the system's Hilbert space. The Lindblad superoperator** is defined as:

$$\mathcal{D}[\hat{L}]\rho = \hat{L} \cdot \rho \cdot \hat{L}^\dagger - \frac{1}{2} \left(\hat{L}^\dagger \cdot \hat{L} \cdot \rho + \rho \cdot \hat{L}^\dagger \cdot \hat{L} \right) \quad (1.1.49)$$

The master equation (1.1.48) can then be put in the diagonal form:

$$\frac{d\rho}{dt} = -\frac{i}{\hbar}[\mathcal{H}, \rho] + \sum_{i=1}^{N^2-1} \gamma_i \left[\hat{L}_i \cdot \rho \cdot \hat{L}_i^\dagger - \frac{1}{2} \left(\hat{L}_i^\dagger \cdot \hat{L}_i \cdot \rho + \rho \cdot \hat{L}_i^\dagger \cdot \hat{L}_i \right) \right] \quad (1.1.50)$$

where N is the dimensionality of the system, \hat{L}_i form an orthonormal operator basis and the summation extends to $N^2 - 1$ as we take \hat{L}_{N^2} to be proportional to the unit matrix, in which case the Lindblad superoperator is zero. The γ_i couplings are all positive.

The Lindblad superoperator form implies that each decoherence process is modeled as a stochastic process, wherein the system is coupled to a Markovian reservoir and we are only interested in the dynamical evolution of the system.

**Sometimes also called the *decoherence superoperator*.

Obviously, for this description to be applicable, reservoir correlations must decay much more rapidly than system state correlations; a prerequisite which is met by a wide range of decoherence phenomena. In these cases where the Lindblad form of the master equation can be applied, it represents the most general trace preserving, completely positive, Markovian (memoryless) master equation describing non-unitary evolution of the density matrix of a system. In Ch.I:3 we will encounter a case of application of the Lindblad equation. Finally, we must stress the fact that putting the master equation in its most general Lindblad form is not always straightforward and, more importantly, not always advisable or desirable, since other, simpler forms of the decoherence terms might provide more insight to the underlying physical processes.

In the following we discuss how the various interactions taking place inside a glass cell containing alkali and buffer gas vapors are approached physically and mathematically. We split this discussion in two sections: one describing terms included in the Liouville (Hamiltonian) part of the master equation and another describing decoherence producing terms. However, light propagation through the vapor cell and spin exchange collisions are treated separately at the end of the following discussion due to their particular importance.

1.1.4.2 Hamiltonian

▷ a:/ Hyperfine interaction

The hyperfine structure of atoms is mainly due to the magnetic interaction of the dipole moment of the nucleus with the magnetic fields produced by the electron spins and orbital motion and to the electric interaction of the quadrupole moment of the nucleus with electric field gradients in the electronic charge distribution. To the best of our knowledge, no conclusive measurements of higher order contributions (magnetic octupole etc.) have been made to date. In alkali metals, the most important manifestation of hyperfine structure is that of their $n^2S_{1/2}$ ground state, where only the magnetic dipole term contributes and is dominated by the Fermi contact interaction originating from the non-zero value of the s -orbital wavefunction at the position of the atomic nucleus. The subject has been extensively studied in the literature ([AIV77, Sob92] or any book on atomic structure).

The Hamiltonian describing the hyperfine structure is given by [AIV77, Ste09]:

$$\mathcal{H}_{\text{hf}} = A_{\text{hf}} \mathbf{I} \cdot \mathbf{J} + B_{\text{hf}} \frac{3 (\mathbf{I} \cdot \mathbf{J})^2 + \frac{3}{2} \mathbf{I} \cdot \mathbf{J} - I(I+1)J(J+1)}{2I(2I-1)J(2J-1)} \quad (1.1.51)$$

yielding the energy splittings:

$$\Delta E_{\text{hf}} = \frac{1}{2} A_{\text{hf}} K + B_{\text{hf}} \frac{\frac{3}{2} K(K+1) - 2I(I+1)J(J+1)}{4I(2I-1)J(2J-1)} \quad (1.1.52)$$

where $K = F(F+1) - I(I+1) - J(J+1)$, A_{hf} is the magnetic dipole constant, B_{hf} is the electric quadrupole constant and the magnetic octupole term has been omitted. Only the magnetic dipole term is non-zero for $J = \frac{1}{2}$ states.

▷ *b:/ Interaction with static magnetic fields*

The Hamiltonian term describing the interaction of atoms with a static, external magnetic field can take a number of forms depending on the relative strength of the field compared to the spin-orbit and hyperfine coupling strengths:

$$\begin{aligned} \mathcal{H}_{\text{B}} &= \frac{\mu_{\text{B}}}{\hbar} (g_{\text{S}} \mathbf{S} + g_{\text{L}} \mathbf{L} + g_{\text{I}} \mathbf{I}) \cdot \mathbf{B} && \text{Very strong fields} \\ &= \frac{\mu_{\text{B}}}{\hbar} (g_{\text{J}} \mathbf{J} + g_{\text{I}} \mathbf{I}) \cdot \mathbf{B} && \text{Strong fields} \\ &= \frac{\mu_{\text{B}}}{\hbar} g_{\text{F}} \mathbf{F} \cdot \mathbf{B} && \text{Weak fields} \end{aligned} \quad (1.1.53)$$

where, approximately, the g-factors are $g_{\text{S}} \simeq 2$, $g_{\text{L}} \simeq 1$ and experimental values of the nuclear g_{I} are given in Table A#1. When the magnetic field induced energy level splitting is small compared to the fine structure, J is a good quantum number, one can use the second form of the above given Hamiltonian and the Landè factor is*:

$$\begin{aligned} g_{\text{J}} &= g_{\text{L}} \frac{J(J+1) - S(S+1) + L(L+1)}{2J(J+1)} + g_{\text{S}} \frac{J(J+1) + S(S+1) - L(L+1)}{2J(J+1)} \\ &\simeq 1 + g_{\text{S}} \frac{J(J+1) + S(S+1) - L(L+1)}{2J(J+1)} \\ &= 2 \quad [\text{for the } {}^2\text{S}_{1/2}], \quad \frac{2}{3} \quad [\text{for the } {}^2\text{P}_{1/2}], \quad \frac{4}{3} \quad [\text{for the } {}^2\text{P}_{3/2}] \end{aligned} \quad (1.1.54)$$

For even weaker magnetic fields, inducing splittings small compared to the hyperfine structure, F becomes a good quantum number, the third form of the Hamiltonian term can be used and the hyperfine Landè factor is:

*Small corrections to the posted values come from taking into account relativistic effects and the multielectron structure of the atom. We don't quote these values here, nor do we quote the exact values for g_{S} and g_{L} . The reader may refer to the relevant part of the bibliography [Geh03, Tie10, Ste09, AIV77]. We did, however, use exact values for all calculations.

$$\begin{aligned}
g_F &= g_J \frac{F(F+1) - I(I+1) + J(J+1)}{2F(F+1)} + g_I \frac{F(F+1) + I(I+1) - J(J+1)}{2F(F+1)} \\
&\simeq g_J \frac{F(F+1) - I(I+1) + J(J+1)}{2F(F+1)}
\end{aligned} \tag{1.155}$$

For weak fields and to lowest order, the energies scale linearly with the applied magnetic field as:

$$\Delta E_{|F, m_F\rangle} = \mu_B g_F m_F B_z \tag{1.156}$$

where \hat{z} is taken as the quantization axis. The energy level splittings in this regime constitute the, so called, *Zeeman effect*. For strong fields, where the externally applied field dominates the hyperfine interaction and F is no longer a good quantum number, the energy splittings are derived by treating hyperfine components as perturbations. To lowest order such a treatment yields:

$$\begin{aligned}
E_{|J, m_J; I, m_I\rangle} &= \mu_B (g_I m_I + g_J m_J) B_z + \\
&+ A_{\text{hf}} m_I m_J + B_{\text{hf}} \frac{3(m_I m_J)^2 + \frac{3}{2} m_I m_J - I(I+1)J(J+1)}{2I(2I-1)J(2J-1)}
\end{aligned} \tag{1.157}$$

Splittings in this regime make the *Paschen-Back effect*. For intermediate fields one must generally diagonalize the $H_{\text{hf}} + H_B$ numerically. An important exception is the Breit-Rabi formula, which applies to the ground state of the D-transitions:

$$E_{|J=\frac{1}{2}, m_J; I, m_I\rangle} = -\frac{\Delta E_{\text{hf}}}{2(2I+1)} + g_I \mu_B m B \pm \frac{\Delta E_{\text{hf}}}{2} \sqrt{1 + \frac{4mx}{2I+1} + x^2} \tag{1.158}$$

with the hyperfine splitting $\Delta E_{\text{hf}} = A_{\text{hf}}(I + \frac{1}{2})$, $m = m_I \pm \frac{1}{2}$ and $x = \frac{(g_I - g_J)\mu_B B}{\Delta E_{\text{hf}}}$.

At very high fields, Zeeman and Paschen-Back effects for the fine structure arise and higher order Zeeman terms become important as well (quadratic Zeeman effect).

▷ c:/ Interaction with static electric fields

Analogous to the Zeeman effect is the *dc Stark effect* induced by a static, external electric field. The Hamiltonian is given by:

$$\mathcal{H}_E = -\frac{1}{2}\alpha_0 E_z^2 - \frac{1}{2}\alpha_2 E_z^2 \frac{3J_z^2 - J(J+1)}{J(2J-1)} \tag{1.159}$$

where the field is taken along the \hat{z} -axis and α_0 and α_2 are the *scalar* and *tensor polarizabilities*, respectively (α_2 vanishes for $J = \frac{1}{2}$ states). The scalar term shifts

states of the same J by the same amount, while the tensor term splits levels, but retains the degeneracy between states of the same $|m_F|$. For weak fields (relative to the hyperfine splittings) the Stark shifts are given by:

$$\Delta E_{|J,I;F,m_F\rangle} = -\frac{1}{2}\alpha_0 E_z^2 - \frac{1}{2}\alpha_2 E_z^2 \frac{[3m_F^2 - F(F+1)][3X(X-1) - 4F(F+1)J(J+1)]}{J(2J-1)F(2F-1)(2F+2)(2F+3)} \quad (1.1.60)$$

where $X = F(F+1) + J(J+1) - I(I+1)$. For strong fields, energy shifts become proportional to $|m_J|$; an analog to the Paschen-Back effect.

1.1.4.3 Relaxation

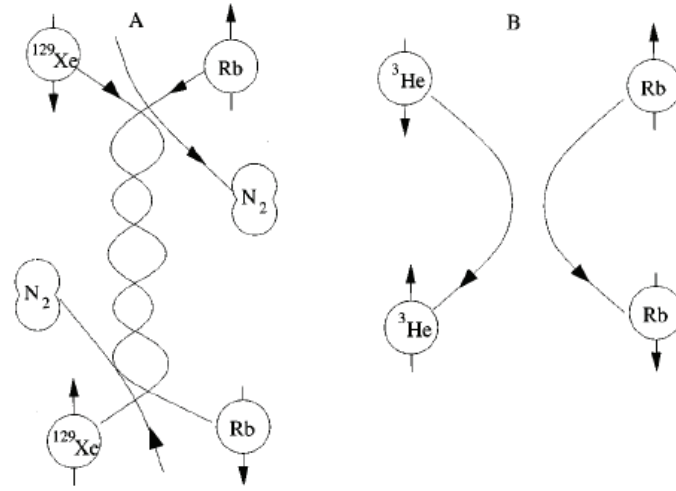
▷ a:/ Binary Collisions and van der Waals molecule formation

Binary collisions is one of the most important families of relaxation phenomena appearing in vapor cells of alkali metals and other atoms. The term generically implies a rapid collision (durations typically on the order of a picosecond) between alkali atoms of the same or different species or isotopic weight or between an alkali atom and a buffer gas atom or molecule. Such a collision results in wavefunction dephasing of the colliding particles, in spin polarization decay and, possibly, to spin polarization transfer from the alkali atom to the nucleus of the buffer gas atom; this is the basis of the, so called, *spin exchange optical pumping* where noble gas nuclei are polarized through collisions with optically pumped alkali atoms [WH97, ABE⁺98]. Although sudden with respect to the nuclear polarization, binary collisions do affect the spin state of the nucleus indirectly, since the nuclear and the electronic spins are recoupled in-between collisions. In the case of the heavier noble gas atoms another type of collision is possible and - presumably - dominant: a three body collision where an alkali and a noble gas atom form a weakly bound and relatively long-lived van der Waals molecule, with the third particle (usually nitrogen) carrying away the excess kinetic energy. An illustration of the collisional processes is given in Fig.1:1-3, taken from [WH97].

By far the most important member of this relaxation class is alkali-alkali spin exchange collisions. In fact it is so important that we do not discuss it in this paragraph, but rather we treat it separately in subsection 1.1.4.4. The formalism developed therein can be, under certain assumptions, applied to the generic case. In general, however, the evolution of the density matrix due to binary collisions is given by an equation of the form:

$$\frac{d\rho}{dt} = -\frac{i}{\hbar}[\mathcal{H} + \mathcal{V}^c, \rho] - \frac{1}{T}(\rho - \rho^c) \quad (1.1.61)$$

where \mathcal{V}^c is a - possible - energy level shift produced by the relaxation process which is usually treated perturbatively, ρ^c is the density matrix after the collision and $1/T$ is the characteristic relaxation rate given by:

**Figure I:1-3**

Collisions leading to relaxation in alkali metals and, possibly, to polarization transfer to noble gas nuclei.

A. The formation of van der Waals molecules is the dominant polarization transfer process for heavy noble gas atoms.

B. Binary collisions is the dominant process for the lighter nobles. The same picture can be used to describe alkali - alkali binary collisions.

(Figure taken from [WH97])

$$\frac{1}{T} = n_{c.p.} \bar{v} \sigma \quad (\text{I.1.62})$$

with $n_{c.p.}$ the number density of the colliding partner species[†], $\bar{v} = \sqrt{8k_B T / (\pi M)}$ is the mean relative velocity and σ is the characteristic cross section of the relaxation process. Here we proceed to describe some of the most important binary collisions appearing in alkali metal - buffer gas mixtures, other than spin exchange.

Alkali-alkali *S-damping* or *spin destruction* collisions [Fra59, BPCH80, Kni89, KAW98, ELH⁺00] can be described by a generic reaction of the form:



As seen above, such collisions do not preserve the electronic spin; hence the characterizations “damping” and “destruction”. They are believed to stem from a spin-axis interaction of the form [BPCH80]:

$$\mathcal{V}_{SD} = \frac{2}{3} \lambda(R) (3S_\zeta S_\zeta - S(S+1)) \quad (\text{I.1.64})$$

[†]i.e. in a collision of A and B , if Eq. (I.1.62) describes the evolution of the density matrix of A , then $n_{c.p.}$ will be the number density of B .

where λ is a coupling coefficient and $S_\zeta = (\mathbf{S}_1 + \mathbf{S}_2) \cdot \hat{\mathbf{r}}$ is the projection of the total electronic spin on the internuclear axis, with $\hat{\mathbf{r}} = \mathbf{R}/R$ being the unit vector on that axis. Although an S-damping collision is a spin-spin interaction at first sight, it effectively couples the electronic spin also to the orbital angular momentum of the colliding pair through a second order spin-orbit contribution to λ . However, it has been observed that the effectiveness of the S-damping process is severely suppressed by external magnetic fields on the order of a few thousand Gauss [KAW98], thus not all such relaxation can be attributed to sudden binary collisions, as these are too fast to be affected by fields of this magnitude. In [ELH⁺00] the authors prove that much of the observed relaxation is due to the spin-axis interaction acting on triplet dimers (A-A quasi-molecules on the triplet potential curve), although these account to less than 10^{-6} of the monomers density-wise. Nevertheless, a complete understanding of several aspects of this kind of relaxation is still unavailable. Mathematically, in terms of Eqs.(1.1.61) and (1.1.62), the density matrix after the collision is simply the pre-collision purely nuclear part, φ , and spin destruction cross sections are given, where available, in Table A#1.

Collisions between alkali and noble gas atoms are, predominantly, of three different types, all of which cause relaxation to the alkali density matrix. They can be described through the operator:

$$\mathcal{V}_{A-N} = \mathcal{V}_{SO} + \mathcal{V}_{HF} + \mathcal{V}_{SN} \quad (1.1.65)$$

with $\mathcal{V}_{SO} = \gamma(R) \mathbf{L} \cdot \mathbf{S}$	the spin-orbit interaction
$\mathcal{V}_{HF} = h\delta A(R) \mathbf{I} \cdot \mathbf{S}$	a hyperfine perturbation interaction
and $\mathcal{V}_{SN} = \alpha(R) \mathbf{N} \cdot \mathbf{S}$	the spin-nuclear exchange interaction

The spin-orbit interaction couples the electronic spin, \mathbf{S} , to the relative angular momentum, \mathbf{L} , of the colliding pair. It originates from both the direct interaction of the moving valence electron of the alkali and the electric field presented by the noble gas atom, as well as from excitation of virtual π states of the valence electron; the latter being typically more important. As the collisions are fast, the spin orbit interaction leads to electron randomization ($d\rho/dt$ following Eq.1.1.61, with $\rho^c = \varphi$).

The second interaction in Eq.(1.1.65), proportional to $\delta A \mathbf{I} \cdot \mathbf{S}$, is a collision-induced change in the contact interaction between the nucleus of the alkali atom and the valence electron, which leads to slight changes in the hyperfine couplings [Hap72]. For large interatomic separations (large impact parameters) and for the heavier, highly polarizable noble gas atoms (Ar, Kr, Xe), the interaction is dominated by van der Waals forces pulling the electron away from its nucleus; hence $\delta A < 0$. For small interatomic separations (small impact parameters) and for the lighter noble gas atoms (He, Ne) or other inert buffer gas molecules (H_2 , N_2), the interaction is mainly due to exchange forces between the valence

electron of the alkali and the electronic cloud of its colliding partner, which results in the alkali atom being concentrated more strongly to its core; hence $\delta A > 0$. This interaction is responsible for the pressure shifts of the hyperfine transition frequencies of the alkali atoms in buffer gas mixtures. However it does not seem to contribute significantly to the alkali relaxation.

The third interaction describes the exchange of polarization between the electronic spin and the nucleus of the noble gas atom with which it collides. It sits at the basis of spin-exchange optical pumping of the nobles [WH97, ABE⁺98] and originates from the isotropic Fermi contact interaction between the alkali electron and the noble gas nucleus[‡]. It is largely described as a spin-exchange interaction between two species A and B , following the formalism of subsection 1:1.4.4.

All the interactions above come into play also in the case of van der Waals molecule formation, but the formalism becomes significantly more convoluted. Rather analytical studies of this aspect of the alkali - noble gas atoms collisions are given in [WH97, ABE⁺98].

▷ *b:/ Wall collisions and Diffusion*

In optical pumping and spectroscopy experiments, a major source of relaxation is the *time-of-flight* relaxation. The term refers to the process where the heated alkali metal atoms in the vapor pass through the interaction area defined by the light beam traversing the cell or by the dimensions of the cell itself (if the light beam illuminates the whole cell), carrying away spin polarization and coherence, either to the cell volume not illuminated by the beam or to the cell walls where alkali atoms are completely randomized. These time-of-flight relaxation rates are usually quite large, since for an alkali vapor to acquire a pressure adequate for good signal to noise ratios, the temperature must be considerably high, which leads to large mean atomic velocities, according to Maxwell's distribution, and, thus, rapid loss of polarization and coherence. Two ways have been introduced to eliminate this issue: cell wall coatings and buffer gas induced diffusion.

When an alkali atom collides with the glass cell wall, it is trapped by the surface potentials for a considerable amount of time, in the course of which it will, most likely, become completely randomized with respect to the rest of the vapor. For typical cell dimensions and vapor temperatures, the relaxation rates caused by such collisions are on the order of $10^3 - 10^4$ Hz [KWH88]. The interactions pertaining this mechanism are similar to those for binary collisions (electron-nuclear spin-spin interaction, spin-orbit interaction and such, between the alkali atom and the cell material), but it is the comparably longer residence time relative to binary collisions which renders them particularly effective. However, it has

[‡]The term "contact" is indeed justified by the pronounced peak of the electronic wavefunction at the site of the noble gas nucleus. Anisotropic terms may also contribute to the exchange interaction, albeit at no more than a few percent [WH97]

been observed that certain chemically inert substances such as paraffin C_nH_{2n+2} or certain organosilanes, if applied as a thin coating on the inside of the cell, can prolong coherence and polarization lifetimes by 3 to 4 orders of magnitude. That is to say, in a well prepared, coated cell, the coherent state of an alkali atom can survive up to $\sim 10^4$ wall collisions before collapsing, allowing spin lifetimes on the order of 1 sec for typical conditions ([Hap72, KWH88] and references therein). Wall coatings allow the experimentalist to conduct low temperature experiments with pure alkali metal filled cells (no buffer or quenching gases), a situation which can be desirable for a number of reasons (narrow resonance lines, suppression of various sources of relaxation etc.).

Paraffin coatings, with melting points typically somewhere between 47°C and 64°C, are generally unsuitable for high-temperature experiments. Also, it may be the case that the interaction area defined by the light beam is smaller than the whole cell, in which case coherence is still lost as alkali atoms exit this area, although they may later return, still polarized after bouncing off the wall. So, another way of keeping the alkali atoms within the interaction area is by introducing an inert gas acting as a buffer. Coherence and polarization of the alkali metal atoms can be preserved for as many as $\sim 10^9$ collisions with appropriate buffer gas atoms, such as noble gases or molecular nitrogen (which also doubles as a radiation quenching agent). For sufficiently high pressures of the buffer gas, the mean free path between alkali-buffer collisions can become much smaller than the dimensions of the cell or the interaction area and the motion of the alkali metal atoms becomes diffusive and is described as a stochastic random walk. The diffusion equation governing the evolution of the density matrix will be:

$$\frac{\partial \rho}{\partial t} = D \nabla^2 \rho \quad (1.1.66)$$

where D is the diffusion constant, depending on the temperature and the pressure of the buffer gas. Diffusion constants are determined experimentally and are usually expressed relative to the 760 Torr / 0°C value, D_0 , via:

$$D = \frac{760}{P} D_0, \quad (P \text{ in Torr}) \quad (1.1.67)$$

where the temperature dependence comes from the ideal gas law. Values for the D_0 diffusion constants for some alkali metal - buffer gas combinations are tabulated in Table 1.1.1 (values taken from [WC94, Hap72] and references therein).

In a real system, the solution of Eq. (1.1.66) is generally intractable. So, many a time, decomposing the density matrix through a - complete, but not necessarily orthogonal - set of eigenobservables[§], each of which, by definition,

[§]For a more detailed account of the notion of eigenobservables and the corresponding density matrix decomposition, the reader is directed to [Hap72, KWH88] and the previous discussion in paragraph 1.1.3.2 e./.

Buffer ↓ gas ↓	Alkali metal		
	Na	Rb	Cs
He	0.92	0.54 - 1.5	0.2 - 0.37
Ne	0.50	0.31 - 0.5	0.15 - 0.4
Ar		0.24 - 0.4	0.13 - 0.23
N ₂	0.54	0.28 - 0.33	0.07 - 0.22
H ₂		1.34	

Table I:1#1

Alkali metal - buffer gas D_0 diffusion constants in cm^2/sec

decays at a characteristic rate, can lead to great simplification of the calculations. The evolution of an eigenobservable, Q , is described by:

$$\frac{\partial \langle \hat{Q} \rangle}{\partial t} = D \nabla^2 \langle \hat{Q} \rangle - \gamma \langle \hat{Q} \rangle \quad (\text{I:1.68})$$

where γ is the bulk relaxation rate due to processes other than diffusion. The solution to Eq. (I:1.68) will generally depend on the initial spatial dependence of the observable and there will be an infinite number of diffusion modes involved. However, in many cases it suffices to account for the influence of only the fundamental diffusion mode [WC94], in which case the induced relaxation rate for the two most commonly used cell geometries takes the form [KWH88]:

$$\frac{1}{T} = \frac{\pi^2}{r^2} \frac{760}{P} D_0 + \gamma \quad (\text{Spherical cell of radius } r) \quad (\text{I:1.69})$$

$$\frac{1}{T} = \left[\frac{\pi^2}{l^2} + \frac{2.405^2}{r^2} \right] \frac{760}{P} D_0 + \gamma \quad (\text{Cylindrical cell of radius } r \text{ and length } l) \quad (\text{I:1.70})$$

▷ c:/ Inhomogeneous magnetic fields

When an atom moves through a spatially inhomogeneous magnetic field, its nuclear spin[¶] may not be able to follow the field direction adiabatically. This results in effectively random changes in the angle between the spin and the local field vector, which, in turn, induce relaxation. By following an effective magnetic field approach one can show that the induced relaxation rate is given by:

$$\frac{1}{T} = \frac{1}{6} \frac{K(K+1)\tau_c v^2}{1 + (\omega\tau_c)^2} \frac{|\nabla H_x|^2 + |\nabla H_y|^2}{H^2} \quad (\text{I:1.71})$$

where τ_c is the correlation time and is on the order of the time between velocity-changing collisions, $v^2 = \frac{3k_B T}{M}$ is the mean square velocity, K is the spin and

[¶]And, thus, also its total spin.

$\mathbf{H} = H_x \hat{\mathbf{x}} + H_y \hat{\mathbf{y}} + H_z \hat{\mathbf{z}}$ is the effective field. For rapidly relaxing species such as the alkali metals, the relaxation induced by small inhomogeneities in the magnetic field is generally negligible.

▷ d:/ *Radiation trapping, coherence narrowing and quenching*

Radiation trapping refers to the situation where a spontaneously emitted photon is reabsorbed by the vapor before it leaves the interaction area. The phenomenon becomes important when the vapor is optically thick for some fluorescence decay mode. Then it poses a serious problem as it causes depolarization of the vapor and forms an isotropic, noisy, resonant background of light, which competes with the optical pumping and probing beams.

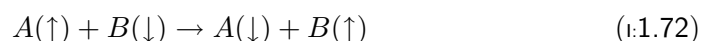
An interesting side effect is that, since radiation is trapped and reabsorbed, the effective lifetime of the excited state becomes larger. Thus, effectively, atoms in the excited state appear to decay at a slower rate and experimental measurements which scale inversely proportionally to the relaxation rates, become narrower, perhaps even to tens of percent. This effect is called *coherence narrowing* ([Hap72] and references).

In typical experimental conditions, radiation trapping is dealt with by means of some *radiation quenching* agent. The term implies that another system takes up the excess energy of the excited atom, non-radiatively. Usually, this system is another atom or molecule and the quenching mechanism relies on collisions with the excited atom. Molecules seem to be more effective in this task, a property conjectured to be via the excitation of the molecular vibrational and rotational degrees of freedom during the collisions. On the other hand, direct conversion of the excitation energy into recoil kinetic energy in atom-atom collisions is highly unlikely. In our experiments, even at temperatures as high as 400°K and more, a few hundred Torr of molecular nitrogen sufficed, as no indications of radiation trapping were observed.

1.1.4.4 Spin exchange: a special mention

▷ a:/ *Origins*

Spin exchange dominates the binary collisions relaxation class, especially for paramagnetic atoms such as the alkali metals. It is a case of *strong* collision in the sense that the density matrices of the colliding particles can be drastically changed by even a single event. A spin exchange collision between two $^2S_{1/2}$ atoms is traditionally represented in the bibliography by a reaction of the form:



with the arrows indicating the direction of the electronic spin and the equation being quite self explanatory in showing the exchange of spin orientations between

the two atoms. This type of interaction originates from the competition between the bonding (singlet) and anti-bonding (triplet) parts of the molecular potential of the dimer formed by the colliding particles. These potential curves are shown in Fig. 1:1-4 and can be represented by:

$$V_{\text{SE}}(r) = V_0(r) + V_1(r) \mathbf{S}_A \cdot \mathbf{S}_B \quad (1.1.73)$$

where \mathbf{S}_A , \mathbf{S}_B are the spin operators of the two atoms and for spin- $\frac{1}{2}$ particles the singlet and triplet parts take the form:

$$V_{\text{SE}}^{(s)}(r) = V_0(r) - \frac{3}{4} V_1(r) \quad (1.1.74)$$

$$V_{\text{SE}}^{(t)}(r) = V_0(r) + \frac{1}{4} V_1(r) \quad (1.1.75)$$

with analogous, but more complicated expressions being true for $S > \frac{1}{2}$ atoms.

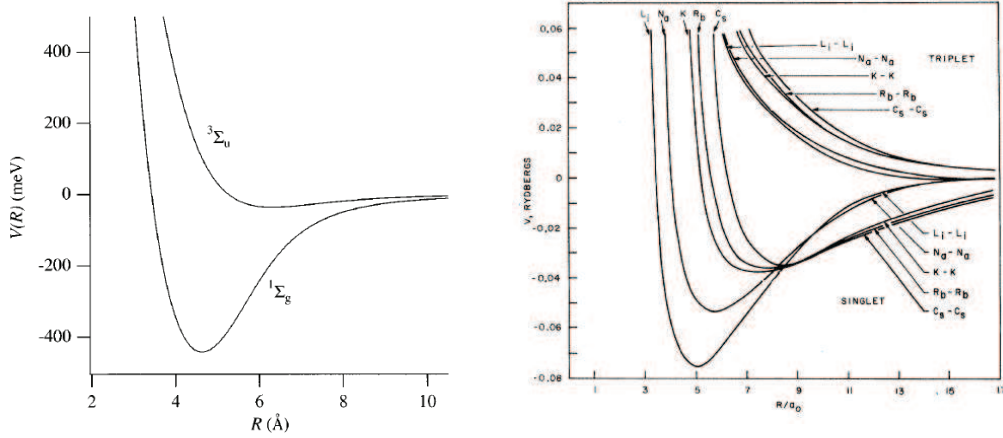


Figure 1:1-4

Left: Singlet and triplet molecular potential curves of two colliding Cs atoms [WH97].
 Right: Comparative figure of the same potentials for all alkali atoms [CW69].
 Plots are versus internuclear separation, either in Å (left) or in Bohr radii, α_0 (right).

Even at this early point, we can figure out a few physical properties of this interaction. The most important is that, since $\mathbf{S} = \mathbf{S}_A + \mathbf{S}_B$ commutes with $\mathbf{S}_A \cdot \mathbf{S}_B$, the total electronic spin is conserved during spin exchange collisions. Also, we expect the interaction to show quite large cross sections as the exchange potentials, being as they are of electrostatic nature, are themselves quite large. Typical values are $V \sim \text{eV}$ and $\sigma \sim 10^{-14} \text{cm}^2$.

▷ *b:/ Mathematical treatment*

In the literature, spin exchange was originally approached through two different, but ultimately equivalent methods. In [PF56, WD56] the authors followed a

classical impact parameter approach wherein the constituent spins rotate about the total spin, which is conserved throughout the collision. The total rotation angle, θ , is given by the accumulated phase difference:

$$\theta = \frac{1}{\hbar} \int_0^\infty (V_{\text{SE}}^{(t)} - V_{\text{SE}}^{(s)}) dt \quad (1:1.76)$$

and the cross section is obtained by averaging the exchange probability, $\frac{1}{2}(1 - \cos \theta)$, over impact parameters, b :

$$\sigma_{\text{SE}} = 2\pi \int_0^\infty \frac{1}{2}(1 - \cos \theta) b db \quad (1:1.77)$$

In [Dal61, Gla63, BHP64, CW69] partial wave analysis was used to determine the l -wave phase shifts, δ_l^s and δ_l^t , for scattering from the singlet and triplet potentials. The formula arrived at for the cross section is:

$$\sigma_{\text{SE}} = \frac{\pi}{k^2} \sum_{l=0}^{\infty} (2l+1) \sin^2(\delta_l^s - \delta_l^t) \quad (1:1.78)$$

with k being the propagation constant of the incident wave.

Specifically in the context of alkali atoms, dealing also with the complications arising from indistinguishable particle collisions, the first extensive analysis was performed by F. Grossetête [Gro64, Gro68], while an in depth experimental study and theoretical treatment of alkali-alkali differential spin exchange scattering was carried out by D.E. Pritchard *et al* [PCCK70, PC70]. Ultimately, all theories converge to the same evolution equation for the density matrix of an atomic species A undergoing spin exchange collisions with species B:

$$\frac{d\rho_A}{dt} = -\frac{i}{\hbar} [\mathcal{H}_o + \delta\mathcal{H}_{\text{SE}}^{(AB)}, \rho_A] + \frac{1}{T_{\text{SE}}^{(A)}} [\varphi_A (1 + 4\langle \mathbf{S}_B \rangle \cdot \mathbf{S}_A) - \rho_A] \quad (1:1.79)$$

where φ_A is the purely nuclear part in the expansion $\rho = \varphi + \Theta \cdot \mathbf{S}$ introduced in Eq.(1:1.44) and $1/T_{\text{SE}}^{(A)}$ is the spin exchange rate defined as:

$$\frac{1}{T_{\text{SE}}^{(A)}} = n_B \bar{v} \sigma_{\text{SE}}^{(AB)} \quad (1:1.80)$$

with n_B the number density of species B and $\bar{v} = \sqrt{8k_B T / \pi M}$ the mean relative velocity of the colliding pair. The energy shift Hamiltonian contribution, $\delta\mathcal{H}_{\text{SE}}^{(AB)}$, is given by:

$$\delta\mathcal{H}_{\text{SE}}^{(AB)} = \frac{2\hbar \kappa_{AB}}{T_{\text{SE}}^{(AB)}} \langle \mathbf{S}_B \rangle \cdot \mathbf{S}_A \quad (1:1.81)$$

The parameter $\kappa_{AB} = \frac{\pi}{\sigma} \int_0^\infty \sin \theta b db$ in the classical path theory or $\kappa_{AB} = \frac{\pi}{2k^2\sigma} \sum_{l=0}^{\infty} (2l+1) \sin[2(\delta_l^t - \delta_l^s)]$ in the partial wave approach, is generally quite

small, typically on the order of 10^{-2} . In the case of identical particles, dropping the indices and substituting \mathbf{S}_A and \mathbf{S}_B with \mathbf{S} is generally considered a justified assumption.

▷ c:/ *Case of $\langle S \rangle = 0$*

Spin exchange relaxation becomes much more tractable when the mean spin of either one or each of the colliding species is zero. Then spin exchange reduces to an electron randomization process described previously (in paragraph 1:1.4.3.a:/), as is immediately evident from setting $\langle \mathbf{S}_A \rangle = \langle \mathbf{S}_B \rangle = 0$ in Eq.(1:1.79). Due to the induced simplicity in this case, spin exchange cross sections are usually measured under such conditions, typically through the relaxation rate of some eigenobservable of the system, which is bound to be connected in a simple manner to the spin exchange relaxation rate. The most widely used such measurement is that of $\langle \mathbf{S} \cdot \mathbf{I} \rangle$ which relaxes precisely at $1/T_{SE}$. Experimental values of spin exchange cross sections are given in Table A#1.

▷ d:/ *Case of $\langle S \rangle \neq 0$ and the Spin-temperature limit*

When the average spin of the vapor is non-zero, the spin exchange interaction becomes rather complicated. It is, however, quite often the case that spin exchange relaxation is much more rapid than any other relaxation mechanism in the system. Then, it can be shown ([Hap72, KWH88, WC94] and references therein) that the atomic polarization is defined by a *spin temperature*, β , with the density matrix,

$$\rho(\beta) = N e^{\beta F_z}, \quad (1:1.82)$$

being invariant under both the hyperfine Hamiltonian and spin exchange collisions, i.e.:

$$\frac{d\rho(\beta)}{dt} = 0 \quad (1:1.83)$$

The density matrix in Eq.(1:1.82) can be factored into a nuclear and an electronic part:

$$\rho(\beta) = N_I(\beta) e^{\beta I_z} N_S(\beta) e^{\beta S_z} \quad (1:1.84)$$

where the normalization constants are just the inverse of the corresponding spin partition function, which for an arbitrary spin, K , is given by:

$$N_K(\beta) = \frac{1}{Z_K(\beta)} = \frac{\sinh[\beta(K + 1/2)]}{\sinh(\beta/2)} \quad (1:1.85)$$

Implementing a multipole expansion on the density matrix constituents, one can obtain [Hap72]:

$$N_K(\beta) e^{\beta K_z} = \sum_L \langle T_{L,0}(KK) \rangle T_{L,0}(KK) \quad (1.1.86)$$

where the expansion coefficients are given by:

$$\langle T_{L,0}(KK) \rangle = i^L \sqrt{2\pi} N_K(\beta) f_L(K, i\beta) \quad (1.1.87)$$

with f_L being the *periodic Bessel functions*:

$$f_L(K, x) = \frac{1}{i^L \sqrt{2\pi}} \sum_m (-1)^{m-K} \mathbb{C}_{m,-m,0}^{K,K,L} e^{-imx} \quad (1.1.88)$$

By use of Eqs. (1.1.86) and (1.1.87) one can express the expectation value of any observable in terms of β . Of particular importance is the mean value of the \hat{z} -projection of the arbitrary spin K :

$$\langle K_z \rangle = \frac{\varepsilon(K, \beta)}{2} \tanh\left(\frac{\beta}{2}\right) \quad (1.1.89)$$

with the *paramagnetic factor*, ε , being defined as:

$$\varepsilon(K, \beta) = 2\langle K(K+1) - K_z^2 \rangle. \quad (1.1.90)$$

For the sake of illustration, in Fig. 1.1-5a we depict a case of spin exchange collision between two $I = \frac{3}{2}$, $J = \frac{1}{2}$ (and, so $F = 1, 2$) alkali atoms, each initially in the state $|2, 1\rangle$. As it is seen, the collision redistributes the populations among the hyperfine sublevels. However, a trivial calculation reveals that the total electronic spin is conserved. After a number of such collisions, the sublevel populations converge to a spin temperature distribution depicted in Fig. 1.1-5b.

▷ e:/ *Effects of rapid spin exchange*

A surprising phenomenon related to spin exchange surfaces in the regime of very rapid spin exchange collisions, i.e. at high densities where the alkali vapor becomes very optically thick. It has to do with the occurrence of narrow RF magnetic resonance lines around a frequency which is a constant fraction of the Larmor frequency. The fraction is characteristic of the alkali metal at hand and the width of the resonances scales inversely proportionally to the spin exchange rate [HT73]. A rather exhaustive treatment of the underlying process has been given in [HT77], where the authors approach the subject in as many as four different ways. Since in our lab we can fulfill the initiating conditions of this phenomenon with relative ease, we devote this paragraph for its description. The following discussion is largely - and naturally - based on [HT77].

For sufficiently rapid spin exchange, it may be argued that the spin polarization follows a spin temperature distribution at all times. If the spin temperature is assumed to be small, the density matrix is, to first order in β :

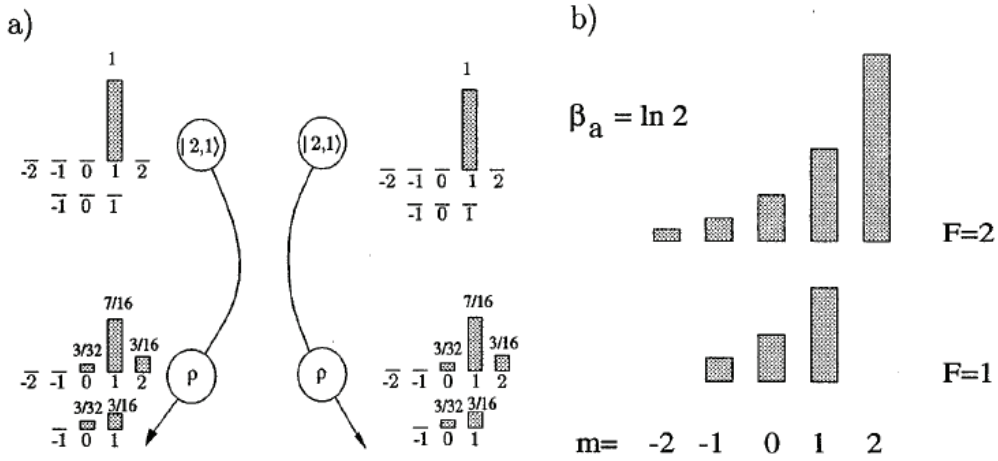


Figure I:1-5

(a) Spin exchange collision between two alkali atoms. The total spin is conserved, but the hyperfine sublevel populations are redistributed.

(b) The spin temperature distribution is arrived at after many spin exchange collisions. (Figure taken from [WH97]).

$$\rho = \frac{1 + \boldsymbol{\beta} \cdot \mathbf{F}}{(2I + 1)(2S + 1)} + \mathcal{O}(\beta^2) \quad (\text{I:1.91})$$

From the above or from Eq.(I:1.89) and (I:1.90) we get:

$$\langle \mathbf{K} \rangle = \frac{1}{3} K(K + 1) \boldsymbol{\beta} + \mathcal{O}(\beta^2), \quad \text{where } K = I, S \quad (\text{I:1.92})$$

The fraction of the total angular momentum carried by the electron is easily seen to be:

$$q = \frac{S(S + 1)}{I(I + 1) + S(S + 1)} + \mathcal{O}(\beta^2) \quad (\text{I:1.93})$$

The factor q is termed the *slowing down factor* and is listed for the alkali metals in Table A#1 (for $\beta \ll 1$).

As the electronic spins are randomized by weaker binary collisions, such as those with buffer gas atoms or spin destruction collisions with other alkali atoms, the density matrix decays at this randomization rate, $1/T$, but all along following adiabatically a spin temperature distribution. Then, the rate of decay of the total angular momentum and, consequently, of the spin temperature will be:

$$\frac{d\langle \mathbf{F} \rangle}{dt} = -\frac{1}{T} \langle \mathbf{S} \rangle \Leftrightarrow \frac{d\boldsymbol{\beta}}{dt} = -\frac{q}{T} \boldsymbol{\beta} \quad (\text{I:1.94})$$

that is, the spin temperature declines more slowly than the average electronic spin, since it can only decay *through* the electronic spin and the latter holds just a fraction q of the total angular momentum of the system.

We now apply a transverse external magnetic field, \mathbf{B} , such that the Larmor frequency is much smaller than the spin exchange rate:

$$\omega_o T_{SE} \ll 1, \quad \text{with } \omega_o = \frac{1}{I(I+1)} \frac{g_J \mu_B B}{\hbar} \quad (1.1.95)$$

Since $g_J \gg g_I$, the electronic spin is more heavily affected by the external field than the nuclear spin. If Eq.(1.1.95) is well justified, the torque equation will yield approximately:

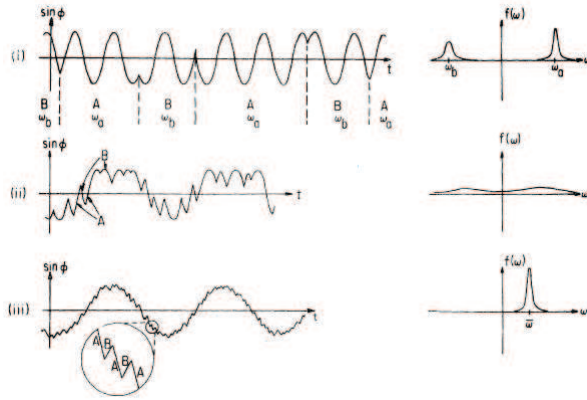
$$\frac{d\langle \mathbf{F} \rangle}{dt} = -\frac{g_J \mu_B}{\hbar} \mathbf{B} \times \langle \mathbf{S} \rangle \quad \Leftrightarrow \quad \frac{d\vec{\beta}}{dt} = \vec{\omega}_\infty \times \vec{\beta} \quad (1.1.96)$$

with the “infinitely rapid” spin exchange precession frequency being quite different than the normal, low density Larmor frequency in Eq.(1.1.95) and given by:

$$\omega_\infty = q \frac{g_J \mu_B B}{\hbar} = \frac{3(2I+1)}{3+4I(I+1)} \omega_o \quad (1.1.97)$$

These intuitive arguments demonstrate the effect that very rapid spin exchange collisions have on the magnetic properties and the evolution of an alkali metal vapor and can be verified by more a more rigorous, multipole expansion approach.

However, the discussion above does not make clear why the magnetic resonance lines become narrower in the very rapid spin exchange regime, i.e. how very rapid spin exchange ultimately decouples the atomic system from the spin exchange mechanism. To understand this, we produce another intuitive picture of the inner workings of the system. The situation for various spin exchange rates is depicted in Fig.1-1-6. For a spin exchange rate which is slow relative to the low density Larmor frequency, ω_o , the atom remains on each hyperfine level for substantial time periods, sufficient for its spin to precess about the external magnetic field. Then, through a spin exchange collision, the atom hops to the other hyperfine level, where, again, it precesses about the magnetic field, albeit in the opposite direction. The Fourier spectrum yields two pronounced peaks at $\pm\omega_o$, with a width determined by the occasional phase jumps produced by the spin exchange collisions. This is the situation in Fig.1-1-6(i). As the spin exchange rate becomes comparable to the Larmor frequency [Fig.1-1-6(ii)], the atom has barely the time to precess about the magnetic field before hopping to the other hyperfine multiplet and the resonant peaks become wider and begin to overlap. At very rapid spin exchange [Fig.1-1-6(iii)], the two hyperfine multiplets become locked together and the atom precesses in the same direction at the effective frequency ω_∞ . The more the spin exchange rate grows larger, the less jagged the precession of the atom becomes and, consequently, the narrower the resonant peak. Effectively, spin exchange stops being a limiting factor in the precision of magnetic resonance related measurements in this regime, and other processes

**Figure 1:1-6**

Effect of spin exchange at various rates on the precession of an atom about an external magnetic field and the corresponding Fourier spectrum (Figure taken from [HT77]).

- (i) Slow, $1/T_{SE} \ll \omega_0$
- (ii) intermediate, $1/T_{SE} \sim \omega_0$
- (iii) and rapid, $1/T_{SE} \gg \omega_0$ spin exchange rate.

assume this role, such as the alkali atom-buffer gas collisions, alkali-alkali spin destruction collisions, diffusion etc. The transverse relaxation rate related to spin exchange in this case is given by [ALKR02]:

$$\frac{1}{T_2^{(SE)}} = \frac{\omega_0^2 T_{SE}}{2 q^2} [1 - q^2 (2I + 1)^2] \quad (1.1.98)$$

1.1.5 Light propagation

We give here a theory of light propagation based on the Columbia/Princeton approach, developed by Prof. William Happer and colleagues [HM67a, HM67b, MTH70, Hap72, WKH⁺86]. Other equivalent approaches exist in the literature (see for example [CTL67b, CTL67a, GSM06]; also any book on atom-light interactions), but over the years and due to scientific affinity relations, we have become accustomed to this particular treatment. More than that, since the rest of the work is treated in the framework developed by these authors, a consistent nomenclature and formalism is easier to maintain throughout the text.

1.1.5.1 Polarizability and susceptibility

The propagation of light through the alkali vapor is determined by the expectation value of the dielectric susceptibility operator. The general picture is that the electric field of the incoming light induces oscillations of the valence electrons of the alkali atoms, by means of the electric dipole interaction. The specific form of these oscillations is determined, of course, by the polarization and amplitude of the electric field of the light, but also by the polarization state of the vapor, as described by its dielectric susceptibility. The oscillating vapor, then, acts as a source in the wave equations describing the evolution of light, affecting it both in intensity and phase and imprinting on it characteristics of the atomic polarization.

In the semi-classical picture we will be using^{||} the incoming light can be described as a composition of many monochromatic plane waves of the form:

$$\mathbf{E} = \mathcal{E}(z, t) e^{i(\mathbf{k}\cdot\mathbf{r}-\omega t)} + \text{complex conjugate} \quad (1.1.99)$$

where $\mathcal{E} = \hat{e} \mathcal{E}$, with \hat{e} being the - complex - light polarization vector and \mathcal{E} a slowly varying function of time, t , and distance along the propagation direction, z , with $z = (1/k)\mathbf{k} \cdot \mathbf{r}$.

The oscillating field induces an oscillating dipole moment, \mathbf{d} , in each atom, thus we may write:

$$\mathbf{d} = \wp e^{i(\mathbf{k}\cdot\mathbf{r}-\omega t)} + \text{c.c.} \quad (1.1.100)$$

For weak fields** the dipole moment amplitude is proportional to the electric field amplitude:

$$\wp = \langle \ddot{\alpha} \rangle \mathcal{E} \quad (1.1.101)$$

where the *polarizability dyadic*, $\langle \ddot{\alpha} \rangle$, is the expectation value of the ground state polarizability operator, $\langle \ddot{\alpha} \rangle = \text{Tr}(\rho_g \ddot{\alpha})$, with ρ_g the ground state density matrix.

For a vapor with number density of atoms n_d , the *dielectric susceptibility* operator and, consequently, the dielectric susceptibility dyadic of the vapor which is its expectation value, are just:

$$\ddot{\chi} = n_d \ddot{\alpha} \Rightarrow \langle \ddot{\chi} \rangle = \text{Tr}(\rho_g \ddot{\chi}) \quad (1.1.102)$$

that is to say, the susceptibility is the polarizability per unit volume or, inversely, the polarizability is the susceptibility per atom.

The macroscopic polarization of the vapor, which will act as a source for further propagation of the electromagnetic wave, can then be written as:

$$\mathbf{P} = n\mathbf{d} = \mathcal{P} e^{i(\mathbf{k}\cdot\mathbf{r}-\omega t)} + \text{c.c.} \quad (1.1.103)$$

Using any combination of defined elements, $\mathcal{P} = \langle \ddot{\chi} \rangle \mathcal{E} = n_d \langle \ddot{\alpha} \rangle \mathcal{E}$. It is important to note two things at this point. The first one is that the susceptibility dyadic contains, in general, both real and imaginary components, which are passed on to the polarization of the vapor. Real components will cause phase changes to the beam, while imaginary ones will cause attenuation. This will become clearer immediately below where we define the - more familiar - index of refraction. The second thing is that, although the vapor is driven by a monochromatic field, the

^{||}A picture routinely employed, wherein the atoms are treated quantum mechanically and the light as a classical electromagnetic wave.

**One measure of “weak” field is to compare its Rabi frequency, $\Omega = \wp \cdot \mathcal{E}/\hbar$ to the spontaneous decay rate, Γ ; it must be much smaller. In any case, weak is a field which is absorbed at a rate much slower than Γ .

induced oscillating polarization may contain a multitude of sideband frequencies, owing to possible, non-zero coherences (off-diagonal elements) in the ground state density matrix, which oscillate at the various ground state transition frequencies and which are inherited by the polarizability and the susceptibility.

In the general case, the susceptibility is frequency dependent and can be put in the form:

$$\langle \ddot{\chi}(\omega, z, t) \rangle = \sum_{\omega'} \langle \omega' | \ddot{\chi} | \omega \rangle e^{i[(k'-k)z - (\omega' - \omega)t]} \quad (1.1.104)$$

where the sum is such that all coherence frequencies are included in the difference frequencies $\omega - \omega'$. Eq. (1.1.104) implies that, apart from polarization changes and attenuation of the light beam, the susceptibility can also induce frequency mixing. However, in many realistic cases the susceptibility of the vapor is more or less spatially homogeneous and slowly varying and the frequency mixing elements in the equation above become δ -correlated:

$$\langle \omega' | \ddot{\chi} | \omega \rangle = \delta_{\omega, \omega'} \langle \ddot{\chi}(\omega) \rangle \quad (1.1.105)$$

so no frequency mixing is induced. Under these conditions, the electric field of the light wave takes the form:

$$\mathbf{E}(z, t) = \mathcal{E}(0, t) e^{i(\tilde{n} k z - \omega t)} + c.c. \quad (1.1.106)$$

where to conclude the definition of familiar and frequently quoted quantities, the *dielectric tensor* and the *index of refraction* are related to the susceptibility through:

$$\ddot{\epsilon} = 1 + 4 \pi \langle \ddot{\chi} \rangle \quad (1.1.107)$$

$$\tilde{n} = \sqrt{\ddot{\epsilon}_{\perp}} \simeq 1 + 2 \pi \langle \ddot{\chi}_{\perp} \rangle \quad (1.1.108)$$

We point out a few things here. First of all, we note that the transverse components of $\ddot{\epsilon}$ or $\langle \ddot{\chi} \rangle$ have been used for the definition of the refractive index, since longitudinal components produce longitudinal components of the polarization, which can not affect the propagation of light, since electric dipoles do not radiate along their axes. The transverse susceptibility is obtained through:

$$\langle \ddot{\chi}_{\perp} \rangle = \ddot{\mathbf{P}}_{\perp}(\hat{\mathbf{k}}) \cdot \langle \ddot{\chi} \rangle \cdot \ddot{\mathbf{P}}_{\perp}(\hat{\mathbf{k}}) \quad (1.1.109)$$

where the transverse projection operator is $\ddot{\mathbf{P}}_{\perp}(\hat{\mathbf{k}}) = \mathbf{1} - \hat{\mathbf{k}}\hat{\mathbf{k}}$. The above discussion is also true for when the macroscopic polarization is used to propagate the light beam, but there it is not necessary to explicitly keep out the longitudinal component of $\ddot{\chi}$, since it is rigorously dropped through the inner product with the - necessarily transverse - polarization of the light field.

Another thing to note is that the refractive index always has two transverse eigenvectors, \hat{e}_λ , which represent the eigenpolarizations of the wave surfaces of the vapor and for which $\hat{n} \hat{e}_\lambda = n_\lambda \hat{e}_\lambda$. In the most common case of \hat{z} -propagation, these are just the \hat{u}_\pm vectors defined in Eq. (1.1.15) and correspond to σ^\pm -polarization.

Finally, to illustrate how the complex nature of the susceptibility causes both phase and amplitude alterations to the travelling wave, we consider the simple case of an isotropic, homogeneous vapor, in which case the susceptibility reduces to a scalar $\langle \ddot{\chi} \rangle \equiv \chi = \Re(\chi) + i\Im(\chi) \equiv \chi' + i\chi''$. The refractive index is then $n = 1 + 2\pi(\chi' + i\chi'') \equiv n' + in''$ and a plane wave traversing the medium propagates proportionally to $\exp[i(nk_{\text{vac}}z - \omega t)] = \exp[i(n'k_{\text{vac}}z - \omega t)] \exp(-n''k_{\text{vac}}z)$, according to Eq. (1.1.106), where $k_{\text{vac}} = 2\pi/\lambda_{\text{vac}}$ is the vacuum wave number. Thus, n' causes phase changes and n'' causes attenuation. In a more general context, the travelling index of refraction, i.e. the real part of \hat{n} along the direction of propagation, and the *absorptivity* of the vapor, i.e. the power absorbed per unit volume and per unit flux from a light wave of frequency ω , are related to the expectation value of the susceptibility via:

$$n(\omega, z, t) = 1 + (2\pi \hat{e}^* \cdot \langle \ddot{\chi}(\omega, z, t) \rangle \cdot \hat{e} + \text{c.c.}) \quad (1.1.110)$$

$$h(\omega, z, t) = -i2\pi k \hat{e}^* \cdot \langle \ddot{\chi}(\omega, z, t) \rangle \cdot \hat{e} + \text{c.c.} \quad (1.1.111)$$

1.1.5.2 Polarizability of the alkali atoms

As the dielectric susceptibility, $\langle \ddot{\chi} \rangle$, or, equivalently the dielectric polarizability, $\langle \ddot{\alpha} \rangle$, largely determine the propagation of light through the vapor, it becomes desirable to have general expressions for these quantities for alkali atoms. The discussion below deals with this issue and expressions for the alkali polarizabilities are derived in two different ways.

▷ a:/ In terms of the dipole moment expectation value

The first approach is to relate the polarizability of an atom with the expectation value of the dipole operator. The wave function of an atom can be written as:

$$|\psi\rangle = \sum_{\mu} a_{\mu} |\mu\rangle e^{-i\omega_{\mu}t} + \sum_{m} b_m |m\rangle e^{-i\omega_m t} \quad (1.1.112)$$

where Greek and Latin letters refer to ground and excited states, respectively. Under the influence of the electric field of the light, the amplitudes of the excited states evolve as:

$$i\hbar b'_m(t) = - \sum_{\mu} \mathcal{E} \cdot \mathbf{d}_{m\mu} a_{\mu} e^{i\delta_{m\mu}t} - i\hbar \frac{\gamma}{2} b_m \quad (1.1.113)$$

where $\mathbf{d}_{m\mu} = \langle m | \mathbf{d} | \mu \rangle$, $\delta_{m\mu} = \omega_{m\mu} - \omega = \omega_m - \omega_\mu - \omega$ and γ is the collisionally broadened excited state damping rate. We assume here that the light wave is sufficiently weak so as not to perturb the ground state amplitudes significantly. Then, the steady state solution of Eq. (1.113) is:

$$b_m = \sum_{\mu} \frac{\boldsymbol{\mathcal{E}} \cdot \mathbf{d}_{m\mu}}{\hbar} \frac{1}{-i\gamma/2 - \delta_{m\mu}} a_{\mu} e^{i\delta_{m\mu}t} \quad (1.114)$$

Substituting Eq. (1.114) into Eq. (1.112) yields the density matrix:

$$\begin{aligned} \rho = |\psi\rangle\langle\psi| &= \sum_{\mu\nu} a_{\mu} a_{\nu}^* |\mu\rangle\langle\nu| e^{-i\omega_{\mu\nu}t} + \\ &+ \sum_{\substack{\mu\nu \\ mn}} \frac{\boldsymbol{\mathcal{E}} \cdot \mathbf{d}_{m\mu} \mathbf{d}_{\nu n}^* \cdot \boldsymbol{\mathcal{E}}^*}{\hbar^2} \cdot \frac{a_{\mu} a_{\nu}^* e^{i(\omega_{m\mu} - \omega_{n\nu})t}}{(-i\gamma/2 + \delta_{m\mu})(i\gamma/2 + \delta_{n\nu})} |m\rangle\langle n| + \\ &+ \sum_{\mu,\nu,m} \frac{\boldsymbol{\mathcal{E}} \cdot \mathbf{d}_{m\nu}}{\hbar} \cdot \frac{a_{\nu} a_{\mu}^* e^{i(\omega_{m\nu} - \omega)t}}{-i\gamma/2 + \delta_{m\nu}} |m\rangle\langle\mu| + \text{c.c.} \\ &= \rho_g + \rho_e + \rho_{eg} + \rho_{ge} \end{aligned} \quad (1.115)$$

Since the selection rules for the electric dipole interaction require that $\Delta L = \pm 1$, the dipole moment matrix elements vanish within the ground and the excited state multiplets, i.e. $\langle \mu | \mathbf{d} | \nu \rangle = \langle m | \mathbf{d} | n \rangle = 0$. Thus, only the ρ_{ge} and ρ_{eg} portions of the density matrix contribute to the calculation of expectation value of the dipole moment. After some manipulation (and having interchanged indices μ and ν) we get:

$$\langle \mathbf{d} \rangle = \text{Tr}[(\rho_{eg} + \rho_{ge})\mathbf{d}] = \sum_{\mu,\nu,m} \frac{\mathbf{d}_{\mu m} \mathbf{d}_{m\nu}}{\hbar} \frac{1}{-i\gamma/2 + (\omega_{m\nu} - \omega)} \rho_{\nu\mu} \boldsymbol{\mathcal{E}} e^{-i\omega t} + \text{c.c.} \quad (1.116)$$

with $\rho_{\nu\mu} = a_{\nu} a_{\mu}^* e^{-i\omega_{\nu\mu}t}$. Then, according to Eqs. (1.100) and (1.101), the atomic polarizability will be given by:

$$\langle \ddot{\alpha} \rangle = \sum_{\mu,\nu,m} \frac{\mathbf{d}_{\mu m} \mathbf{d}_{m\nu}}{\hbar} \frac{1}{-i\gamma/2 + (\omega_{m\nu} - \omega)} \rho_{\nu\mu} \quad (1.117)$$

In a spherical tensor expansion, we then get (in thermal equilibrium only the $\mu = \nu$ terms survive):

$$\langle \ddot{\alpha} \rangle = \sum_{q,l} \langle \alpha_{ql} \rangle \hat{\mathbf{u}}_q \hat{\mathbf{u}}_l^*, \quad \text{with: } \langle \alpha_{ql} \rangle = \sum_{\mu,\nu,m} \frac{1}{\hbar} \frac{(\mathbf{d}_{\mu m}^q)^\dagger \mathbf{d}_{m\nu}^l}{-i\gamma/2 + (\omega_{m\nu} - \omega)} \rho_{\nu\mu} \quad (1.118)$$

▷ *b:/ In terms of eigenobservables*

Eq. (1.118) is directly expandable in terms of the basis dyadics, by virtue of Eq. (1.17). However, before we write down this expansion, we shall make our results a little more realistic in the following sense. For hot vapors and small magnetic fields, the Zeeman splittings are quite smaller than the Doppler widths of the transitions. In this case, the transition frequencies are replaced by $\omega_{m\mu} \rightarrow \omega_{m\mu} + \mathbf{k} \cdot \mathbf{v}$, with \mathbf{v} the mean thermal velocity of the atoms, and an averaging has to be performed over a Maxwellian velocity distribution. The particulars of this procedure are quite cumbersome to be presented here, but we do present the resulting, physically realistic expression for the atomic polarizability [HM67a]:

$$\ddot{\alpha} = \sum_L \ddot{\alpha}_L = \sum_L \sum_{f, f', M} A_L(f f') (-1)^M \ddot{\mathbf{Q}}_{L, -M} T_{L, M}(f, f') \quad (1.119)$$

where f, f' refer to the ground state and:

$$A_L(f f') = \sum_{F_e} G \xi_L(f f'; F_e) Z(F_e, f') \quad (1.120)$$

with $G = \frac{\lambda_{\text{vac}}^2 (J_g, J_e) e^2 f_{ge}}{8\pi^2 m c^2} \sqrt{\frac{m c^2}{2k_B T}}$. Here $Z(v)$ is the plasma dispersion function:

$$Z(v) = \frac{1}{\sqrt{\pi}} \int_{-\infty}^{\infty} \frac{e^{-u^2}}{u - v} du \quad (1.121)$$

and the particular quantity shown in Eq. (1.120) is defined as:

$$Z(F', F) \equiv Z(x(F', F) + iy) \text{ with } \begin{cases} x(F', F) = \sqrt{\frac{m c^2}{2k_B T}} \frac{\omega - \omega_{F'F}}{\omega} \\ y = \sqrt{\frac{m c^2}{2k_B T}} \frac{\frac{\Gamma}{2} + \gamma_c}{\omega} \quad (\gamma = \frac{\Gamma}{2} + \gamma_c) \end{cases} \quad (1.122)$$

In this term lies the dependence on the frequency of the incoming light wave. Finally, the coefficient ξ in Eq. (1.120) contains all the geometric features of the dyadic expansion and is shown to be:

$$\begin{aligned} \xi_L(f f'; F_e) &= 3(-1)^{F_e - f' - 1} \sqrt{(2f + 1)(2f' + 1)(2J_g + 1)(2F_e + 1)} \times \\ &\times \mathbb{W}(11 f f'; L F_e) \mathbb{W}(J_e F_e J_g f; I1) \mathbb{W}(J_e F_e J_g f'; I1) \end{aligned} \quad (1.123)$$

Although the expression derived above is completely legitimate, decomposing the polarizability in terms of eigenobservables, as discussed earlier, facilitates

gaining a more intuitive feeling of the various interactions. We pursue such a decomposition here. The polarizability operator can be written as a sum of three components:

$$\ddot{\alpha} = (\alpha_{\text{eq}} + \alpha_{\text{hf}} \mathbf{I} \cdot \mathbf{J}) \ddot{\mathbf{1}} + i \sum_{f,f'} \alpha_{\text{gt}}(f, f') \mathbf{J}(f, f') \times + \sum_{f,f'} \alpha_{\text{br}}(f, f') \ddot{\mathbf{Q}}(f, f') \quad (\text{I.1.124})$$

The first term is *isotropic*, i.e. independent of the expectation value of operators which define preferred spatial directions, and comprises an equilibrium and a hyperfine structure component. The second term is *gyrotropic* and depends on the electronic polarization, $\langle \mathbf{J} \rangle$. The final term is *birefringent* and depends on the expectation value of the quadrupole operators, $\langle \ddot{\mathbf{Q}}_{2,m} \rangle$. We pause to remind to the reader the discussion in paragraph I.1.3.2 d:/ about the multipole expansions of the density matrix and how light can couple at most to quadrupole moments. Here this discussion becomes formally founded, with the polarizability of the atom shown to couple indeed to multipoles of maximum rank $L = 2$. The existence of possible octupole or higher order population structure in the ground state density matrix can not be interrogated by a weak probing light beam. We now proceed to study each of the terms in Eq. (I.1.124) separately.

Isotropic polarizability: The equilibrium polarizability, α_{eq} , is independent of the state of the vapor and it represents the response of a vapor in thermal equilibrium, i.e. as if the vapor was described by $\rho_{\mu\nu}^{(\text{eq})} \simeq \frac{\delta_{\mu\nu}}{(2J_g+1)(2I+1)} (1 - \frac{E_\mu}{k_B T})$, with $E_\mu \ll k_B T$. The hyperfine structure polarizability appears when there is population imbalance between the two hyperfine multiplets, i.e. when $\langle \mathbf{I} \cdot \mathbf{J} \rangle \neq 0$. The isotropic polarizability is collectively written as:

$$\alpha_0 = (\alpha_{\text{eq}} + \alpha_{\text{hf}} \mathbf{I} \cdot \mathbf{J}) \ddot{\mathbf{1}} \quad (\text{I.1.125})$$

where $\ddot{\mathbf{1}} = \sum_q \hat{q} \hat{q}^* = \sqrt{3} \ddot{\mathbf{Q}}_{0,0}$ is the unit dyadic. Using the dyadic expansion (I.1.119), we get the response functions:

$$\alpha_{\text{eq}} = \frac{1}{2\sqrt{3}(2I+1)} \sum_f A_0(ff) \sqrt{2f+1} \quad (\text{I.1.126})$$

$$\alpha_{\text{hf}} = \frac{2}{\sqrt{3}(2I+1)} \sum_f \frac{A_0(ff)}{\sqrt{2f+1}} (-1)^{I+\frac{1}{2}-f} \quad (\text{I.1.127})$$

From Eq. (I.1.110) we derive the absorptivity induced by the equilibrium and hyperfine structure polarizability:

$$h_{\text{eq}} = 4 \pi k n_d \Im(\alpha_{\text{eq}}) \quad (\text{I.1.128})$$

$$h_{\text{hf}} = 4 \pi k n_d \langle \mathbf{I} \cdot \mathbf{J} \rangle \Im(\alpha_{\text{hf}}) \quad (\text{I.1.129})$$

from which we verify that the equilibrium polarizability induces absorption independent of the state of the vapor, while the absorption due to the hyperfine structure polarizability depends on the population difference between the two hyperfine multiplets, but not on the particular polarization state in these multiplets.

The isotropic part of the polarizability does not affect the wave surfaces of the light wave, which remain spherical, and the shape of the light beam is not affected in any way other than the change of the spatial rate of dispersion. Attenuation is induced, but the polarization state of light remains unaffected.

A note on the eigenobservable expansion: Before proceeding any further and to understand the origins of the eigenobservable decomposition and its frequency response functions, we study the $L = 0$ component of the multipole expansion of α . Taking into account that for $L = 0$, both $A_0(f, f') = 0$ and $T_{0,0}(f, f') = 0$ for $f \neq f'$ and that the unit dyad is $\ddot{\mathbf{I}} = \sqrt{3}\ddot{\mathbf{Q}}$, we get:

$$\alpha_0 = \ddot{\mathbf{I}} \sum_f \frac{1}{\sqrt{3}} A_0(f, f) T_{0,0}(f, f) \quad (1.130)$$

It is easily seen that the 0-order spherical tensor can be put in the form:

$$T_{0,0}(f, f) = \frac{\sqrt{2f+1}}{2(2I+1)} + (-1)^{I+\frac{1}{2}-f} \frac{2}{(2I+1)\sqrt{2f+1}} \mathbf{I} \cdot \mathbf{J} \quad (1.131)$$

The expression above is enlightening in the sense that, if the density matrix was isotropic it would be just:

$$\rho = \sum_f \frac{T_{0,0}(f, f)}{\sqrt{2f+1}} = \frac{1}{2(2I+1)} + (-1)^{I+\frac{1}{2}-f} \frac{2}{(2I+1)(2f+1)} \mathbf{I} \cdot \mathbf{J} \quad (1.132)$$

that is to say that, as is reasonable, the population of each magnetic sublevel will be the equilibrium value, $\frac{1}{(2\frac{1}{2}+1)(2I+1)}$, plus or minus a quantity dependent on the f value of the state and corresponding to the population imbalance between the hyperfine multiplets, i.e. to the expectation value of $\mathbf{I} \cdot \mathbf{J}$. From here on, decomposing the isotropic polarizability according to Eq. (1.125) and obtaining the equilibrium and hyperfine frequency responses is a trivial task. Analogous discussions can be held for the gyrotropic and birefringent polarizabilities of the vapor.

Gyrotropic polarizability: The gyrotropic polarizability of the vapor is anisotropic and depends on the expectation value of the electronic spin, $\langle J \rangle$, that is it induces alterations on the field, dependent on the specific orientation of the electronic polarization vector. We remind here that the latter may contain coherences between the hyperfine multiplets, since the multipole expansion of \mathbf{J} in terms of the hyperfine spherical tensor basis, contains terms both with $f = f'$, as well as with $f \neq f'$, as is seen in Eq. (1.29). It is given by^{††}:

$$\alpha_1 = i \sum_{f, f'} \alpha_{\text{gt}}(f, f') \bar{\mathbf{J}}(f, f') \times \quad (1.133)$$

^{††}The “ \times ” at the end of the expression is the vector cross product operator; not a typo.

where $\bar{\mathbf{J}}(f, f') = \sum_{\mu, \mu'} |f\mu\rangle\langle f\mu| \mathbf{J} |f'\mu'\rangle\langle f'\mu'|$. Using:

$$\begin{aligned} \bar{\mathbf{J}}(f, f') &= \sum_q (-1)^q \hat{\mathbf{u}}_{-q} T_{1,q}(ff') \mathbb{W}(1J_g f I; J_g f') \times \\ &\times \sqrt{\frac{J_g(J_g+1)(2J_g+1)(2f+1)(2f'+1)}{3}} \end{aligned} \quad (1.1.134)$$

and the dyadic decomposition of the vector cross product, Eq. (1.1.20), the frequency response functions are found to be:

$$\begin{aligned} \alpha_{\text{gt}}(f, f') &= -6G \sum_{F_e} (-1)^{F_e-f} (2F_e+1) Z(F_e, f') \times \\ &\times \frac{\mathbb{W}(11ff'; 1F_e) \mathbb{W}(J_e F_e \frac{1}{2}f; I1) \mathbb{W}(J_e F_e \frac{1}{2}f'; I1)}{\mathbb{W}(1\frac{1}{2}fI; \frac{1}{2}f')} \end{aligned} \quad (1.1.135)$$

In the absence of hyperfine coherence, the gyrotropic absorptivity is given by:

$$h_{\text{gt}} = 4\pi k n_d \sum_f \langle \bar{\mathbf{J}}(ff) \rangle \cdot \hat{\mathbf{s}} \Im(\alpha_{\text{gt}}(ff)) \quad (1.1.136)$$

where $\hat{\mathbf{s}}$ is the, so called, *mean photon spin* and it is a unit vector parallel (anti-parallel) to the direction of propagation for right (left) circularly polarized light, or lies somewhere in between these extremes:

$$\hat{\mathbf{s}} = i \hat{\mathbf{e}} \times \hat{\mathbf{e}}^* \quad (1.1.137)$$

The gyrotropic part of the polarizability causes the electric displacement field to acquire a non-zero component along the electronic spin polarization. This causes physical deformation of the wave surfaces, which become ellipsoids; in opposite senses for the two eigenpolarizations. A beam of circular cross section will become more and more elliptical as it propagates through the medium. This type of polarizability both attenuates the beam and induces changes in its state of polarization. As the medium responds differently to the two eigenpolarizations of light, the polarization vector of linearly polarized incident light will be rotated by the difference in the phase acquired by the two eigenpolarization components and will become elliptical due to their different attenuation rates.

Birefringent polarizability: The birefringent polarizability is anisotropic and depends on the expectation values of quadrupole operators, that is it induces alterations on the field dependent on the alignment of the vapor populations^{‡‡}. Birefringence in alkali metals becomes noticeable only for the heaviest members

^{‡‡} *Aligned* is a non-equilibrium distribution for which $\rho_{\mu, \mu} = \rho_{-\mu, -\mu}$

of the family (Rb, Cs), as it requires an appreciable excited state hyperfine splitting relative to the Doppler widths of the absorption lines. The birefringence polarizability is given by:

$$\ddot{\alpha}_2 = \sum_{f,f'} \alpha_{\text{br}}(f, f') \ddot{\mathbf{Q}}(f, f') \quad (1.138)$$

where the quadrupole operators are defined as:

$$\ddot{\mathbf{Q}}(f, f') = \sum_{\mu} (-1)^{\mu} \ddot{\mathbf{Q}}_{2,\mu} T_{2,-\mu}(f, f') \quad (1.139)$$

and the frequency response functions:

$$\alpha_{\text{br}}(f, f') = A_2(f, f') \quad (1.140)$$

In the absence of hyperfine coherence, the birefringent absorptivity is:

$$h_{\text{br}} = 4 \pi k n_d \sum_f \hat{\mathbf{e}}^* \cdot \langle \ddot{\mathbf{Q}}(ff) \rangle \cdot \hat{\mathbf{e}} \Im(\alpha_{\text{br}}(ff)) \quad (1.141)$$

dependent, as expected, on the expectation value of the quadrupole operators.

The birefringent polarizability of the vapor causes a behavior identical to that of a birefringent crystal (albeit weaker), with the axis of the quadrupole operator corresponding to the fast axis of the crystal. In the absence of hyperfine coherence, the vapor behaves as a uniaxial crystal. Wave surfaces of light polarized perpendicularly to this axis (ordinary ray) are unaffected spheres, while they become ellipsoids for parallel polarization (extraordinary ray). Polarization changes come about through the different phase velocities of the ordinary and extraordinary components.

▷ c:/ *Faraday rotation*

In this paragraph we assume that linearly polarized light propagates along the \hat{z} -axis. The eigenpolarizations in this case are the $\hat{\mathbf{u}}_{\pm}$ corresponding to the σ^{\pm} components into which the linear polarization is decomposed. Should the indices of refraction for the two components were different, each would accumulate different phase traversing the medium, due to the different phase velocities. As a result, the emerging light has a polarization which is rotated by some angle relative to the polarization plane of the incident light. This process constitutes the *Faraday effect*, with the angle, θ , easily shown to be:

$$\theta = \frac{\pi(n_+ - n_-)l}{\lambda_{\text{vac}}} \quad (1.142)$$

where l is the traversed medium length and λ_{vac} is the vacuum wavelength of the light wave.

To quantify the effect, we give the expressions for the indices of refraction. Starting from Eq. (1.110) and the general expressions for the atomic polarizabilities, (1.124), (1.125), (1.133) and (1.138), after some manipulation, we arrive at:

$$n_{\pm} = 1 + \delta n_0 + \delta n_{\pm} \quad (1.143)$$

with the isotropic, δn_0 , and gyrotropic, δn_{\pm} , parts being given by*:

$$\delta n_0 = \sum_f \frac{\pi n_a e^2 f_{ge}}{m_e c \omega_f} \frac{\omega - \omega_f}{(\omega - \omega_f)^2 + \gamma^2} p_f \quad (1.144)$$

$$\delta n_{\pm} = \sum_f \frac{\pi n_a e^2 f_{ge}}{m_e c \omega_f} \frac{\omega - \omega_f}{(\omega - \omega_f)^2 + \gamma^2} \frac{11 - 4J_e(J_e + 1)}{4} \langle \bar{\mathbf{J}}(f, f) \rangle \cdot \hat{\mathbf{s}}_{\pm} \quad (1.145)$$

where p_f is the f -hyperfine multiplet population, related to $\langle \mathbf{I} \cdot \mathbf{J} \rangle$ via ($J = 1/2$):

$$p_f = \frac{2}{f(f+1) - I(I+1) - 3/4} \frac{2f+1}{2(2I+1)} \times \\ \times \left[\frac{(2f-1)(2f+3) - 4I(I+1)}{8} + \left(\frac{2(2I+1)}{2f+1} - 1 \right) \langle \mathbf{I} \cdot \mathbf{J} \rangle \right]$$

$$\text{or, simply, for the } a = I + 1/2 \text{ and } b = I - 1/2 \quad (1.146)$$

$$p_a = \sqrt{2a+1} \text{Tr}[\rho.T_{0,0}(a, a)] = \frac{I+1+2\langle \mathbf{I} \cdot \mathbf{J} \rangle}{2I+1}$$

$$p_b = \sqrt{2b+1} \text{Tr}[\rho.T_{0,0}(b, b)] = \frac{I-2\langle \mathbf{I} \cdot \mathbf{J} \rangle}{2I+1}$$

The inverse relation is:

$$\langle \mathbf{I} \cdot \mathbf{J} \rangle = \sum_f \frac{f(f+1) - I(I+1) - \frac{3}{4}}{2} p_f = \\ = \frac{I}{2} p_a - \frac{I+1}{2} p_b \quad (1.147)$$

Also in Eq. (1.145), $\bar{\mathbf{J}}(f, f)$ is defined in Eq. (1.134), the mean photon spin is $\hat{\mathbf{s}}_{\pm} = \pm \hat{\mathbf{u}}_0$ and the excited state hyperfine structure and quadrupole terms have been neglected. We note here that, as mentioned in a previous discussion, the excited state hyperfine structure of the heavier alkali atoms can not be neglected

*These are in CGS units and with $\hbar = 1$. To return to SI, one has to divide the expressions by $1/(4\pi\epsilon_0)$ and replace the ω 's in the central fraction by $\hbar\omega$ (note: the ω_f in the leftmost fraction remains as is).

under normal circumstances. However, in the far wings of the dispersion profiles where our experiments were carried out, even the ground state can be ignored and one can work with just the fine splitting states. But even closer to resonance, in realistic conditions the influence of the excited hyperfine structure can be taken into account as a small correction in the Lorentzian profiles of the calculated line shapes. As expected, the indices of refraction share a common, isotropic part dependent on the equilibrium polarizability and the hyperfine multiplet population difference, but also contain an anisotropic contribution dependent on the electronic spin polarization, which is of opposite sign for the two eigenpolarizations. We capitalize on the Faraday effect in Ch.I:3 and Appendix C, both as a tool for the determination of alkali vapor densities, as well as the main process leading to the observed signals in spin noise measurements.



With this we conclude the chapter on the description and theoretical approach of alkali atoms. A significant part of this mathematical arsenal has been used in our group, while the rest provides a much wider scope than what we have encountered. Although complicated, mainly due to the existence of hyperfine structure, we believe this formalism to provide a clear and intuitive understanding of the physical processes involved and great versatility in calculations once the general framework has been implemented.

Chapter 1:2

Laboratory

In this chapter we describe our laboratory. It is divided in four parts: the “patient” refers to the atomic vapor related parts, which suffers in our hands, the “operating theater” comprises the tables and shields upon and into which the patient and the instruments reside, the “surgical instruments” are the lasers and optics and “life support” help us keep him alive.

1:2.1 *The “patient”: Alkali metal vapors*

Alkali metals reside inside pyrex cells in the form of solid droplets. Heating the cell causes the droplet to partly evaporate, with the vapor pressure and number density roughly following the Killian formula:

$$\text{Pressure}_{[\text{Atm}]} : P = 10^{A+B/T} \quad , \quad \text{density}_{[\text{cm}^{-3}]} : n_d = \frac{101\,325}{10^6 k_B} \frac{10^{A+B/T}}{T} \quad (1:2.1)$$

where k_B and T are the Boltzmann constant and temperature (in °K), respectively, while A and B are element specific parameters summarized in Tab.A#1.

The cells used in our lab were filled either with pure alkali metal droplets or with mixtures of alkali metals plus buffer gas at various pressures. Alkali metals used in our experiments were rubidium and cesium, while xenon, helium or molecular nitrogen were used as buffer gases. Pure alkali cells were used mainly for laser-locking and wavelength calibration of our wavemeters, since they provide nice Doppler-broadened absorption spectra at room temperature. However, for our actual experiments, two main reasons forced the use of buffer gas filled cells: the first one was that the operating pressures of the alkali vapors were high

enough to lead to radiation trapping of spontaneously emitted photons. Molecular nitrogen is ideal for quenching such radiation. The second was that in pure alkali cells and at the high temperatures needed to produce high pressures, the combination of large time-of-flight broadening and decoherence of the alkali atoms due to collisions to the cell walls, dictates that a buffer gas is used to turn the free flight of the alkali atoms into a slow diffusive motion through the numerous buffer gas atoms. This increases the interaction time of the alkalis with the laser beam, while using the appropriate buffer gas preserves coherence even after billions of alkali-buffer gas collisions. In our case, the nitrogen used for quenching doubled acceptably as a diffusion buffer gas, although at very high pressures one would be forced to use something more drastic, such as a few Atmospheres of He.



Figure 1:2-1

Vacuum setup for filling pyrex cells with alkali metals and buffer gases.

The cells were either built-to-order by commercial suppliers (Triad Technology at Boulder, Colorado, USA, <http://www.triadtechno.com>) or filled and sealed in the vacuum setup in our lab shown in Fig.1:2-1. The setup consisted of standard vacuum components, three types of pumps (an Alcatel mechanical and a Varian Technologies turbo and ion pumps) capable of bringing the pressure below 10^{-6} Torr, a supply of buffer gases and a pyrex extension with protruding, empty, cylindrical or spherical cells. The alkali was deposited in a specific area of the pyrex extension and sealed and the system was subsequently mildly heated and evacuated. Then the pyrex extension was isolated from the rest of the system and a few droplets of the alkali metal were driven from the deposition area into the cell with an oxy-propane torch. The technique involves using a reducing (i.e. propane-rich) flame to heat the pyrex tube close to the alkali, which causes it to liquefy and flow into the hot area. By moving the heat along a continuous line, one eventually ends up with a few droplets of the metal inside the cell. The next step was to create the mixture of buffer gases at the desired pressures and allow it to flow into the extension area, filling also the

preparing cell. Finally, the inner cone of a neutral or oxidizing flame (i.e. balanced or oxygen-rich flame) was used to melt the pyrex tube holding the cell, at which point, carefully pulling the cell away would seal and detach it from the extension. Time permitting, the cells were then allowed to cure in a heated oven

before use. Unfortunately, not all cells were cured before use. In the course of our work we made cylindrical, spherical and cross cells, as shown in the bottom part of the figure (although the cross cell depicted therein is commercial), with typical pull-off pressures for the pure alkali metal filled cells on the order of 10^{-6} Torr and buffer gas pressures of $\sim 10^2$ Torr either for nitrogen or xenon.

1.2.2 The “operating theater”

1.2.2.1 Magnetic shield

Since our work aimed at low magnetic fields, the alkali metal cells had to reside inside an area shielded from external magnetic fields. To this end we used a magnetic shield comprising five concentric cylindrical layers of Mu-metal with varying thicknesses (top of Fig.1:2-2). Inside the inner layer, a plastic cylinder covered with thin layers of Mu-metal and Metglas provided further shielding and, embedded on this cylinder, was an array of coils able to produce locally homogeneous, weak magnetic fields and/or gradients [Del05] (bottom of Fig.1:2-2).

Shown also in the figure is the locally made, precision, multi-channel controller capable of providing AC or DC voltage to the coils. With the aid of this facility we were able to eliminate any remaining magnetic fields at the location of the cell and, additionally, create desired magnetic fields or gradients along any axis in three dimensional space. The controller could be operated manually or remotely, via ASCII signals through a RS232 serial port.

At the right part of the open shield in the top left figure, the degaussing wires which ran between the layers of the magnetic shield are also seen. These were used to degauss the shield, i.e. to eliminate any residual, unwanted magnetization. Six wires, each 2mm thick, were running parallel to the axis of the shield between layers and were powered by a 8.2kW ($36\text{A} \times 230\text{V}$), 3-phase variac (Belotti Variatori, Milano, Italy, <http://www.belotti.it>). A slow increase of the current and, thus, of the magnetic field produced by the wires, saturates the shield magnetization. Subsequently, slowly decreasing the current drives the shield magnetization along the

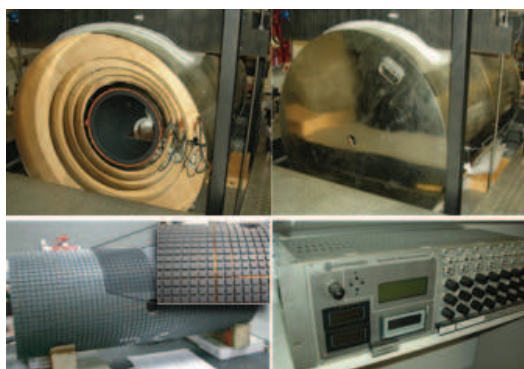


Figure 1:2-2

Top: Main Mu-metal magnetic shield with and without the end caps.

Bottom: Inner cylinder with coils and multi-channel controller.

hysteresis curve to - near - zero. The need for such a powerful transformer was, of course, dictated by the massive shield we had to degauss. The remaining, bias magnetization of the shield and possible noise magnetic fields produced by Eddy currents in the inner shield layer, were shielded by the Mu-metal and Metglas layers of the inner plastic cylinder.

A note on materials: Mu-metal is a nickel-iron alloy (usually at a $\sim 75:15$ ratio, plus other elements at low percentages). The name stems from the Greek letter *mu* (μ), the symbol of magnetic permeability and indeed implies the high relative permeability values of the alloy; typically on the order of 80,000 to 100,000. Its main use is in magnetic shielding where it is typically used in layers, each of which successively reduces the field inside it. The shielding comes not from actually blocking magnetic lines, but by providing them with a favorable path along the surface of the material, thus dictating a closed, smoothly curved shape for the shield.

Metglas is an amorphous, cobalt-based alloy ribbon produced by rapid solidification ($\sim 10^6$ °C/s). The non-crystalline structure provides unique magnetic properties to the material, such as extremely high permeability (typically $\sim 10^6$) and rapid magnetization/demagnetization times. The ultra-thin ribbons ($\sim 10\mu\text{m}$) saturate easily, though, and are thus used only inside the innermost layer of the Mu-metal shield.

All magnetic shielding materials in our lab were purchased from Less-EMF inc. (Albany, NY, USA, <http://www.lessemf.com>)

1:2.2.2 Cell heating and ovens

As described in Sec.1:2.1, our cells contained alkali metals in the solid phase. For the creation and maintenance of the desired vapor pressure, the temperature of the cell had to be kept constant by the application of heat in a controlled manner. Wrapping the cells with flexible electrical heat-bands or immersing the cells in a resistance-heated liquid container would be ideal solutions, were it not for the fact that such solutions were unacceptable; the operating currents of the heating devices (typically some form of resistor) would produce magnetic fields at the location of the cell, much larger than the geo-magnetic field we had struggled to shut out. Consequently, our cells were heated by a continuous flow of hot air around them. Air, available in the lab at a pressure of a few bars, was passing through a heater located outside the magnetic shield and, subsequently, guided onto the cell through non-magnetic tubing (high temperature plastics insulated to prevent heat losses along the way). The temperature of the cell was monitored by a platinum RTD probe, compared to a set value and a PID controller adjusted the current of the heater accordingly.

The process was complicated by the demand that the flow of air should not

pass in front of the laser input and output windows of the cell, as the turbulence would cause unpredictable changes in the index of refraction along the beam path, resulting in measurement noise. To satisfy this demand, special ovens (cell enclosures) were designed and built from special high temperature plastics in the machine shop. One such oven, out of several designs and actualizations, is shown in Fig.1:2-3. The cell was mounted inside the inner, cross-shaped enclosure and an RTD element was attached to its mount, making thermal contact through a high temperature thermal paste. This enclosure was itself enclosed inside a larger, cube-shaped box, through which the hot air was flowing. The windows of the inner enclosure reached the outer sides of the cube walls, thus never making contact with the flow of air and avoiding the aforementioned complications related to index of refraction induced noise. Assembly of the parts was done with plastic screws and all contacts were sealed tight with high temperature silicone and allowed to cure overnight. The oven was then wrapped in an insulating fiberglass fabric, mounted at the center of the magnetic shield and the air inflow and outflow tubes were attached. In a world of four spatial dimensions, the design of such an oven would be a considerably less involved task.

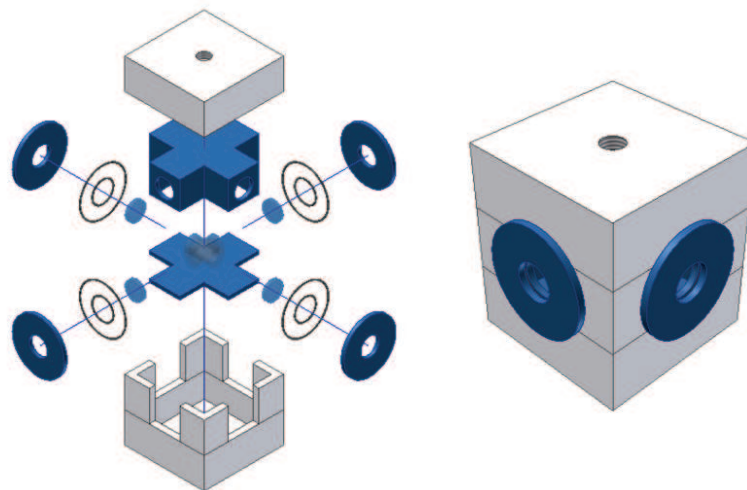


Figure 1:2-3

Alkali cell heating oven. Air flows into the white outer box from top to bottom, heating the embedded, hermetically sealed, cross-shaped cell enclosure and, eventually, the cell. In this way, air flow in the beam pathway is avoided. Parts are held together by plastic screws and air-tight sealing is achieved with high temperature silicone.

In practice the performance of the cell heating apparatus described above was acceptable, although less than ideal. Regardless of the experimentalist's good intentions or mechanical, design and electronic prowess, a number of parameters render the whole scheme inefficient. First of all, the high air pressure required by the heater so that it does not get fried, causes turbulence in the oven and

weakens the silicone sealing, eventually leading to air leakage. Turbulence is undesirable for two reasons. One is that it causes temperature inhomogeneities and, since the vapor pressure formula is - steeper than - exponential, small temperature gradients may induce large pressure gradients inside the cell; a fact with various consequences on our measurements. The second is practical: turbulence can create regions of substantially lower pressure, causing oven parts in these regions to heat up excessively and eventually melt; a rather unfortunate circumstance half way through a month-long experiment. However, these were just nuisances compared to the greater problem of the heating process, which was its unrepeatability. The culprit was the existence of the, necessary yet problematic, inner plastic enclosure. The problem was that the temperature was measured from (and set for) the cell *inside* the enclosure, while the hot air flow was *outside*. The PID circuit, trying to heat the cell, would heat the enclosure instead. When the heat finally penetrated the plastic walls, the cell temperature would rapidly overshoot (by a lot) and the PID would completely shut down the current. This caused rapid cooling of the enclosure, eventually leading to the reverse effect. As a result, achieving a steady state temperature for the cell was a matter of many hours, further prolonged by the changes in the ambient temperature of the lab due to the daily schedule of the central air conditioning. The only conceivable workaround was to put the RTD sensor directly in the air flow in order to control the PID circuit in a reasonable manner. However, in this way we could use a second sensor merely to monitor the cell temperature, but could not set it to a desired value. Thus, with a stable, heated cell, all measurements had to be taken in a row, because once the system was shut down and cooled, it would be virtually impossible to reproduce the exact same cell temperature. Nevertheless, and having said all that, one has to note the fact that, once stable, the temperature of the cell would remain constant for indefinite amounts of time, allowing for the five to ten hour runs of measurements.

1:2.2.3 Optical tables

In optics experiments, especially in those requiring precision in the relative alignment of two or more spatially separated beams (such as interferometry, pump - probe techniques etc.), it is important that the surface on which the optical elements are laid out is particularly rigid and vibration-free. Optical tables, formerly made from solid blocks of marble or granite (some still are), are nowadays made of steel in thick layers of honeycomb lattice structure. Fine tuning the speed of sound inside the material and the structure composition, moves the frequency of the first vibrational eigenmode



Figure 1:2-4

Melles-Griot optical table

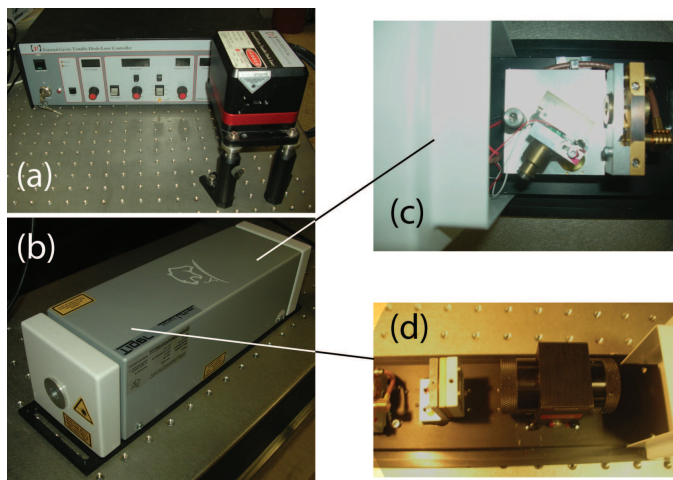
to a high figure, causing the material to critically damp vibrations below that frequency. Vibrations are further damped by using pneumatic dampers as legs for the table. More than that, the tabletop surface is flattened usually to within $\pm 0.1\text{mm}$ per 1m length in any direction, while special materials are used and are subject to special thermal treatment, so as to maximize rigidity and minimize thermal distortion of the table. Finally, to facilitate setting up experiments, optical tables come with a grid of threaded holes, in two flavors: either M6 holes at a 25mm center-to-center distance (metric) or 1/4"-20TPI at 1" c-c (imperial).

1.2.3 The “surgical instruments”: lasers and optics

1.2.3.1 Diode lasers

The advent of diode lasers (DL) initiated a breakthrough in the study of atomic systems, especially of alkali atoms, as they provided a highly monochromatic and stable coherent source, in tune with their most prominent transitions. Laser diodes are direct bandgap semiconductor junctions and they fall generally into six frequency bands: three distinct bands used in fiber optics systems are from InGaAs and InGaAsP diodes emitting around 1550nm, 1300nm and 1200nm, then there is the 750-890nm band dominated by AlGaAs diodes and is the band we use, the 670nm InGaAlP band used in commercial optoelectronics and the most recent addition, the blue, 470nm GaN diodes. The laser cavity is usually formed by simply cleaving the edges along some selected crystallographic plane. The cross section of the active region is a parallelogram with the short and long sides differing significantly. This results in highly elliptical beams at the output, which are usually corrected initially with a small- f collimator lens placed almost in contact with the diode, followed by various combinations of optics, such as dedicated variable anamorphic prism pairs etc.

The amplitude noise of DLs is smaller than that of other tunable lasers, but still a nuisance. Shot noise is characteristic of the particular semiconductors and power and temperature dependent. The frequency spectrum of DLs is characterized by two natural scales: the spacing of modes due to the free spectral range (FSR) of the cavity (typically $\sim 150\text{GHz}$) and the linewidth of single cavity modes, owing to Schawlow-Townes linewidth (\sim few MHz due to small cavity length) and to fluctuations in carriers, temperature, complex susceptibility etc. (typically $\sim 10\text{-}500\text{MHz}$). The central emitted frequency is, of course, determined by the bandgap of the specific semiconductor combination, but usually DLs are tunable over about 20nm. This is done by either varying the temperature or the

**Figure 1:2-5**

(a) New focus, Rb D2 laser (780nm)

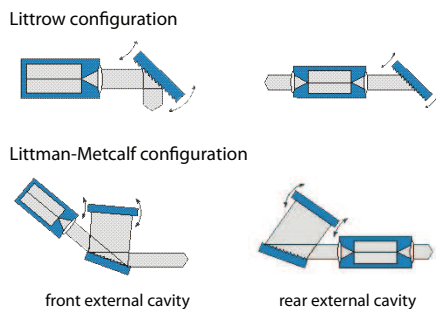
(b) Sacher Laser Technik Tiger, Rb D1 laser (795nm)

(c) External cavity of the laser in the Littrow configuration

(d) An optical isolator is positioned before the exit of the beam, in order to avoid unwanted optical feedback

injection current density, with the latter being generally preferable.

However, in most sensitive applications, where tunable single mode operation is required, the best method is to extend the cavity of the laser by applying an anti-reflection coating on one edge of the DL and arranging an optical apparatus which will feed some portion of the emitted power back to the diode. In this way, at the expense of a significant amount of power, two desirable qualities are achieved: the laser beam becomes purely monochromatic, since the wavelength which is fed back to the diode dominates under the gain curve, and it becomes easy to tune the wavelength, by micro-adjusting the optical cavity extension, thus manipulating the feedback wavelength. The two most common configurations for an *external cavity diode laser* (ECDL) are the “Littrow” and “Littman-Metcalf” configurations shown in Fig. 1:2-6].

**Figure 1:2-6**

Littrow and Littman-Metcalf ECDL configurations (see text for details / figures taken from Sacher Lasertechnik and rearranged).

In the Littrow configuration the external cavity comprises just a grating, usually a silver or gold plated one, with anywhere between 1200 and 1800 grooves/mm. The -1 diffraction order of the desired wavelength is sent back into the diode and the output is the zero order (reflected) beam. Small changes in the angle of the grating, typically performed by a piezoelectric actuator, result in the frequency of the output beam being tuned smoothly across a *mode-hop free region*, on the order of tens of GHz. In the Littman-Metcalf configuration the grating is fixed and the external cavity is terminated at a mirror, positioned opposite

to the grating. The -1 diffraction order is now incident on the mirror and fed back

to the laser and the reflected beam on the grating is again the output. Tuning is achieved by rotation of the mirror. The obvious advantage of this configuration is the fixed orientation of the output beam, but the setup is more complicated and with greater losses. During our experiments we used two commercial lasers, one from New Focus and one from Sacher Lasertechnik, which are depicted in Fig. 1:2-5, as well as a few custom designs, designed in our group and implemented by the machine shop of the institute, utilizing diodes from Eagleyard, Thorlabs, Sanyo and more. All the lasers were variations of the Littrow configuration.

1:2.3.2 Optics

Our lab was equipped with a full arsenal of optical elements. These included circular lenses and mirrors (1" and 2" diameter), cylindrical lenses, objective microscope lenses, gratings, beam splitters (polarizing or not), $\lambda/2$ and $\lambda/4$ waveplates, linear polarizers, irides, optical isolators, variable anamorphic prism pairs (which serve as beam shapers for diode laser beams), Faraday rotator crystals, neutral density filters, optical fibers and fiber couplers, optics mounts of various degrees of freedom, translator stages and also some active components, such as acousto- and electro-optic modulators and electro-mechanical choppers. Optics were sourced from various vendors (Thorlabs, Melles Griot, Isowave, Electro Optics Technology, Toptica, Newport and more).

1:2.4 The "life support": measurement and power

1:2.4.1 Wavelength-Frequency meters

▷ a./ Thorlabs Fabry-Perot resonator

The Thorlabs SA200-7A scanning Fabry Perot interferometer is a high finesse spectrum analyzer. It consists of a confocal cavity that contains two high reflectivity mirrors; by varying the mirror separation with a piezoelectric transducer the cavity acts as a very narrow band-pass filter. For a more complete discussion on the operation of Fabry Perot cavities, see, for example, [Ver95].

Knowing the free spectral range (FSR) of the Fabry Perot cavity allows the time-base of an oscilloscope to be calibrated to facilitate quantitative measurements of a laser line shape. So, with a 1.5GHz FSR and a finesse in excess of 200, the resolution of the interferometer was better than 7.5MHz, which was fine for our diode lasers with typical linewidths on the order of 10MHz.



Figure 1:2-7

Thorlabs SA200-7A Fabry Perot interferometer.

▷ *b:/ Ocean Optics spectrometer*

The Ocean Optics HR4000 is a fiber optic spectrometer. It follows the operating principle of the Czerny-Turner monochromator, as shown at the top of Fig.1:2-8.

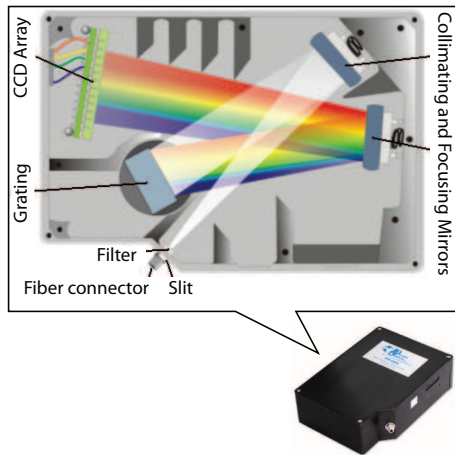


Figure 1:2-8

Ocean Optics HR4000 fiber optic spectrometer.

Light couples to an optical fiber and enters the spectrometer through the connector and slit. A filter at the entrance makes a pre-selection of wavelengths. The beam is then collimated by a mirror, which also reflects it on the analyzing grating. The analyzed beam is focused (negatively) by a second mirror and sent on a CCD array. Different wavelengths are collected at different positions on the CCD array, following the spatial resolution of the grating-focusing mirror system, and the onboard micro-controller defers this information and transmits it to the system specific software installed on a connected computer through USB.

The spectrometer uses a 3648-element linear silicon CCD array made by Toshiba, responding to wavelengths ranging from 200 to 1100nm, with a sensitivity of about 100 photons at 800nm (which more or less defined the relevant area of wavelengths for our experiments). Our model was calibrated for the 730-900nm range, with a 1200-groove grating blazed at 750nm, a longpass filter transmitting wavelengths $>560\text{nm}$ and a $5\mu\text{m}$ entrance slit. The resulting optical resolution of the spectrometer at these wavelengths was $\sim 0.005\text{nm}$ corresponding to $\sim 2.5\text{GHz}$ frequency spread. Of course, such an accuracy in frequency was not adequate for precision operations such as laser locking and the like, but was enough for the general frequency monitoring, for long-range tuning and for experiments involving far off-resonant beams.

▷ *c:/ HighFinesse wavelength meter*

The HighFinesse Ångstrom series are probably the most accurate wavelength meters in the industry today. Specific to our wavelength range of interest is the WS/7 Super Precision model depicted in Fig.1:2-9. The principle of operation is also shown at the top of the same figure. The light is coupled into the device via a fiber and then collimated by a mirror, before splitting into several beams (not shown here; in particular, our WS/7 uses two sets of multiple interferometers in a proprietary geometric configuration). Each beam passes through a solid-state Fizeau-interferometer of specific length to generate distinct interferometric patterns. The interference patterns are projected by a cylindrical lens onto CCD

photodiode arrays. This recorded pattern is transferred to the operator's computer via a USB connection which allows data acquisition rates of up to 500Hz. The software fits and compares the pattern to a previously recorded calibration spectrum to calculate the wavelength, taking into account the ambient temperature.

Probably the most significant advantage of this series of instruments is the absence of mechanical moving parts. Even the Fizeau interferometers are micro-machined in solid-state, a fact which ensures stability and robustness against vibrations, provided that the coupling of light to the optical fiber of the instrument is also shielded from such external perturbations. A welcome side-effect of this manufacturing philosophy is the prolongation of the lifetime of the instrument relative to what it would be if moving parts were present. Of course, as is to be expected, all good things are reflected in the price tag.

In terms of performance, the wavelength meter provided a 60MHz absolute and <10MHz relative accuracy in frequency. These figures are excellent for virtually any kind of precision operation, such as micro-adjustments in laser frequency for the acquisition of atomic spectra, laser locking etc. More than that, the instrument required no warm-up time, light coupling to the optical fiber was easily achieved and a LabView virtual instrument extension was also provided for the integration of measurements into more complicated, automated LabView schemes.

1:2.4.2 Lock-In amplifier

A lock-in amplifier is sine qua non in virtually any type of physics laboratory. It employs phase-sensitive techniques to detect small AC signals, embedded in - possibly orders of magnitude stronger - noise, by matching the phase and frequency of the signal to an externally applied reference. The Stanford Research Systems SR810 and SR830 models available in our lab are capable of detecting signals with frequencies ranging from 1mHz to 102.4kHz, with >100dB dynamic

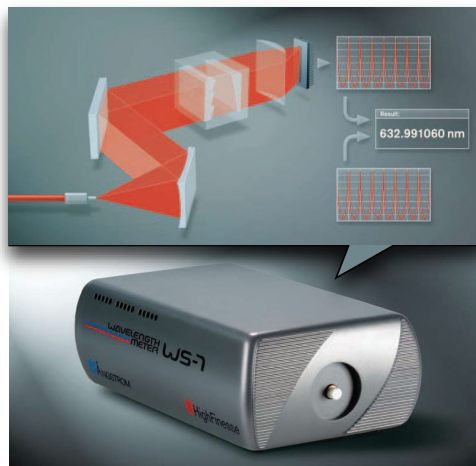


Figure 1:2-9

HighFinesse Ångstrom WS/7 wavelength meter.

reserve* and a 0.01° phase resolution. For a detailed discussion on the properties of lock-in amplifiers the reader is advised to visit the SRS webpage (see Table 1:2#1 at the end of the chapter) or any other of numerous printed and online resources available.



Figure 1:2-10

Stanford Research Systems
Lock-In amplifier

In the course of our experiments, lock-in amplifiers were used in a variety of tasks, including, but not exhausted to, laser frequency locking and laser diode current modulation, polarimetry and generic signal subtraction, signal differentiation, photodiode characterization, absorption measurements and more. Even our main experimental results, the spontaneous spin noise signals could have been recorded by the lock-in amplifiers,

were it not for the presence of yet another extraordinary piece of equipment available in our lab, the spectrum analyzer described below.

1:2.4.3 Spectrum analyzer

Probably the most important instrument in the measurement department for the experiments conducted in our lab, was the SR785 Dynamic Signal Analyzer from Stanford Research Systems. The main job of the analyzer is to perform - hardware driven - FFT transformations on incoming signals and display the resulting frequency spectrum. Looking at the frequency spectrum of a signal, chaotically complicated in the time domain, can - more often than not - reveal all the important structural features underlying its origins. An in depth discussion of the operation principles of the SR785 and of spectrum analyzers, in general, can be found in the manual of the instrument at the website of the company (see Table 1:2#1). We hereby mention just a few of its characteristics as a general description.

The instrument works by digitizing the input signal at a high sampling rate (262kHz). According to Nyquist's theorem, a signal input in the device can be reproduced accurately if the sampling rate is at least twice the highest frequency component of the signal. To this end, an analog anti-aliasing filter rejects frequencies above 102.4kHz (to be on the safe side and allow for the filter drop-off). The resulting time domain signal is fast Fourier transformed and a frequency spectrum with half as many points (or *frequency bins*) as the time record is re-

*The dynamic reserve of a lock-in amplifier at a given full-scale input voltage is the ratio (in dB) of the largest interfering signal to the full-scale input voltage. The largest interfering signal is defined as the amplitude of the largest signal at any frequency that can be applied to the input before the lock-in cannot measure a signal with its specified accuracy.

turned. To understand how this works we use the example from the instrument manual:

If one takes 1024 samples at 262 kHz, the time record is acquired in 3.9 ms. The FFT yields 512 frequency points and it remains to be found over what frequency range. The highest frequency will be determined by the period of 2 time samples or 131 kHz. The lowest frequency is just the period of the entire record or $1/(3.9 \text{ ms})$ or 256 Hz. The output spectrum thus represents the frequency range from DC to 131 kHz with 512 points spaced every 256 Hz. The advantage here is the speed at which the spectrum is returned, at the expense of resolution. Reducing the desired frequency span implies increasing the acquisition time, either by reducing the sampling rate or by increasing the number of recorded signal values, and yields a better frequency resolution.

All commonly used window functions are available to provide periodical boundaries to the time records (uniform, flattop, BMH, Kaiser etc.). The spectra acquired are, normally, baseband spectra (i.e. starting at DC), but can be shifted at any frequency by means of heterodyning. Several averaging modes are offered (RMS, vector or peak hold average), both in linear (one-off) or exponential (continuous) modes. Amplitude values in the results are displayed in absolute units, in dB, in peak to peak or - and this was the most important for us - in power spectral density (PSD) units. PSD is the energy in each frequency bin normalized to the noise bandwidth of the bin. The noise bandwidth is calculated from the FFT linewidth and the window function. This allows comparison of results taken at different spans and with different windows. This is the norm when measuring noisy signals and the amplitudes are given in $V/\sqrt{\text{Hz}}$, or V^2/Hz .

Of equal importance are the available, predefined and displayable functions, as well as the ability given to the user to display custom combinations of time or frequency domain measurements. For example, apart from the direct FFT spectra the instrument can display power spectral densities, cross spectra between the two channels, auto- and cross-correlation time functions and coherence plots, or any user defined combination.

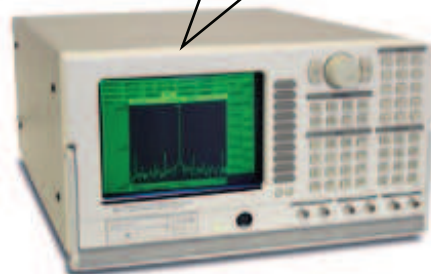


Figure I:2-11

SRS SR785 Dynamic Signal Analyzer and a typical narrow (inset top) and wide (inset bottom) band FFT spectrum for signals received in the two channels.

1:2.4.4 Flux gate magnetometer



Figure 1:2-12

Bartington Mag-03 fluxgate sensor and power supply.

A three-axis fluxgate magnetometer from Bartington, UK, was used in all procedures requiring either the application or compensation of a magnetic field, as well as for the characterization of the magnetic shield. The magnetometer had a range of $\pm 70 \mu\text{T}$, with a noise level of less than $6 \text{ pT rms per } \sqrt{\text{Hz}}$ measured at 1 Hz. It was particularly useful during the spin noise experiments, where the stability of the magnetic field was of paramount importance.

The ability to monitor all three components of the magnetic field with a single sensor, at approximately the same area, was crucial to locking it in both direction and amplitude.

1:2.4.5 LabView virtual instruments

LabView (abbr. “Laboratory Virtual Instrumentation Engineering Workbench”) is a dataflow programming workbench. Signals, in the form of voltages, are interfaced to the computer, usually via a PCI card and a BNC connector extension (in our case it was the NI-DAQ 7 card and BNC 2090 rack), but also through any connected I/O device. A block diagram and an interacting graphical front end define actions to be taken on the incoming flow of data and also the respond to the processed signals. The program is called a *virtual instrument* (vi). By taking advantage of nowadays computers number-crunching powers, immensely complex operations can be performed in real-time on data sampled at rates up to the Mbps range. In our experiments, we exploited both the versatility of *LabView* and the fact that along with most recent instruments came factory built vi’s for interfacing to the computer. So, custom vi’s were used for monitoring, compensating and applying magnetic fields within the magnetic shield, for laser frequency monitoring and locking, as extra lock-in amplifiers or oscilloscopes and, of course, for the acquisition of random numbers in the quantum random number generator experiment, described in Ch. 1:3.

1:2.4.6 Rest of supporting equipment

The rest of the measuring and power supplying equipment in the lab was pretty standard for an optics lab and included oscilloscopes (from B&K Precision, Tektronix and EZ Digital), constant current/voltage power supplies (from AFX, EZ

Digital, Mastech and Amarad), programmable function generators (B&K Precision and EZ digital), built-to-order computers (from local suppliers), photodiodes (Thorlabs, Melles Griot) and CCD cameras (Sony).



Type	Supplier	Location	URL
Alkali cells	Triad technologies	USA	http://www.triadtechno.com
Vacuum pumps and components	Varian (subs. of Agilent)	USA	http://www.varianinc.com
	Alcatel vacuum (adixen)	France	http://www.adixen.com
	MDC Vacuum Products	USA	http://www.mdc-vacuum.com
High Amp variac	Belotti Variatori	Italy	http://www.belotti.it
Magnetic Shielding	Less EMF	USA	http://www.lessemf.com
Temperature control	Omega	USA	http://www.omega.com
Fabry Perot	Thorlabs	USA	http://www.thorlabs.com
Fiber spectrometer	Ocean Optics	USA	http://www.oceanoptics.com
Wavelength meter	HighFinesse	Germany	http://www.highfinesse.com
Diode lasers, controllers and photodiodes	New Focus	USA	http://www.newfocus.com
	Sacher Lasertechnik	Germany	http://www.sacher-laser.com
	Eagleyard Photonics	Germany	http://www.eagleyard.com
	Thorlabs	USA	http://www.thorlabs.com
	Sanyo	Japan	http://sanyo.com
Lock-In amplifiers	Stanford Research Systems	USA	http://www.thinksrs.com
Spectrum analyzer	Stanford Research Systems	USA	http://www.thinksrs.com
Oscilloscopes and function generators	B&K Precision	USA	http://www.bkprecision.com
	Tektronix	USA	http://www.tek.com
	EZ Digital Co.	S. Korea	http://www.ezdgt.com
Optics, tables and fixtures	Thorlabs	USA	http://www.thorlabs.com
	Melles Griot	France	http://www.cvimellesgriot.com
	Isowave	USA	http://www.isowave.com
	Electro Optics Technology	USA	http://www.eotech.com
	Newport	USA	http://www.newport.com
	Toptica	USA	http://www.toptica.com
	Fluxgate magnetometer	Bartington	UK
Power supplies	AFX, EZ, Mastech, Amrad	various	
DAQ solutions	National Instruments	USA	http://www.ni.com

Table I:2#1 List of suppliers

Chapter 1:3

Experimental work

1.3.1 *Measurement of Transverse Spin Relaxation rate*

1.3.1.1 Spin noise

The term *spin noise* refers to the fluctuations in the spin polarization of an ensemble of non-zero spin particles. Being a fundamental, quantum source of noise, it sets ultimate limits in the attainable precision of measurements employing spin-polarized systems. As such, its presence is considered unavoidable and the amount of precision it allows is usually called the *fundamental quantum limit*. Examples of spin noise limited measurements in atomic systems can be found ranging from magnetometers [ALKR02, KAKR03] to atomic clocks [IBB⁺93] and more. Therefore, its study and understanding is essential.

However, another, more intriguing aspect of spin noise, is that it conveys information about the quantum system it emanates from. Finding ways to “read” the noise can, thus, reveal this information, without the need for specific state preparation and, usually, in a non-destructive way if the system is already in a prepared state. Specifically in atomic systems, spin noise measurements can reveal isotope abundance ratios, g-factors, nuclear magnetic moments and spins, spin coherence lifetimes, hyperfine splittings just to name a few. Recently, spontaneous noise spectroscopy was performed on thermal alkali vapors, both absorptive [Mit00] and dispersive [CRBS04, MCR⁺06]. In the former case, noise was attributed to the stochastic properties of resonant photon scattering which interrupt the Larmor precession of the atoms, while in the latter case it was claimed to arise from stochastic spin-spin correlations.

1.3.1.2 Stochastic system evolution

▷ a:/ *The QSD evolution equation*

Open quantum systems, i.e. systems interacting with a broader, usually uncorrelated quantum system aptly named “the environment”, “the reservoir” or, simply, “the bath”, have the tendency to evolve in a stochastic manner. This stochastic evolution can be modeled through a multitude of theories; quantum trajectories, random jumps, measurement theory, state diffusion etc. What all these theories have in common is that the behavior of an ensemble of atoms is unraveled into a collection of the histories of its constituents, each of which evolves in a stochastic way through a Brownian-like motion under the influence of the atom-bath interactions. Taking the ensemble average of these histories determines the macroscopic qualities of the system. The main qualitative difference between theories is whether these individual histories are considered as real (i.e. one atom actually evolves as described) or virtual (i.e. the description describes the impact of virtual processes on the single atom evolution).

In our work, we approach spin noise through the *quantum state diffusion* (QSD) theory, developed mainly by N. Gisin and I. Percival [Per98, GP92, GC92]. QSD is a real-history theory, wherein each particle in the ensemble evolves stochastically all along remaining in a pure state, as this state is considered to be continuously interrogated by the environment and, thus, localized. We will not dive into a discussion about the general validity of this or such theories in all conceivable cases; suffice it to say that for the particular case of quantum noise, the assumptions of the theory seem rather well justified. We will not even dwell deep into the theory itself, as it would be unnecessarily complicated, since we only use its basic evolution equation to initiate the description.

We have already mentioned in the discussion about the master equation governing the evolution of alkali atoms (c.f. subsection 1.1.4.1), that the Lindblad form of the master equation, Eq.(1.1.50), is the most general for open systems coupled to Markovian reservoirs:

$$\frac{d\rho}{dt} = -\frac{i}{\hbar}[\mathcal{H}, \rho] + \sum_i \left[\hat{L}_i \cdot \rho \cdot \hat{L}_i^\dagger - \frac{1}{2} \left(\hat{L}_i^\dagger \cdot \hat{L}_i \cdot \rho + \rho \cdot \hat{L}_i^\dagger \cdot \hat{L}_i \right) \right] \quad (1.1.50)$$

where we have absorbed the rates γ_i into the operators to give the equation a cleaner look. The master equation of Eq. (1.1.50) is a deterministic equation, as is every master equation. On the other hand, the equations satisfied by the wavefunctions, $|\psi\rangle$, of the constituent particles are stochastic. In QSD, the basic stochastic equation for the particle wavefunctions is such, that the density matrix, which is the ensemble average over the projectors $|\psi\rangle\langle\psi|$, satisfies the Lindblad equation. One starts from the variation of $|\psi\rangle$ for a time increment dt , which

comprises a deterministic part (*drift* term) and a fluctuating part (*fluctuation* term):

$$|d\psi\rangle = |\text{drift}\rangle dt + |\text{fluctuation}\rangle d\xi \quad (1.3.1)$$

where $d\xi = d\xi_R + id\xi_I$ is a complex stochastic variable, which is usually modeled as a normal (Gaussian) random variable of mean 0 and variance dt times a random, complex, unit exponential. The QSD equation is arrived at uniquely under four conditions

1. The state vector evolves continuously (no quantum jumps)
2. The state vector remains normalized
3. The differential stochastic fluctuation, $d\xi$, has independent, fluctuating real and imaginary parts, i.e. $\mathcal{M}d\xi = 0$, $\mathcal{M}(d\xi)^2 = 0$, $\mathcal{M} |d\xi|^2 = dt$, where \mathcal{M} denotes the ensemble average.
4. Fluctuations at different times are statistically independent (Markov)

Under these and after some manipulation, one obtains the QSD equation:

$$|d\psi\rangle = -\frac{i}{\hbar}\mathcal{H}\psi dt + \sum_i \left(\langle L_i^\dagger \rangle L_i - \frac{1}{2}L_i^\dagger L_i - \frac{1}{2}\langle L_i^\dagger \rangle \langle L_i \rangle \right) |\psi\rangle dt + (L_i - \langle L_i \rangle) |\psi\rangle d\xi \quad (1.3.2)$$

The fluctuations corresponding to different Lindblads are independent and normalized, i.e. $\mathcal{M}d\xi_i = 0$, $\mathcal{M}(d\xi_i d\xi_j) = 0$, $\mathcal{M}(d\xi_i^* \xi_j) = \delta_{ij} dt$.

It is worth noting here that the QSD equation is *nonlinear*, as the $\langle L_i \rangle$ depend quadratically on $|\psi\rangle$, and it is also *nonlocal*, that is its solutions depend on arbitrarily distant influences. Finally, the solution is non-differentiable and its Fourier transform is that of white noise.

▷ *b:/ Spin noise evolution in the QSD scheme*

Before writing the QSD state evolution equation for a hot alkali vapor, we must bring the master equation in the Lindblad form and identify the Lindblad operators. Since the vapor is assumed to be in thermal equilibrium, its evolution will be governed by the simple master equation (1.1.61), which we recite here, slightly modified, for reference:

$$\frac{d\rho}{dt} = -\frac{i}{\hbar}[\mathcal{H} + \mathcal{V}^c, \rho] + \frac{1}{T_2}(\varphi - \rho) \quad (1.1.61)$$

where $\rho = \varphi + \Theta \cdot \mathbf{S}$ [c.f. Eq. (1.1.44)] and the decoherence processes (collisions, diffusion etc.) are considered strong enough to completely dephase the atom,

so that ρ^c in Eq. (1.1.61) is substituted by φ . Also, the various Hamiltonian perturbations and light shift operators are included in \mathcal{V}^c . Finally, the collective transverse relaxation rate, $1/T_2$, includes contributions from all decoherence processes which affect the vapor and its measurement is the pursued goal of this experiment. We return to its discussion after sorting out the evolution of the system.

Using Eq. (1.1.45) and the single atom identity:

$$\mathbf{s} \cdot \mathbf{s} = s_x^2 + s_y^2 + s_z^2 = s_z^2 - s_+s_- - s_-s_+ = \frac{3}{4} \mathbb{I} \quad (1.3.3)$$

where $s_q = \frac{\hbar}{2}\sigma_q$ (σ the Pauli matrices) we can put the dissipative part of Eq. (1.1.61) in the form:

$$\frac{d\rho}{dt} \propto \frac{1}{T_2} \left([s_z\rho s_z - \frac{1}{2}(s_z^2\rho - \rho s_z^2)] - \sum_{q=\pm} [s_q\rho s_{-q} - \frac{1}{2}(s_q s_{-q}\rho + \rho s_q s_{-q})] \right) \quad (1.3.4)$$

We can now define the Lindblad operators as:

$$\hat{L}_q = \frac{1}{\sqrt{T_2}} s_q, \quad (\text{note that } \hat{L}_q^\dagger = (-1)^q \hat{L}_{-q}) \quad (1.3.5)$$

and, after restoring the Hamiltonian term, the master equation takes the Lindblad form of Eq. (1.1.61).

Under Eq. (1.3.2), the change in the expectation value of a single atom operator, \hat{o} , during the time increment dt is found to be:

$$d\langle \hat{o} \rangle = \langle \psi | \hat{o} | d\psi \rangle + \langle d\psi | \hat{o} | \psi \rangle + \langle d\psi | \hat{o} | d\psi \rangle = \quad (1.3.6)$$

$$= \sum_i \langle \hat{L}_i^\dagger \hat{o} \hat{L}_i - \frac{1}{2} \hat{L}_i^\dagger \hat{L}_i \hat{o} - \frac{1}{2} \hat{o} \hat{L}_i^\dagger \hat{L}_i \rangle dt + \quad (1.3.7)$$

$$+ \sum_i \left[\sigma(\hat{o}^\dagger, \hat{L}_i) d\xi_i + \sigma(\hat{L}_i, \hat{o}^\dagger) d\xi_i^* \right]$$

where one is obliged to keep the term $\langle d\psi | \hat{o} | d\psi \rangle$ in order to retain products of fluctuating terms involving $d\xi_i d\xi_i^*$, which sum up to dt in the ensemble average. In the relation above, the *quantum covariance* function was used, defined by:

$$\sigma(\hat{o}, \hat{p}) = \langle \hat{o}^\dagger \cdot \hat{p} \rangle - \langle \hat{o}^\dagger \rangle \langle \hat{p} \rangle \quad (1.3.8)$$

a special case of which is the variance of the expectation value of an operator, $\sigma(\hat{o}) = \langle \hat{o}^\dagger \hat{o} \rangle - |\langle \hat{o} \rangle|^2$. As we shall explain below, the observable in our experiment is, essentially, the electronic spin along the propagation direction, $\langle s_y \rangle$. Using the operator identities ($\hbar = 1$):

$$\begin{aligned}
s_{\pm}s_y &= s_y s_{\mp} = -\frac{i}{2\sqrt{2}} \left(\frac{\mathbb{I}}{2} \pm s_z \right) \\
s_{\mp}s_{\pm}s_y &= s_y s_{\pm}s_{\mp} = -\frac{i}{2\sqrt{2}} s_{\mp} \\
s_{\pm}s_y s_{\mp} &= 0 \\
s_z s_y &= -s_y s_z = -\frac{i}{2} s_x \\
s_z s_z s_y &= s_y s_z s_z = -s_z s_y s_z = \frac{1}{4} s_y
\end{aligned} \tag{1.3.9}$$

the stochastic evolution of $\langle s_y \rangle$, as given by Eq. (1.3.7), becomes:

$$d\langle s_y \rangle = d\langle s_y \rangle_{\text{D}} + d\langle s_y \rangle_{\text{F}} \tag{1.3.10}$$

with the deterministic (drift) part being simply:

$$d\langle s_y \rangle_{\text{D}} = -\frac{i}{\hbar} \langle [\mathcal{H}, s_y] \rangle - \frac{1}{T_2} \langle s_y \rangle \tag{1.3.11}$$

and the fluctuating part:

$$\begin{aligned}
d\langle s_y \rangle_{\text{F}} &= \frac{1}{\sqrt{T_2}} \left\{ -d\xi_z'' \langle s_x \rangle - 2d\xi_z' \langle s_y \rangle \langle s_z \rangle + \sqrt{2}(d\xi_+' - d\xi_-') \langle s_x \rangle \langle s_y \rangle + \right. \\
&\quad \left. + \sqrt{2} \left[d\xi_+'' \left(\frac{1}{4} - \langle s_y \rangle^2 - \frac{\langle s_z \rangle}{2} \right) + d\xi_-'' \left(\frac{1}{4} - \langle s_y \rangle^2 + \frac{\langle s_z \rangle}{2} \right) \right] \right\}
\end{aligned} \tag{1.3.12}$$

where the stochastic variables have been split into real and imaginary parts, $d\xi = \Re(d\xi) + i \Im(d\xi) = d\xi' + i d\xi''$. As one can see from the equation above, the existence in the vapor of net electronic polarization induces a rather complicated stochastic evolution. In spin noise experiments, however, where the vapor is in thermal equilibrium, the fluctuating terms proportional to $\langle s_x \rangle$, $\langle s_y \rangle$ and $\langle s_z \rangle$ are negligibly small compared to the constant terms. Thus, Eq. (1.3.12) simplifies to:

$$d\langle s_y \rangle_{\text{F}} = \frac{\sqrt{2}}{4\sqrt{T_2}} (d\xi_+'' + d\xi_-'') \tag{1.3.13}$$

where the $d\xi_{\pm}''$ are two normal random variables of zero mean and variance dt . The addition of two such variables results in a new normal random variable of zero mean and variance $2dt$ or, equivalently, in one with zero mean and variance dt times a factor of $\sqrt{2}$. So, finally, Eq. (1.3.13) can be written as:

$$d\langle s_y \rangle_{\text{F}} = \frac{1}{2\sqrt{T_2}} d\eta \tag{1.3.14}$$

and substituting (1.3.11) and (1.3.14) into (1.3.10), we get:

$$d\langle s_y \rangle = -\frac{i}{\hbar} \langle [\mathcal{H}, s_y] \rangle - \frac{1}{T_2} \langle s_y \rangle + \frac{1}{2\sqrt{T_2}} d\eta \tag{1.3.15}$$

▷ c:/ *The power spectrum of spin noise*

According to Eq. (1.3.15), the stochastic evolution of $\langle s_y \rangle$ is a, so called, *Ornstein-Uhlenbeck* (O-U) process. O-U processes are routinely encountered whenever some form of Wiener process (Brownian motion) causes relaxation and are, thus, well understood and extensively studied. In the general case, the characteristic fluctuation time frame is not related to the drift time frame. However, this is not the case for spin noise according to Eq. (1.3.15). By identifying the various collisional processes as the sources of fluctuations in the evolution of the wavefunction of a single particle, we have connected them to the characteristic rate, $1/T_2$, which governs the dissipation of an ensemble of such particles away from equilibrium. This is a clear demonstration of the *fluctuation-dissipation theorem* (FDD) and it is this particular property of spin noise which allows us to deduct the macroscopically observed, out-of-equilibrium relaxation rate $1/T_2$ from experiments performed at thermal equilibrium.

If the magnetic field is along the \hat{z} -axis, the magnetic part of the Hamiltonian will be of the form $\mathcal{H}_B = \omega_L s_z$, with ω_L the Larmor frequency. Taking into account the commutation relation $[s_i, s_j] = i\hbar \varepsilon_{ijk} s_k$ and the equivalence of $\langle s_x \rangle$ and $\langle s_y \rangle$, Eq. (1.3.15) leads to:

$$\begin{aligned} d\langle s_x \rangle &= \omega_L \langle s_y \rangle - \frac{1}{T_2} \langle s_x \rangle + \frac{1}{2\sqrt{T_2}} d\eta_x \\ d\langle s_y \rangle &= -\omega_L \langle s_x \rangle - \frac{1}{T_2} \langle s_y \rangle + \frac{1}{2\sqrt{T_2}} d\eta_y \end{aligned} \quad (1.3.16)$$

The above can be written alternatively as:

$$d\langle s_\perp \rangle = -D \cdot \langle s_\perp \rangle + F \cdot d\eta_\perp \quad (1.3.17)$$

$$\begin{aligned} \text{where: } \langle s_\perp \rangle &= \begin{pmatrix} \langle s_x \rangle \\ \langle s_y \rangle \end{pmatrix} & d\eta_\perp &= \begin{pmatrix} d\eta_x \\ d\eta_y \end{pmatrix} \\ D &= \begin{pmatrix} 1/T_2 & -\omega_L \\ \omega_L & 1/T_2 \end{pmatrix} & F &= \frac{1}{2\sqrt{T_2}} \begin{pmatrix} 1 & 0 \\ 0 & 1 \end{pmatrix} \end{aligned} \quad (1.3.18)$$

The evolution of $\langle s_\perp \rangle$ is a bivariate O-U process and, according to Gardiner's analysis [Gar90], its stationary time correlation matrix will be given by:

$$G(t-s) = \mathcal{M}\langle s_\perp(t) s_\perp(s) \rangle = \sigma e^{-D|t-s|} \quad (1.3.19)$$

where σ is the stationary variance, found to be:

$$\sigma = \frac{\det(D) F \cdot F^T + [D - \text{Tr}(D)\mathbb{I}] \cdot F \cdot F^T \cdot [D - \text{Tr}(D)\mathbb{I}]^T}{2 \text{Tr}(D) \det(D)} \quad (1.3.20)$$

From Eq. (1.3.19), by virtue of the Wiener-Khinchin theorem,

$$S(\omega) = \frac{1}{2\pi} \int_{-\infty}^{\infty} e^{-i\omega\tau} G(\tau) d\tau \Leftrightarrow G(\tau) = \int_{-\infty}^{\infty} e^{-i\omega\tau} S(\omega) d\omega \quad (1.3.21)$$

one can extract the frequency spectrum matrix, which after some manipulation takes the form:

$$S(\omega) = \frac{1}{2\pi} (D + i\omega\mathbb{I})^{-1} \cdot F \cdot F^T \cdot (D^T - i\omega\mathbb{I})^{-1} \quad (1.3.22)$$

From Eqs. (1.3.22) and (1.3.18), the power spectrum of the observable $\langle s_y \rangle$, in PSD units, will just be the $\{2, 2\}$ element of the $S(\omega)$ matrix:

$$\mathcal{P}_{\langle s_y \rangle}^{(\text{PSD})} = \frac{1}{8\pi T_2} \frac{(1/T_2^2) + (\omega^2 + \omega_L^2)}{[(1/T_2^2) + 2(\omega^2 + \omega_L^2)]/T_2^2 + (\omega^2 - \omega_L^2)^2} \quad (1.3.23)$$

In the course of our experiments, the Larmor frequency was significantly larger than the spin relaxation rate ($\omega_L \gg 1/T_2$) and we were taking spectra for frequencies near the Larmor frequency ($|\omega - \omega_L| \simeq \text{a few } 1/T_2 \ll \omega + \omega_L$). Under these conditions, Eq. (1.3.23) simplifies into the more familiar form:

$$\mathcal{P}_{\langle s_y \rangle}^{(\text{PSD})} = \frac{1}{16\pi T_2} \frac{1}{\frac{1}{T_2^2} + (\omega - \omega_L)^2} \quad (1.3.24)$$

i.e. a Lorentzian with a width $\frac{1}{T_2}$ which peaks to $\frac{1}{16\pi T_2}$ at the Larmor frequency. Note here that the frequencies ω appearing in these equations are the frequencies of the power spectrum recorded by our spectrum analyzer and should not be confused with the frequency of the laser beam, which is also denoted by ω .

▷ *d:/ Stochastic evolution of the Faraday rotation angle*

The Faraday rotation angle is given by Eq. (1.1.142), which we recite here for reference:

$$\theta = \frac{\pi(n_+ - n_-)l}{\lambda_{\text{vac}}} \quad (1.1.142)$$

with

$$n_{\pm} = 1 + \delta n_0 + \delta n_{\pm} \quad (1.1.143)$$

$$\delta n_0 = \sum_f \frac{\pi n_d e^2 f_{ge}}{m_e c \omega_f} \frac{\omega - \omega_f}{(\omega - \omega_f)^2 + \gamma^2} p_f \quad (1.1.144)$$

$$\delta n_{\pm} = \sum_f \frac{\pi n_d e^2 f_{ge}}{m_e c \omega_f} \frac{\omega - \omega_f}{(\omega - \omega_f)^2 + \gamma^2} \frac{11 - 4J_e(J_e + 1)}{4} \langle \bar{\mathbf{J}}(f, f) \rangle \cdot \hat{\mathbf{s}}_{\pm} \quad (1.1.145)$$

In the experimental setup, which is depicted in Fig. 1:3-1, linearly polarized light propagates along \hat{y} -axis and traverses the alkali cell, which is subject to a small \hat{z} -magnetic field. Thus, the whole discussion and the derived formulas about Faraday rotation are still valid in our case, only now, the \hat{s}_{\pm} vectors appearing in Eq. (1:1.145) will be:

$$\hat{s}_{\pm} = \hat{y}_{\pm} = -\frac{i}{2}(\hat{z} \mp i\hat{x}) \times (\hat{z} \pm i\hat{x}) \quad (1:3.25)$$

Since we are probing the D2 line of rubidium, it will be*:

$$\theta = -\frac{\pi l}{\lambda_{\text{vac}}} \left(\sum_f \frac{\pi N/(Al)e^2 f_{ge}}{m_e c \omega_f} \frac{1}{\omega - \omega_f} \right) \langle s_y \rangle = N\theta_o \langle s_y \rangle \quad (1:3.26)$$

where we substituted $n_d = N/(Al)$, with N the total number of atoms probed by the laser beam and A the beam cross sectional area, $[11 - 4J_e(J_e + 1)]/4 = -1$ for the D2 line ($J_e = 3/2$) and we have assumed that we are working sufficiently off resonance, so that the ground state hyperfine splitting, as well as the collisional broadening of the transition are much smaller than the frequency detuning. Indeed, owing to the fact that these quantities appear squared, for the 45 GHz detuning used in the experiment, the ~ 5 GHz half-width of the collisional broadening accounts for a $\sim 1\%$ correction, making our assumption justifiable; and more so for the significant simplification it provides. In this case, the mean electronic spin is pulled out of the summation and is substituted by $\langle \mathbf{J} \rangle \cdot (\hat{s}_+ - \hat{s}_-) = \langle s_y \rangle$.

It is clear, then, that fluctuations in $\langle s_y \rangle$ will propagate to contaminate θ . Identifying $\theta_o \langle s_y \rangle$ as the average Faraday rotation per atom and since the noise contribution of uncorrelated atoms to the noise of the ensemble scales as \sqrt{N} , the power spectral density of the Faraday rotation angle will be:

$$\mathcal{P}_{\theta}^{(\text{PSD})}(\omega) = N \theta_o^2 \mathcal{P}_{\langle s_y \rangle}^{(\text{PSD})}(\omega) \quad (1:3.27)$$

1:3.1.3 Experiment

The setup used for the acquisition of spin noise signals is diagrammatically shown in Fig. 1:3-1. The various instruments are described in the previous chapter. The vapor cell, containing rubidium in natural abundances and 300 Torr of molecular nitrogen, which acts both as a diffusion suppression, as well as a radiation quenching agent, is heated in the range of 80 to 120°C by a flow of hot air and the oven-cell system resides inside the mu-metal magnetic shield. A set of coils inside the inner layer of the shield, powered by a home-bred, computer controlled, precision voltage source, allows for the application precisely manipulated magnetic fields and for the suppression of remnants of stray external fields. The

*We remind the reader here that the expressions are in CGS and with $\hbar = 1$.

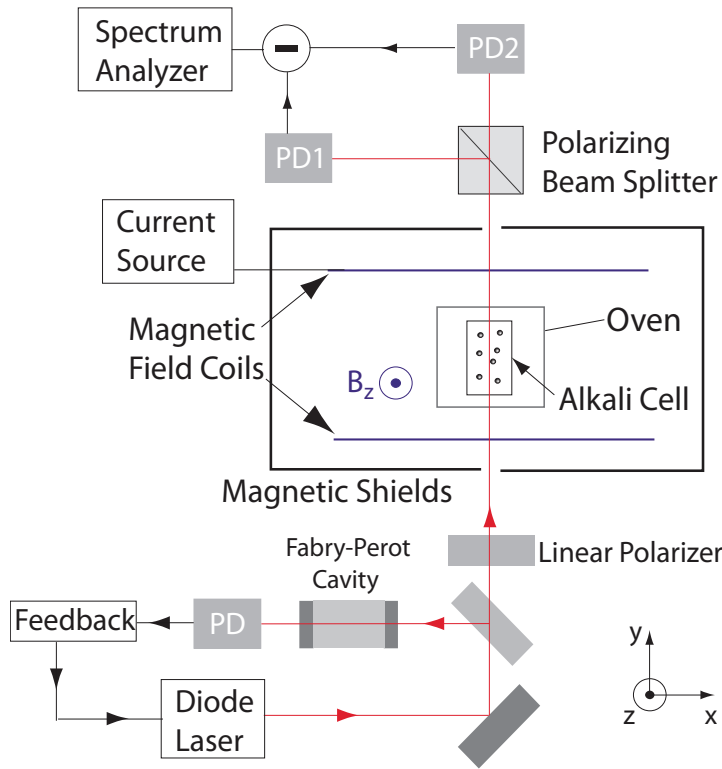


Figure I:3-1
Experimental setup for the acquisition of spin noise spectra. See text for details.

magnetic field in the vicinity of the cell was monitored by a flux gate magnetometer, the readings of which were fed to a custom-made *LabView* routine, which, in turn, micro-tuned the current to the coils. As we discussed in the previous section, a small magnetic field shifts the peaks of the spin noise spectrum to the vicinity of the Larmor frequency and it is required in order to avoid the near-DC, ever present sources of noise ($1/f$, vibrational and other electronic and technical sources). For $B_z = 53.6$ mG the resulting Larmor frequency is $\omega_L = g_J \mu_B B / I(I+1)\hbar = 2\pi \times 25\text{kHz}$ for ^{85}Rb (and $= 2\pi \times 59.5\text{kHz}$ for ^{87}Rb).

Turning to the light characteristics, a portion of the diode laser beam enters the Fabry-Perot cavity, the length of which oscillates sinusoidally, scanning the lineshape of the laser. The F-P signal is differentiated and fed to a PID controller, which controls the grating of the external cavity of the laser, by means of supplying voltage to a piezo-electric actuator. Thus the laser is actively locked in frequency and at a 45 GHz red detuning relative to the D2 resonance. The cross sectional intensity distribution of the laser beam was found to be elliptical with approximate Gaussian profiles in both axes and with a full width at $1/e$ dimensions of 0.6×2.3 mm. This measurement was performed both with a moving razor - photodiode combination, as well as with attenuation of the beam by neutral density filters and CCD photography.

The laser is linearly polarized before entering the cell and, upon emergence, its polarization is monitored by a balanced polarimeter. The current of each

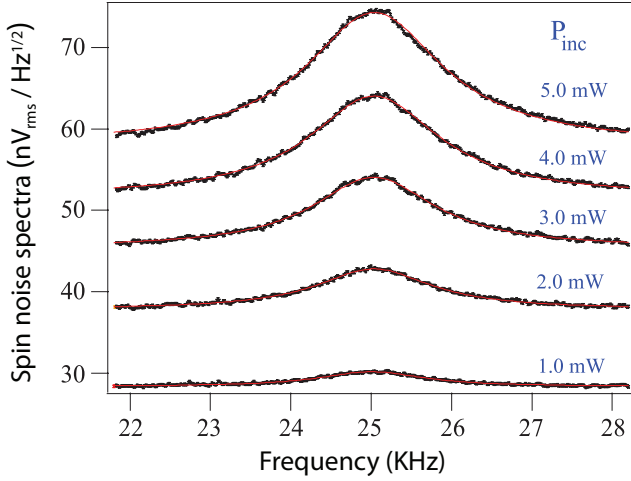


Figure 1:3-2

Spin noise spectra at a temperature of $T = 120.5^\circ\text{C}$ for various incident light powers. Extrapolation of the widths of the curves to zero power yields the $1/T_2$ relaxation rate. The $\sqrt{P_{\text{inc}}}$ scaling of the background indicates that it is dominated by photon shot noise.

photodiode is converted to voltage on a load resistor of $R_L = 3.9\text{k}\Omega$ at the inputs of the spectrum analyzer. The spectrum analyzer subtracts the signals, produces the Fourier spectrum of the difference and displays a 6.4 kHz frequency span of this spectrum (in PSD units), centered at the Larmor frequency, with a frequency bin of 8 Hz. Averages were taken for a little more than 30 min, which is the maximum the memory of the instrument allowed, and a characteristic set of such spin noise spectra for a given temperature and a range of incident laser powers are shown in Fig. 1:3-2.

The figure shows the noise of uncorrelated spins manifesting as well defined, Lorentzian shaped curves. The background noise is dominated by photon shot noise of the transmitted light, as one can easily verify by plotting against P_{inc} and observing its scaling as $\sqrt{P_{\text{inc}}}$ (c.f. Appendix B). The dark current noise of the photodiodes was measured to about $16\text{ nV}/\sqrt{\text{Hz}}$ and is quite insignificant as noise contributions are added in quadrature.

1:3.1.4 Data analysis

The power spectral density of the measured voltage signal will comprise contributions from photon shot noise, from electronic noise in the devices and, of course, from the spin noise spectra. All contributions are added in quadrature and the result, in V^2/Hz and in the nomenclature of Appendix B, will be:

$$\mathcal{P}_V^{(\text{PSD})}(\omega) = [\mathbf{v}_{\theta, \text{rms}}^{(\text{PSD})}]^2 + [\mathbf{v}_{\text{SN}, \text{rms}}^{(\text{PSD})}]^2 + [\mathbf{v}_{\text{el}, \text{rms}}^{(\text{PSD})}]^2 \quad (1:3.28)$$

The transmitted power, P , is converted to current in the photodiodes with an efficiency $r = \eta e/hf$ [see Eq. (B.1)] and the current is converted to voltage on a load resistor R at the input of the spectrum analyzer. Then the spin noise contribution can be written as:

$$[\mathbf{v}_{\theta, \text{rms}}^{(\text{PSD})}]^2 = (2rPR)^2 \mathcal{P}_{\theta}^{(\text{PSD})}(\omega) \quad (1.3.29)$$

Taking into account that the shot noise of the difference signal is $\sqrt{2}$ times that of the single channel, Eq. (B.7) leads to:

$$[\mathbf{v}_{\text{sn}, \text{rms}}^{(\text{PSD})}]^2 = (2rPR)^2 (\delta\varphi)^2 \quad \text{with } \delta\varphi = \frac{1}{\eta\dot{N}} = \frac{1}{\eta P/(hf)} \quad (1.3.30)$$

Finally, as stated above, electronic noise was measured to about:

$$\mathbf{v}_{\text{el}, \text{rms}}^{(\text{PSD})} = 16\text{nV}/\sqrt{\text{Hz}}, \quad (1.3.31)$$

a negligible amount compared to the other two sources. Collectively, Eq. (1.3.28) can be recast in the following form:

$$\mathcal{P}_V^{(\text{PSD})}(\omega) = (2rPR)^2 [\mathcal{P}_{\theta}^{(\text{PSD})}(\omega) + (\delta\varphi)^2] + [\mathbf{v}_{\text{el}, \text{rms}}^{(\text{PSD})}]^2 \quad (1.3.32)$$

Before attempting to pursue the goal of extracting the transverse relaxation rate of the alkali atoms from the observed spectra, one has to be convinced that they are indeed due to spin noise. The spin noise spectra are of magnetic origin and are expected to appear at the Larmor frequency. This is obviously verified as the signal peaks appeared at the expected positions, both for ^{85}Rb and ^{87}Rb and shifted accordingly as the magnetic field was modified. This fact also provided an alternative means of monitoring the stability of the applied magnetic field, although the slow build up of the signals would allow for the identification of small field fluctuations only in retrospect, since a fluctuating magnetic field would produce a broader lineshape than expected. More than that, though, the integrated spin noise spectra are expected to scale linearly both with the incident laser power at a given temperature [see Eq. (1.3.32)], as well as with the alkali number density [see Eq. (1.3.27)]. These exact plots we show in Fig. 1.3-3 and the linear scaling is verified.

We now turn to the calculation of the alkali transverse relaxation rate, $1/T_2$. Since the parameters of the experiment do not fall into the rapid spin exchange - low magnetic field regime described in section 1.1.4.4e/, spin exchange is the dominant source of relaxation. Rubidium - nitrogen and rubidium - rubidium spin destruction collisions are also present and are taken into account, although the related relaxation proves to be insignificant in the end. The cross sections for the spin exchange and spin destruction processes are given in Table A#1. Nitrogen acts both as a diffusion, as well as a radiation quenching agent. The relaxation it induces due to quenching of the excited state can be ignored [Hap72], but the same is not true for the diffusion process, which determines the interaction time of the rubidium atoms with the laser beam. The contribution of the diffusive process to the transverse relaxation rate is that given in Eq. (1.1.70), with $l = 3\text{cm}$

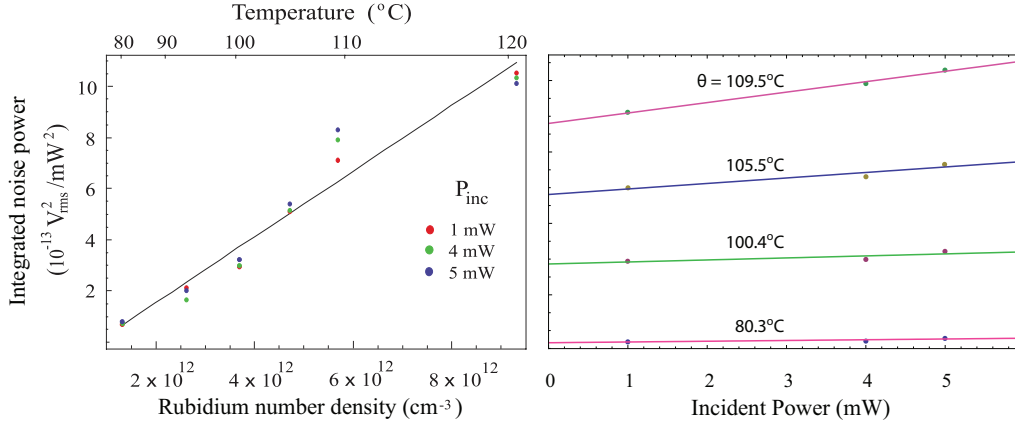


Figure 1:3-3

Integrated spin noise versus number density (left) and incident laser power (right). In both plots the integrated spectra scale linearly as expected.

the length of the cell and $r = \sqrt{r_1 r_2}$ the geometrical mean of the beam shape ellipse half-axes. Combined, the terms above give for the relaxation rate:

$$\frac{1}{T_2} = \frac{1}{T_{SE}} + \frac{1}{T_{SD}} + \gamma_D = \quad (1.3.33)$$

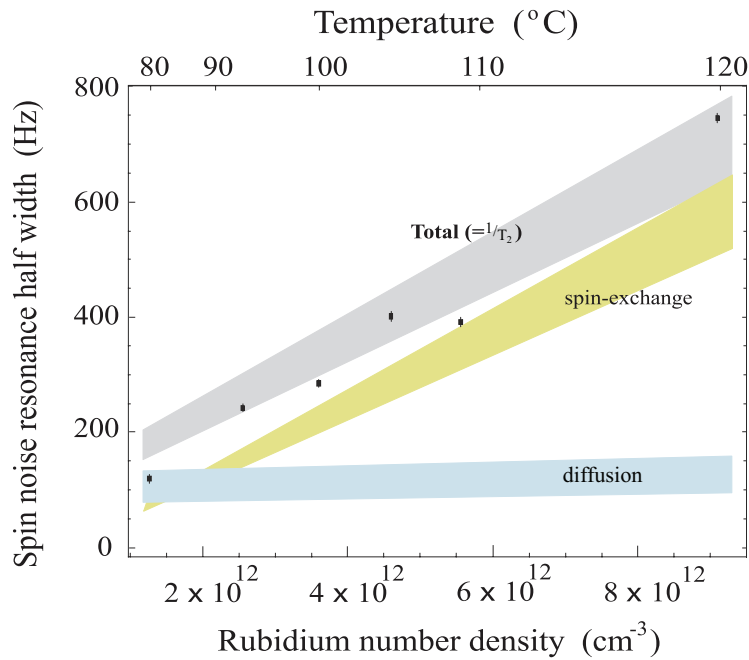
$$= n_d \sigma_{SE} \bar{v} + n_d \sigma_{SD} \bar{v} + n_d^{N_2} \sigma_{SD}^{Rb-N_2} \bar{v}_{Rb-N_2} + \left[\frac{\pi^2}{l^2} + \frac{5.8}{r^2} \right] \frac{760}{P} D_0 \quad (1.3.34)$$

where, unless specified, quantities refer to rubidium and rubidium-rubidium collisions.

Ultimately, for each temperature and for various input laser powers, spin noise spectra such as in Fig. 1:3-2 are obtained. Each of these is fitted to a function of the form:

$$\text{Fit function: } \sqrt{a + \frac{b(P)}{c/T_2^2 + (\omega - \omega_L)}} \quad (1.3.35)$$

where a accounts for shot and electronic noise, b is dependent on the input power and c is a small correction factor, on the order of a few percent, required to fit the data to a single Lorentzian, rather than to the exact Eq. (1.3.23). To eliminate the influence of optical pumping of the vapor from the probe laser, the transverse relaxation rate at each temperature is extracted by extrapolation of the measured widths to zero input laser power. In Fig. 1:3-4 the main results of the experiment are presented. The measured spin noise spectra widths, corresponding to the transverse spin relaxation rate of rubidium are superimposed on the calculated error bands of spin exchange relaxation, diffusion and total $1/T_2$. Spin destruction is omitted as it lied well below diffusion and was deemed negligible.

**Figure I:3-4**

Measured spin noise spectra half-widths (points), corresponding to the alkali transverse spin relaxation rates, plotted against number density. The calculated values for diffusion, spin exchange and total relaxation rates appear as error bands.

The measured and calculated values show reasonable agreement, taking into account the delicate nature of the measurement. The main source of discrepancy was our incomplete knowledge of the number density of rubidium in the cell for the various temperatures. Indeed, as described in Appendix C, the glass cell we used was “uncured”, that is to say that the inner cell walls and the rubidium vapor had not reached an equilibrium state at the beginning of our experiment. As a result the experimentally measured density values, which were used throughout the experiment, were significantly lower than the ones expected from the bibliography. However, the curing process can last for days or weeks, during which the expected density of the vapor at a given temperature rises. It is thus quite possible, almost certain to be exact, that the density values we used for the data analysis were obsolete, even since the first days of measurements; a fact that was recognized too late. We do point out here, though, that performing the calculations using the tabulated values of the Killian formula parameters, brings the experimentally measured relaxation rates right into the theoretical error band for the total $1/T_2$.

Still, our measurements reveal that spin noise can provide information about the system in a non-perturbative way, here by means of an off-resonant laser beam sensitive to spin fluctuations probing a thermal vapor, but with more possibilities available, both in terms of detection schemes or of operating parameters.

1.3.2 A Quantum Random Number Generator

1.3.2.1 Random number generators

▷ a:/ Why random numbers?

By the general term *random number generator* (RNG), a method or a process is implied, which produces a random outcome, be it in the form of a symbol or an action. For example, using a computer algorithm to produce random sequences of numbers or picking numbered balls from a jar somewhere in Texas until somebody yells “bingo!”, are processes which can both be regarded as RNGs. RNGs are of quintessential importance in a widely diverse range of applications: from encryption and cryptography to Monte-Carlo modeling of complex systems and from gambling applications to art. It is, thus, important that such generators are developed.

In the remainder of this section, we briefly review the currently employed RNGs and discuss proposed ways for testing them. Then we proceed to propose a true random number generator, based on the quantum process of spin noise.

▷ b:/ Computational generators and pseudo-randomness

With the advent of computers, the need to generate random numbers for statistical calculations became very strong, as the opportunity was presented to the scientific - and not only - community, to attack problems of previously unsurpassable complexity. These algorithms, going under names such as “linear congruential generators”, “linear feedback shift registers” or “Blum Blum Shub” and “Mersenne twister”, produce sequences of random numbers, which are, by definition, only *seemingly* random. All sequences are periodic and can be reproduced exactly if one starts from the same initial value, otherwise known as the *seed* or *key*. This is the reason for which such algorithms are termed *pseudo-random number generator* (PRNG) , or, otherwise, *deterministic random bit generator* (DRBG) , where the latter term cues the fact that any deterministic random number generator produces ultimately a sequence of pseudo-random numbers.

However, we must point out the fact that, through the years, PRNGs have grown to be extremely robust [MvOV86], with produced sequences of numbers asserted to be very nearly truly random [MN98] and with very rapid production rates; the fastest PRNG produces 300Gbps [KAR⁺10]. More than that, in certain types of applications, such as the Monte Carlo modeling of physical systems, the repeatability of the PRNG sequences may be desirable.

▷ c:/ Physical generators and true randomness

Before the development of computers, some physical process, which was expected to demonstrate random behavior, was repeated to generate random numbers.

Since the rate of production was usually low, as is to be expected from a mechanically actuated procedure, the outcome of such processes was often tabulated and distributed as lists of random numbers. Early forms of random number generation included, but were not exhausted to, dice rolling, coin flipping, drawing lottery notes from a box etc., and have evolved nowadays to the observation of natural phenomena, with the randomness in this case coming either from chaotic complexity of the particular system or from quantum mechanical uncertainty. The ultimate goal of the ever increasing level of sophistication put into these schemes is that of true randomness. A true random number generator (TRNG), as its name implies and within the anthropocentric approach, is a RNG which produces sequences of numbers utilizing a procedure, which is beyond human anticipation. That is to say, the procedure is purely non-deterministic and no amount of knowledge and computational power can predict the next number.

At present, the best approaches to TRNGs are based on the complex dynamics of chaotic systems or on taking advantage of quantum mechanical properties of systems, and random numbers are available either as provided services or as standalone devices. An example of the former type, that of a *chaotic random number generator* (CRND), can be found in www.random.org and is based on atmospheric noise. There is a long standing debate as to whether a chaotic system is actually non-deterministic and, consequently, whether the produced sequences of numbers can be regarded as being truly random. The obvious answer to the first question is, of course, *no*: a chaotic dynamical system, however complex, is uniquely determined by its initial conditions. So, *strictly* it is deterministic. The answer to the latter question, however, is not that straightforward, since the complexity of the number producing process is usually so vast, that it becomes impractical to attempt to predict the sequence. For example, in a real-life situation, if a CRND produces a 128-bit encryption key and vast computational power was in the hands of an eavesdropper, he would prefer to crack the key by brute force rather than calculate the trajectory and velocity of every particle in the atmosphere of the earth at the moment of the creation of the key, so as to extract the exact seed of the CRND which led to it. Here we do not debate this matter any further and we also seize the discussion of CRNDs, since they are beyond the scope of this work, which is the *quantum random number generators* (QRNG) .

QRNGs rely on the inherent indeterminacy of some quantum property of subatomic particles. The two most common processes in use are the time stamp of the decay of radioactive nuclei or the which-way information measured by single-photon detection of a photon going through a 50/50 beamsplitter. Services based on both these processes are available commercially today. In the former category, we find *HotBits*, an online project of Fourmilab in Switzerland (<http://www.fourmilab.ch/hotbits/>). HotBits are generated by timing successive

pairs of radioactive decays detected by a Geiger-Müller tube interfaced to a computer. Bits are produced at a somewhat small rate (100bps) and the generator continuously fills an inventory of data for future use. Once a portion of the inventory is used, it is discarded.

With the growth and development of the quantum information discipline in recent years, an increased interest in single atom manipulation and single photon generation and detection has arisen. An offspring of the research on the latter is the quantum random number generators employing properties of single photons. There is an increasing number of experimental publications on variations of the existing techniques (e.g. [SGG⁺00, WK10] and more) and at least two different commercial applications of this kind:

- ID Quantique produces a USB or PCI device implementing a single-photon-on-beamsplitter scheme, with detection of the photon in one arm of the beamsplitter, or the other corresponding to 0 and 1. The device produces data at 4Mbps.
- The “Quantum Random Bit Generator” (QRBG121) is used at the Ruder Bošković Institute, in the Centre for Informatics and Computing (Zagreb, Croatia). It is an online resource (<http://random.irb.hr/>) based on random emission of photons in a semiconductor and its subsequent detection via the photoelectric effect. The timing information of detected photons is used to generate random binary digits, with the production rate being 12Mbps. Recently, a variation of this technique achieved a 40Mbps production rate [WK10]

We note here that the production rates are limited mainly by the dead time of the detectors and remind the reader that the maximum reported rate for PRNGs is at 300Gbps, about 4 to 6 orders of magnitude higher than current QRNGs. We also note that, due to the particular implementation of a specific scheme or the influence of other external sources, the generator may become *biased*, that is it may favor the production of one out of the two bit species (i.e. more 0’s or more 1’s). This does not imply, however, that the generator is not random. For example, in an experiment where a single photon is incident on a beam splitter and detectors are placed on the two possible output pathways, a small misalignment may result in a biased result, but this is not to say that the which-way choice of the photon on the beam splitter is not random. To resolve the biasing issue, algorithms have been developed, which de-bias the random sequence at the expense of a percentage of the total number of bits being discarded [Neu51, Per92]. Today, debiasing efficiencies of more than 90% can be achieved.

▷ *d:/ Verification of randomness*

Verifying that a sequence of numbers is truly random is, in principle, impossible, at least when only the sequence is available. In the end, one could argue that, however improbable, even a periodic sequence of numbers can constitute the possible outcome of a TRNG. Thus, the only way to actually *prove* that a sequence is indeed random, is to prove that its generator is a TRNG, based on the particular physical process upon which it is implemented. However, for practical applications a RNG can be characterized by putting its output under a series of tests developed over the years, which search for a variety of non-random characteristics in the sequence. Failure to pass the tests does not mean that the RNG is not true and, vice versa, passing the tests does not make it true. Nevertheless, the tests provide a framework under which the various RNGs can be characterized within some confidence interval. In our work we used the Statistical Test Suite developed in NIST [RSN⁺01]. Additional tests, such as the bit-autocorrelation test, or variances of the tests included in [RSN⁺01] were taken from [MvOV86, SGG⁺00] and from online sources, predominantly the “diehard” and “dieharder” battery of tests [Mar, BEB]. Below we give a quick description of the tests we used for the characterization of our random number sequences.

- *Frequency or monobit test*

It is the elementary assumption that in a sufficiently large, non-biased sequence, the probabilities of 0’s and 1’s are both equal to $1/2$. It can be proved that the distribution of the binomial sum, normalized by the square root of the sequence length, \sqrt{N} , must tend to a normal distribution. The fraction of 0’s (or 1’s) is expected to lie within the deviation predicted by the normal distribution for the given N . The returned value of the test is:

$$p = \operatorname{erfc} \left(\frac{1}{\sqrt{2N}} \left| \frac{N}{2} - \sum_{i=1}^N x_i \right| \right) \quad (1.3.36)$$

where x_i are the numbers in the sequence and erfc is the complementary error function [$\operatorname{erfc}(x) = 1 - \operatorname{erf}(x)$]. A decision rule of 1% is put in place for this and for the majority of the tests, meaning that a p -value smaller than 0.01 fails the test.

- *Frequency test within a block*

In this test the ordered sequence of length N is split into n non-overlapping subsequences, each of length m , and deviations from the expected fifty-fifty distribution are probed by means of a χ -squared test. The χ -squared distribution with n degrees of freedom is the distribution of a sum of the squares of n independent standard normal random variables. It has a mean

and variance equal to n and $2n$, respectively. The return value of the test is:

$$p = Q\left(\frac{n}{2}, \frac{\chi_{\text{obs}}^2}{2}\right) \quad \chi_{\text{obs}}^2 = 4m \sum_{i=1}^n (\pi_i - 1/2) \quad (1.3.37)$$

where $Q(a, x)$ is the regularized complementary (or upper) incomplete gamma function[†] and π_i is the proportion of 0's (or 1's) in block i . A small p -value indicates a large deviation from the fifty-fifty distribution in at least one block. The decision rule of 1% applies here as well.

- *Runs test*

The test examines the occurrence of bit-runs, that is of sequences of identical bits of specific length, bound from the opposite bits on both sides. In essence, the test examines whether the sequence demonstrates oscillations ($0 \leftrightarrow 1$ jumps), which are too fast or too slow. For a random sequence of length N , the number of occurrences of a run of length n is expected to scale as $1/2^N$. The return value of the test is:

$$p = \text{erfc}\left(\frac{\sum_{i=1}^{N-1} (\delta_{x_i, x_{i+1}} - 1) - 2N\pi(1 - \pi)}{2\sqrt{2N}\pi(1 - \pi)}\right) \quad (1.3.38)$$

with large (small) p -values indicating fast (slow) oscillations.

- *Longest run of 0's or 1's in a block*

The number sequence is split into blocks and the test probes if the frequency of the longest run of 0's or 1's within a block is consistent with the expected frequency for a truly random distribution and for the chosen block length. And vice versa: from the frequency of the longest run of a bit within a block it is determined whether this run has the appropriate length. Note that an irregularity for 0's implies an inverse irregularity for 1's, so the test needs only be run for one of the two bits. Splitting the sequence of length N into m blocks of length n , the returned value of the test is:

$$p = Q\left(\frac{k}{2}, \frac{\chi_{\text{obs}}^2}{2}\right) \quad \chi_{\text{obs}}^2 = \sum_{i=1}^k \frac{(\nu_i - n\pi_i)^2}{m\pi_i} \quad (1.3.39)$$

[†]There is some disambiguation here in [RSN⁺01] as they use the term “incomplete gamma function”, for the *regularized* versions of both the regularly defined incomplete gamma function *and* its complementary.

where π_i has already been defined and each block has been partitioned into k run-length classes (k is dependent on n) with ν_i being the frequency of the i_{th} class within the block. Large χ_{obs}^2 indicate clustering of the bit under study within the block.

- *Non-overlapping and overlapping template matching tests*

In the non-overlapping test a predefined “template” string is searched either within the whole sequence of random numbers or within independent blocks. Starting from the first bit in the block, a window equal to the length of the template is compared to the template. If there is no match, the window shifts by one bit and the search is resumed. If it is found, the search resumes from the bit after the matched pattern. The aim of the test is to reject sequences exhibiting too many or too few occurrences of a given aperiodic pattern. The returned value is:

$$p = Q\left(\frac{n}{2}, \frac{\chi_{\text{obs}}^2}{2}\right) \quad \chi_{\text{obs}}^2 = \sum_{i=1}^n \frac{W_i - \mu}{\sigma^2} \quad (1.3.40)$$

where n is the number of independent blocks, W_i is the number of occurrences of the template in block i and the mean and variance are given by:

$$\mu = \frac{M - m + 1}{2^m} \quad \text{and} \quad \sigma^2 = m \left(\frac{1}{2^m} - \frac{2m - 1}{2^{2m}} \right) \quad (1.3.41)$$

with m the length of the template and M the length of each block. A very small p -value implies that the sequence contains an irregular amount of the template strings.

The overlapping template test differs by shifting the studied window by one bit, even if the template is matched. Analogous formulas for the returned p -value can be derived.

- *Serial test and approximate entropy test*

Closely related to the previous two tests are the serial test and the entropy test. The focus of the former is the frequency of all overlapping patterns of length m across the entire sequence. Since the assumption of randomness demands that all m -bit patterns are equiprobable, no particular pattern is expected to stand out. The latter seeks the same goal by comparing the frequency of overlapping blocks of two adjacent lengths (m and $m+1$)

against the expected result for a random sequence. We performed these as a side-tests, as they were considered largely redundant to other tests.

- *Spectral test*

This test applies a *discrete Fourier transform* (DFT) to the sequence looking for periodicities, which would imply deviations from a true random behavior. The transformation yields:

$$f_j = \sum_{i=1}^N x_i e^{i2\pi(i-1)j/N} \quad (1.3.42)$$

where the x_i 's are coded as ± 1 , rather than 0 and 1 and only the values from 0 to $N/2 - 1$ are considered owing to the symmetry of the real to complex value transformation. A threshold percentage, q , is set and we expect $q\%$ of the moduli of the f_j to be less than $\sqrt{\ln[1/(1-q)]N}$. The returned value of the test is:

$$p = \operatorname{erfc} \left(\frac{|n_{\text{obs}} - n_{\text{exp}}|}{2\sqrt{Nq(1-q)}} \right) \quad (1.3.43)$$

where n_{exp} and n_{obs} are the expected and observed number of peaks lower than the threshold value.

- *Bit autocorrelation*

Another spectral type test is the bit autocorrelation test. It examines the correlation between bits at a distance m according to the formula [SGG⁺00]:

$$G(m) = \frac{1}{N} \sum_{i=0}^{N-1} x_i \oplus x_{(i+m) \bmod N} \quad (1.3.44)$$

and is expected to be equal to $1/2$ within statistical deviation. The symbol “ \oplus ” denotes an exclusive-OR operation.

- *Maurer's “Universal Statistical” test and Lempel-Ziv compression test*

These two tests try to determine whether a given sequence can be significantly compressed without loss of information. If it can, then it is probably non-random. Random sequences can not be compressed, since, in a sense, information is completely delocalized within them; the sequence, as it is, *is* the contained information. Maurer's test checks the distance between matching patterns, while the Lempel-Ziv test focuses on the number of

cumulatively distinct patterns (words). The particulars of their implementation are not presented here, since, in the analysis of our data, these two algorithms were used only as indicators of randomness. The reason is that they both work better with large data sets, which we didn't have. No apparent compression was observed in our data, though, but still the results of these tests will have to be regarded as inconclusive.

- *Cumulative sums test*

In this test the random sequence, adjusted to ± 1 's, is thought of as a random walk around 0. Cumulative (recursive) sums are the random walk steps and the excursions from 0 are compared to the excursions expected from a truly random walk. The reference distribution here is, of course, the normal distribution. A variation of this test is the random excursions test, which examines the frequency of cycles in the cumulative sums random walk, i.e. the frequency of excursions starting and ending at the same distance from the mean. A variation of the latter focuses on the total number of times that a particular state was visited. In our analysis, we mostly used the cumulative sums test.

We remind the reader at this point that all these tests, however strongly they might indicate that a sequence of numbers is indeed random or not, their results are just, as the word says: indications. No such thing as a proof of randomness exists on the basis of just examining a sequence of numbers. That's what makes them sequences pretty.

1:3.2.2 The spin-noise QRNG

▷ a:/ *Method and experiment: Spin noise transient signals*

Here we present a QRNG based on the spin noise of hot alkali atoms. The experimental setup used for the generator is depicted in Fig. 1:3-5. Technically it differs from the setup of Fig. 1:3-1 in that we used a different laser (Sacher LaserTechnik Tiger), blue detuned by about 30GHz from the D1 line of rubidium, which would provide up to 30-40 mW of power. Conceptually, the difference with Fig. 1:3-1 is in the final leg, where, instead of feeding the polarimeter signal to the spectrum analyzer, we pass it through a low-noise bandpass filter (BPF) centered at the Larmor frequency, aiming to isolate the frequencies in the spectrum where spin noise is expected to have a strong influence. After a small amplification step, the signal is fed to the DAQ card and, subsequently, a custom made *LabView* routine records the input signal, as a discrete time series at a sampling rate of

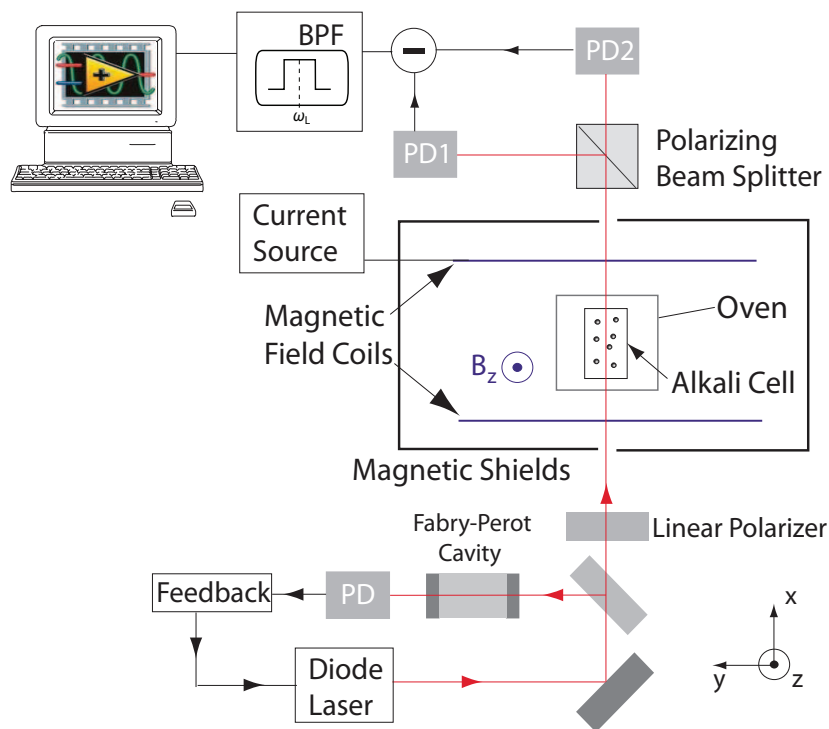


Figure 1:3-5

A quantum random number generator.

250kHz, and proceeds to the processing and extraction of the random number sequence. The procedure implemented in the routine is the following:

1. Magnetic field off: Monitoring the polarimeter signal yields, predominantly, shot noise fluctuations (white trace in Fig. 1:3-6a).
2. Define an upper (positive) and lower (negative) signal threshold, beyond which, shot noise is highly unlikely to reach. Since it is easy to verify that shot noise follows a Gaussian distribution, we chose these thresholds to be at five standard deviations, where about 1 in 10.000.000 shot noise signal values ever strays.
3. Magnetic field on: Monitoring the polarimeter signal yields spin and shot noise fluctuations (black trace in Fig. 1:3-6a). Since noise contributions are added in quadrature, the large increase of the signal implies that spin noise is much stronger than shot noise in the studied region of frequencies. So we conclude that the observed fluctuations are mainly due to the creation and decay of random polarization coherences within the vapor

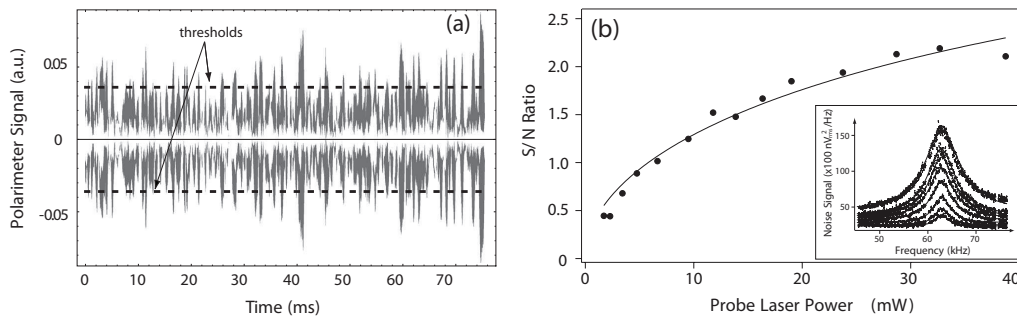


Figure I:3-6

(a) Transient polarization oscillations (black) and shot noise (white). Transient signals crossing the thresholds yield random bits 1 or 0, dependent on whether the positive or negative threshold was crossed first.

(b) Scaling of Signal-to-Noise ratio with probe laser power. The saturation behavior indicates that the signals are indeed due to spin noise and not due to coherent perturbations, such as optical pumping.

Inset: the spin noise spectra from which the main figure is derived. These were not taken at the Larmor frequency, detuning and temperature used in the QRNG, but for the purpose they serve this is irrelevant.

4. If the positive threshold is crossed, generate a random bit “1” and go to the next step, else, if the negative threshold is crossed, generate a random bit “0” and go to the next step. The idea here is that the component of the vapor polarization fluctuation along the direction of propagation can peak while being either parallel or anti-parallel to the wave vector. The two situations induce polarimetric signals out-of-phase by π rad and isotropy demands that they must occur with equal probabilities.
5. Wait for time of a few T_2 . Because the decoherence of the spontaneously created polarization fluctuations is governed by the transverse relaxation rate of the alkali atoms, $1/T_2$, attempting to acquire a random number immediately after the acquisition of another, might result in correlated output. Increasing the waiting time, decreases the probability of correlations, but also the production rate.
6. Go to step 3.

The extracted sequences of numbers were put through a number of statistical tests, described in the previous section. However, before we discuss the results of the tests, we have to persuade ourselves about four things:

a. Is spin noise indeed of quantum origin?

If this is not the case, then our generator is not a QRNG, but, rather, falls into the category of CRNGs. Spin noise, however, *is* of quantum origin. The outcome of a spin dependent collision of the various types taking place between alkali atoms depends on their relative trajectory, which is a classical, yet a good chaotic random variable in its own right, and the their spin-spin interaction, which, for uncorrelated spins, fully bears the indeterminacy inherent in purely quantum mechanical processes. Thus, the collective spin of the vapor, which is the incoherent sum of individual spins, will also be a quantum random variable. In the worst case scenario, the chaotic part of the inherited randomness may introduce a bias in the QRNG outcome, which, as discussed above, does not constitute a fatal flaw. In our physically and magnetically isolated vapor, no such bias is expected, nonetheless. A more elaborate argument on the quantum random nature of spin noise can be found in our related publication at the end of this thesis.

b. Are the observed polarization fluctuations indeed due to spin noise?

Since we are probing the medium with a, largely, coherent beam, it is conceivable that fluctuations in the characteristics of the beam might induce coherent transients to the medium. In such a case, the conversation has to be transferred to whether the fluctuations in the light, e.g. polarization fluctuations, are of quantum origin or not. If they are, then we still have a QRNG, albeit of different nature. To verify that we are observing the noise structure of the vapor, rather than an optical pumping effect related to fluctuations in the polarization of the laser, in Fig. 1:3-6(b) we plot the Signal-to-Noise ratio of the spin noise peaks as a function of the incident laser power. The power broadened width of the spin noise lines is of the form $aI + b$, where I is the incident laser intensity and b is the collisional and diffusional width. The polarimeter signal is proportional to the Faraday rotation angle and to the light intensity, i.e. it is of the form $I\Theta_F$, where Θ_F is, in turn, proportional to the expectation value of the vapor spin along the direction of propagation and both quantities are independent of the laser power. The peak of the PSD of the spin noise spectrum is then proportional to $I^2\Theta_F^2/(aI + b)$ (in V^2/Hz units). On the other hand, the background is dominated by shot noise, which is proportional to I , thus, altogether, the signal to noise ratio will be of the form $S/N = cI/(aI + b)$ and will demonstrate a saturating behavior for large intensities, as is indeed the case in 1:3-6(b). If optical pumping occurred, then the Faraday rotation angle would also be proportional to the incident laser power, the Signal-to-Noise ratio would be of the form $(S/N)_{op} = c'I^3/(aI + b)$ and the plot would not saturate. We, thus, conclude that the main signal contribution is, indeed, noise.

c. Is our random sequence expected to contain correlated bits?

This is not a physically significant question, but a practical one. If too much correlation is present, we have to increase the dead-time between bit acquisitions, a fact which will have an impact on the production rate of the generator. The actual correlation of the sequences is examined in the statistical tests below, but this is a question as to whether we expect correlation theoretically. Since spin noise evolution is an Ornstein-Uhlenbeck process, as described in the introductory text about spin noise, its autocorrelation will decay as $e^{-\tau/T_2}$. Thus, acquiring 1 bit every $10 T_2$, as was our goal, would result in an autocorrelation on the order of 10^{-5} or, equivalently, 1 correlated random bits every 10^5 . In practice, one defines a specific waiting time between acquisitions, guided by the known or estimated T_2 at the given experimental conditions. However, due to the exponential dependence of the autocorrelation on T_2 , the percentage of correlated bit pairs within the sequence can be dramatically influenced by small changes in the temperature of the cell or the detuning or power of the laser.

d. Does shot noise generate too many erroneous bits?

This is also a practical question, as a positive answer would force us to increase the threshold values and would, subsequently, result in a decrease of the production rate. Our aim is to attribute a value 1 (0) to the spontaneously generated spin polarizations of the vapor, which peak along the positive (negative) propagation axis. An erroneous bit occurs when shot noise (or any other source of noise for that matter) forces the signal to cross the opposite threshold than that corresponding to the polarization fluctuation at hand. So, if the probability distribution function of the spin noise signal and the joint probability distribution function for the two uncorrelated random variables of spin and shot noise signals are denoted by $f(S_{sp})$ and $g(S_{sp}, S_n)$, respectively, then the probability that noise will push the signal beyond the wrong threshold will be one half times the conditional probability of spin noise being within thresholds and shot noise being at least equal to the threshold minus spin noise, $P = \frac{1}{2} \int_{-S_{th}}^{S_{th}} f(S_{sp}) dS_{sp} \int_{S_{sp}=-S_{th}}^{S_{th}} \int_{S_n=S_{th}-S_{sp}}^{\infty} g(S_{sp}, S_n) dS_{sp} dS_n$, where S_{th} is the threshold value and the $1/2$ comes from the fact that half the times, shot noise induces the acquisition of a correct random bit which would have not been detected otherwise, i.e. it forces a below threshold positive (negative) polarization to cross the positive (negative) threshold. In our case, where the variance of the spin noise was slightly greater than double the shot noise variance, the argument above leads to a probability of about $1/1000$, i.e. 1 erroneously generated bit per 1000. This is not a small probability and it appears that we had exaggerated its value in the published work. However, we remind the reader that this is not a crucial flaw of the generator, as it

can be remedied by increasing the threshold value, at the expense of production rate. It is to be noted, though, that laser shot noise is a quantum random process in its own right and the characterization “erroneous” for bits coming from shot noise may be a little harsh. If one wants to avoid it nonetheless, another remedy, which does not affect the production rate, would be to decrease the Larmor frequency, as this would effectively increase the variance of the spin noise signal distribution, by allowing more spin relaxation damping per oscillation. However, this technique is limited from below by low frequency noise. Of course, the most straightforward improvement would be to increase the Signal-to-Noise ratio, but this is beyond the point here.

We believe we have established, with the minor exception of point (d) above which, though, is of technical nature, that the proposed experimental scheme is expected to qualify as a true QRNG. We now proceed to analyze the sequences of random numbers acquired by the generator.

▷ b:/ Testing randomness

The statistical tests described in 1.3.2.1d:/ are applied to sequences of 10^5 to 10^6 random numbers recorded in our apparatus. The length of our sequences is not considered sufficiently large for some tests, so these were performed indicatively. Nevertheless, no deviation from random behavior was observed in these tests. In all tests, the defined, returned p -values are all compatible with the random assumption.

Few tests produce a more illustrative result and we present these in Fig. 1:3-7. In (a) the frequency of 1’s is shown versus sample size and a comparison to the PRNG routine of *Mathematica* is made. The probability of 1’s tends to the expected value of $1/2$ for sufficiently large sample, as expected. In (b) the runs of 1’s (solid line) and 0’s (dashed line) are counted and are seen to scale as $1/2^n$, with n the length of the studied run, as expected. In (c) we show the result of testing bit autocorrelation at various bit distances. The expected, unbiased result of $1/2$ is obtained. Finally, in (d) the result of the spectral test is depicted, which also demonstrates normal random behavior. No test indicated any sign of incompatibility with the assumption that our generator indeed produced random numbers.

Conclusively, we have presented a robust, unbiased, true quantum random number generator. Its production rate is limited by the transverse spin relaxation rate; a rate which the experimentalist routinely tries to minimize, we needed it to be large. In alkali atoms and typical experimental conditions, the production of uncorrelated random numbers will be, perhaps, on the order of a few kbps. However, the exact same principle can be used with spin noise spectra observed

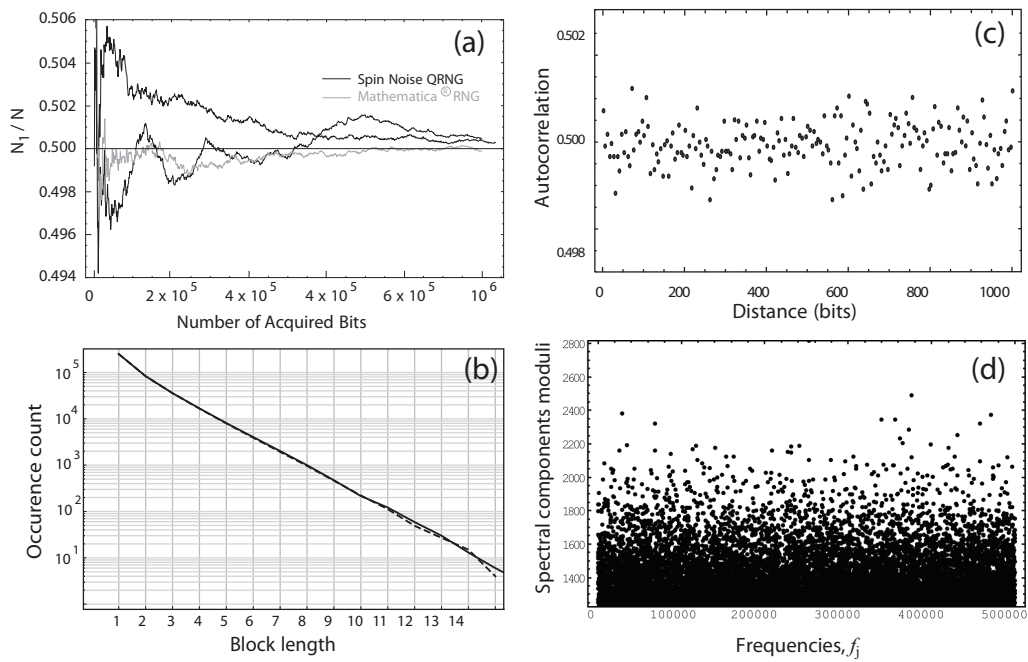


Figure 1:3-7

Few of the statistical tests which were performed to probe the randomness of our bit-sequences produce an illustrative result.

- (a) Frequency test
- (b) Runs test
- (c) Bit-autocorrelation test
- (d) Spectral test

in semiconductors [ORHH05, SZK⁺07, MORH10], where the corresponding relaxation rates reach up to the GHz range and could potentially lead to QRNGs of similar production rates.



Bibliography @ Spin Noise

- [ABE⁺98] S Appelt, BA Baranga, CJ Erickson, MV Romalis, AR Young, and W Happer, *Theory of spin-exchange optical pumping of ^3He and ^{129}Xe* , Phys Rev A **58** (1998), no. 2, 1412.
- [AIV77] E Arimondo, M Inguscio, and P Violino, *Experimental determinations of the hyperfine structure in the alkali atoms*, Rev Mod Phys (1977), no. 49, 31.
- [ALKR02] JC Allred, RN Lyman, TW Kornack, and MV Romalis, *High-sensitivity atomic magnetometer unaffected by spin-exchange relaxation*, PRL **89** (2002), no. 13, 130801.
- [BEB] RG Brown, D Eddelbuettel, and D Bauer, *Dieharder: A random number test suite*, Online resource, Duke University, Physics Department, <http://www.phy.duke.edu/~rgb/General/dieharder.php>.
- [BHP64] LC Balling, RJ Hanson, and FM Pipkin, *Frequency shifts in spin-exchange optical pumping experiments*, Phys Rev **133** (1964), A607.
- [Blu96] K Blum, *Density matrix theory and applications*, 2nd ed., Plenum Press, New York, 1996.
- [BPCH80] ND Bhaskar, J Pietras, J Camparo, and W Happer, *Spin destruction in collisions between cesium atoms*, PRL **44** (1980), no. 14, 930.
- [CRBS04] SA Crooker, DG Rickel, AV Balatsky, and DL Smith, *Spectroscopy of spontaneous spin noise as a probe of spin dynamics and magnetic resonance*, Nature **431** (2004), 49.
- [CTL67a] C Cohen-Tannoudji and F Laloë, *Modification de la matrice polarisation d'un faisceau lumineux lors de la traversée d'une vapeur atomique soumise au pompage optique. - deuxième partie*, Journal de Physique **28** (1967), 722.
- [CTL67b] ———, *Modification de la matrice polarisation d'un faisceau lumineux lors de la traversée d'une vapeur atomique soumise au pompage optique. - première partie*, Journal de Physique **28** (1967), 505.
- [CW69] CK Chang and RH Walker, *Calculations of spin-exchange cross sections of alkali atoms by partial-wave analysis*, Phys Rev **178** (1969), no. 1, 198.

- [Dal61] A Dalgarno, *Spin-change cross sections*, Proc R Soc **262** (1961), 132.
- [Del05] AT Dellis, *Design, construction and characterization of coils for the creation of weak magnetic fields and gradients*, Master's thesis, Univ. of Crete, dept. of Physics, 2005, Diploma Thesis.
- [ELH⁺00] CJ Erickson, D Levron, W Happer, S Kadlecěk, B Chann, LW Anderson, and TG Walker, *Spin relaxation resonances due to spin-axis interaction in dense rubidium and cesium vapor*, PRL **85** (2000), no. 20, 4237.
- [Fan57] U Fano, *Description of states in quantum mechanics by density matrix and operator techniques*, Rev Mod Phys **29** (1957), 74.
- [Fra59] W Franzen, *Spin relaxation of optically aligned rubidium vapor*, Phys Rev **115** (1959), no. 4, 850.
- [Gar90] CW Gardiner, *Handbook of stochastic methods, for physics chemistry and the natural sciences*, second ed., Springer-Verlag, Berlin Heidelberg, 1990.
- [GC92] N Gisin and MB Cibils, *Quantum diffusions, quantum dissipation and spin relaxation*, J Phys A: Math Gen **25** (1992), 5165.
- [Geh03] ME Gehm, *Properties of ⁶Li*, Tech. report, JETLab at Univ. of Duke, dept. of Physics, 2003, <http://www.phy.duke.edu/research/photon/qoptics/techdocs/pdf/PropertiesOfLi.pdf>.
- [Gla63] AE Glassgold, *Spin-exchange in collisions between atoms*, Phys Rev **132** (1963), 2144.
- [GP92] N Gisin and IC Percival, *The quantum state diffusion model applied to open systems*, J Phys A: Math Gen **25** (1992), 5677.
- [Gro64] F Grossetête, *Relaxation by spin exchange collisions*, J Physique **25** (1964), 383.
- [Gro68] ———, *Relaxation by spin exchange collisions (II)*, J Physique **29** (1968), 456.
- [GSM06] JM Geremia, JK Stockton, and H Mabuchi, *Tensor polarizability and dispersive quantum measurement of multilevel atoms*, PRA **73** (2006), 042112.
- [Hap72] W Happer, *Optical pumping*, Rev Mod Phys **44** (1972), no. 2, 169.
- [HM67a] W Happer and BS Mathur, *Effective operator formalism in optical pumping*, Phys Rev **163** (1967), no. 1, 163.
- [HM67b] ———, *Off-resonant light as probe of optically pumped alkali vapors*, PRL **18** (1967), no. 15, 577.
- [HT73] W Happer and H Tang, *Spin-exchange shift and narrowing of magnetic resonance lines in optically pumped alkali vapors*, PRL **31** (1973), no. 5, 273.
- [HT77] W Happer and AC Tam, *Effect of rapid spin exchange on the magnetic-resonance spectrum of alkali vapors*, PRA **16** (1977), no. 5, 1877.

- [IBB⁺93] WM Itano, JC Bergquist, JJ Bollinger, JM Gilligan, DJ Heinzen, FL Moore, MG Raizen, and DJ Wineland, *Quantum projection noise: Population fluctuations in two-level systems*, PRA **47** (1993), 3554.
- [KAKR03] IK Kominis, JC Allred, TW Kornack, and MV Romalis, *A subfemtotesla multichannel atomic magnetometer*, Nature **422** (2003), 596.
- [KAR⁺10] I Kanter, Y Aviad, I Reidler, E Cohen, and M Rosenbluh, *An optical ultrafast random bit generator*, Nature photonics **4** (2010), no. 1, 58.
- [KAW98] S Kadlecěk, LW Anderson, and T Walker, *Measurement of potassium-potassium spin relaxation cross sections*, Nuclear Instruments and Methods in Physics Research A **402** (1998), 208.
- [Kni89] RJ Knize, *Spin destruction in rubidium-rubidium and potassium-potassium collisions*, PRA **40** (1989), no. 11, 6219.
- [KWH88] RJ Knize, Z Wu, and W Happer, *Optical pumping and spin exchange in gas cells*, Advances in Atomic and Molecular Physics **24** (1988), 223.
- [Leg01] AJ Leggett, *Bose-Einstein condensation in the alkali gases: some fundamental concepts*, Rev Mod Phys **73** (2001), no. 2, 307.
- [Mar] G Marsaglia, *Diehard battery of tests of randomness*, Online resource / cd-rom, Florida state university, <http://www.stat.fsu.edu/pub/diehard/>.
- [MB98] M Merawa and D Bèguè, *Dipole polarizabilities of the potassium atom in its ground (4^2S) and excited (4^2P , 5^2S) states, and long-range dispersion interactions between two K atoms*, J Chem Phys **108** (1998), no. 13, 5289.
- [MCR⁺06] B Mihaila, SA Crooker, DG Rickel, KB Blagoev, PB Littlewood, and DL Smith, *Quantitative study of spin noise spectroscopy in a classical gas of $^4\text{1K}$ atoms*, PRA **74** (2006), 043819.
- [Mit00] T Mitsui, *Spontaneous noise spectroscopy of an atomic magnetic resonance*, PRL **84** (2000), no. 23, 5292.
- [MKJ⁺09] J Ma, A Kishinevski, YY Jau, C Reuter, and W Happer, *Modification of glass cell walls by rubidium vapor*, PRA **79** (2009), 042905.
- [MN98] M Matsumoto and T Nishimura, *Mersenne twister: a 623-dimensionally equidistributed uniform pseudo-random number generator*, ACM Transactions on Modeling and Computer Simulation **8** (1998), no. 1, 3.
- [MORH10] GM Müller, M Oestreich, M. Römer, and J Hübner, *Semiconductor spin noise spectroscopy: Fundamentals, accomplishments, and challenges*, arXiv/cond-mat:1008.2191 (2010), Physica E: invited review.
- [MTH70] BS Mathur, HY Tang, and W Happer, *Light propagation in optically pumped alkali vapors*, PRA **2** (1970), no. 3, 648.
- [MvOV86] AJ Menezes, PC van Oorschot, and SA Vanstone, *Handbook of applied cryptography*, CRC press, 1986, fifth reprint.

- [Neu51] J Von Neumann, *Various techniques used in connection with random digits*, Applied Mathematics Series **12** (1951), 36.
- [NIS] NIST, *NIST-F1 cesium fountain atomic clock*, <http://www.nist.gov/phylab/div847/grp50/primary-frequency-standards.cfm>.
- [ORHH05] M Oestreich, M Römer, RJ Haug, and D Hägele, *Spin noise spectroscopy in GaAs*, PRL **95** (2005), 216603.
- [PC70] DE Pritchard and FY Chu, *Alkali-Alkali differential spin-exchange scattering II*, PRA **2** (1970), no. 5, 1932.
- [PCCK70] DE Pritchard, GM Carter, FY Chu, and D Kleppner, *Alkali-Alkali differential spin-exchange scattering I*, PRA **2** (1970), no. 5, 1922.
- [Per92] Y Peres, *Iterating von neumann's procedure for extracting random bits*, Annals of Statistics **20** (1992), no. 1, 590.
- [Per98] IC Percival, *Quantum state diffusion*, Cambridge University Press, 1998.
- [PF56] EM Purcell and GB Field, *Influence of collisions upon population of hyperfine states in hydrogen*, Astrophysics Journal **124** (1956), 542.
- [RSN+01] A Rukhin, J Soto, J Nechvatal, M Smid, E Barker, S Leigh, M Levenson, M Vangel, D Banks, A Heckert, J Dray, and S Vo, *A statistical test suite for random and pseudorandom number generators for cryptographic applications*, Special publication 800-22, NIST, 2001, Revised April 2010, LE Bassham III NIST STS website: <http://csrc.nist.gov/groups/ST/toolkit/rng/index.html>.
- [SGG+00] A Stefanov, N Gisin, O Guinnard, L Guinnard, and H Zbinden, *Optical quantum random number generator*, J Mod Opt **47** (2000), no. 4, 595.
- [Sob92] I.I. Sobelman, *Atomic spectra and radiative transitions*, 2nd ed., Springer Series on Atoms and Plasmas, vol. 12, Springer-Verlag, Berlin and Heidelberg, 1992.
- [Ste09] DA Steck, *Alkali D line data*, Tech. report, Univ. of Oregon, dept. of Physics / Los Alamos National Laboratory, 2009,
Na: <http://steck.us/alkalidata/sodiumnumbers.pdf>
Rb⁸⁵: <http://steck.us/alkalidata/rubidium85numbers.pdf>
Rb⁸⁷: <http://steck.us/alkalidata/rubidium87numbers.pdf>
Cs: <http://steck.us/alkalidata/cesiumnumbers.pdf>.
- [SvOP80] D Szostak, G von Oppen, and WD Porschmann, *Tensor polarizabilities of 1snd ¹D levels in He I*, Phys Lett **76A** (1980), no. 5,6, 376.
- [SVR10] V Shah, G Vasilakis, and MV Romalis, *High bandwidth atomic magnetometer with continuous quantum non-demolition measurements*, PRL **104** (2010), 013601.

- [SZK⁺07] D Stich, J Zhou, T Korn, R Schulz, D Schuh, W Wegscheider, MW Wu, and C Schöller, *Effect of initial spin polarization on spin dephasing and the electron g factor in a high-mobility two-dimensional electron system*, PRL **98** (2007), 176401.
- [Tie10] TG Tiecke, *Properties of potassium*, Tech. report, van der Waals-Zeeman institute, Univ. of Amsterdam, the Netherlands, 2010, <http://www.tobiastiecke.nl/archive/PotassiumProperties.pdf>.
- [Ver95] JT Verdeyen, *Laser electronics*, third ed., Prentice Hall, 1995.
- [WC94] ME Wagshul and TE Chupp, *Laser optical pumping of high-density Rb in polarized ^3He targets*, PRA **49** (1994), no. 5, 3854.
- [WD56] JP Wittke and RH Dicke, *Redetermination of the hyperfine splitting in the ground state of atomic hydrogen*, Phys Rev **103** (1956), no. 3, 620.
- [WH97] TG Walker and W Happer, *Spin-exchange optical pumping of noble-gas nuclei*, Rev Mod Phys **69** (1997), no. 2, 629.
- [WK10] MA Wayne and PG Kwiat, *Low-bias high-speed quantum random number generator via shaped optical pulses*, Optics Express **18** (2010), no. 9, 9351.
- [WKH⁺86] Z Wu, M Kitano, W Happer, M Hou, and J Daniels, *Optical determination of alkali metal vapor number density using Faraday rotation*, Applied Optics **25** (1986), no. 23, 4483.
- [WMZJ92] L Windholz, M Musso, G Zerza, and H Jäger, *Precise Stark-effect investigations of the lithium D_1 and D_2 lines*, Phys Rev A **46** (1992), no. 9, 5812.
- [Zap82] VS Zapasskii, *Highly sensitive polarimetric techniques*, Zhurnal Prikladnoi Spektroskopii **37** (1982), no. 2, 181.

Part II

Quantum Biology

Chapter II:1

Spin Chemistry

II.1.1 *Introduction*

It has been a long held belief that quantum phenomena do not belong to the macroscopic world. Thermal decoherence is too strict an homogenizer to allow for delicate quantum intricacies to surface. Although a couple such phenomena, as is superconductivity * and superfluidity do reach out of the microscopic realm, they do so at cryogenic temperatures and/or sterilized laboratory conditions. Not too many years back, the notion that a wealth of coherent quantum procedures could be at play in the wet and warm environment of bio-molecules would be frowned upon and the bearer of such ideas would be, no doubt, cast out of scientific community as mentally disturbed. Luckily, nature cares not for the lack of fantasy on behalf of the human species, nor for her status as a member of the scientific community and, apparently, takes immense pleasure in capsizing the scientific status quo time after time after time.

In photosynthesis, highly specialized absorptive molecules, strategically positioned on a protein substrate and exposed to sunlight, play the role of light harvesting *antennae*. The captured energy is channeled to the photosynthetic *reaction centers*, the biological analogue to solar cells. Impressively, in typical conditions energy transfers occur with almost *unit quantum efficiency* at distances of tens on nm through immensely complex potential energy landscapes created by hundreds of molecules in times often smaller than a ps [CWW⁺10]. Until recently the effect was poorly understood, since common scientific sense dictated that energy should be transferred by charge incoherently hopping from one site to the next down the ladder, until it reached the reaction center. However, such a mechanism would be inefficient and slow; energy transfer in the

*and the related quantization of magnetic flux and the Josephson junctions.

early stages of photosynthesis is efficient and fast and, in fact, it is the speed of the process which makes it so efficient. In the last few years, studies basically using 2D electronic spectroscopy, a method developed by the Fleming group in Berkeley, and a few other monitoring techniques, have revealed that energy is transferred in a *coherent, wave-like* manner through the tunnel of molecular potentials [ECR⁺07, LCF07, SIFW10, CWW⁺10]. This is an impressive find since it implies coherent excitation of the receptor and large scale correlated motion of the protein matrix, shaping the potential landscape to protect this coherence. Essentially, the state of the system simultaneously samples all the potential energy pathways and chooses the most efficient one, much like a quantum computer would do.

But coherence within the life giving process of photosynthesis does not stop at that. It has been observed that the outcome of some of the chemical reactions involved in photosynthesis can be perturbed by the presence of weak magnetic fields, a fact attributed to the influence the external field can have on the hyperfine interaction induced, coherent spin motion of certain reacting ionic pairs[†] [SU89, HMB79, SCS07]. The early studies on bacterial photosynthesis [HRGD77, BSP77, HMB79] revealed that within 10ps of photoexcitation, a pair is formed comprising two radical ions, a bacteriochlorophyll dimer (BChl₂⁺) and bacteriopheophytin (BPh⁻). The pair is formed in the Singlet spin state and, during its lifetime, evolves into a coherent mixture of Singlet and Triplet spin states, a conversion mediated by hyperfine interactions between the nuclei and the unpaired electrons of the molecules. Eventually the pair of ions will charge recombine to one of two product states, depending on its spin state: the Singlet state can fall back to the ground states of BChl₂ and BPh and the Triplet to the excited ³BChl₂^{*}. Since an external magnetic field exerts forces to the constituent elements of the pair, which are of the same nature as the hyperfine interaction, it is likely to influence the relative occupations of the Singlet and Triplet states in the S-T superposition state of the pair and thus affect the relative amounts of outcome products. As it turns out, such pairs of radical ions are a major player in virtually all of biology (among other areas) and it is their magnetic properties that make the main subject of Spin chemistry and the focus of our work. But what is a radical ion pair?

II.1.2 Radical Ion Pairs

In chemistry, a structured cluster of atoms, molecules or ions with unpaired electrons in an open shell configuration which reacts as a single entity, is called a *radical*. The unpaired electrons are responsible for the high chemical reactivity of

[†]The effect is discussed to some more detail in the next section. All mathematical descriptions are reserved for the next chapter.

radicals transforming them into key players in a wide range of chemical reactions; from combustion and polymerization to a wealth of biochemical processes.

A *radical pair* or *radical ion pair* (abbreviated as RP or RIP from time to time) is formed through charge transfer in photo-excited radical dyads, where the electron of the *Donor* radical is paired to the electron of the *Acceptor* radical. Neutral radical pairs can also be formed through cleavage of chemical bonds by means of UV or visible radiation (homolysis, radiolysis, photolysis). The interesting feature about a radical pair is that it is formed in a spin-correlated state and the products of its charge recombination are - usually - spin dependent. A number of dynamical processes (coherent and incoherent) taking place within a RIP can be influenced by external magnetic fields and this influence can, many a time, be deduced from monitoring the products of the reaction. This forms the basis of the magnetic sensing ability of radical ion pairs.

II.1.3 *Magnetic Field Effects in Radical Ion Pairs: a roundup of experimental observations*

In this section we present a number of experimental works demonstrating the various magnetic field effects taking place in radical ion pairs and each is given a qualitative description. A more detailed discussion of the origins of these effects and their mathematical representations is reserved for the next chapter (see section II.2.2), where master equations for the description of RIP dynamics are introduced. Also, pictorial representations of the various effects through proposed vector models are given in App. D.

II.1.3.1 **The Normal or High Field Effect**

Magnetic field effects in RIP reactions were identified in the 70s when it was realized that fields on the order of a few hundred Gauss can significantly suppress the yield of Triplet products for Singlet-born pairs, relative to the zero field value. In [SSW⁺76] the authors study the Pyrene [Py] and 3,5-dimethoxy-N,N-dimethylaniline [DMDMA] (as well as the Pyrene [Py] and N,N-dimethylaniline [DMA]) radical pair formed by photo-induced electron transfer in a methanol solution. The pair can recombine from the Singlet state to the ground $^1\text{Py}^* + ^1\text{DMDMA}$ (slow) or from the Triplet to the excited $^3\text{Py}^* + ^1\text{DMDMA}$ (rapid).

Two phases of recombination were identified: the fast *geminat*e phase and the slow *homogeneous* phase. The former is due to the ability of the pair to recombine on site, within a few ns from its creation and the latter is due to constituents of pairs drifting apart in the solution and recombining at random with other drifters, a process happening in the $\sim 1000\text{ns}$ time scale. The latter is also a random orientation process where radical encounters happen at a 3:1

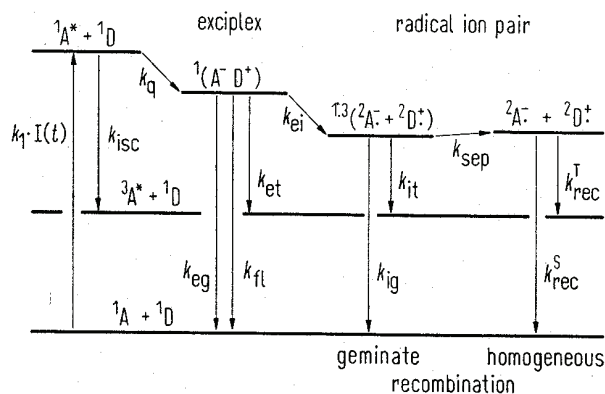


Figure II:1-1

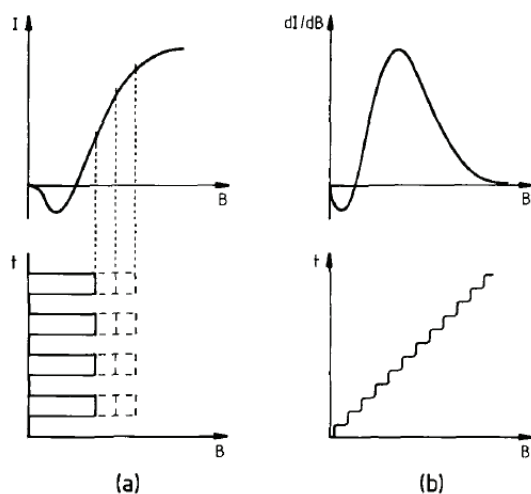
Py + DMDMA reaction scheme in methanol [SSW⁺76]

Triplet to Singlet ratio, giving a fixed ratio of products, insensitive to magnetic fields. More interesting phenomena arise in the geminate phase.

In the geminate phase it was observed that Triplet products are formed very rapidly within ns from the creation of the pair. An explanation of this phenomenon was given via the hyperfine interaction of the nuclei of the constituent molecules with the paired electrons. The hyperfine interaction can redistribute angular momentum among the nuclei and the electronic pair, thus enabling the spin state of the latter to be transformed from the initial Singlet state to Triplet. For the particular pairs studied, Triplet recombination is energetically preferred and so, pairs reaching the Triplet quickly recombine to give the observed products. The hyperfine model was found to be compatible with experimental data and was further strengthened by the experiment reported in [WSW78], where the authors used perdeuterated versions of the reacting molecules to prove that the geminate recombination was affected by the nuclear gyromagnetic ratios, as is to be expected from reactions dependent on the hyperfine interaction.

The influence of an external magnetic field on the products of the reaction comes about as follows: in the case of zero field, the Singlet and all three Triplet states are degenerate. Thus the Singlet can follow three pathways toward the Triplet manifold. When an external field is applied, the Triplet degeneracy is lifted and when its strength exceeds the magnitude of the hyperfine couplings, the $|S\rangle \rightleftharpoons |T_{\pm}\rangle$ transitions become forbidden and the Singlet is left with only one pathway to the Triplet (namely the $|S\rangle \rightleftharpoons |T_0\rangle$), thus the Triplet yield is reduced.

Another example of this type of effect was already mentioned in the introduction. In bacterial photosynthesis, the bacteriochlorophyll dimer ($BChl_2^+$) and bacteriopheophytin (BPh^-) form a RIP which can decay slowly to the ground $BChl_2 + BPh$ through the Singlet state or rapidly to the excited ${}^3BChl_2^* + BPh$

**Figure II:1-2**

Magnetic field modulation of reaction yields (MARY) used for the study of LFE [HHMS88].

(a) square-wave modulation of the total field for different field amplitudes yields the normal MARY curve directly. I is a monitored absorption or fluorescence intensity quantifying the MFE.

(b) sinusoidal modulation of linearly varied field gives the field-derivative of the spectrum shown in (a).

The low-field feature of opposite phase relative to the familiar high-field behavior is evident.

through the Triplet. The same observation is made: a magnetic field on the order of a few hundred Gauss all but eliminates Triplet yield, by virtue of the above described magnetic field effect.

II:1.3.2 The Low Field Effect

The discussion in the previous section would seem to imply that a rising magnetic field monotonically increases the Singlet to Triplet product ratio (or, equivalently, decreases the Singlet to Triplet conversion efficiency) of Singlet born pairs, up to some saturation value. However, experiments involving absorption or fluorescence monitoring and weak modulation of the magnetic field, have revealed that Singlet-Triplet conversion demonstrates a local maximum for weak fields on the order of the hyperfine couplings.

The effect has been observed in radiolytically created RPs [SLTM95], in photochemically created RPs in polar solutions [HHMS88, BKMS93], in RPs confined in micelles [STB91] etc. Two theoretical explanations have been put forward to account for the origins of the phenomenon, both of which are actually true in certain systems, with one of the two, however, being of more fundamental value and general applicability. The first idea is based on the Singlet-Triplet energy level splitting caused by the spin exchange interaction. As an external field is applied and increased, the Triplet degeneracy is lifted, $|T_{-}\rangle$ state is lowered energetically and, at some point, crosses with the Singlet state, thus providing a pathway for Singlet to Triplet conversion and, consequently, the local Triplet product maximum. This is the, so-called, *J-resonance* and is a typical level-crossing resonance with a width determined by the hyperfine couplings [HMP89, SU89]. A second explanation and a more prominent one is based on the

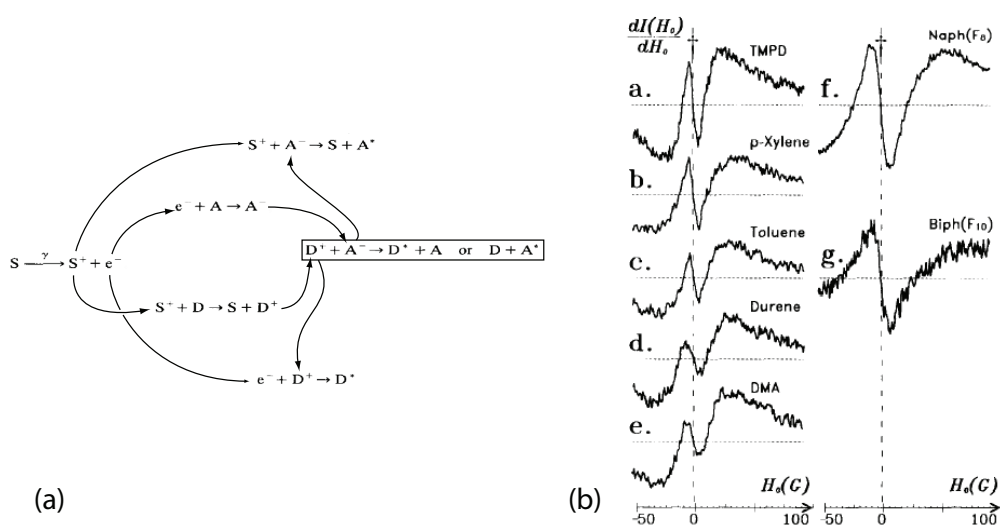
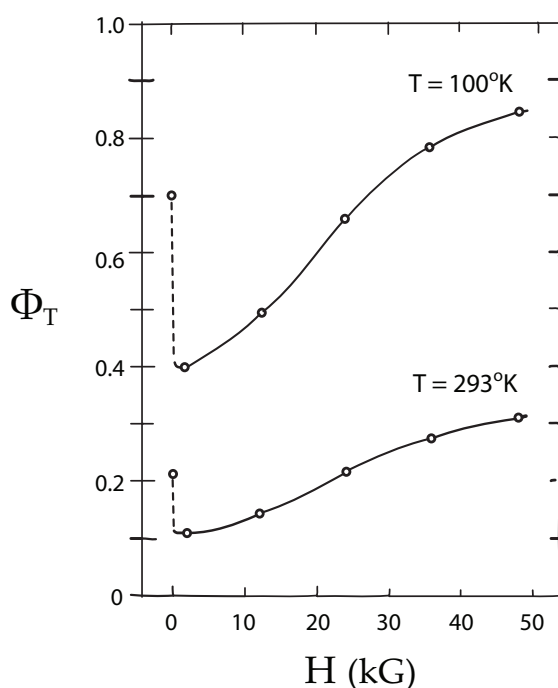


Figure II:1-3

- (a) Reactions in [SLTM95] (S=Squalane, A=Acceptor, D=Donor)
 (b) MARY curves showing the field dependence of the MFE for various donor and acceptor radicals. The curves give the field derivative of the monitored intensity, as in Fig.II:1-2b . LFE here is evident in weak fields and is hyperfine induced.

notion that zero-field degeneracies of coherent nuclear-electron states are lifted by small magnetic fields allowing the state of the electronic pair to span a larger portion of spin space, thus enhancing Singlet-Triplet conversion, provided, of course, that spin relaxation is sufficiently slow. Theoretically the subject is covered in [HHMS88, BKMS93, Bro76, BM96] and more rigorously in [TTB⁺98]. Here it is discussed in more detail in the next chapter and in App.D.

As an example, in [SLTM95] various radicals were used as donors and acceptors in radiolytically created radical pairs in squalane solution. Donors included N,N,N,N-tetramethyl paraphenylenediamine (TMPD)⁺•, paraxylene⁺•, N,N-dimethylaniline (DMA)⁺•, toluene⁺• and tetramethylbenzene (durene)⁺•, while naphthalene was used as both donor and acceptor due to its ability to either donate or accept an electron (naphthalene-h_g⁺ or -•, -d_g⁺ or -•, -F_g⁺ or -•). The reaction scheme and some resulting experimental curves are shown in Fig.II:1-3 where the low field feature is evident. A significant aspect of this experiment is that when radical pairs are formed through radiolysis, the initial pair separation is quite large. As a consequence, spin exchange interaction is suppressed and the lifted degeneracy mechanism for the explanation of the LFE can be verified.

**Figure II:1-4**

Effect of the Δg mechanism on the Triplet yield in bacterial photosynthetic centers (Rhodospseudomonas sphaeroides). The dashed line shows the Triplet yield reduction due to the normal field effect. At high fields, the Δg mechanism, which is of opposite phase, acts to enhance the Triplet yield.

The temperature dependence of spin relaxation is seen as well, which acts to reduce the lifetime of radical pairs, thus inhibiting the Singlet-Triplet conversion and, consequently, the triplet yield.

(Figure from [BCR82])

II.1.3.3 Other effects

A number of other effects are at play within the radical pair mechanism, which have the power to affect the magnetic behavior of the reaction, either directly or indirectly. We hereby mention the most important ones in a rather epigrammatic way, as we revisit them in the next chapter.

▷ a:/ Δg mechanism

The electronic gyromagnetic ratio in the molecular environment can differ from its free electron value. If the two electrons in the radical pair experience different gyromagnetic ratios, then they precess about external fields at different frequencies. As a result, Singlet-Triplet mixing can occur. Obviously, it is a mechanism of opposite phase than the normal field effect, in the sense that it enhances Triplet generation as opposed to the reduction caused by the latter. However, such differences in gyromagnetic ratios are rather small and the effect kicks in at very high fields. Experimentally it has been observed routinely in a variety of contexts, as for example in [CRB80, BCR82] where the Triplet product formation of the $[\text{BChl}_2^+, \text{BPh}^{\bullet-}]$ RIP reaction in photosynthetic bacteria (Rhodospseudomonas sphaeroides) was studied for magnetic fields up to 5T (Fig.II:1-4).

▷ b:/ Spin exchange

Spin exchange interaction in molecules is similar to its atomic physics counterpart (see Part I and, also, the Hamiltonian terms discussion in the next chapter).

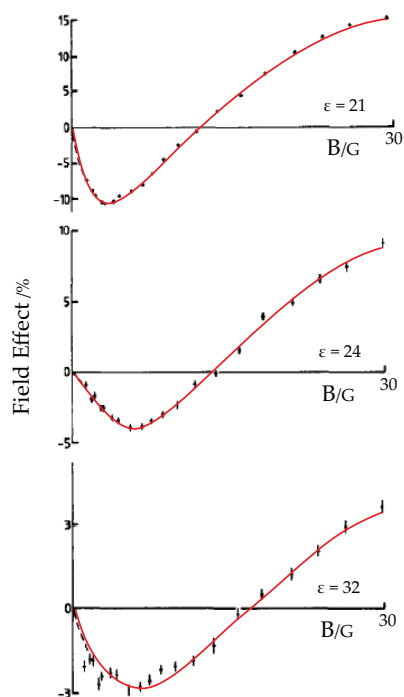


Figure II:1-5

Existence of J-resonances in $\text{Py}^{\bullet+} + {}_{1,3}\text{DCB}^{\bullet-}$ is proved by the low field effect curves in solutions of different relative permittivity, ε . The shift of the LFE peak to higher fields is not compatible with a hyperfine induced explanation. (Figure adapted from [HMP89])

Effectively it introduces a bonding potential for the Singlet state and an antibonding for the Triplet, thus splitting energetically the two manifolds. This results in the suppression of the main mechanism of MFEs, the hyperfine interaction. Still, as mentioned earlier (and later), in conjunction with the Zeeman effect it can give rise to the J-resonance MFE [HMP89, BM96]. Spin exchange decays exponentially with inter-radical separation and is expected to be negligible in pairs more than a few nm apart, as for example in radiolysis RIP experiments [SLTM95].

As an example, in [HMP89] J-resonances are observed in $\text{Py}^{\bullet-} + \text{DMA}^{\bullet+}$ and in $\text{Py}^{\bullet+} + \text{DCB}^{\bullet-}$. The proof that LFE actually originates from spin exchange is given by the curves in Fig.II:1-5, where solutions of $\text{Py}^{\bullet+}$ and the 1,3 isomer of $\text{DCB}^{\bullet-}$ of varying relative permittivities are studied. The shift of the LFE peak to higher fields is consistent with the expected increase in the J parameter of spin exchange, whereas hyperfine couplings are not expected to be altered significantly in this range of permittivities.

▷ c:/ *Dipolar interaction*

The dipolar interaction corresponds to the interaction of the magnetic moments of the electrons. In high magnetic fields where spins are locked in precession about the external field axis, the dipolar interaction is anisotropic, shifting the energy levels of $|T_0\rangle$ and $|T_{\pm}\rangle$ in opposite directions, away from the unaffected $|S\rangle$, at amounts proportional to the angle (to the squared cosine of the angle,

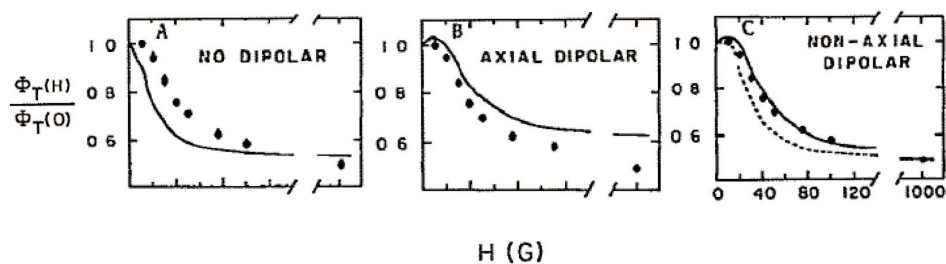


Figure II:1-6

Inclusion of a non-axial dipolar interaction in the calculations in quinone-depleted photosynthetic centers, accounts for the discrepancies between theory and experiment (Figure adapted from [RCB82])

actually) between the inter-radical vector and the magnetic field[‡]. At weak fields the interaction becomes isotropic, but its effect rather less straightforward. In all cases, though, the dipolar interaction is believed to inhibit the hyperfine induced S-T conversion. For weak fields, in particular, the general consensus is that it can completely suppress the LFE [OCG⁺05]. In the next chapters we argue that nature may have provided the radical pairs with more robust defenses against exchange and dipolar interactions than what is currently believed. The magnitude of the dipolar interaction decreases as $1/r^3$, where r the RIP separation, making it a more influential mechanism than spin exchange for distances over $\sim 1\text{nm}$ (note: spin exchange interaction decays exponentially).

In experiments in quinone-depleted, photosynthetic reaction centers it has been argued that the inclusion of a non-axial dipolar interaction term can account for theory-experiment discrepancies (Fig.II:1-6 [RCB82]).

II.1.4 *Magnetoreception: the avian compass*

Magnetoreception is the ability to sense a magnetic field and perceive magnitude, direction, altitude or location. Since this has been the incentive for our group to become involved in the field of quantum biology, we hereby give an account of the concept.

II.1.4.1 **Earth's magnetic field and compass types**

Earth is a huge magnet. Magnetic field lines emerge from its crust at the North magnetic pole (near the South geographic pole) and reenter at the South magnetic

[‡]However, averaging to - effectively - zero occurs at strong fields in solution, due to the diffusive thermal motion of molecules around each other. This, of course, ceases to be true for molecules in rigid formations.

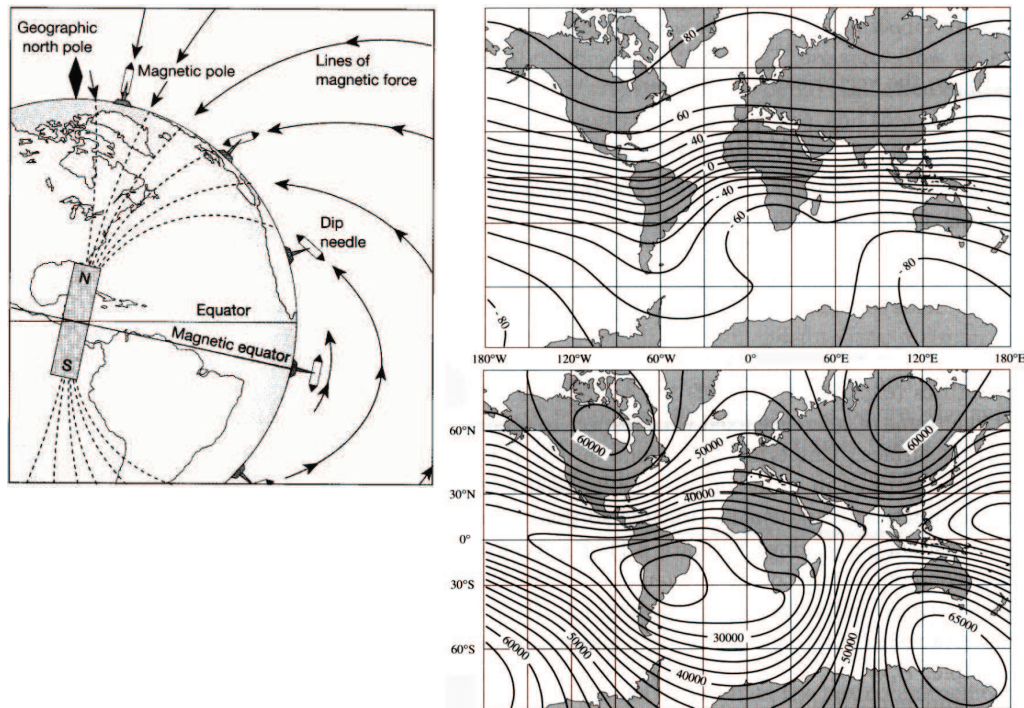


Figure II:1-7

Left: Dip needles (vertically rotating compasses) show the inclination of Earth's magnetic field (http://gravmag.ou.edu/mag_earth/mag_earth.html)

Right: Isoclinic (constant inclination contours / top) and isodynamic (constant intensity contours in nT / bottom) maps of the magnetic field of the Earth (R.J. Blakely, IGRF 1990)

pole (near the North geographic pole)[§], always pointing North, much like they would do in a bar magnet. Near the poles the field is strong and the magnetic lines almost vertical while at the equator the field is horizontal and at its weakest. In between the intensity of the field forms a gradient and its vector is inclined, pointing upward over the southern hemisphere and downward over the northern. The situation is summarized in Fig.II:1-7.

Although magnetic anomalies and modulations occur at various - spatial and temporal - instances, mainly due to ferromagnetic material concentrations under the Earth's crust or due to solar magnetic activity, the magnetic field of the Earth is a quite reliable, omnipresent feature of the environment, able to provide navigational information. This information may be of two different kinds: *directional* information, provided directly by the polarity of the field vector[¶] and *positional*

[§]Unfortunately, as is common in science, two - out of two possible! - nomenclatures are used for the magnetic poles. The northern magnetic pole is often referred to as southern magnetic pole, as a reference to its geographical position. Polarity wise, however, the northern magnetic pole is the one under the southern rotation pole.

[¶]and perhaps indirectly by comparing intensities and/or inclinations among different regions

information via the construction of a navigational “map” of total intensity and/or inclination.

II.1.4.2 **Experimental observations**

There are at least 50 species of animals, including birds (even long time domesticated chicken), mammals, insects, amphibians, reptiles, fish etc. which are known to be using Earth’s magnetic field for navigational purposes. Even photosynthetic and other reactions in plants are affected by it. Before proceeding to describe the two main mechanisms proposed for the explanation of animal magnetoreception, we present an assortment of experimental observations related to the phenomenon. We focus mainly on studies conducted on birds since birds are by far the most studied species, but also because of our particular interest in the radical pair mechanism of magnetoreception described in the next subsection. This presentation is largely based on the excellent review by W. and R. Wiltschko ([WW07] and references therein).

▷ *a:/ Magnetic field for orientation: the avian compass*

In orientation experiments, a change of the bird’s preferred heading is anticipated as a response to an induced change in the direction of the magnetic field vector. The first demonstration of such behavior was given in a study of European Robins, a member of the passerine migrants family. Helmholtz coils were used to rotate the magnetic field experienced by the Robins, through a specific angle on the horizontal plane. It was observed (see Fig. II:1-8) that the Robins are able to adjust completely to a change in the direction of the magnetic field vector. Since then the possession of that same ability was confirmed for over 20 other avian species originating from all over the world and travelling different distances at different times of the day, even including non-migratory birds such as the carrier pigeons and domestic chickens.

The study of the working principles of the avian compass proved to be very interesting. First of all, tests in European Robins revealed that the avian compass is actually an inclination compass; a compass sensitive to the inclination of the magnetic field vector, rather than to its polarity. As such it is able to detect the alignment of the magnetic field, but not its orientation. The experiment consisted of a reversal of the perpendicular component of the magnetic field, which caused the Robins to reverse their heading. Simultaneous reversal of both the horizontal and vertical components (that is a total reversal of the field) had no effect on the heading of the birds, as the inclination remained unchanged (see Fig. II:1-9). So, instead of being sensitive to north and south, the birds head “poleward” (magnetic field points downward) or “equatorward” (magnetic field points upward). This type of compass has obvious merits. For example, it is one,

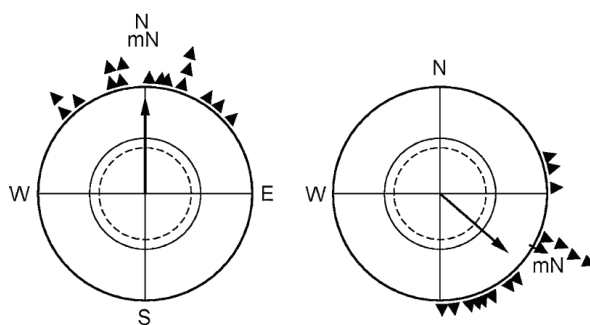


Figure II:1-8

A change in the direction of the magnetic field vector redefines the preferred heading of European Robins (Figure taken from [WW07])

unique mechanism for birds in both the south and the north hemisphere; a bird of the northern hemisphere accustomed to migrate to the south, if transferred to the southern hemisphere, it would still fly equatorward in the autumn, rather than go south and, well, die. Another advantage of the inclination compass is that it is insensitive to the interchange of the north and south magnetic poles, a scenario which has played out numerous times in Earth's history.

The second important characteristic of the avian compass is that it is functional only within a rather small window of magnetic field strengths. A $\pm 30\%$ change in the field intensity causes birds to become completely disoriented. However, birds "learn" new fields: if subjected to a new field for a prolonged period of time, they eventually reorient within it, while maintaining their sense of orientation in the old one. This, though, is not an extension or shift of the functional window of the compass, as birds remain insensitive to intermediate fields in between the old one and the new.

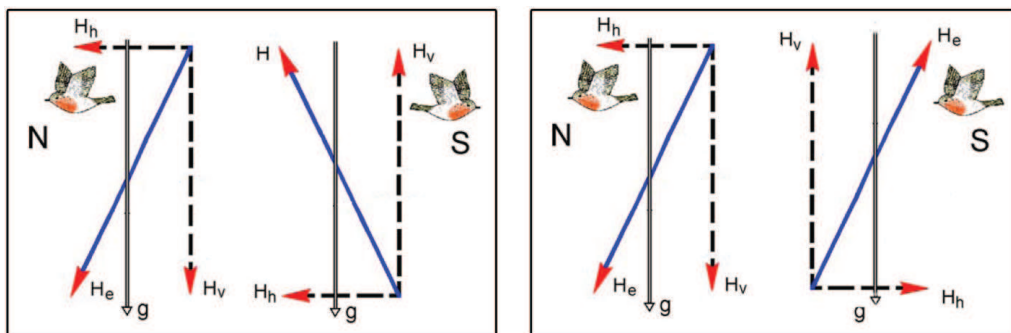


Figure II:1-9

The avian compass is an inclination compass, sensitive to the alignment of the magnetic field, but not to its orientation (Figure adapted from [WW07])



Figure II:1-10

The avian compass is activated by light and is wavelength dependent. Short wavelengths (UV to green) are needed to trigger it, while the birds become disoriented for large wavelengths (yellow, red) (Figure adapted from [WW07])

▷ *b:/ Non-compass uses of the magnetic field*

Orientation is not the only bit of information given away by the magnetic field of the Earth. Magnetic intensity and/or inclination have been shown to provide information on position and birds are known to create a sort of mental navigational “map” during their lifetime. On this map, certain waypoints can trigger specific behaviors. For example, the central European Pied Flycatchers begin their migration flying southwest, toward the Iberian peninsula. They do so to avoid having to fly over the Alps, the Mediterranean and central Sahara; all three forming a formidable ecological barrier. Sensing the magnetic field of northern Africa, triggers their turning southward. More impressively, simulating the magnetic field of northern Egypt on caged Thrush nightingales, triggers their... appetite; they gain weight faster as they are preparing to cross the Saharan desert. Transequatorial migrants, like the Garden Warblers, have to reverse their desired heading once they cross the equator, if they are to fly deep into the southern hemisphere; the event here is indeed triggered by the horizontal equatorial field.

More than triggering events though, the total intensity of the field can provide equatorward and poleward orientation, since intensity is higher near the poles and lower near the equator. Conditioned experiments have provided proof of the ability of - at least - homing pigeons to sense the total field strength. This is also verified by their disorientation in magnetic anomalies, in direct correlation to the local gradient.

▷ *c:/ Electromagnetic characteristics of the avian compass*

It is commonly accepted that whatever the mechanism of the avian compass, it is triggered by light. Experiments on European Robins, Australian Silvereyes, European Garden Warblers and homing pigeons have revealed that birds become disoriented when irradiated with light of long wavelengths (yellow, red), while reorientation occurs for the entire spectrum of short wavelengths (from green to UV), as is schematically depicted in Fig.II:1-10. The transition from orientation

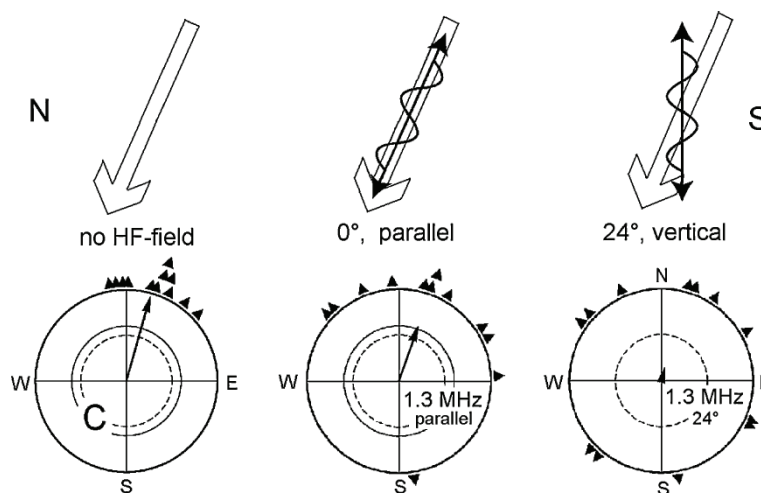


Figure II:1-11

Disruption of the avian compass by a weak RF field (Figure from [RTP⁺04, WW07])

to disorientation is rather abrupt. Also, the change to a fixed (NW) or axial (E-W) response at high intensities for certain short wavelengths [WW01] and the ability of birds to reorient at long wavelengths if irradiated for extended periods of time [WMG⁺04], indicates that a complex photoreceptor scheme must be at play, independent of that of normal vision and probably comprising antagonistic contributions from different photoreceptors. In fact, the fixed response at high intensities may even be related to the unanticipated interplay between the two magnetoreception mechanisms described below, brought about by pushing these sensory organs out of normal operating conditions.

Another observation made regarding the avian compass is the disruption of its operation by application of weak electromagnetic radiation in the MHz regime [RTP⁺04]. As is seen in Fig.II:1-11, application of a vertical RF field at a frequency of 1.315MHz, leads to complete disorientation. The same was verified for a 7MHz field and for RF noise in the 0.1-10MHz range. Application of a single frequency parallel to the field vector is, on the other hand, tolerated.

II:1.4.3 Proposed mechanisms for magnetoreception

▷ a:/ *The magnetite hypothesis*

Magnetite is a ferrimagnetic mineral, one of many forms of iron oxide Fe_3O_4 , and is considered to be the most magnetic of all the naturally occurring minerals on Earth. Its magnetic properties depend on its shape and size. Spin interactions between adjacent atoms can lead to the creation of domains of aligned magnetic moments. In large particles the multitude of domains, arbitrarily magnetized

relative to each other, diminishes the net magnetization of the material, but particles on the order to 0.01 to 1 μm usually comprise a single domain and behave as tiny permanent magnets. Smaller nano-particles are superparamagnetic: in the absence of an external magnetic field, their magnetic moments randomly flip due to thermal fluctuations, but application of the field can easily orient them; much like a paramagnetic material, but with a very high magnetic susceptibility value.

Magnetite has been found in bacteria, insects, fish, birds and humans. In particular, findings in the 1970s that certain bacteria oriented in external magnetic fields through a single-domain, magnetite-based mechanism, inspired the idea that the same could hold true for higher animals. The notion was further provoked by the finding in birds of single-domain magnetite particles in the orbital and nasal cavities and, more importantly, superparamagnetic particles under the skin in the upper beak. A variety of magnetoreception models has been put forward ever since, involving single-domain or superparamagnetic particles and predicting polar or axial sensitivity; no commonly accepted model exists yet.

Today magnetite based magnetoreception is not considered to play any essential role in the orientation procedure; besides, experiments performed after anesthetizing the upper beak of birds showed no disorientation of the birds. It is, however, essentially a magnetometer, recording differences in the field intensity, and helps in the creation of the bird's navigational map.

▷ *b:/ The radical pair hypothesis*

The notion that the avian compass may be mediated by chemical - and specifically, radical pair - reactions was originally proposed by Schulten [Sch82, SW86] in the early 1980s, but a possible scheme was published and analyzed only in 2000, by Ritz, Adem and Schulten [RAS00]. The model is based on the LFE exhibited in radical pairs formed in photoreceptors - presumably - located on the retina of the bird. Initially, light is absorbed by the photoreceptor and a radical pair is formed through a charge transfer process. The reaction of the pair is modified by the weak geomagnetic field, courtesy of the LFE, and the end products - somehow - trigger a sensory stimulus which can be perceived by the bird's brain and translated in field orientation information. The proposed scheme is outlined in the rather extravagant Fig.11-12.

There are certain requirements on the supposed radical pair involved in the magnetoreception process. The most important one is that it must couple anisotropically to the external magnetic field. By this we mean that the products of the reaction, and thus the perceived orientation information, has to be dependent on the relative direction of the vector of the magnetic field and some particular axis rigorously definable within the RIP. Indeed, through an isotropic coupling, the RP reaction, rather than being sensitive to the orientation of the field, it

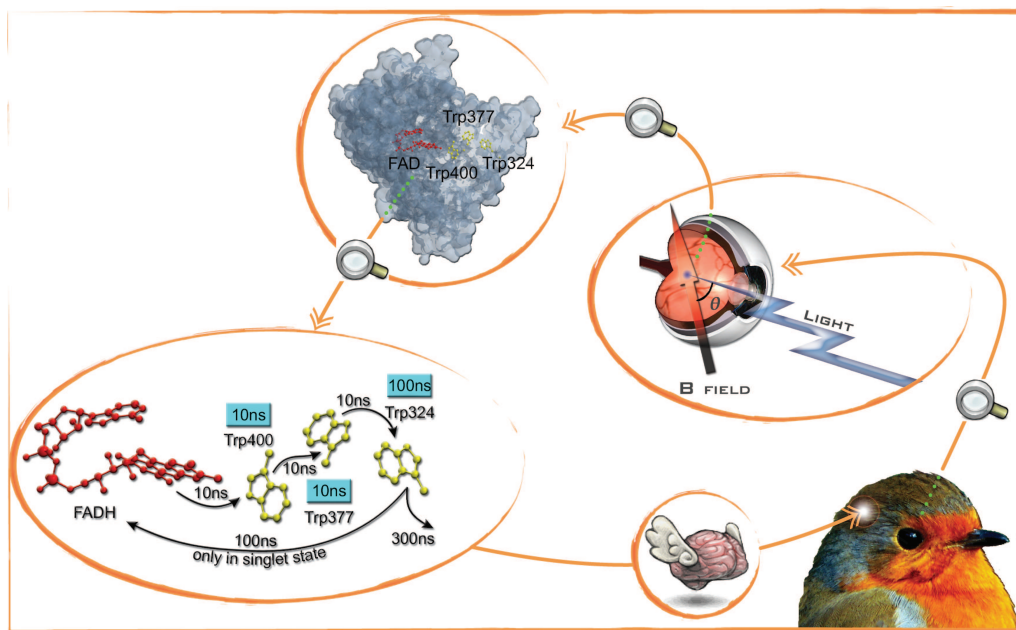


Figure II:1-12

Radical pair mechanism for magnetoreception. Cryptochrome photopigments in the -right - eye of the bird absorb short wavelength radiation. An electron transfer process commences, which results in the formation of an $[A^{\bullet-}D^{\bullet+}]$ radical pair in the Singlet state. Singlet-Triplet balance is affected by the orientation of the magnetic field. Recombination toward neutral ground state molecules occurs from the Singlet state or the reaction may continue from the Triplet to yield a signaling product, which - somehow - creates a stimulus detectable from the bird's brain. Above the flavin-tryptophan scheme is depicted (see below). The cryptochrome, flavin and tryptophan drawings are from [Rod09]. The bird is actually a European Robin (*Erithacus rubecula*).

would merely be sensitive to its intensity, at best, which is not a particularly useful quality in a magnetic compass. This anisotropy has to originate in the hyperfine interaction. In solution, the hyperfine interaction is isotropic, as any possible anisotropies are averaged out by the thermal motion of the molecules. However, if the constituents of the pair are embedded in a rigid structure, as it is, presumably, in the protein matrix of large photoreceptors in the retinas of birds, then the hyperfine coupling tensor can, and usually is, anisotropic.

Another important issue is the lifetime of the pairs. If the reaction is to be influenced by the weak geomagnetic field ($\sim 0.5G$), it has to survive for times at least comparable to the inverse of the Larmor frequency; typically on the order of $\sim 0.1-1\mu s$. This would seem to imply that the recombination rates (the rates at which the total RIP population is depleted) have to be comparable to or smaller than the Larmor frequency. In Chapter II:3 we argue that this may not necessarily be true.

Finally, radical pairs have to not only survive long enough for the magnetic

field to leave an impression, but their quantum state must also maintain coherence during their lifetime, at least to some degree. This means that the separation between the Donor and Acceptor molecules has to be short enough for recombination to be efficiently spin-selective without suffering substantial spin relaxation, but also long enough for spin exchange and dipolar interactions to become, somehow, weaker than the Larmor frequency. That's a tough one, since the two requirements are contradicted: the former results in the requirement $r \lesssim 2.5\text{nm}$ and the latter to $r \gtrsim 3.5\text{nm}$. This obstacle has led theorists in the field to propose a rather elaborate mechanism of mutual cancellation of the spin exchange and the dipolar interaction for certain regions of parameters and distances, thus allowing low field effects to resurface at inter-radical separations compatible with spin selective recombination [EH08, RH09]. Although "elaborate" does not necessarily mean "false" (natural selection and evolutionary patterns have many a time redefined the word "elaborate"), we believe that the mechanism which enables radical pair reactions to sense magnetic fields is more robust to the destructive effects of spin-spin interactions than what is believed (nature has many a time redefined "elegance" and "simplicity", as well). We will pursue this subject in Chapter II:3.

The dominant candidate for the photopigment position in the RIP magnetoreception scheme is *cryptochrome*, a blue light photoreceptor protein found in plants and animals. Among other things, the family of cryptochromes is involved in the germination, elongation and other processes in higher plants and in the regulation of the circadian rhythm of both plants and animals. Cryptochromes are closely related to *photolyase*, a bacterial enzyme that is activated by light and participates in DNA damage repair. Conclusive evidence that the cryptochromes are actively involved in magnetic field sensing has been provided for the plant *Arabidopsis thaliana*, where the growth behavior was found to be influenced by magnetic fields when the plant was irradiated by blue light, but not so when the wavelength shifted to red ([SCS07] and references therein), and for the fruit fly *Drosophila melanogaster*, which owes its magnetic sensing abilities to cryptochromes [GCWR08]. In birds, it has been observed that two types of cryptochromes (CRY1 and CRY2) exist in the retinas of European Robins [MSWS04] and Garden Warblers [MJBL⁺04], both nocturnal migrants. More importantly, in the latter case CRY1 was concentrated in ganglion cells and in large displaced ganglion cells, in which they co-localized with neuronal activity markers activated during the night; the natural migration time of day for the Warblers. Also, in the same work it was realized that the CRY1 is expressed in a significantly different way than in non-migratory birds, especially in the large displaced ganglion cells, which are exclusively connected to a brain area where neuronal activity has been reported during the processing of magnetic information [MJBL⁺04]. Nevertheless, the role of cryptochrome as the mediator of magnetoreception has not been

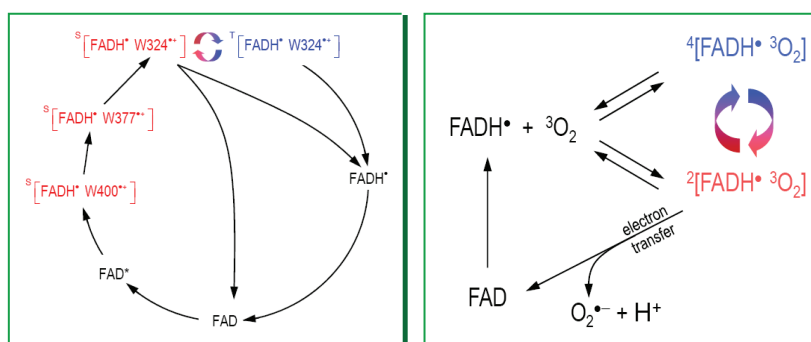


Figure II:1-13

Two radical pairs proposed for the cryptochrome-base explanation of magnetoreception. The $[\text{FADH}^\bullet \text{ W324}^{\bullet+}]$ pair formed during the reduction of FAD to FADH^- and the $[\text{FADH}^\bullet \text{ O}_2]$ pair formed during its re-oxidation (See text for details / Figure adapted from [RH09])

proved yet, despite the - growing - body of supporting evidence described above.

Assuming cryptochrome is the mediator of magnetoreception in birds, then by far the most commonly cited radical pair scheme for actually detecting the field is the FAD - tryptophan cycle, hinted in Fig.II:1-12 and shown in more detail in Fig.II:1-14. *Flavin adenine dinucleotide* (FAD) is the fully oxidized form of a cofactor involved in a number of important reaction, mainly in metabolism. Its full reduction to FADH^- by electron transfer through a chain of tryptophans (Trp or W / one of the 20 standard amino acids used in protein biosynthesis) creates two short lived and one long lived radical pair, apparently suitable for magnetoreception. Recently, another radical pair candidate was proposed, formed in the re-oxidization of FAD, rather than in its reduction, and involves an O_2 molecule mediating in the oxidization reaction (Fig.II:1-13). The former pair has been analyzed theoretically to great extents and is known to be responsible for the magnetic effects in - at least - *Arabidopsis thaliana*. The latter is promising in that the devoid of hyperfine couplings O_2 would enhance magnetic effects^{||}, but, more importantly, it would explain the insensitivity of the mechanism to the application of an RF field parallel to the magnetic field vector [RTP⁺04, WW07, RH09]. However, the existence of such a pair has not been confirmed in cryptochromes.

To get a feeling of the procedures and the timescales involved, we give a brief description of the flavin-tryptophan cycle shown in Fig.II:1-14. The tryptophan chain involved in the reduction of FAD comprises the Trp-324, Trp-377, and Trp-400; Trp-324 is further away from FAD, some $\sim 2\text{nm}$, and Trp-377 and Trp-400 are nearer to the flavin cofactor. The fully oxidized FAD cofactor absorbs blue photons and is excited (FAD^*). The excited state is then protonated (FADH^+)

^{||}Here it is argued, on physical intuition grounds, that the greater the imbalance in hyperfine couplings between donor and acceptor, the more pronounced the magnetic effect. The absence of magnetic nuclei in O_2 would thus enhance any such effect.

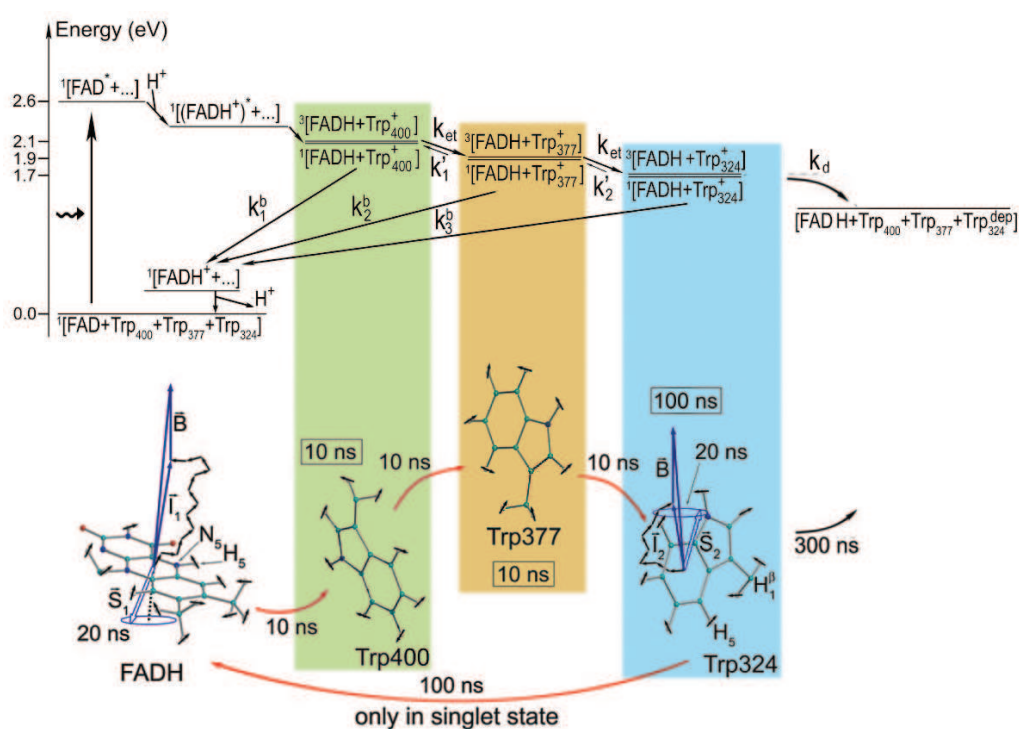


Figure II:1-14

The commonly proposed radical pair chain in cryptochrome (See text for details / Figure adapted from [SCS07])

and the electron transfer process commences. The electron hole left behind by the excited electron of the FAD^* is pushed outward forming in sequence the $[\text{FADH}^\bullet \text{Trp}400^{\bullet+}]$ (lifetime $\sim 10\text{ns}$), $[\text{FADH}^\bullet \text{Trp}377^{\bullet+}]$ (lifetime $\sim 10\text{ns}$) and $[\text{FADH}^\bullet \text{Trp}324^{\bullet+}]$ (lifetime $\sim 100\text{-}300\text{ns}$) pairs. The long lived, final pair largely determines the magnitude of the magnetic effect. Back transferring of the electron to any of the tryptophans can occur at any time, giving FADH^+ and suppressing the reaction, but only if the electronic state of the existent pair at that moment is Singlet. Finally, with the $[\text{FADH}^\bullet \text{Trp}324^{\bullet+}]$ in the Triplet state, deprotonation of $\text{Trp}324^{\bullet+}$ can occur, thus fixing the electron in FADH and forming the signaling state.

In the figure, the semi-classical vector model described in App.D is also employed: the electronic spins (outlined vectors) are shown to precess about a local magnetic field produced by the addition of the external magnetic field and the hyperfine “field” from the - randomly oriented - nuclear spins of the two radicals. For a large number of nuclear spins, this total field can be considered a classical vector, to a good approximation. The electronic spins are initially drawn in a Singlet (antiparallel) state, but the different local fields induce precession at different frequencies and eventually Singlet and Triplet states mix.

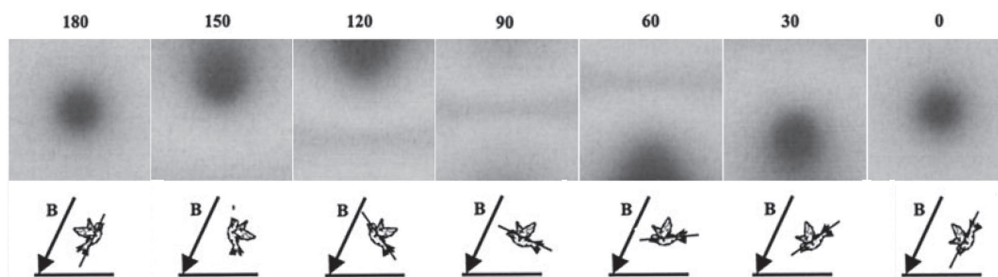
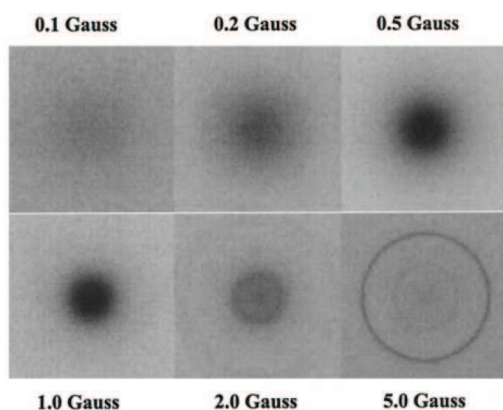


Figure II:1-15

Possible magnetic field induced, visual patterns perceived by birds (See text for details / Figure adapted from [RAS00])

The first analytical proposal of the flavin-tryptophan mechanism for magnetic sensing, as well as a description of the possible workings for the complete sensory procedure was given in [RAS00]. In this work the authors adopt a generic radical pair model with only two nuclei, one at the donor and one at the acceptor site. One of the two electrons is experiencing an isotropic and the other an anisotropic hyperfine interaction; as a whole the recombination of the pair will depend on the angle between the magnetic field vector and the anisotropy axis defined by the hyperfine coupling tensor of the latter electron, thus providing information on the orientation of the field. In order for this information to be blended with a sensory transduction pathway of the animal in a meaningful way, the molecular structure containing the reacting pairs must be fixed. This is a usual case for cellular membranes involved in sensory transduction; for example, in vision the photoreceptors of the rod and cone cells are oriented tangentially to the retina of the eye. The authors assume here that the photoreceptors involved in magnetoreception are fixed at the back of the - perfectly spherical - retina of the eye, normal to its surface, thus making different angles to the magnetic field vector due to the curvature. Further assuming that the reaction products are blended with the visual signals acquired by the bird's eye (equally well another sense could be involved), different - angle dependent - products are perceived differently, leading to the formation of visual patterns which enable the bird to actually *see* the magnetic field. Calculations based on a phenomenological set of equations (more on that in the next chapters) yield patterns of the form shown in Fig.II:1-15. These patterns, are of course, exaggerated for clarity and somehow simplistic due to the assumptions for a perfectly spherical retina located at the center of the head, a two-nuclei model etc. Nevertheless, these patterns immediately reveal that the radical pair mechanism satisfies one of the basic criteria for an avian compass, namely to be an inclination compass. This is evident from the fact that the patterns are identical when the bird flies parallel or anti-parallel to the magnetic field.

Another feature of the avian compass with a plausible explanation in the

**Figure II:1-16**

Different patterns may be blended with visual signals for different field intensities, thus disorienting the bird. Acclimatization with the new patterns may enable reorientation to the new field, as well as maintaining its ability at the old field. This does not imply, however, that the bird can orient at intermediate fields, since the corresponding patterns may be substantially different (Figure from [RAS00])

context of the radical pair mechanism, is that of the functional window. As described earlier, birds become disoriented when a significant change occurs in the intensity of the field, but reorient in the new field when subject to it for a substantial time period. They do so without losing their ability to orient inside the original field and without being able to do so in intermediate fields. As seen in Fig. II:1-16, a change in the intensity of the field significantly alters the perceived visual patterns, both qualitatively and quantitatively. This may cause the bird to fail to realize the meaning of the new pattern, but, given time, it is conceivable that it will come to understand its significance and identify it. It doesn't follow, though, that the bird will orient in intermediate fields, since the correspondent patterns may differ from both the original and the new one.

Experiments involving the exposure of birds to radio-frequency (RF) fields were first proposed in [RAS00], as well, and the RF-induced disorientation reported in [RTP⁺04] also supports the radical pair magnetoreception scheme. Indeed, in the radical pair system, weak radio-frequency radiation resonant to the external field induced Zeeman splittings, would destroy coherences by leveling out the populations in the $\pm\frac{1}{2}$ electron spin states, thus inhibiting magnetic effects. This is exactly what has been observed. On the other hand, the relatively heavy magnetite particles are not expected to be able to follow the fast oscillations of the RF field.

Further evidence supporting the radical pair hypothesis are the findings in [MJBL⁺04, MSWS04] of the existence of cryptochromes in the retinas of birds and their spatial coincidence with neuronal markers and connection with areas of the brain known to exhibit activity during magnetic navigation. The cryptochrome is considered a significant find, since it has already been connected to magnetic field related phenomena in plants and animals. It is also compatible with the light induced initiation of the magnetoreception process and its wavelength dependence. Indeed, in cryptochrome, electron transfers leading to the reduction of FAD are initiated by blue light, while the abrupt disorientation occurring at the green-yellow interface may easily be attributed to the favoring of

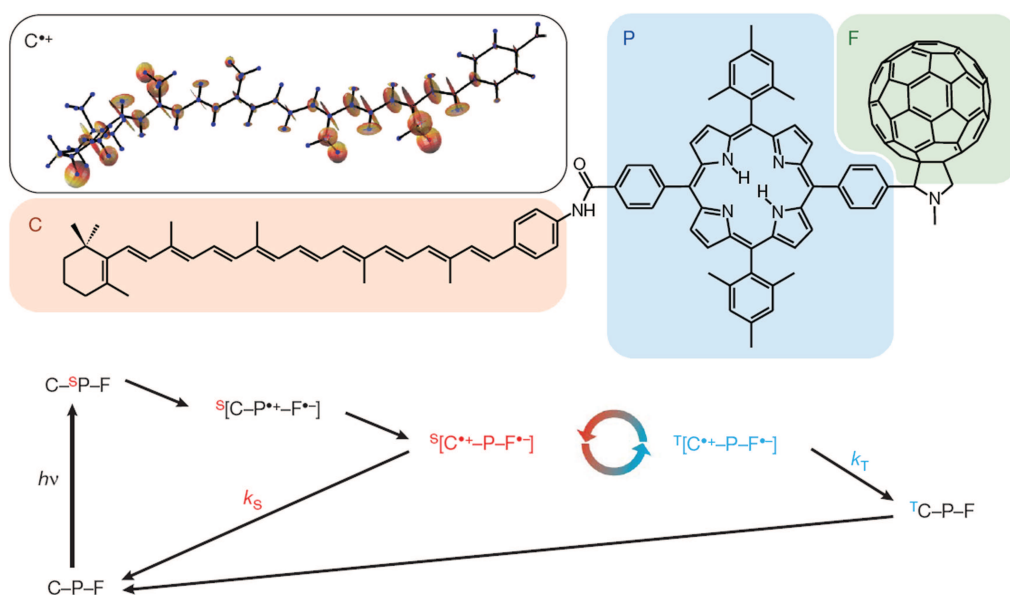


Figure II:1-17

Carotenoid-porphyrin-fullerene model used in [MHC⁺08] for the demonstration of radical pair based magnetoreception. Electron transfer is initiated by green light 532nm and the [C^{•+}-P-F^{•-}] radical pair is formed. Recombination is spin selective, either to the ground C-P-T state (from the Singlet) or to the excited triplet ^TC-P-T (from the Triplet), at different rates.

absorption by a different cofactor around these wavelengths.

Finally, a recent experiment performed by Maeda *et al* [MHC⁺08] has provided much sought-for proof-of-principle that a radical pair reaction can be sensitive to the orientation of a field comparable in strength to the geomagnetic field. The model used was a carotenoid-porphyrin-fullerene triad, as seen in Fig.II:1-17. Both isotropic and anisotropic effects were observed, for fields as low as 39μT for the former and ~3mT for the latter case and at temperatures below 200°K. This is a very important step forward in bringing such behaviors to the laboratory, both for the sake of animal magnetoreception explanation, but also for the possibility of fabrication of sensitive magnetic bio-sensors with desirable characteristics.

Chapter II:2

Quantum Mechanical Description of Radical Ion Pair Dynamics

II.2.1 *Definition of states*

In the following we present the mathematics pertaining to the description of RIPs. Since magnetic fields couple to the electronic spins of RIPs and the latter are coupled to the nuclear spins of the constituent molecules through the hyperfine interaction, the relevant quantum quantities in the desired description are the two electron spins and the spins of the nuclei at the donor and acceptor molecules. In the case of uncorrelated spins we describe the state of a RIP by a density matrix of the form:

$$\rho = \rho_{n_D} \otimes \rho_{n_A} \otimes \rho_{e_D} \otimes \rho_{e_A}, \quad (\text{II.2.1})$$

where the D and A indices stand for *Donor* and *Acceptor*, respectively, and *n* and *e* for *nuclear* and *electronic*. The circled cross symbol, “ \otimes ”, denotes the Kronecker matrix product.

The spin space of the electronic pair is spanned by the singlet and the three triplet basis states, given by:

$$|S\rangle = \frac{1}{\sqrt{2}}(|\uparrow, \downarrow\rangle - |\downarrow, \uparrow\rangle) \quad (\text{II.2.2})$$

$$|T_+\rangle = |\uparrow, \uparrow\rangle$$

$$|T_0\rangle = \frac{1}{\sqrt{2}}(|\uparrow, \downarrow\rangle + |\downarrow, \uparrow\rangle) \quad (\text{II.2.3})$$

$$|T_-\rangle = |\downarrow, \downarrow\rangle$$

If the electronic spins are in a quantum correlated state of the form:

$$|\psi\rangle = \alpha |T_+\rangle + \beta_T |T_0\rangle + \beta_S |S\rangle + \gamma |T_-\rangle \quad (\text{II.2.4})$$

where a quite obvious symbolization has been used, the density matrix of the RIP is given by:

$$\rho = \rho_{n_D} \otimes \rho_{n_A} \otimes |\psi\rangle\langle\psi|. \quad (\text{II.2.5})$$

The singlet state is invariant under rotations, but the triplet states are not. The above set of triplet basis vectors is defined with \hat{z} as the quantization axis. In the following sections, triplet states along different quantization axes are also used and we, thus, need to define the basis vectors for these axes*. These are obtained through rotations of the \hat{z} -vectors by $\pi/2$ about \hat{y} -axis and then by $\pi/2$ about \hat{z} -axis.

$$|T_0\rangle_x = \frac{1}{\sqrt{2}}(-|T_+\rangle_z + |T_-\rangle_z) \quad (\text{II.2.6})$$

$$|T_{\pm}\rangle_x = \frac{1}{2}(|T_+\rangle_z \pm \sqrt{2}|T_0\rangle_z + |T_-\rangle_z)$$

$$|T_0\rangle_y = -\frac{1}{\sqrt{2}}(|T_+\rangle_z + |T_-\rangle_z) \quad (\text{II.2.7})$$

$$|T_{\pm}\rangle_y = \frac{1}{2}(|T_+\rangle_z \pm i\sqrt{2}|T_0\rangle_z - |T_-\rangle_z)$$

The projection operators to the singlet and triplet subspaces are defined as:

$$Q_S = \frac{1}{4}\mathbb{I} - \mathbf{S}_D\mathbf{S}_A \quad (\text{II.2.8})$$

and

$$Q_T = \frac{3}{4}\mathbb{I} + \mathbf{S}_D\mathbf{S}_A \quad (\text{II.2.9})$$

where \mathbb{I} is the $2n_D \times 2n_A \times (2\frac{1}{2} + 1) \times (2\frac{1}{2} + 1)$ identity matrix, with n_D (n_A) being the number of nuclear spins (all assumed equal to $\frac{1}{2}$) at the donor (acceptor) site and the components of \mathbf{S}_D and \mathbf{S}_A are given by $\mathbb{I}_{2n_D} \otimes \mathbb{I}_{2n_A} \otimes s_i \otimes \mathbb{I}_2$ and $\mathbb{I}_{2n_D} \otimes \mathbb{I}_{2n_A} \otimes \mathbb{I}_2 \otimes s_i$, respectively, with $s_i = \frac{1}{2}\sigma_i$, $i = x, y, z$ and σ the Pauli matrices.

II.2.2 Master equation

The observation that spin dynamics are affected if the singlet and triplet levels of the radical pair decay at different rates [SSW⁺76, HMB79], brought by the necessity for a combined treatment of the coherent spin motion and the incoherent

*Note that \uparrow) and \downarrow) are always the single electron spin eigenstates with respect to \hat{z}

spin selective charge recombination. Stochastic Liouville Equations (SLE) had been employed to carry out such tasks in magnetic resonance for many years and were quickly adopted for the description of radical pair dynamics. The simplest way to introduce a SLE description to the radical pair mechanism, and particularly relevant to the study of its magnetoreception properties, is to assume that the pair constituents reside at distinct sites fixed at a certain distance. Such a model is realistic for more or less solid-state-like systems, such as the RIPS produced at photosynthetic reaction centers or at cryptochromes at the retinas of migratory birds; a receptor protein deemed the most likely candidate for the explanation of RIP-based avian magnetoreception. However, the same approach with some modifications has become increasingly popular for the description of radical pairs in liquid solutions. The general form of the equation of motion in this case would be:

$$\frac{d\rho}{dt} = -\frac{i}{\hbar}[H, \rho] + \mathcal{L}[\rho] \quad (\text{II:2.10})$$

where $[A, B]$ denotes a commutator, H is the unitary Hamiltonian of the system and \mathcal{L} is a decoherence/recombination super-operator acting on the density matrix.

II:2.2.1 The Phenomenological Master Equation (PME)

Two forms of \mathcal{L} have been debated in the community, namely:

$$\mathcal{L}[\rho] = -k_{S(T)}\{Q_{S(T)}, \rho\} \quad \text{and} \quad (\text{II:2.11})$$

$$\mathcal{L}[\rho] = -k_{S(T)}Q_{S(T)} \cdot \rho \cdot Q_{S(T)} \quad (\text{II:2.12})$$

where $\{A, B\}$ denotes an anti-commutator and $k_{S(T)}$ are first order decay rates referring to recombination from the Singlet (Triplet) state to the corresponding neutral products. Both of the above preserve the Hermiticity of the density matrix, however in 1976, R. Haberkorn proved that the latter, if used alone, can lead to non-physical situations [Hab76] (negative density matrix diagonal elements). Although he pointed out that linear combinations of the form:

$$\mathcal{L}[\rho] = -k_{S(T)}^{(a)}\{Q_{S(T)}, \rho\} + k_{S(T)}^{(b)}Q_{S(T)} \cdot \rho \cdot Q_{S(T)} \quad (\text{II:2.13})$$

are still plausible, provided that $k_{S(T)}^{(a)} \geq 2k_{S(T)}^{(b)} \geq 0$, the forms in Eq.(II:2.12) and, consequently, in Eq.(II:2.13) were largely abandoned; a rather hasty and ill justified omission as we will see later on.

In the years that followed and until recently, the adopted form (II:2.11) for the \mathcal{L} operator has given the master equation which became the norm in describing RIP dynamics [SSW⁺76, TN82, SU89, CBDS95, RAS00, TCBH01, SCS07]:

$$\frac{d\rho}{dt} = -\frac{i}{\hbar}[H, \rho] - k_S\{\rho, Q_S\} - k_T\{\rho, Q_T\} \quad (\text{II.2.14})$$

We will refer to this equation as the *Phenomenological Master Equation* (PME); and phenomenological it is in the sense that the recombination terms are an educated mathematical guess based on experimental observations rather than a product of concise derivation from some set of basic physical assumptions. The non-preservation of the trace of the density matrix in Eq.(II.2.14) is due to the fact that the RIP population is depleted through the Singlet and Triplet recombination channels at rates k_S and k_T , respectively. On top of that, the anti-commutator terms dampen coherences of the density matrix. This last fact will be crucial should the relaxation structure of the PME is proved to be erroneous. In such a case the supposed suppression of density matrix coherences would be, more likely than not, masking essential coherent quantum phenomena taking place during the geminate phase of the radical pair. In the following we claim that this is indeed the case.

II.2.2.2 The Jones-Hore Master Equation (JHME)

Recently a new theory has been proposed by J.A. Jones and P.J. Hore attempting to bridge the gap between the traditional PME and the Quantum Measurement ME (QMME) obtained by our group in the past year [Kom09b] and described in the next section. This new theory uses elements from quantum measurement theory and a level scheme of radical pair recombination (Fig.II:2-1) wherein the products are described as *shelving states* integral to the density matrix. The master equation arrived at is given by:

$$\frac{d\rho}{dt} = -\frac{i}{\hbar}[H, \rho] - (k_S + k_T)\rho + k_T Q_S \cdot \rho \cdot Q_S + k_S Q_T \cdot \rho \cdot Q_T \quad (\text{II.2.15})$$

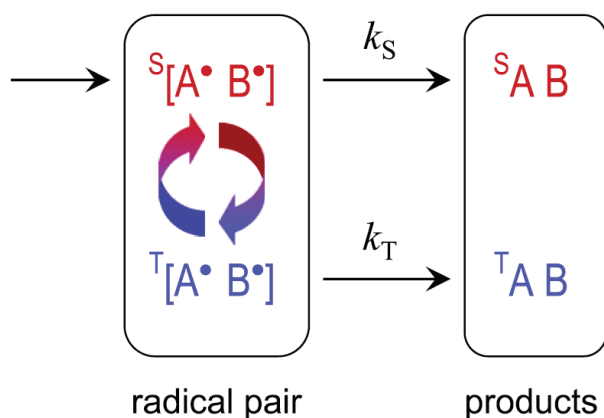


Figure II:2-1

Recombination scheme in the Jones-Hore theory. The products are shelving states described within the density matrix.

It is our opinion that this new theory is not entirely new, but is rather a glorified reiteration of the PME. More than that we feel that the identification of the recombination products with obscure *shelving states*, whereupon the state of the pair is projected directly, is incompatible with quantum measurement theory, while there are also fundamental doubts on its validity [Kom10]. Regardless of our - perhaps debatable - concerns though, we will not further dwell into this theory since its results - as is also verified by the authors - are very similar to those of the PME, at least in the ranges of parameters we will be limiting ourselves to.

II.2.2.3 The Quantum Measurement Master Equation (QMME)

Recently, a new theory for the description of radical pair dynamics was proposed, based on theoretical considerations from the field of quantum measurement [Kom09a, Kom09b]. In this theory, recombination is treated as a quantum tunneling procedure, constituting, in essence, a measurement on the system, the back action of which on the electronic state has to be taken into account. The strength of the measurement is identified as the square root of the recombination rate and the following familiar master equation of the Lindblad form is arrived at:

$$\frac{d\rho}{dt} = -\frac{i}{\hbar}[H, \rho] - (k_S + k_T)(\{\rho, Q_S\} - 2Q_S \cdot \rho \cdot Q_S) \quad (\text{II.2.16})$$

where the identity $Q_S + Q_T = \mathbb{I}$ has been used. A detailed outline of the derivation of the above master equation can be found in [Kom09b]. The relaxation part of the QMME, although derived through a completely different conceptual framework, shares the same functional form with the abandoned Eq.(II.2.13) for $k_{S(T)}^{(a)} = 2k_{S(T)}^{(b)}$. R. Haberkorn describes this case as “spin relaxation without reaction” in [Hab76]. Indeed, it can be easily seen that Eq.(II.2.16) preserves the trace of the density matrix, so there is no reaction, but decoherence is induced. Recombination in this case is thus performed through *stochastic quantum jumps*. In a given time interval, the recombination probabilities through the singlet and triplet channel are given by:

$$dP_S = 2k_S \langle Q_S \rangle dt \quad (\text{II.2.17})$$

$$dP_T = 2k_T \langle Q_T \rangle dt \quad (\text{II.2.18})$$

where $\langle Q_{S(T)} \rangle = \text{Tr}[\rho \cdot Q_{S(T)}]$. The number of RIPs which have not recombined and are still in the S-T subspace at time $t + \delta t$ is:

$$\begin{aligned} N(t + dt) &= N(t) - N(t)(dP_S(t) + dP_T(t)) \Rightarrow \\ &\Rightarrow dN/N = -2(k_S \langle Q_S \rangle + k_T \langle Q_T \rangle)dt \end{aligned} \quad (\text{II.2.19})$$

and taking into account that $\langle Q_S \rangle + \langle Q_T \rangle = 1$

$$\frac{dN}{N} = -2[k_S + (k_T - k_S)\langle Q_T \rangle]dt \quad (\text{II:2.20})$$

The solution of the above differential equation is:

$$N(t) = N_0 e^{-2k_S t} e^{-2(k_T - k_S) \int_0^t \langle Q_T \rangle d\tau} \quad (\text{II:2.21})$$

where N_0 is the initial number of RIPS.

A more thorough discussion of the QMME theory is reserved for the next chapter.

II:2.2.4 The Hamiltonian

The unitary evolution Hamiltonian of the radical pair mechanism comprises a number of different terms and the related MFEs have been described extensively in the literature, for example in the pioneering [SSW⁺76, WSW78] for RIPS in solution, in [SW78, CBDS94, CBDS95] for the development of theoretical descriptions or perturbative calculations of RIP dynamics, in [HMB79, TN82, SCS07] for RIPS in photosynthetic reaction centers, in [SLTM95] for the study of the Low Field Effect, in [RAS00, TCBH01, EH08, EH09] in the context of magnetoreception and, of course, in more general reviews of the field [SU89, Bro02, TH04, Rod09] and that's just to name a few. Here we give a brief description of the various terms and how they give rise to effects related to external magnetic fields; a presentation largely based in combining analogous works from [TH04] and [Rod09][†].

▷ Zeeman (Z) interaction:

The Zeeman interaction was originally studied in the context of atomic physics [Zee97, Sob06]. It is where the external magnetic field enters the equations of motion explicitly, thus making the phenomenon relevant to any MFE. In the rotationally symmetric atomic potentials, the Zeeman interaction term takes the form:

$$\hat{H}_Z = \mu_B (\hat{\mathbf{L}} + g_e \hat{\mathbf{S}}) \cdot \mathbf{B} \quad (\text{II:2.22})$$

where μ_B is the Bohr magneton, $g_e \simeq 2$ the electron g-factor and $\hat{\mathbf{L}}$ and $\hat{\mathbf{S}}$ the orbital and spin angular momenta of the electron. In molecules, L ceases to be a good quantum number since potentials are no longer rotationally symmetric. Instead, their complex structure can be expressed by replacing the electron g-factor with an appropriate g-tensor:

[†]Some qualitative aspects of MFEs given below have also been mentioned in the previous chapter. However, we feel it doesn't hurt to repeat them here for the sake of easy reference.

$$\hat{H}_Z = \mu_B \hat{\mathbf{S}} \cdot \ddot{\mathbf{G}} \cdot \mathbf{B} \quad (\text{II.2.23})$$

The g-tensor can either be determined experimentally or approximated through tools appropriate for studying many-body systems, such as - and predominantly - the density functional theory. Simplifying the situation, in small molecules and weak fields, the g-tensor can be reasonably well approximated by a scalar, thus:

$$\hat{H}_Z = \mu_B g \hat{\mathbf{S}} \cdot \mathbf{B} = -\gamma \hbar \hat{\mathbf{S}} \cdot \mathbf{B} \xrightarrow{\hbar \text{ units}} -\gamma \hat{\mathbf{S}} \cdot \mathbf{B} \quad (\text{II.2.24})$$

where $\gamma = -\mu_B g / \hbar$ is the gyromagnetic ratio of the electron. For most calculations, g is taken to be equal to the free electron g-factor, $g_e \simeq 2.00232$, and the gyromagnetic ratio is then the free electron gyromagnetic ratio, $\gamma_e \simeq -1.761 \times 10^{11} \text{ rad/sT}$. Nuclei are also subject to Zeeman interaction, but their gyromagnetic ratios are usually three to four orders of magnitude smaller than γ_e and the effect is neglected.

For radical pairs, two electrons are involved and the Zeeman term takes the form:

$$\hat{H}_Z = \sum_{X=A,D} \mu_B g^{(X)} \hat{\mathbf{S}}^{(X)} \cdot \mathbf{B} \quad (\text{II.2.25})$$

where we have assumed that the external field is the same at the Donor and Acceptor sites, although in reality small inhomogeneities are not out of the question. In most cases and especially for weak magnetic fields, the approximation $g^{(A)} = g^{(D)} = g_e$ is well justified and is usually made.

Related MFE: The Zeeman interaction is involved in all magnetic field effects manifested in radical pairs. In particular, however, the form of the interaction term in Eq.(II.2.25) clarifies the origins of the Δg mechanism. Electrons with different g-factors rotate at different frequencies about an external magnetic field. As a result, S-T mixing occurs at a rate $\mu_B (g^{(A)} - g^{(D)}) / \hbar$. This type of field effect is obviously linear to the external field and, since g-factors are expected to differ by very little (if at all), the effect becomes important for very large fields.

▷ *Hyperfine (HF) interaction:*

The hyperfine interaction couples the unpaired electron spin to the local magnetic field produced by the nuclear spins of the surrounding nuclei. It comprises two terms.

The first is the dipolar interaction of the magnetic moments of the unpaired electron and the nucleus. For free-moving molecules in a solution the dipolar term averages to zero, but for molecules attached in some sort of rigid formation it makes the hyperfine interaction anisotropic, that is dependent not only on the relative orientation of the magnetic moments, but also on the orientation defined by the underlying structure. This is of paramount importance for the concept of RIP-based magnetoreception as it provides the means for the mechanism to be sensitive to the orientation of the external magnetic field.

The second is the Fermi contact interaction and is manifested when the electronic wavefunction is non-zero within the nucleus, i.e. in an s-orbital. It has been extensively studied in *Electron Paramagnetic Resonance* (EPR) experiments and found to be isotropic, as expected by the theory.

Overall, the hyperfine Hamiltonian for a RIP takes the form:

$$\hat{H}_{\text{HF}} = \sum_{k=1}^{n_A} \hat{\mathbf{S}}^{(A)} \cdot \ddot{\mathbf{A}}_k^{(A)} \cdot \hat{\mathbf{I}}_k^{(A)} + \sum_{l=1}^{n_D} \hat{\mathbf{S}}^{(D)} \cdot \ddot{\mathbf{A}}_l^{(D)} \cdot \hat{\mathbf{I}}_l^{(D)} \quad (\text{II.2.26})$$

where n_X is the number of nuclei at X site, $\hat{\mathbf{I}}_i^{(X)}$ is the i^{th} nucleus of X and $\ddot{\mathbf{A}}_i^{(X)}$ the corresponding hyperfine coupling tensor to the electronic spin. In this work we will be allowing hyperfine interaction to only couple parallel components of the electronic and nuclear spins, in which case the coupling tensors reduce to diagonal 3×3 matrices and Eq.(II.2.26) can be recast as:

$$\hat{H}_{\text{HF}} = \sum_{X=A,D} \sum_{k=1}^{n_X} \hat{\mathbf{S}}^{(X)} \cdot \begin{pmatrix} \alpha_{k,xx}^{(X)} & 0 & 0 \\ 0 & \alpha_{k,yy}^{(X)} & 0 \\ 0 & 0 & \alpha_{k,zz}^{(X)} \end{pmatrix} \cdot \hat{\mathbf{I}}_k^{(X)} \quad (\text{II.2.27})$$

and when the interaction is also isotropic, we get the further simplified:

$$\hat{H}_{\text{HF}} = \sum_{X=A,D} \sum_{k=1}^{n_X} \alpha_k^{(X)} \hat{\mathbf{S}}^{(X)} \cdot \hat{\mathbf{I}}_k^{(X)} \quad (\text{II.2.28})$$

The hyperfine interaction is responsible for the original magnetic field effect observed in radical pairs. The underlying mechanism can be described as follows: Each electron precesses about the vector sum of the external and the local magnetic fields. Since the local field depends on the local

nuclear structure, the two unpaired electrons of the radical pair probably precess at different frequencies. As a result, the two electrons bring different phase contributions to the combined spin wavefunction over time. Thus, the wavefunction of a pair originally in a pure Singlet state will gradually transform into a coherent Singlet-Triplet superposition.

At weak external fields[‡], i.e. when the Larmor frequency is smaller than the hyperfine coupling strengths, all basis states of Eq.(II.2.2) and (II.2.3) are nearly degenerate and the Singlet can inter-convert to and from any of the Triplets. As the field becomes stronger, Zeeman interaction begins to dominate and the precession of both the electronic and nuclear spins is locked to its axis. In this case the projection of the combined electronic spin is conserved and only $|S\rangle \leftrightarrow |T_0\rangle$ transitions are allowed. With the $|S\rangle \leftrightarrow |T_{\pm}\rangle$ transitions suppressed, the available pathways toward Triplet products are reduced from three to one, thus leading to a reduction of the Triplet yield (for a Singlet-born pair). This is the normal magnetic field effect.

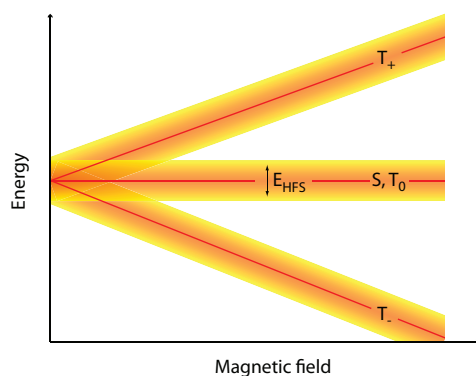


Figure II-2-2

Illustration of the energy separation of the Triplet manifold due to the Zeeman effect. Superimposed are indicative hyperfine induced widths for the states, indicating the passage from *weak* to *strong* fields.

Although it would seem that the application of a magnetic field can only lead to a reduction of S-T interconversion, this is not the case. It has been experimentally observed [HHMS88, BKMS93, STB91, SLTM95] and theoretically justified [Bro76, BM96, TTB⁺98], that weak magnetic fields tend to enhance rather than inhibit the conversion mechanism. Currently this is attributed to degenerate, zero-field, coherent nuclear-electron states [TTB⁺98], the degeneracy of which is lifted for weak magnetic fields. The resultant slow oscillations introduce previously disallowed (due to degeneracy) pathways for Singlet to Triplet conversion, which manifest as increased Triplet yield, if relaxation is sufficiently weak relative to the newly intro-

[‡]and assuming that exchange and dipolar interactions are somehow suppressed.

duced frequencies so as to allow the slow oscillations to evolve significantly[§]. This is the low field effect.

It is worth noting here that, as expected physically, the coupling strength of the hyperfine interaction depends strongly on the nuclear gyromagnetic ratio. This fact is confirmed through perdeuteration experiments, where protons in the nuclei of molecules are replaced by deuterium atoms, for which the gyromagnetic ratio is about 6.5 times smaller than that of the proton [WSW78, TH04, RNH⁺07a, RNH⁺07b, DK09].

Related MFE: The originally observed MFE in RIPS is caused by the hyperfine interaction [see discussion above], as well as the LFE as treated in [Bro76, TTB⁺98, BM96].

▷ *Spin Exchange (SE) interaction:*

Spin exchange originates in the electrostatic interaction between colliding or closely separated particles; the former being the usual case for thermal atoms, as seen in Part I for alkali vapors, and the latter for electrons in the formation of dimers in molecules or slow moving large atoms. Its descriptive name qualitatively implies a reaction of the form:



wherein the reacting particles exchange spin quantum numbers. Physically, it is the evolution of the overlapping wavefunctions of the adjacent particles which creates correlation and produces energetically separated bonding (Singlet) and anti-bonding (Triplet) orbitals, leading to the mixing and possible, upon separation, exchange of spins.

The Hamiltonian term describing spin exchange is of the form:

$$\hat{H}_{SE} = -J\hat{\mathbf{S}}^{(A)} \cdot \hat{\mathbf{S}}^{(D)} \quad (\text{II.2.30})$$

J is an empirical parameter giving the difference in energy between the lowest energy singlet and triplet states. The magnitude of the exchange interaction decreases exponentially with the radical separation, that is:

$$J(r) = J_0 e^{-r/r_J} \quad (\text{II.2.31})$$

with J_0 and r_J being two empirical parameters with typical values $J_0 \sim 10^{17}$ rad/s and $r_J \sim 50$ pm, but heavily dependent on the particular molecules and the surrounding environment.

[§]A more pictorial description of the origins of the LFE is obtained in the context of the vector model described in [BM96] and in App.D.

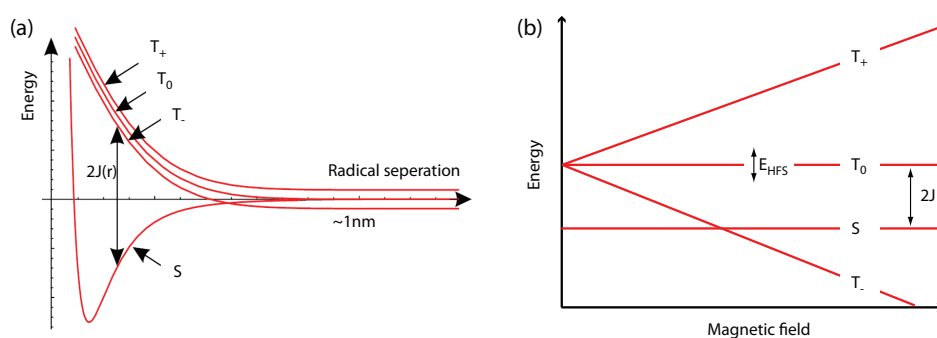


Figure II:2-3

(a) The energy of the spin exchange interaction as a function of the radical separation
 (b) Impact of an external magnetic field on the spin exchange energies for a fixed radical distance. Notice the level crossing of $|T_- \rangle$ and $|S \rangle$, possibly responsible for the J -resonance MFE [BM96]

Fig.II:2-3 seems to imply that in the case of strong or even moderate spin exchange interaction (J much greater than the HF couplings or even just greater than the Larmor frequency), no LFE can be observed, that is weak external fields are muffled in noise. Indeed, in [EH08] the authors, based on the PME claim that a delicate, molecule-specific interplay between spin exchange and dipolar interaction (both much stronger than the field strength in the LFE region; see next entry, too) must be fulfilled if a weak magnetic field is to have any measurable effect on the yields of the reaction. However, according to the more recent QMME theory, no such fine tuning on behalf of nature is necessary, since the quantum Zeno effect renders the LFE mechanism practically immune to both dipolar and spin exchange inhibition, contrary to what was generally believed [Kom09a].

Related MFE: The J – resonance. As seen in Fig.II:2-3b, spin exchange at zero field causes the Singlet state and the degenerate Triplet manifold to become energetically separated by $2J$. This inhibits S-T interconversion and Singlet-born pairs yield, predominantly, Singlet products. An externally applied magnetic field lifts the degeneracy of the Triplet states due to the Zeeman effect. As the field is increased, $|T_- \rangle$ and $|S \rangle$ come closer in energy and eventually cross, thus providing a pathway from Singlet to Triplet and, eventually, to Triplet products. Further increase of the field strength once more inhibits S-T interconversion. This is a typical level-crossing resonance, the width of which is determined by the strength of the hyperfine couplings. The J -resonance mechanism can double as an explanation of the origins of LFE in cases where the spin exchange is only slightly stronger than the hyperfine couplings.

▷ *Dipolar (DP) interaction:*

Dipolar interaction refers to the magnetic interaction experienced by each

of the two electrons due to the magnetic moment of the other. It is given by:

$$\hat{H}_{\text{DP}} = \frac{\mu_0 \mu_{\text{B}}^2 g^{(\text{A})} g^{(\text{D})}}{4\pi \hbar^2 r^3} \left[\hat{\mathbf{S}}^{(\text{A})} \cdot \hat{\mathbf{S}}^{(\text{D})} - \frac{3}{r^2} \left(\hat{\mathbf{S}}^{(\text{A})} \cdot \mathbf{r} \right) \left(\hat{\mathbf{S}}^{(\text{D})} \cdot \mathbf{r} \right) \right] \quad (\text{II:2.32})$$

or, in tensor form:

$$\hat{H}_{\text{DP}} = \hat{\mathbf{S}}^{(\text{A})} \cdot \hat{\mathbf{D}} \cdot \hat{\mathbf{S}}^{(\text{D})} \quad (\text{II:2.33})$$

where the elements of the dipolar tensor, $\hat{\mathbf{D}}$, are extracted from Eq.(II:2.32). For high fields the dipolar interaction either becomes highly anisotropic for RIPS on rigid formations or effectively averages to zero in solutions due to the diffusive motion of radicals around each other. For weak fields there is some controversy about its influence, as was already discussed in the previous entry. The PME approach to RIP dynamics, indicates that dipolar interaction leads to suppression of LFE, unless it is of similar magnitude with the exchange interaction, in which case the mutual cancellation of the two allows LFE to surface again [EH08]. In stark contrast, the new QMME theory applied in the, so called, Zeno regime proposes a mechanism which immunizes the effect of weak fields against both the dipolar and the spin exchange interactions.

Having reached this point, in Fig.II:2-4 a combined schematic of the influence of the various presented terms on the energies of the basis radical pair electronic states is given [TN82].

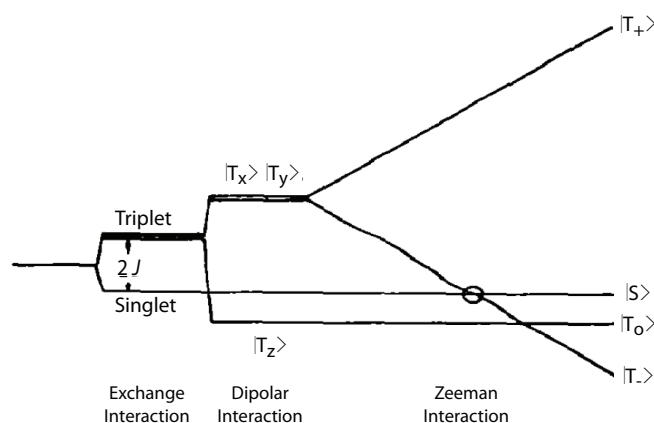


Figure II:2-4

Combined spin exchange, dipolar and Zeeman interactions [TN82]

▷ *Domination regions of the various MFEs:*

A round-up of the relative magnitudes and regions of domination of the various magnetic field effects is given in Fig.II:2-5 [Rod09]. The figure refers to a Singlet-born pair and we ignore spin exchange and dipolar interactions for the sake of conversation. At zero field the yields of the Singlet and Triplet channels are determined by the hyperfine mechanism. A weak magnetic field enhances Singlet-Triplet inter-conversion and increases the Triplet yield, giving rise to the low field effect. At moderate fields, the Zeeman effect splits the energies of the Triplet states sufficiently far apart so that no $|S\rangle \rightleftharpoons |T_{\pm}\rangle$ transitions are possible, thus reducing the pathways to and from the Triplet manifold and, consequently, the Triplet yield. At very high magnetic fields, minute differences in the g-factors of the electrons at the two sites become important and S-T inter-conversion is enhanced again owing to phase mixing due to the different precession frequencies of the electronic spins.

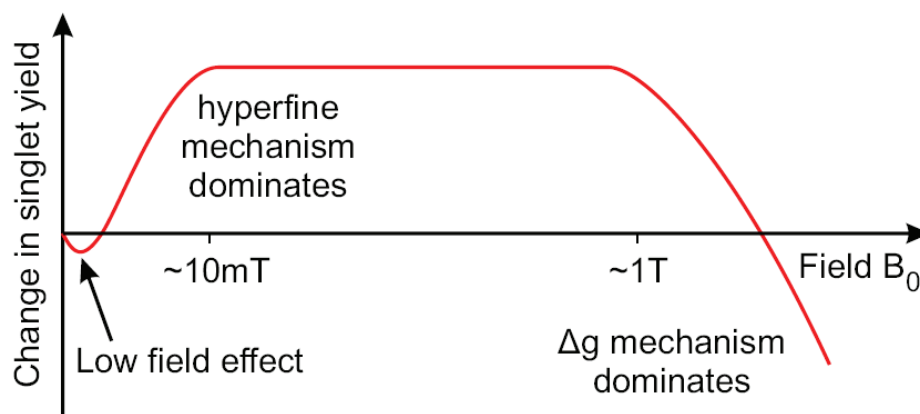


Figure II:2-5

Regions of domination of the various magnetic field effects versus the strength of the field [Rod09]

▷ *Total Hamiltonian:*

Gathering all the terms described above, we arrive at a quite general form for the Hamiltonian used in describing the coherent evolution of RIPS:

$$\begin{aligned}
 \hat{H} = & \sum_{X=A,D} \mu_B g^{(X)} \hat{\mathbf{S}}^{(X)} \cdot \mathbf{B} + && \text{(Zeeman)} \\
 & + \sum_{X=A,D} \sum_{k=1}^{n_X} \hat{\mathbf{S}}^{(X)} \cdot \ddot{\mathbf{A}}_k^{(X)} \cdot \hat{\mathbf{I}}_k^{(X)} - && \text{(Hyperfine)} \\
 & - J \hat{\mathbf{S}}^{(A)} \cdot \hat{\mathbf{S}}^{(D)} + && \text{(Spin exchange)} \\
 & + \hat{\mathbf{S}}^{(A)} \cdot \ddot{\mathbf{D}} \cdot \hat{\mathbf{S}}^{(D)} && \text{(Dipolar)} \quad (\text{II.2.34})
 \end{aligned}$$

For the most part in this work we omit spin exchange and dipolar terms and deal only with the Zeeman and hyperfine interaction, as these are the physically significant contributions to the magnetic properties of radical pairs. This is generally justified for large enough separations of the two sites of the radicals, on the order of few nm. However, as already mentioned above and discussed to a greater extent in the next chapter, the effect of spin exchange and dipolar interactions is largely suppressed in the Zeno regime of the QMME.

II.2.2.5 Effects not accounted for in the Master Equations

▷ *Radical pair generation:*

The creation of radical ion pairs from neutral molecules can be modeled by adding a source term to the density matrix equations, $k_c e^{-k_c t}$, with k_c being the RIP creation rate. This, however, is not a process of fundamental significance and will be neglected. Besides, such creation rates are typically quite large compared to the range of magnetic fields and hyperfine couplings we will be dealing with.

▷ *Spin relaxation:*

First we must note that spin relaxation is routinely neglected in the bulk of the literature; not always justifiably [SU89]. By the term we refer to a variety of mechanisms causing the density matrix to relax toward its fully mixed state, including, but not exhausted to, molecular tumbling in solutions, lattice relaxation in rigid formations, stochastic fluctuations of hyperfine couplings and/or of external magnetic fields, collisions and more. Formally, it can be modeled either as a stochastic term in the Hamiltonian, H_{SR} , if its origins are in magnetic field or hyperfine fluctuations, or as an incoherent term of the form $-k_{SR}\rho$ (for the PME) or $-k_{SR}(\rho - \rho_o)$ (for the

QMME), where $\rho_0 = \frac{1}{16n_A n_D} \mathbb{I}_{16n_A n_D}$ is the fully mixed density matrix, if it originates in more general mechanisms. Of course it should be noted that the relaxation induced by charge recombination is not included in the rate k_{SR} , since it is already accounted for by the recombination rates k_S and k_T . More rigorously, the spin relaxation can be described by a Lindbladian term:

$$\frac{d\rho}{dt} \propto \sum_{X=A,D} \sum_{i=x,y,z} k_X^{(i)} \left(S_X^{(i)} \cdot \rho \cdot S_X^{(i)\dagger} - \frac{1}{2} (S_X^{(i)\dagger} \cdot S_X^{(i)} \cdot \rho + \rho \cdot S_X^{(i)\dagger} \cdot S_X^{(i)}) \right) \quad (\text{II.2.35})$$

which is the form we use in the cases where we incorporate spin relaxation in our calculations. When the environmental noise is isotropic, i.e. is expected to flip spins with equal probabilities, all $k_X^{(i)}$ rates can be substituted with a single rate, k_{SR} .

Physically and from the MFE point of view, spin relaxation can become very important as it can suppress the coherent processes leading to S-T conversion and induce forbidden transitions in the context of mixing the density matrix. For example, in weak magnetic fields, rapid spin relaxation does not allow the slow evolution of the nearly degenerate, coherent nuclear-electron states to manifest the low field effect, whereas in high magnetic fields, where $|S\rangle \rightleftharpoons |T_{\pm}\rangle$ transitions are Zeeman-suppressed, spin relaxation can provide the energy for the transitions to occur, thus washing out the normal field effect.

In this work, spin relaxation will be neglected when we wish to bring out particular physical aspects of the RIP dynamics to which relaxation is irrelevant, but will be occasionally revived when its influence is important in some particular context.

▷ *Diffusion:*

The constituent radicals of a RIP in solution can diffuse into the bulk of the solution and recombine with other, randomly encountered radicals. This is the origin of homogeneous recombination. We neglect it for two reasons. First, because it adds another layer of complexity to the description of system dynamics, without adding any new physical insight and second because when radicals are embedded on rigid structures to provide for anisotropic magnetic phenomena (as is largely the relevant case in this work) they can not diffuse.

II.2.3 Product Yields and Sensitivity

Radical pairs eventually recombine. In some cases, one of the two spin states does not react and the pair diffuses apart to give free radicals. In most cases the recombination rates are different for the Singlet and Triplet channels. But in all cases, radical pairs eventually reach a state which can be considered the final *product* state. For the reaction to be interesting, the products reached through the Singlet or the Triplet recombination channel will have to be, not only different, but physically or chemically discernible and distinguishable. Provided that the products can be identified and measured, we define the *yields* of the reaction and use these to quantify the sensitivity of a RIP to the magnitude and orientation of an external magnetic field.

The Singlet (Triplet) yield, that is the percentage of RIPS having recombined through the Singlet (Triplet) channel at infinite time, is given by:

$$Y_{S(T)} = 100 \int_0^{\infty} \frac{N(t)}{N_0} dP_{S(T)}(t) \quad (\text{II.2.36})$$

The magnetic sensitivity of the RIP reaction in the vicinity of some particular magnetic field B_o is then related to the inverse of the slope of the yield vs field curve calculated at that particular value of B :

$$\delta B = \frac{\delta Y_{S(T)}}{(dY_{S(T)}/dB)|_{B=B_o}} \quad (\text{II.2.37})$$

where $\delta Y_{S(T)} \approx 0.05\%$ is the smallest measurable yield change (see discussion in [Kom09a]). This is a usual sensitivity definition and δB can be identified either as the smallest measurable *increment in the magnitude* of the magnetic field or as the smallest measurable field *magnitude*.

In the case where the system demonstrates an anisotropic behavior to the orientation of the magnetic field vector, a heading error can also be defined to quantify the angular precision with which the direction of the field can be determined:

$$\delta\varphi = \frac{\delta Y_T}{(Y_{S(T),\max} - Y_{S(T),\min})/90^\circ} \quad (\text{II.2.38})$$

where $Y_{S(T),\max(\min)}$ is the maximum (minimum) yield obtained as a magnetic field of given magnitude rotates about a fixed axis and is a quantity dependent on the axis. For unpolarized spin states, the maxima and minima of the yield are 90° apart[¶], hence the division in the denominator of the above definition. Again, $\delta\varphi$ is identified as the smallest detectable change in the magnetic field orientation.

[¶]Thus defined, $\delta\varphi$ is obtained in degrees. For $\delta\varphi$ in radians, substitute 90° with $\pi/2$.

Whether one chooses to use the Singlet or the Triplet yield in the above definitions is theoretically immaterial, since $Y_S = 100\% - Y_T$. Experimentally it would depend on which of the two products can be readily determined.

Chapter II:3

The Quantum Measurement Master Equation

The recent developments in the theoretical treatment of radical pairs, namely the QMME theory [Kom09b], has lead to a new understanding of their inner workings, providing explanations for experimental data, previously unattainable by the traditionally employed PME approach. In this chapter we discuss this new insight and predict some new phenomena related to radical pairs created in coherent Triplet states.

II.3.1 *Explanation of magnetic field effects*

In a recent publication by the P.J. Hore group in Oxford, Maeda *et al* [MHC⁺08] gave the first experimental demonstration of magnetic field effects induced by a field comparable to the geomagnetic field. The theoretical explanation of the findings therein became the incentive for the development of the QMME approach to radical pair reactions. In [Kom09b], I.K. Kominiš gave a proof of his quantum measurement master equation and, using the simplest possible radical pair, i.e. one with a single nucleus at either the donor or the acceptor site, reproduced the experimental results of the Oxford group. Pictorially, the main achievement of that paper is shown in Fig.II:3-1, where the QMME, for a chosen set of parameters, yields a series of theoretical curves which all but coincide with the corresponding experimental ones, while at the same time and for the same set of parameters, the traditionally employed PME fails to do so.

To briefly describe the findings, we start with the reminder that the model used is the simplest possible, that is one with a single spin- $\frac{1}{2}$ nucleus at either the acceptor or donor site, interacting with one of the electrons through an anisotropic

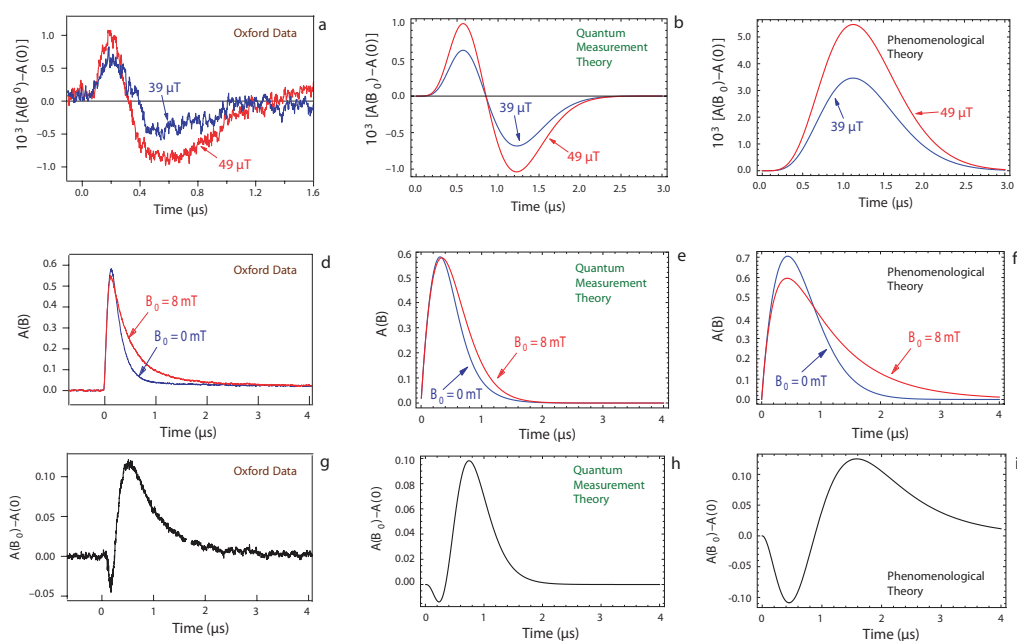


Figure II-3-1

- (a) Measured MFE for two small magnetic fields [MHC⁺08].
 (b) Reproduction of data by the QMME.
 (c) The PME does not reproduce the data for the same set of parameters.
 (d) - (g) Transient absorption and corresponding MFE for zero and high field.
 (e) - (h) Reproduction of data by the QMME.
 (f) - (i) The PME is inferior at reproducing the data for the same set of parameters.
 In the latter figures and for the high magnetic field, the radical pair creation and spin relaxation rates have been reintroduced as is necessary.

hyperfine coupling matrix. Each electronic pair in the initial population of N_0 pairs is assumed to be formed in the Singlet state; its density matrix given by the normalized expression $\rho_0 = \frac{Q_S}{Tr(Q_S)}$. The Hamiltonian comprises the Zeeman and hyperfine terms alone, while spin-exchange and dipolar interactions are temporarily dropped. This is a reasonable take on the subject in the traditional approach, since strong spin-spin interactions would supposedly suppress the effects of very small fields. We do, however, have second thoughts on the actual influence of such interactions and will revisit the subject in the next section. Spin relaxation is also neglected for the initial analysis, since the experimental results show it to be sufficiently slow for the particular molecules and temperatures used, but it will be revived for the discussion of higher field effects.

With passing time, the quantum state of a given pair evolves into an S-T superposition, the coherence of which is gradually diminished by the recombination process. Pairs recombine spin-selectively at rates k_S and k_T , which results in a decrease of the pair population, N , according to Eq.(II.2.21). In the PME theory, the decrease of population is embodied in the decay of the trace of the density

matrix calculated through the master equation. The reaction is considered to be over when enough population has recombined and the measurement limit has been reached; we take that to be at about $\sim 0.05\%$ of the initial population (see discussion in [Kom09a]).

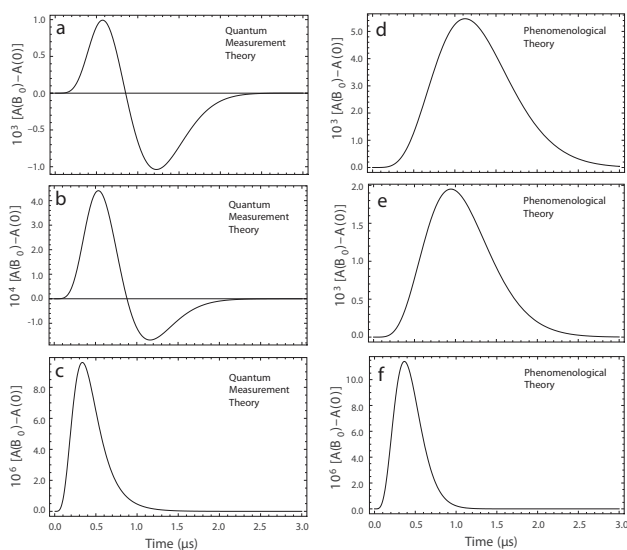
The magnetic field effect is defined as the difference in the transient population for a magnetic field $B \neq 0$, minus that for $B = 0$:

$$A(B, t) = N_B(t) - N_{B=0}(t) = [S(t) + T(t)]_B - [S(t) + T(t)]_{B=0} \quad (\text{II.3.1})$$

where $S(T)(t) = N(t)Tr[\rho(t) \cdot Q_{S(T)}]$ (QMME) or $= N_0 Tr[\rho(t) \cdot Q_{S(T)}]$ (PME) are the total Singlet (Triplet) populations at time t^* . In the top row of Fig. II:3-1 the measured MFE (II:3-1a) in [MHC⁺08] and the attempts for reproduction by the QMME (II:3-1b) and PME (II:3-1c) theories are shown. As is seen in the figure, the QMME theory fully reproduces the experimental data, while the PME does not. For the PME the same set of parameters was used as for the QMME, although it could be argued that better reproduction of the data by the PME might be possible at some other parameter region. Such disputes remain to be settled by future studies. For the time being, however, we keep the fact that the QMME theory shows both qualitative and quantitative agreement with the data. For it to be enabled to do so, we propose that the Triplet recombination rate is much larger than that of the Singlet, $k_T \gg k_S$, while the pairs start at the Singlet state; a proposal to be verified by experiment. This is the condition for the Zeno effect to kick in. In other words, we argue that the strong interrogation of the Triplet state has a profound impact on the system dynamics, although the Triplet state itself remains largely unpopulated.

Analogous discussions can be held for the remaining plots in Fig. II:3-1 which involve the transient absorption signals and corresponding magnetic field effects for zero and for high magnetic fields. We should note here that for the high field case, the creation process of the radical pairs, as well as the spin relaxation (at rates k_c and k_{SR} , respectively) have to be taken into account. Spin relaxation is particularly important, since it can wash out the differences between the QMME and the PME as seen in Fig. II:3-2, where the magnetic field effect for a Singlet geminate pair is shown in the case of a small magnetic field and an increasing k_{SR} . In the figure we see that, indeed, for strong spin relaxation the predictions of the two theories become rather similar. Hence, when the experimental conditions are such that spin relaxation is dominant, it will be very difficult to determine which of the two theories provides the correct description of the radical pair dynamics.

*We remind here that the difference between the QMME and the PME is not too subtle. In the QMME, $N(t)$ is indirectly affected by $\rho(t)$ through the $\langle Q_S \rangle$ and $\langle Q_T \rangle$ [see Eq. (II.2.20)], while $Tr[\rho(t)] = 1$ at all times. In the PME, $N(t)$ is directly determined by the decaying trace of the density matrix, $N(t) = N_0 Tr[\rho(t)]$.

**Figure II:3-2**

Magnetic field effect for a small magnetic field in the QMME (a, b, c) and PME (d, e, f) theories for increasing spin relaxation rates [$k_{\text{SR}} = 0$ (a, d), $1\mu\text{s}^{-1}$ (b, e) and $10\mu\text{s}^{-1}$ (c, f)]. As is evident, the two theories all but coincide for fast spin relaxation, but produce radically different results when spin relaxation is slow. Spin relaxation severely suppresses quantum coherent phenomena, which become evident when spin relaxation is itself suppressed [Kom09b].

II:3.2 Working in the Zeno regime

In the discussion of magnetic field effects in radical pair reactions, it has long been argued that spin-spin interactions, such as spin exchange and dipolar interaction, have to be, somehow, suppressed in order for a small magnetic field to have any measurable impact on the reaction outcome. The reason behind this demand is that such interactions, even if they are moderately strong, introduce energy level splittings which are too large for the small magnetic field to overcome. In [EH08] where the possibility that the FADH - Tryptophan pair in Cryptochrome is indeed the mediator of the avian compass is discussed, the authors, based on - largely incomplete - phenomenological and experimental data, go so far as to attempt to prove that the inter-molecular distance of this particular pair is such that the dipolar and the spin exchange interaction cancel each other precisely enough for the effects of the geomagnetic field to become measurable. Based on [Kom09a], we hereby argue that such far fetched assumptions may be unnecessary if the parameters of the system lie in the Zeno regime.

In Fig.II:3-3 we show the magnetic sensitivity and angular precision for a Singlet geminate pair in the traditional and the Zeno regime and for an increasingly strong spin exchange interaction. For both quantities, a very robust behavior is observed in the Zeno regime. The origin of this behavior lies in the strong continuous measurement of the Triplet subspace, which, regardless of the energy barrier introduced by spin exchange, ultimately leads to complete delocalization of the electronic spin state and, thus, to Triplet products formation, although actually the Triplet states are scarcely occupied [Gur97]. In the traditional regime on the other hand, spin-spin interactions indeed act to deteriorate sensitivity and precision, by inhibiting Singlet to Triplet conversion.

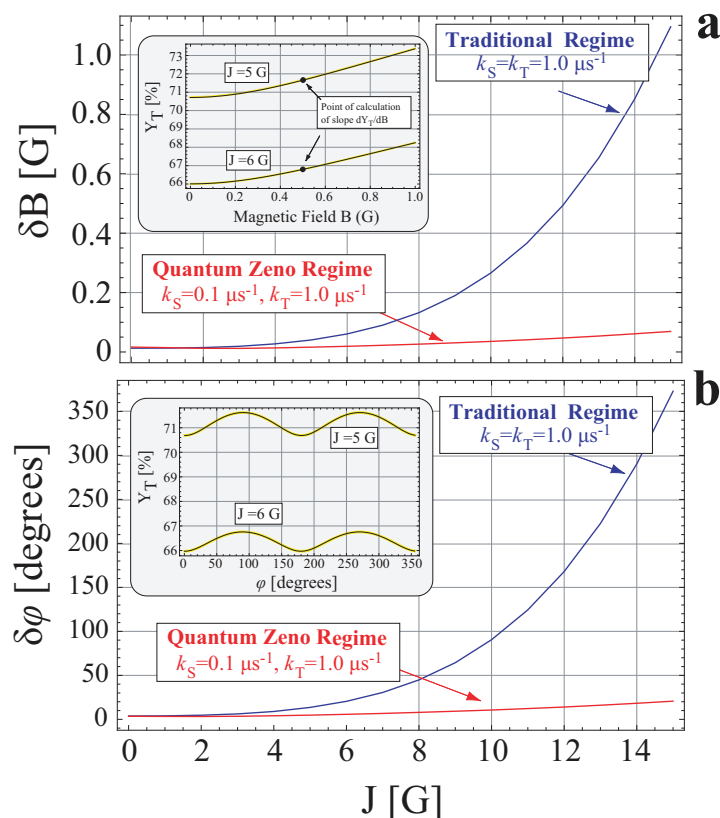
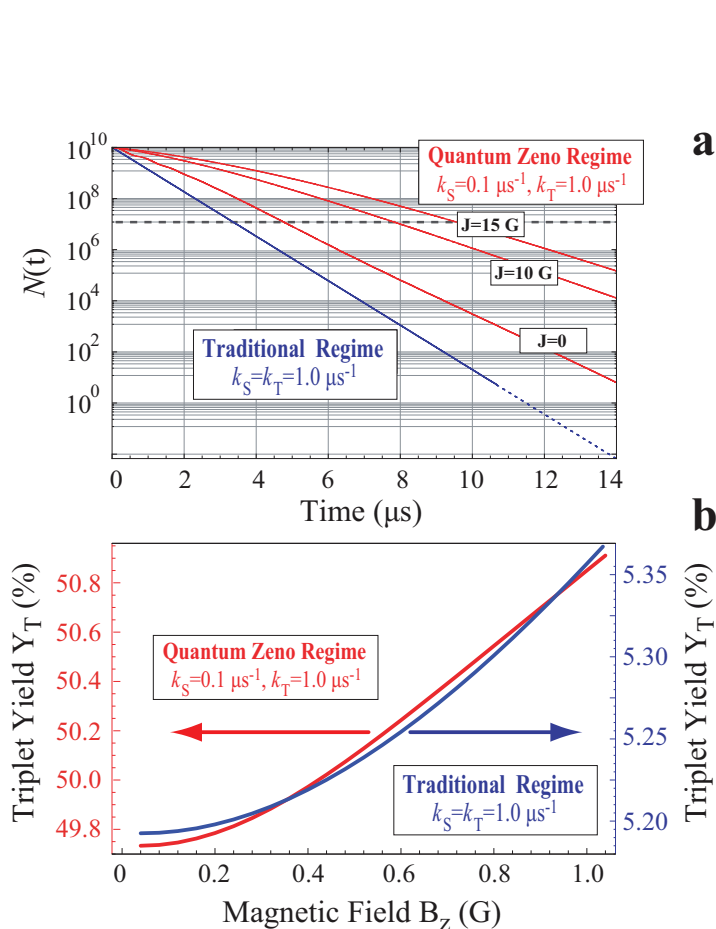


Figure II:3-3 Magnetic sensitivity and angular precision as functions of J in the traditional [blue] and the Zeno [red] regimes. In the latter case, a very robust behavior of the reaction is observed. The origins of this behavior are seen in the insets where the Zeno regime Triplet yield is plotted versus the magnitude (a) and the orientation (b) of the magnetic field, for two different values of J . As seen, similar responses are obtained albeit at different offsets, leading to minute changes in δB and $\delta\phi$ [Kom09a].

However, for the above mentioned, necessary “state delocalization” to take place, longer reaction times would be required, as the pairs would otherwise recombine through the Singlet channel before they had the chance to infiltrate into the Triplet subspace. It can be proved [Kom09a] that, indeed, in the Zeno regime, the presence of strong spin-spin interactions prolongs the lifetime of the radical pairs, whereas it does not do so in the traditional regime, a result depicted in Fig. II:3-4a. In Fig. II:3-4b we see the consequence of the prolongation of the pair lifetime. For a given spin exchange rate, although the relative change in the Triplet yield is about the same for the two parameter regimes, the absolute yield percentage achieved in the Zeno regime is about an order of magnitude higher, thus leading to better sensitivity.

We note at this point that maintaining good sensitivity and angular precision for the radical pair reaction has come from a simple and realistic assumption on the system parameters, without any recourse to system specific geometric or other characteristics. Whether the picture given above actually describes reality is an open question. We do believe, however, that the theory formulated and proposed in [Kom09b] has many interesting implications and alters significantly the way that an important family of chemical reactions, namely the radical pair reactions, is to be perceived. As such, this new theory deserves further investigation, which



(a) Decay of the radical pair population in the traditional [blue] and the Zeno [red] regime, for various values of J . The decay rate does not depend on J in the traditional regime. In the Zeno regime, fast spin exchange in combination with the Zeno condition, slow down the recombination of RIPs.

(b) Triplet Yield for $J = 10\text{G}$. The relative change for the 1G span of the magnetic field is about the same in the two theories, but in the QMME case the absolute value is an order of magnitude higher [Kom09a].

we hope it will indeed receive in future experimental and theoretical studies. For now, having introduced the new theory, we proceed to apply it in situations where the radical pairs are assumed to be formed in coherent Triplet, rather than Singlet, states.

II.3.3 Coherent Triplet excitation

Radical pairs are created in the Singlet state in the vast majority of cases. This is certainly true for pairs resulting from bond cleavage, but is also the dominant scenario for photo-induced pair formation. To this day, even in the cases of Triplet formation, pairs are created in incoherent mixtures of the possible projection states, a situation described by an initial density matrix of the form $\rho_o = \frac{Q_T}{Tr(Q_T)}$. It is, however, conceivable that the initial state of a radical pair could be manipulated toward the creation of a coherent state within the Triplet manifold, with a well defined total, as well as projection of, spin. This could be achieved, for example, by means of magnetic resonance or other spin selective

techniques in the radical pair phase or, perhaps, by biasing the light initiation process in the photoexcitation/charge transfer phase. In this section we examine a few new features which would be brought in by such coherent Triplet states. It is noted and stressed at this point that we are no longer referring to naturally occurring radical pair schemes. Rather, we wish to discuss an interesting feature which could be implemented in a synthesized bio-sensor.

A radical pair excited - coherently - in the Triplet manifold, can assume any of the basis Triplet states of Eq.(II.2.3), repeated here for easy reference[†]:

$$\left. \begin{aligned} |T_+\rangle &= |\uparrow, \uparrow\rangle \\ |T_0\rangle &= \frac{1}{\sqrt{2}}(|\uparrow, \downarrow\rangle + |\downarrow, \uparrow\rangle) \\ |T_-\rangle &= |\downarrow, \downarrow\rangle \end{aligned} \right\} \quad (\text{II.2.3})$$

Any coherent superposition of these states, in the sense of Eq.(II.2.4) and, thus, (II.2.5), is also valid. Of particular interest are the superposition states expressing the basis states along the other two, linearly independent, axes, Eq.(II.2.6/7):

$$\left. \begin{aligned} |T_0\rangle_x &= \frac{1}{\sqrt{2}}(-|T_+\rangle_z + |T_-\rangle_z) \\ |T_{\pm}\rangle_x &= \frac{1}{2}(|T_+\rangle_z \pm \sqrt{2}|T_0\rangle_z + |T_-\rangle_z) \\ |T_0\rangle_y &= -\frac{1}{\sqrt{2}}(|T_+\rangle_z + |T_-\rangle_z) \\ |T_{\pm}\rangle_y &= \frac{1}{2}(|T_+\rangle_z \pm i\sqrt{2}|T_0\rangle_z - |T_-\rangle_z) \end{aligned} \right\} \quad (\text{II.2.6/7})$$

Our main focus is in weak magnetic fields on the order of the geomagnetic field, that is Larmor frequencies are assumed quite smaller than the predominant hyperfine coupling strengths. In this regime, all states defined in Eqs.(II.2.2),(II.2.3) and (II.2.6/7) are, to a very good approximation, degenerate, provided that spin-spin interactions are neglected[‡].

II.3.3.1 An intuitive interaction representation

In order to take maximal advantage of the symmetry provided by the energy degeneracy in weak fields, we will be using a basis set compiled by all the zero-projection states:

[†]As explained in the previous chapter, these states are defined with \hat{z} -axis being the quantization axis

[‡]Spin-spin interactions and generic spin relaxation processes will be neglected for simplicity, as they tend to obscure the significant physical features. We will, however, turn them on from time to time in order to evaluate their influence on our results.

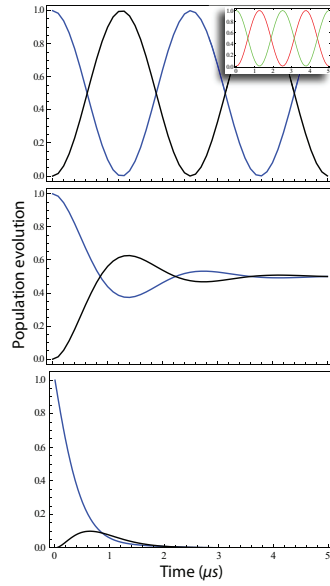
$$\left. \begin{aligned}
 |S\rangle &= \frac{1}{\sqrt{2}}(|\uparrow, \downarrow\rangle - |\downarrow, \uparrow\rangle) \\
 |T_o\rangle_x &= \frac{1}{\sqrt{2}}(-|\uparrow, \uparrow\rangle + |\downarrow, \downarrow\rangle) \\
 |T_o\rangle_y &= -\frac{1}{\sqrt{2}}(|\uparrow, \uparrow\rangle + |\downarrow, \downarrow\rangle) \\
 |T_o\rangle_z &= \frac{1}{\sqrt{2}}(|\uparrow, \downarrow\rangle + |\downarrow, \uparrow\rangle)
 \end{aligned} \right\} \text{Zero-projection basis} \quad (\text{II.3.2})$$

It is apparent that this basis set fully spans the Hilbert space of the electron pair and by using it we can provide an easy and intuitive pictorial representation of magnetic interactions. To this end, first of all we note that if a magnetic field \mathbf{B}_q defines \hat{q} as the quantization axis (where $\hat{q} = \hat{x}, \hat{y}, \hat{z}$), then, in the absence of hyperfine interaction, the Triplet basis states defined along \hat{q} are eigenstates of the magnetic Hamiltonian and are not affected by the field. However, the two states $|T_o\rangle_{k \neq q}$, which are linear combinations of the $|T_{\pm}\rangle_q$, evolve by transforming into one another due to phase mixing. Also, the Singlet state is spherically symmetric and is never affected by magnetic fields common to both electrons. Thus, if the state of the system is expressed in the zero-projection basis [Eq.(II.3.2)[§]], then a magnetic field, \mathbf{B}_z , will leave the $|S\rangle$ and $|T_o\rangle_z$ components of the state unaffected, but it will induce oscillations between the $|T_o\rangle_x$ and $|T_o\rangle_y$ components.

Now we switch off the magnetic field and the recombination and we assume that a single spin- $\frac{1}{2}$ nucleus is present at the site of one of the electrons. The hyperfine interaction appears, which is, in essence, a local magnetic field available to only one of the two electrons. Its main impact is that the locality makes the electronic pair asymmetric, as the nearby electron can exchange spin angular momentum with the nucleus. As a result, the total electronic spin ceases to be a good quantum number and the basis states sets defined above are no longer eigenstates of the Hamiltonian. We do, however, continue to describe the system at these bases, since diagonalizing the new Hamiltonian would be a rather futile endeavor in real molecules as well as a - by definition - system-specific procedure. We further assume that the hyperfine coupling of the nucleus to its corresponding electron is anisotropic, say along the \hat{z} -axis alone[¶]. This coupling scheme will induce a $|S\rangle \rightleftharpoons |T_o\rangle_z$ interconversion. Further, within the Triplet manifold, it will also induce $|T_o\rangle_x \rightleftharpoons |T_o\rangle_y$ oscillations, much like a magnetic field along \hat{z} -axis would do (Fig.II:3-5). This is shown analytically by solving the Liouville equation for $\alpha_{xx} = \alpha_{yy} = 0$, $\alpha_{zz} \neq 0$, and $B = 0$, with a $|T_o\rangle_z$ or a $|T_o\rangle_y$ initial state.

[§]where the usual assumption of \hat{z} being the quantization axis is made

[¶]This is to say that in Eq.(II.2.27) we set $X = A$ or D , $n_X = 1$ and $\alpha_{xx} = \alpha_{yy} = 0$, $\alpha_{zz} \neq 0$.

**Figure II:3-5**

Population evolution for \hat{z} -anisotropic hyperfine interaction with a pair starting in $|T_0\rangle_z$ [blue] and oscillating between this and $|S\rangle$ [black] ($B = 0$).

Top: $k_S = k_T = 0$ (inset: pair starting in state $|T_0\rangle_y$ [green] and interconverting to $|T_0\rangle_x$ [red])

Middle: Decoherence due to $k_S = k_T \neq 0$ included (but no recombination)

Bottom: Recombination included.

Starting from $|T_0\rangle_z$:

$$\left. \begin{aligned} \langle Q_{T_0} \rangle &= \frac{1}{2} + \frac{1}{2} e^{-kt} \left[\cos\left(\frac{1}{2}\sqrt{\alpha^2 - 4k^2}t\right) + \frac{2k}{\sqrt{\alpha^2 - 4k^2}} \sin\left(\frac{1}{2}\sqrt{\alpha^2 - 4k^2}t\right) \right] \\ \langle Q_S \rangle &= \frac{1}{2} - \frac{1}{2} e^{-kt} \left[\cos\left(\frac{1}{2}\sqrt{\alpha^2 - 4k^2}t\right) + \frac{2k}{\sqrt{\alpha^2 - 4k^2}} \sin\left(\frac{1}{2}\sqrt{\alpha^2 - 4k^2}t\right) \right] \\ \langle Q_{T_0^{(x)}} \rangle &= \langle Q_{T_0^{(y)}} \rangle = 0 \end{aligned} \right\} \quad (II.3.3)$$

Starting from $|T_0\rangle_y$ (where a \hat{z} magnetic field has also been included):

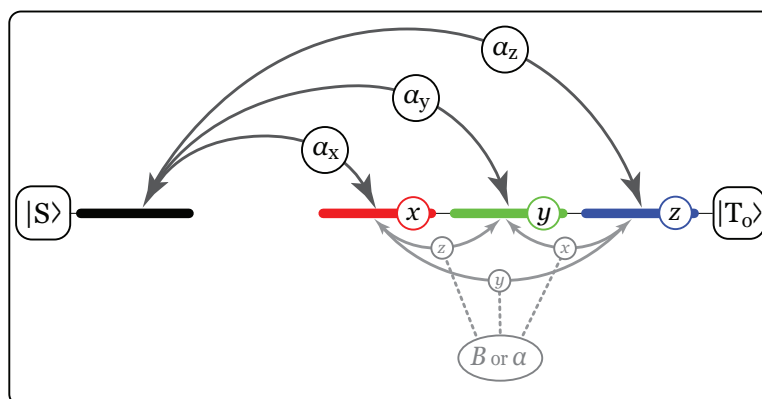
$$\left. \begin{aligned} \langle Q_{T_0^{(x)}} \rangle &= \frac{1}{2} - \frac{1}{4} \left[\cos\left(\frac{1}{2}(\alpha - 4\omega)t\right) + \cos\left(\frac{1}{2}(\alpha + 4\omega)t\right) \right] \\ \langle Q_{T_0^{(y)}} \rangle &= \frac{1}{2} + \frac{1}{4} \left[\cos\left(\frac{1}{2}(\alpha - 4\omega)t\right) + \cos\left(\frac{1}{2}(\alpha + 4\omega)t\right) \right] \\ \langle Q_{T_0} \rangle &= \langle Q_S \rangle = 0 \end{aligned} \right\} \quad (II.3.4)$$

where $k = k_S + k_T$ and $\langle Q_A \rangle = Tr(\rho \cdot |A\rangle\langle A|)$. Fig. II:3-5 is plotted based on these equations. Completely analogous situations occur for anisotropic hyperfine interactions along the remaining two axes. The above result is also justified in App.D in a more intuitive way. The combined influence of the various hyperfine terms and possible magnetic field orientations are schematically depicted in Fig. II:3-6.

II.3.3.2 Anisotropic effects in isotropic material

▷ a:/ *Sensitivity to the alignment of the field*

Figures like II:3-6 can reveal interesting features stemming from the coherent Triplet excitation of a population of radical pairs. Assume that the hyperfine interaction is isotropic (i.e. $\alpha_{xx} = \alpha_{yy} = \alpha_{zz} = \alpha$) and an external magnetic field

**Figure 11:3-6**

Scheme of transitions induced by possible magnetic fields and hyperfine interaction components. A magnetic field $\mathbf{B} \parallel \hat{q}$ -axis and the α_{qq} component of the hyperfine interaction induce inter- $|T_0\rangle_{k \neq q}$ oscillations ($q = x, y, z$). The α_{qq} component also causes $|S\rangle \rightleftharpoons |T_0\rangle_q$ interconversion. This is a simplistic picture derived from a single nucleus radical pair model. However, the general idea remains true for higher complexity systems.

is rotating on the (xz) -plane. As should be evident from the figure, a pair starting from the Singlet state is converted to all Triplet states at the same rate, α , and the orientation of a subsequently acting magnetic field can not have any effect on the chemical destiny of the reaction. However, if the radical pair is initially in the $|T_0\rangle_z$ state, the situation looks different, as is seen in Fig.11:3-7. In this figure, the black and gray lines indicate procedures initiated at different times; black transitions start at time zero and gray transitions follow. In Fig.11:3-7a, the pair is subject to a \hat{z} -axis field. Since such a field has no immediate effect on the initial state, $|T_0\rangle_z$, as described earlier, the system begins its evolution with the hyperfine interaction converting the state into a Singlet (through the α_{zz}) and into $|T_0\rangle_x$ and $|T_0\rangle_y$ (through the α_{yy} and α_{xx} , respectively). As the $|T_0\rangle_x$ and $|T_0\rangle_y$ acquire population, the magnetic field kicks in by inducing oscillations between these two populations, while the hyperfine interaction continues to produce its own inter-Triplet oscillations and $|S\rangle \rightleftharpoons |T\rangle$ conversion. When the field is rotated to point along the \hat{x} -axis, the situation changes to that of Fig.11:3-7b. In this case, the magnetic field immediately draws population from the $|T_0\rangle_z$ state, retaining it within the Triplet manifold and inhibiting the initial $|S\rangle \rightleftharpoons |T\rangle$ conversion. It is, thus, expected that the two cases will yield products at different percentages in the Singlet and Triplet channel and, in this way, provide anisotropic, orientational dependence to an otherwise isotropic system.

Moreover, the degree to which the magnetic field suppresses the Singlet-Triplet interconversion in the $\mathbf{B} \parallel \hat{x}$ case will depend on the relative values of α_{zz} and B ; the higher the field, the stronger it couples the $|T_0\rangle_z$ with the $|T_0\rangle_y$, the

weaker the $|S\rangle \rightleftharpoons |T\rangle$ conversion. The opposite is true in the $\mathbf{B} \parallel \hat{z}$ case, where a strong magnetic field actually facilitates conversion to Singlet, by Zeeman-splitting the $|T_{\pm}\rangle_z$ states so far apart, that no other recourse is left to the pair.

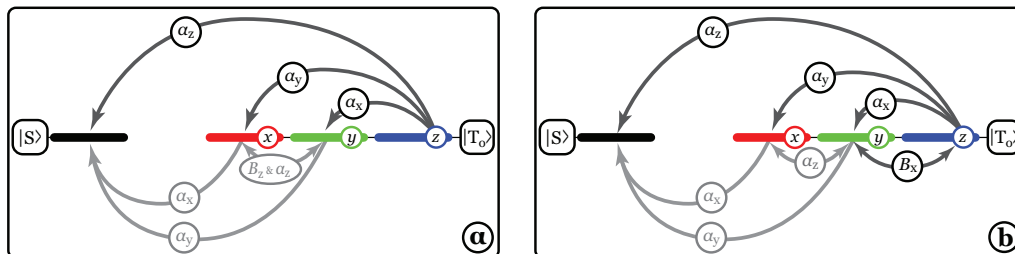


Figure 11:3-7

A pair starting in $|T_0\rangle_z$

In Fig.11:3-8a the angular dependence of the Triplet yield is shown, following the qualitative description above. It is seen that the yield is higher in the $\mathbf{B} \parallel \hat{x}$ and lower in the $\mathbf{B} \parallel \hat{z}$ case, due to the immediate - or not - involvement of the magnetic field. An increasing magnetic field magnifies this yield difference, by both raising the \hat{x} -yield and lowering the \hat{z} -yield, as expected. The resulting angular precision of the pair reaction, as defined in Eq.(11:2.38), is shown in Fig.11:3-8b. For fields on the order of tens of Gauss, the angular sensitivity achieves spectacular values, but is also quite acceptable for fields on the geo-magnetic field order. Remember that this is an isotropic medium, which is not naturally fit for this type of operation. The necessary anisotropy for angular variation is stemming purely from the Triplet nature of the initial state.

To see how spin-spin interactions may affect radical pair reactions, spin exchange is switched on in Fig.11:3-8c. The same angular dependence plot as in Fig.11:3-8a is given for various values of the spin exchange parameter, J , for specific values of the magnetic field, hyperfine interaction couplings and recombination rates (see figure for details). Evidently, the spin exchange interaction acts to level out angular variations in yield production produced by magnetic fields along different axes, while also suppressing Singlet-Triplet interconversion, altogether. This leads to deterioration of the angular precision of the reaction, as is seen in Fig.11:3-8d [blue line]. Qualitatively, the same impact on the workings of the system is expected from the dipolar interaction or the various incoherent spin relaxation mechanisms. This is indeed the case, but we refrain from reproducing more-of-the-same figures as they would seem redundant.

So far, all features described are also reproduced by the PME. However, the red line in the same figure shows the merits of working in the Zeno regime, predicted by the QMME: by changing the recombination rate values so that $k_S \gg k_T$, while preserving all other parameters, the reaction becomes robust to spin-spin interactions, maintaining excellent values of angular precision for a wide

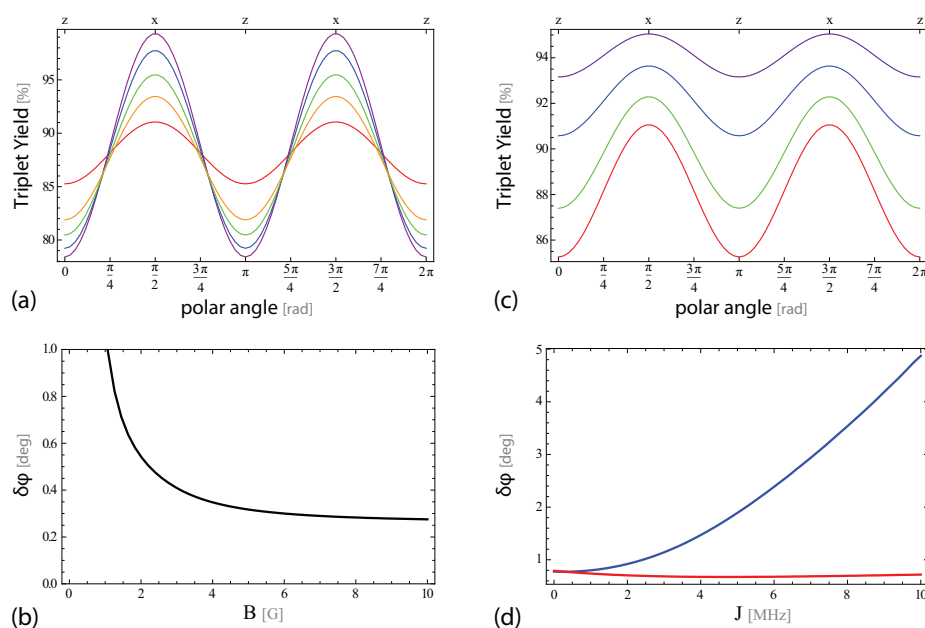


Figure II:3-8

- (a) Angular variation of yield for increasing field (red to violet: $B=1$ to 10G)
 (b) Angular precision, $\delta\varphi$, versus magnetic field.
 (c) Influence of spin exchange (red to violet: $J=1$ to 10MHz)
 (d) Angular precision for $B = 1\text{G}$ and for $k_S = k_T = 1\text{MHz}$ [blue / traditional regime] and $k_S = 5\text{MHz}$, $k_T = 0.5\text{MHz}$ [red / quantum Zeno regime]
 Parameters: $\alpha_{xx} = \alpha_{yy} = \alpha_{zz} = 5\text{MHz}$, $k_S = k_T = 1\text{MHz}$ [except (d)].

range of J 's. This is not true for the PME.

▷ *b:/ Sensitivity to the orientation of the field*

In this paragraph we deal with oriented spin states of the radical pair, that is states with a non-zero expectation value of both the total spin and its projection along some axis. We show that such states can provide information not only about the alignment of the field in space, but also about its orientation.

This is true in both the QMME as well as the PME. For the single nucleus model we examine, the effect appears only if all the diagonal components of the hyperfine coupling matrix, $\mathbb{A}^{(D)}$, are non-zero, albeit not necessarily equal (i.e. isotropic). Also, the recombination rates have to be non-zero, so the effect can not afford an explanation based solely on the coherent evolution of the electronic state.

We describe the situation schematically in Fig.II:3-9. At zero field, a pair starting in the $|T_+\rangle$ state is brought to a steady state by the isotropic hyperfine interaction and the decoherence induced by the recombination rates (charge recombination jumps are suppressed for now). This steady state comprises the

$|T_+\rangle$, $|T_0\rangle_z$ and $|S\rangle$ states. Switching on a weak magnetic field with its orientation either parallel or anti-parallel to the \hat{z} unit vector, perturbs the temporal evolution of the system. In the former case, conversion to $|S\rangle$ is slightly favored compared to $|T_0\rangle_z$, while the opposite is true in the latter case, although the same steady state is ultimately reached in both cases. Allowing charge recombination to occur, we see that the above described asymmetry leads to slightly different $|S\rangle$ and $|T_0\rangle_z$ time evolution curves and, since the yield is proportional to the area under these curves, slightly different yield values are obtained. And so it is that the reaction is sensitive to the orientation of the magnetic field.

An outline of the explanation of this phenomenon goes as follows: the combined action of the hyperfine interaction and recombination induced decoherence brings the system in a state which is a mixture of a $|T_+\rangle$ part and a - relatively pure - coherent superposition of $|S\rangle$ and $|T_0\rangle_z$. The amplitudes of the $|S\rangle$ and $|T_0\rangle_z$ in this superposition depend on the hyperfine couplings, the recombination rates and the Larmor frequency. Since the sign of the Larmor frequency is different for the two opposite senses of magnetic field vector orientation, the balance is slightly tilted in favor of the $|S\rangle$ amplitude in one case or of the $|T_0\rangle_z$ amplitude in the other.

II.3.3.3 Effects in anisotropic materials

In this section we assume that the hyperfine coupling is anisotropic and apply a rotating magnetic field to study the angular sensitivity of the reaction for a pair starting in one of the $|T_0\rangle$ states. We compare the two theories proposed in Ch.II:2, the PME and the QMME, for recombination rates in the two distinct regions already mentioned: in the *traditional* regime ($k_S = k_T$) and the *quantum Zeno* regime ($k_S \gg k_T$).

We start with a pair in the $|T_0\rangle_y$ state, in a system with an axial \hat{z} -anisotropy ($\alpha_{xx} = \alpha_{yy} = 0$, $\alpha_{zz} \neq 0$) and a magnetic field revolving about the \hat{y} -axis. Following the logic of Fig.II:3-6 and II:3-7, we can see why this reaction is sensitive to the orientation of the magnetic field. Indeed, in Fig.II:3-10 we can see that conversion from the Triplet manifold to the Singlet state can only occur through state $|T_0\rangle_z$. However, when the magnetic field is along \hat{z} -axis, this state is never populated and the pair remains trapped in the Triplet yielding 100% products in the Triplet channel. When the field is rotated, $|T_0\rangle_z$ state is populated and conversion to Singlet commences leading to a non-zero Singlet yield. Thus, this reaction is clearly sensitive to the direction of the field.

The same is, of course, true for a pair starting in the Singlet state, which is the setup of the reaction traditionally studied in the context of the radical pair based compass. By following the arrows "backward" in Fig.II:3-10 we see that the Singlet state is converted to $|T_0\rangle_z$. If the field is along \hat{z} , the converted population remains in $|T_0\rangle_z$ until it jumps back to the Singlet. If the field is along \hat{x} , some

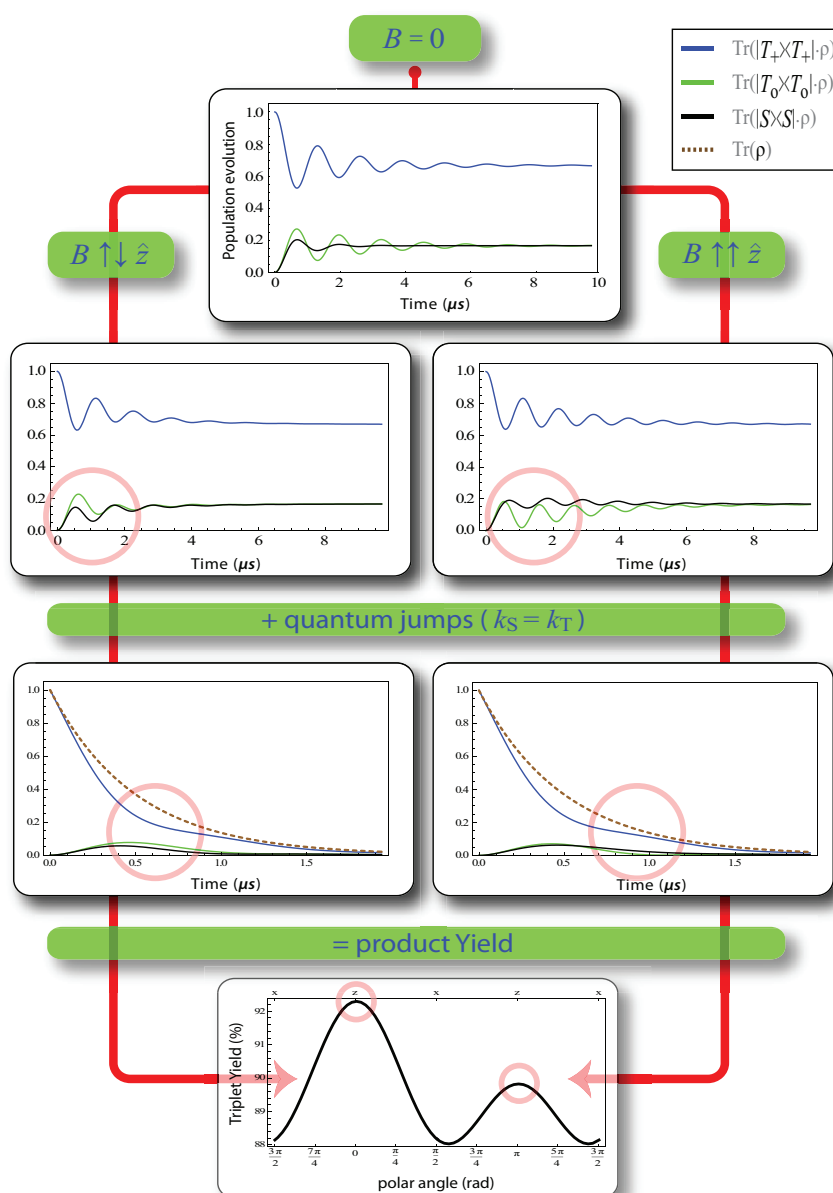
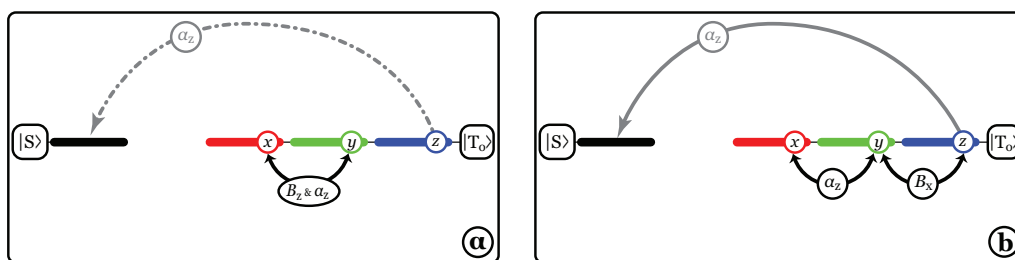


Figure II-3-9

Oriented $|T_+\rangle$ initial state in isotropic medium. In the absence of a magnetic field, the total population oscillates between the $|T_+\rangle$ and the $|T_0\rangle$ and $|S\rangle$ states, and tends to steady state due to decoherence induced by the k_S and k_T rates (actual recombination is turned off). Turning on the $\mathbf{B} \uparrow\uparrow \hat{z}$ field, mainly suppresses the conversion to $|T_0\rangle$, while the $\mathbf{B} \uparrow\downarrow \hat{z}$ field suppresses conversion to $|S\rangle$. Allowing the pairs to recombine and calculating the yields, the sensitivity of this radical pair reaction to the orientation of the magnetic field becomes evident.

(The red circles are just visual aids)

**Figure II:3-10**

Transition scheme for a $|T_0\rangle_y$ state experiencing a \hat{z} -anisotropic hyperfine coupling and a magnetic field on the (xz) -plane. When the field is along \hat{z} -axis, the $|T_0\rangle_z$, and thus $|S\rangle$, state is never populated, and the Triplet yield is 100%. When the field is along the \hat{x} -axis, $|T_0\rangle_z$ acquires population and so does $|S\rangle$. The Triplet yield is now below 100% and the reaction shows angular sensitivity

of the $|T_0\rangle_z$ population is converted into $|T_0\rangle_y$, leaving less population available to make the transition back to the Singlet. Thus, in the latter case the Singlet yield will be smaller than in the former case and the reaction will be directionally sensitive. The great difference between this case and the previous one, is that in this case there is no possible combination of hyperfine couplings/magnetic field direction capable of yielding 100% products in one channel, whereas in the previous case there is. The ability of a certain configuration to trap all population in a single channel gives the incentive to search for ways to maximally deplete this channel in the perpendicular direction of the field, so as to maximize the angular sensitivity.

The above discussion is also valid for the PME, and the angular dependence of the Triplet yield is plotted for both theories and for a $|S\rangle$ or $|T_0\rangle_y$ initial state in Fig. II:3-11. In the left column the plots are in the traditional regime of parameters, $k_S = k_T$, and in the right column in the quantum Zeno regime, $k_S \ll k_T$ for a pair starting in the Singlet or $k_S \gg k_T$ for a pair starting in the Triplet. The results are spectacular. In the traditional regime, both theories predict roughly the same behavior. Also, in the Zeno regime and with the pair starting in the Singlet state, the two theories, although deviating qualitatively, predict that angular sensitivity is suppressed^{||}. However, in the case of a pair starting in a coherent Triplet state, namely in $|T_0\rangle_y$ here, the PME and the QMME deviate widely, with the QMME predicting Triplet yield variations on the order of $\sim 50\%$, corresponding to an angular precision of $\sim 0.1^\circ$; some ten times lower than that predicted by the PME.

^{||}The phase change in the PME case can be explained by a detailed account of the way decoherence due to the recombination rates is affecting the $|S\rangle \rightleftharpoons |T\rangle$ interconversion, but this is a quite elaborate procedure and out of the scope of this work.

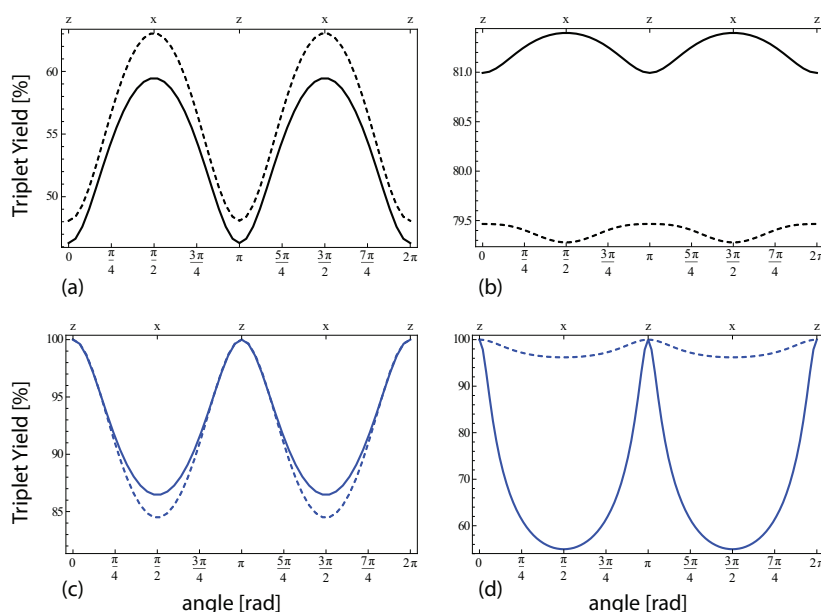


Figure II-3-11

Angular sensitivity of triplet yield for a \hat{z} -anisotropic hyperfine coupling. In (a) and (b) the radical-ion pair starts out in the singlet state, whereas in (c) and (d) the initial state is the triplet cat state, $|T_0\rangle_y$. Left column (a and c) is the traditional $k_S = k_T$ regime with $k_S = k_T = 0.5\text{MHz}$, whereas the right column is the quantum Zeno regime with asymmetric recombination rates. In (b) $k_S = 0.3\text{MHz}$, $k_T = 3\text{MHz}$ and for (d) $k_S = 35\text{MHz}$, $k_T = 0.5\text{MHz}$. Solid (dashed) lines are the results following from the quantum-measurement (phenomenological) theory. For all plots the hyperfine coupling was $\alpha_{zz} = 10\text{MHz}$ and the magnetic field $B = 0.5\text{G}$.

▷ a:/ *Explanation of the effect*

Toward explaining the effect we first note that, in the QMME, the lifetime of a pair starting in the Triplet and having a Singlet recombination rate comparable to or larger than the Triplet recombination rate, will roughly be equal to $\frac{1}{k_S} + \frac{1}{k_T}$. So, regardless of how much the k_S rate is increased, the lifetime of the pair will never become dramatically short, as it will fall - at most - to $\sim \frac{1}{k_T}$. During this lifetime, some population will be transferred from the Triplet to the Singlet state and, perhaps, recombine from there to yield Singlet products. In the $k_S \simeq k_T$ case, the total amount of transferred population is larger, as is to be expected, but in the $k_S \gg k_T$ case the Singlet population recombines more efficiently to give neutral products. So, the question which of the two cases gives a higher Singlet yield boils down to how the reciprocal actions of population transfer versus Singlet recombination efficiency play out.

In Fig. II-3-12a we plot the evolution of the Singlet population when starting from $|T_0\rangle_z$, with $k_S = k_T$ (solid line) and $k_S = 5k_T$ (dashed line). We see that, indeed, in the former case more or less double the population is transferred to

the Singlet. In Fig.11:3-12b, however, we multiply the results by $2k_S$, so that the area under the curves is the Singlet yield. We, thus, see, that the efficiency of recombination in the latter case more than makes up for the lower population transfer and the Singlet yield is higher in the Zeno regime.

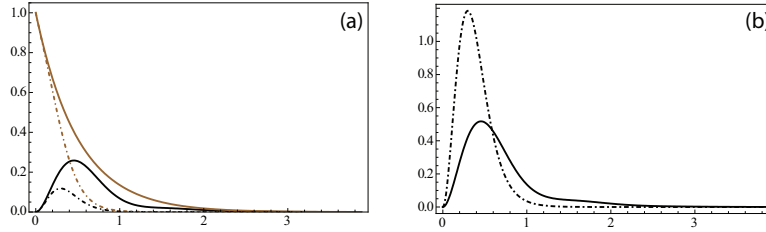


Figure 11:3-12

Starting from the $|T_o\rangle_z$ state

(a) Singlet [black] and total [brown] population evolution in the traditional [solid] and Zeno [dashed] regime of parameters.

(b) Singlet population multiplied by $2k_S$. The area under the curves is the Singlet yield. The more efficient Singlet recombination in the Zeno regime makes up for the smaller transferred population.

The situation is different in the context of the PME, where the increase of the k_S rate practically eliminates all population transfer to the Singlet state, hence the suppression of angular sensitivity observed in Fig.11:3-11d. Formally, the Singlet population time evolution when starting from $|T_o\rangle_z$ is given by:

$$\langle Q_S(t) \rangle = \frac{1}{2} \frac{\left(\frac{\alpha}{2}\right)^2}{(k_S - k_T)^2 - \left(\frac{\alpha}{2}\right)^2} \left[\cosh \left(t \sqrt{(k_S - k_T)^2 - \left(\frac{\alpha}{2}\right)^2} \right) - 1 \right] e^{-(k_S + k_T)t} \quad (11:3.5)$$

where we have set $B = 0G^{**}$. From Eq.(11:3.5) it follows that for any finite values of the other parameters, $\langle Q_S \rangle \rightarrow 0$ as $k_S \rightarrow \infty$. Physically this corresponds to a situation where, starting from a Triplet state, the decoherence due to a high Singlet recombination rate instantly diminishes the coherence between $|T_o\rangle_z$ and $|S\rangle$ created by the hyperfine interaction, before it has the time to be transformed into a real Singlet population. So, deep in the Zeno regime, the system is trapped in the triplet subspace where it evolves and from where it recombines at the triplet recombination rate, k_T . For comparison, in the QMME, for a pair starting, as assumed, in a $|T_o\rangle_y$ state, when the magnetic field is along \hat{x} , some population is transferred to the $|T_o\rangle_z$. If the field is small enough, the conversion from $|T_o\rangle_z$ to $|S\rangle$ is approximately described by Eq.(11:3.3). Clearly, the limiting value of Singlet population for $k_S \rightarrow \infty$ is $\frac{1}{2}$, implying complete delocalization of the electronic

**This is fine since the magnetic field affects singlet population insofar as it converts other Triplet components to $|t_o\rangle_z$, which can then be converted to Singlet through the hyperfine interaction.

pair state in the strong measurement regime, a peculiar, but nonetheless expected, result for strong continuous quantum measurement schemes [Gur97].

The angular precision for the two theories is plotted in Fig.II:3-13 versus the recombination rates. We see that for a pair starting in the Singlet state, the PME fares better than the QMME as k_T is increased. However, for a pair starting in a coherent Triplet state, the state delocalization induced by the strong measurement of the Singlet state produces the above described effect, which leads to exquisite values of angular precision in the context of the QMME.

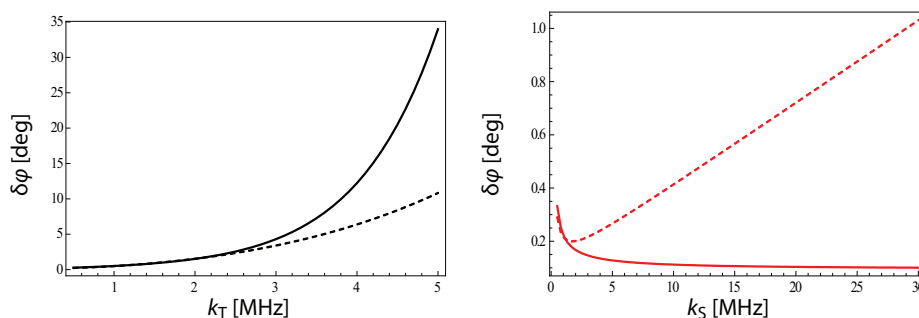


Figure II:3-13

Avian compass heading error for a \hat{z} -anisotropic hyperfine coupling. For both plots $\alpha_{zz} = 10$ MHz and $B = 0.5$ G. (a) Heading error as a function of k_T with a Singlet initial state and $k_S = 0.5$ MHz. (b) Heading error as a function of k_S for a $|T_0\rangle_y$ initial state and $k_T = 0.5$ MHz. Solid (dashed) lines for the quantum-measurement (phenomenological) theory.

▷ *b:/ Influence of real-life effects*

In a real-life radical pair, a number of factors or processes might affect the above described effect. Here we account for some of such processes by evaluating their impact on the angular precision of the reaction.

We start by including a non-zero spin exchange interaction or a non-zero spin relaxation rate, as described in the previous chapter. In Fig.II:3-14 we see their impact on the angular sensitivity of the reaction. From the figure it is seen that in the case of the QMME, the reaction is all but immune to spin exchange; the same can not be said for the PME. This is due to the delocalization of the electronic state induced by the strong, continuous interrogation of the Singlet recombination channel. On the other hand, spin relaxation produces rapid deterioration of the angular sensitivity in both theories, since it acts to suppress any coherences created between the two manifolds of states.

The most severe penalty to angular sensitivity, at least in the QMME theory, comes from the possibility that the hyperfine coupling tensor is non axial (i.e. $\alpha_{xx}, \alpha_{yy} \neq 0$) or that the nuclei at the second site of the pair exert a differently aligned hyperfine interaction to the local electron (i.e. if we have set $\alpha_{zz}^{(D)} \neq 0$ so

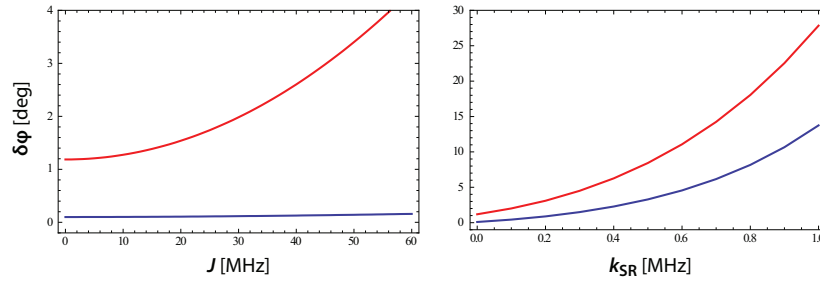


Figure II:3-14

Impact of spin exchange (left) and spin relaxation (right) on angular precision, for the QMME [blue] and the PME [red]. We see that the QMME theory predicts immunity to spin exchange, while spin relaxation rapidly deteriorates the angular sensitivity in both cases. The rest of the parameters are as in Fig.II:3-11d.

far, we now allow a $\alpha_{yy}^{(A)} \neq 0$, as well). The situation is graphically depicted in Fig.II:3-15. The deterioration of the angular sensitivity here has its roots in the fact that the state of the system is no longer trapped in the Triplet manifold in the $\mathbf{B} \parallel \hat{z}$ case. Indeed, for a system with only a \hat{z} -anisotropy, a magnetic field along the same axis could not transform the initial $|T_o\rangle_y$ state into a $|T_o\rangle_z$ so that it could convert to a Singlet. Now, though, the \hat{y} -anisotropy can directly cause the state to convert into a Singlet, while the magnetic field and the \hat{x} and \hat{z} parts of the hyperfine coupling transform the state into $|T_o\rangle_x$ and $|T_o\rangle_z$, from where it can also convert to Singlet.

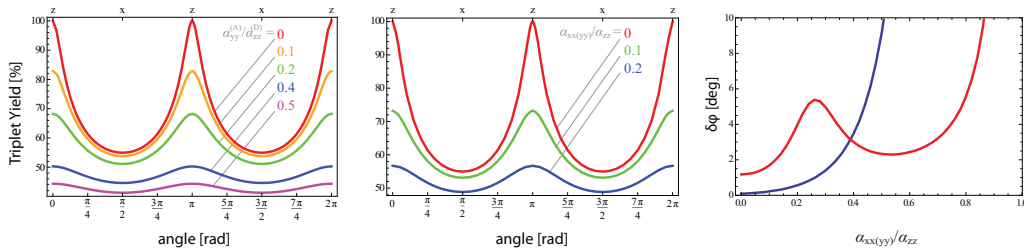


Figure II:3-15

Top and middle: Impact of a second, differently oriented [top] or non-axial, single-site [mid] hyperfine interaction on the angular variation of the Triplet yield. Bottom: Angular precision versus $\alpha_{xx(yy)}/\alpha_{zz}$ ratio for the QMME [blue] and the PME [red].

As is evident in the figure, the impact of this mechanism is greater in the QMME and has to do with the quality that gave it great sensitivity in the \hat{z} -only anisotropy case, namely its ability to yield Singlet products even for $k_S \gg k_T$. Now, the inclusion of small, non-zero hyperfine components along the other two axes rapidly leads to a flat angular variation of the yield, thus diminishing the ability of the reaction to determine the alignment of the field. In the PME on the

other hand, the $k_S \gg k_T$ condition suppresses Triplet to Singlet conversion from *all* Triplet states, thus allowing the magnetic field to play a more significant role in the outcome of the reaction.



Radical ion pairs are formed predominantly in a Singlet spin state. However, it is conceivable that the creation process could be manipulated toward the creation of coherent Triplet pairs. We studied how this would influence the response of the pairs to external magnetic fields, both in the context of the widely employed phenomenological theory (PME), as well as in the recently introduced quantum measurement theory (QMME). We found that a coherent Triplet state can provide sensitivity to the alignment, but also to the orientation of an external field, even in a pair which bears an isotropic hyperfine interaction. This, of course, is not possible in the case of Singlet (i.e. isotropic) excitation of the pair. More than that, under the influence of real life effects, such as spin exchange and dipolar interactions, the QMME shows great robustness, with the RIPs studied under this theory maintaining excellent angular precision characteristics, despite decoherence. Finally, the case of coherently exciting pairs in anisotropic media was studied, where sensitivity to the alignment of the field was found to exist for both the PME and the QMME. Again, however, the QMME theory predicted angular precisions well beyond the expected from the PME. It is to be noted here, though, that the debate on which theory correctly describes RIP reactions, is still open in the community and has stirred much controversy. As in all things scientific, time will tell.

Bibliography @ Quantum Biology

- [BCR82] SG Boxer, CED Chidsey, and MG Roelofs, *Use of large magnetic fields to probe photoinduced electron-transfer reactions: An example from photosynthetic reaction centers*, J Am Chem Soc **104** (1982), 1452–1454.
- [BKMS93] SN Batchelor, CWM Kay, KA McLauchlan, and IA Shkrob, *Time-resolved and modulation methods in the study of the effects of magnetic fields on the yields of free-radical reactions*, J Phys Chem **97** (1993), 13250.
- [BM96] B Brocklehurst and KA McLauchlan, *Free radical mechanism for the effects of environmental electromagnetic fields on biological systems*, Int J Radiat Biol **69** (1996), no. 1, 3–24.
- [Bro76] B Brocklehurst, *Spin correlation in the geminate recombination of radical ions in hydrocarbons. part 1.theory of the magnetic field effect*, J Chem Soc Faraday Trans II **72** (1976), 1869.
- [Bro02] ———, *Magnetic fields and radical reactions: Recent developments and their role in nature*, Chem Soc Rev **31** (2002), 301–311.
- [BSP77] RE Blankenship, TJ Schaafsma, and WW Pason, *Magnetic field effects on radical pair intermediates in bacterial photosynthesis*, Biochim. Biophys. Acta **461** (1977), 297–305.
- [CBDS94] JM Canfield, RL Belford, PG Debrunner, and KJ Schulten, *A perturbative theory treatment of oscillating magnetic fields in the radical pair mechanism*, Chem Phys **182** (1994), 1–18.
- [CBDS95] ———, *A perturbative treatment of oscillating magnetic fields in the radical pair mechanism using the liouville eq*, Chem Phys **195** (1995), 59–69.
- [CRB80] CED Chidsey, MG Roelofs, and SG Boxer, *The effect of large magnetic fields and the g-factor difference on the triplet population in photosynthetic reaction centers*, Chem Phys Lett **74** (1980), no. 1, 113.
- [CWW⁺10] E Collini, CY Wong, KE Wilk, PMG Curmi, P Brumer, and GD Scholes, *Coherently wired light-harvesting in photosynthetic marine algae at ambient temperature*, Nature **463** (2010), doi:10.1038/nature08811.

- [DK09] AT Dellis and IK Kominiis, *Quantum measurement theory explains the deuteration effect in radical ion pair reactions*, arXiv-0906.5254 (2009).
- [ECR⁺07] GS Engel, TR Calhoun, EL Read, TK Ahn, T Mancal, YC Cheng, RE Blankenship, and GR Fleming, *Evidence for wavelike energy transfer through quantum coherence in photosynthetic complexes*, *Nature* **446** (2007), no. 782-786.
- [EH08] O Efimova and PJ Hore, *Role of exchange and dipolar interactions in the radical pair model of the avian magnetic compass*, *Biophysical Journal* **94** (2008), 1565–74.
- [EH09] ———, *Evaluation of nuclear quadrupole interactions as a source of magnetic anisotropy in the radical pair model of the avian magnetic compass*, *Molecular Physics* **107** (2009), no. 7, 665.
- [GCWR08] RJ Gegear, A Casselman, S Waddell, and SM Reppert, *Cryptochrome mediates light-dependent magnetosensitivity in drosophila*, *Nature* **454** (2008), 1014–1018.
- [Gur97] SA Gurvitz, *Measurements with a noninvasive detector and dephasing mechanism*, *Phys Rev B* **56** (1997), 15215.
- [Hab76] R Haberkorn, *Density matrix description of spin-selective radical pair reactions*, *Molecular Physics* **32** (1976), no. 5, 1491–93.
- [HHMS88] CA Hamilton, JP Hewitt, KA McLauchlan, and UE Steiner, *High resolution studies of the effects of magnetic fields on chemical reactions*, *Mol Phys* **65** (1988), 423–438.
- [HMB79] R Haberkorn and ME Michel-Beyerle, *On the mechanism of magnetic field effects in bacterial photosynthesis*, *Biophys. J.* **26** (1979), no. 3, 489–498.
- [HMP89] CA Hamilton, KA McLauchlan, and KR Peterson, *J-resonances in many and rydmr spectra from freely diffusing radical ion pairs*, *Chem Phys Lett* **162** (1989), 145.
- [HRGD77] AJ Hoff, H Rademaker, R Van Grondelle, and LNM Duysens, *On the magnetic field dependence of the yield of the triplet state in reaction centers of photosynthetic bacteria*, *Biochim. Biophys. Acta* **460** (1977), 547–554.
- [Kom09a] IK Kominiis, *Is the quantum zeno effect evolutions choice for the avian compass?*, arXiv-0908.0763v3 (2009).
- [Kom09b] ———, *Quantum zeno effect explains magnetic-sensitive radical ion pair reactions*, *Phys Rev E* **80** (2009), 056115.
- [Kom10] ———, *The jones-hore theory of radical-ion-pair reactions violates the first and second law of thermodynamics*, arXiv-1003.1442v2 (2010).
- [LCF07] H Lee, YC Cheng, and GR Fleming, *Coherence dynamics in photosynthesis: Protein protection of excitonic coherence*, *Science* **316** (2007), 1462.

- [MHC⁺08] K Maeda, KB Henbest, F Cintolesi, I Kuprov, CT Rodgers, PA Liddell, D Gust, CR Timmel, and PJ Hore, *Chemical compass model of avian magnetoreception*, *Nature* **453** (2008), 387.
- [MJBL⁺04] H Mouritsen, U Janssen-Bienhold, M Liedvogel, G Feenders, J Stalleicken, and R Weiler, *Cryptochromes and neuronal-activity markers colocalize in the retina of migratory birds during magnetic orientation*, *PNAS* **101** (2004), no. 39, 1429499.
- [MSWS04] A Moller, S Sagasser, W Wiltschko, and B Schierwater, *Retinal cryptochrome in a migratory passerine bird: A possible transducer for the avian magnetic compass*, *Naturwissenschaften* **91** (2004), 585588.
- [OCG⁺05] A O’Dea, AF Curtis, NJB Green, CR Timmel, and PJ Hore, *Influence of dipolar interactions on radical pair recombination reactions subject to weak magnetic fields*, *J Phys Chem* **109** (2005), 869–873.
- [RAS00] T Ritz, S Adem, and K Schulten, *A model for photoreceptor-based magnetoreception in birds*, *Biophysical Journal* **78** (2000), 707–718.
- [RCB82] MG Roelofs, CED Chidsley, and SG Boxer, *Contributions of spin-spin interactions to the magnetic field dependence of the triplet quantum yield in photosynthetic reaction centers*, *Chem Phys Lett* **87** (1982), no. 6, 582.
- [RH09] CT Rodgers and PJ Hore, *Chemical magnetoreception in birds: The radical pair mechanism*, *PNAS* **106** (2009), no. 2, 353–360.
- [RNH⁺07a] CT Rodgers, SA Norman, KB Henbest, CR Timmel, and PJ Hore, *Determination of radical re-encounter probability distributions from magnetic field effects on reaction yields*, *J. Am. Chem. Soc.* **129** (2007), 6746.
- [RNH⁺07b] ———, *Determination of radical re-encounter probability distributions from magnetic field effects on reaction yields*, Oxford University publication (2007).
- [Rod09] CT Rodgers, *Magnetic field effects in chemical systems*, *Pure Appl Chem* **81** (2009), no. 1, 19–43.
- [RTP⁺04] T Ritz, P Thalau, JB Phillips, R Wiltschko, and W Wiltschko, *Resonance effects indicate a radical-pair mechanism for avian magnetic compass*, *Nature* **429** (2004), 177–180.
- [Sch82] K Schulten, *Magnetic fields effects in chemistry and biology*, *Adv Solid State Phys* **22** (1982), 61–83.
- [SCS07] IA Solov’yov, DE Chandler, and K Schulten, *magnetic field effects in *arabidopsis thaliana* cryptochrome-1*, *Biophysical Journal* **92** (2007), 2711–2726.
- [SIFW10] M Sarovar, A Ishizaki, GR Fleming, and BK Whaley, *Quantum entanglement in photosynthetic light-harvesting complexes*, *Nature*, online publication, doi:10.1038/nphys1652, 2010.

- [SLTM95] DV Stass, NN Lukzen, BM Tadjikov, and YN Molin, *Manifestation of quantum coherence upon recombination of radical ion pairs in weak magnetic fields*, Chem Phys Lett **233** (1995), 444–450.
- [Sob06] I Sobelman, *Theory of atomic spectra*, Alpha Science, 2006.
- [SSW⁺76] K Schulten, H Staerk, A Weller, HI Werner, and B Nickel, *Magnetic field dependence of the geminate recombination of radical ion pairs in polar solvents*, Z Phys Chem Neue Folge **101** (1976), 371–390.
- [STB91] IA Shkrob, VF Tarasov, and AL Buchachenko, *Electron spin exchange in micellized radical pairs. ii. magnetic field and magnetic isotope effects in multinuclear pairs*, Chem Phys **153** (1991), 443–455.
- [SU89] UE Steiner and T Ulrich, *Magnetic field effects in chemical kinetics and related phenomena*, Chem Rev **89** (1989), no. 1, 51–147.
- [SW78] K Schulten and PG Wolynes, *Semi-classical description of electron spin motion in radicals including the effect of electron hopping*, J Chem Phys **68** (1978), no. 7, 3292.
- [SW86] K Schulten and A Windemuth, *Model for a physiological magnetic compass*, Biophysical effects of steady magnetic fields (G Maret, N Boccara, and J Kiepenheuer, eds.), Springer, 1986, pp. 99–106.
- [TCBH01] CR Timmel, F Cintolesi, B Brocklehurst, and PJ Hore, *Model calculations of magnetic field effects on the recombination reaction of radicals with anisotropic hyperfine interaction*, Chem Phys Lett **334** (2001), 387.
- [TH04] CR Timmel and KB Henbest, *A study of spin chemistry in weak magnetic fields*, Phil Trans R Soc Lond A **362** (2004), 2753–2589.
- [TN82] J Tang and JR Norris, *Calculations of radical pair kinetics*, Chem Phys Lett **92** (1982), 136.
- [TTB⁺98] CR Timmel, U Till, B Brocklehurst, KA McLauchlan, and PJ Hore, *Effects of weak magnetic fields on free radical recombination reactions*, Molecular Phys **95** (1998), no. 1, 71–89.
- [WMG⁺04] W Wiltschko, A Moller, M Gesson, C Noll, and R Wiltschko, *Light-dependent magnetoreception in birds analysis of the behaviour under red light after pre-exposure to red light*, J Exp Biol **207** (2004), 1193–1202.
- [WSW78] HJ Weller, H Staerk, and A Weller, *Solvent isotope and magnetic field effects in the geminate recombination of radical ion pairs*, J Chem Phys **68** (1978), no. 5, 2419.
- [WW01] W Wiltschko and R Wiltschko, *Light-dependent magnetoreception in birds: the behavior of european robins, erithacus rubecula, under monochromatic light of various wavelengths*, J Exp Biol **204** (2001), 3295–3302.
- [WW07] ———, *Magnetoreception in birds: Two receptors for two different tasks*, J Ornithol **148** (2007), S61–S76.

- [Zee97] P Zeeman, *The effect of magnetisation on the nature of light emitted by a substance*, *Nature* **55** (1897), 347.

Appendices

Appendix A

Table of alkali constants & D1 and D2 transitions

In the following table, a range of alkali metal related parameters are assembled from [Geh03, WMZJ92, Tie10, MB98, Ste09, AIV77, SvOP80] for principal properties, as well as from [Hap72, CW69, WC94] for the collisional characteristics.

Table A#1: Alkali metals properties and parameters

	Lithium, Li	Sodium, Na	Potassium, K	Rubidium, Rb	Cesium, Cs
--	--------------------	-------------------	---------------------	---------------------	-------------------

General properties

Z	3	11	19	37	55
n (shells)	2	3	4	5	6
Isotopes	⁶ Li [7.5%] ⁷ Li [92.5%]	²³ Na [100%]	³⁹ K [93.3%] ⁴¹ K [6.7%]	⁸⁵ Rb [72.2%] ⁸⁷ Rb [27.8%]	¹³³ Cs [100%]
Nuclear Spin, I	⁶ Li: 1 ⁷ Li: 3/2	3/2	³⁹ K: 3/2 ⁴¹ K: 3/2	⁸⁵ Rb: 5/2 ⁸⁷ Rb: 3/2	7/2

Values below from: http://www.rsc.org/chemsoc/visualelements/pages/data/intro_groupi_data.html

Density [kg/m ³]	534	971	862	1532	1873
Atomic radius [Å]	1.52	1.85	2.27	2.47	2.65
Melting point [°K]	453.7	371	336.8	312.2	301.6
Ionization energy [kJ/mol]	513.3	495.8	418.8	403	375.7

Saturated vapor density parameters for the Killian formula 1:2.1

A	5.717	5.298	4.961	4.857	4.711
B (°K)	-8387	-4646	-4964	-4215	-3999

Continued on next page...

...continued from previous page

	Lithium, Li	Sodium, Na	Potassium, K	Rubidium, Rb	Cesium, Cs
--	--------------------	-------------------	---------------------	---------------------	-------------------

D1 transition: $n^2S_{1/2} \rightarrow n^2P_{1/2}$

λ_{vacuum} [nm]	⁶ Li: 670.992 ⁷ Li: 670.976	589.756	³⁹ K: 770.1084 ⁴¹ K: 770.1079	⁸⁵ Rb: 794.9790 ⁸⁷ Rb: 794.7988	894.593
τ [ns]	27.102	16.299	26.37	27.679	34.791
f^*	0.249056	0.3199	0.33715	0.34231	0.3449
α_0 [a.u.] [†] : $n^2S_{1/2} \triangleright$	163.9	162.6	290.2	319.0	400.8
$n^2P_{1/2} \triangleright$	126.8	360.6	697.4	810.4	1371.1
$\langle J = 1/2 er J' = 1/2 \rangle$	2.3465 ea_o [‡]	2.4923 ea_o	2.925 ea_o	2.9931 ea_o	3.1869 ea_o

D2 transition: $n^2S_{1/2} \rightarrow n^2P_{3/2}$

λ_{vacuum} [nm]	⁶ Li: 670.978 ⁷ Li: 670.951	589.158	³⁹ K: 766.7009 ⁴¹ K: 766.7004	⁸⁵ Rb: 780.24137 ⁸⁷ Rb: 780.24121	852.347
τ [ns]	27.102	16.249	26.37	26.2348	30.405
f	0.498088	0.64	0.66834	0.69577	0.7164
α_0 [a.u.]: $n^2S_{1/2} \triangleright$	163.9	162.6	290.2	319.0	400.8
$n^2P_{3/2} \triangleright$	127.1	363.5	697.4	857.4	1640.7
α_2 [a.u.] [§] : $n^2P_{3/2} \triangleright$	1.631	-88.268	-158.8	-163.1	-262.3
$\langle J = 1/2 er J' = 3/2 \rangle$	3.3183 ea_o	3.5246 ea_o	4.1092 ea_o	4.2275 ea_o	4.4837 ea_o

Hyperfine structure

Magnetic Dipole, A_{hf}/h [MHz]

$n^2S_{1/2} \triangleright$	⁶ Li: 152.137 ⁷ Li: 401.752	885.813	³⁹ K: 230.8699 ⁴¹ K: 127.0069	⁸⁵ Rb: 1011.911 ⁸⁷ Rb: 3417.341	2298.158
$n^2P_{1/2} \triangleright$	⁶ Li: 17.386 ⁷ Li: 45.914	94.44	³⁹ K: 27.775 ⁴¹ K: 15.245	⁸⁵ Rb: 120.527 ⁸⁷ Rb: 407.24	291.9201
$n^2P_{3/2} \triangleright$	⁶ Li: -1.155 ⁷ Li: -3.055	18.534	³⁹ K: 6.093 ⁴¹ K: 3.363	⁸⁵ Rb: 25.002 ⁸⁷ Rb: 84.7185	50.2883

Electric Quadrupole, B_{hf}/h [MHz]

$n^2P_{3/2} \triangleright$	⁶ Li: -0.01 ⁷ Li: -0.221	2.724	³⁹ K: 2.786 ⁴¹ K: 3.351	⁸⁵ Rb: 25.790 ⁸⁷ Rb: 12.4965	0.560
-----------------------------	---	-------	--	---	-------

Ground state slowing down factor, q

[see Eq.(t.1.93)]

q	⁶ Li: 3/11 ⁷ Li: 1/6	1/6	1/6	⁸⁵ Rb: 3/38 ⁸⁷ Rb: 1/6	1/22
-----	---	-----	-----	---	------

Continued on next page...

* Absorption oscillator strength, derived from $\Gamma = \frac{e^2 \omega_o^2}{2\pi \epsilon_o m_e c^3} \frac{2J+1}{2J'+1} f$.† Scalar polarizability. 1 a.u. = $0.2489 \times 10^{-3} \text{Hz}/(\text{V}/\text{cm})^2$ [$\hbar=1$] = $1.6492 \times 10^{-41} \text{Cm}^2/\text{V}$ [S.I.]‡ This is the reduced electric dipole matrix element in units of ea_o , where $e \simeq 1.602 \times 10^{-19} \text{C}$ is the electron charge and $a_o \simeq 0.529 \text{\AA}$ is the Bohr radius. Its value is not identically the same for the various isotopes of an element, but it is close (at least to the precision depth shown).§ Tensor polarizability; vanishes for $J = 1/2$.

...continued from previous page

	Lithium, Li	Sodium, Na	Potassium, K	Rubidium, Rb	Cesium, Cs
--	--------------------	-------------------	---------------------	---------------------	-------------------

Spin Exchange cross sections [¶]		Collisional parameters				[units: 10^{-14}cm^2]
Lithium, Li	~ 1 (theory)	N/A	N/A	N/A	N/A	N/A
Sodium, Na		1.10 ± 0.15	N/A	N/A	N/A	N/A
Potassium, K			1.7 ± 0.7	~ 2	N/A	N/A
Rubidium, Rb				2.1 ± 0.5	2.1 ± 0.4	2.1 ± 0.4
Cesium, Cs					2.2 ± 0.4	2.2 ± 0.4

Spin Destruction cross sections		[approximate, rounded values / where available][units: cm^2]			
Self [$\times 10^{-18}$]	N/A	0.5	1	9	200
Helium, He [$\times 10^{-25}$]	N/A	0.2	8	3 - 90	30 - 300
Neon, Ne [$\times 10^{-23}$]	N/A	0.2	1	5	0.5 - 9
Argon, Ar [$\times 10^{-23}$]	N/A	9	N/A	10 - 40	3 - 100
Krypton, Kr [$\times 10^{-21}$]	N/A	2	N/A	6 - 25	2
Xenon, Xe [$\times 10^{-20}$]	N/A	2.5	N/A	1 - 10	5
N₂ [$\times 10^{-23}$]	N/A	0.4	N/A	10	5 - 60

[¶]Averaged values from various experimental and theoretical sources. To be treated with caution as they are also mildly temperature dependent. Values here refer to temperatures in the range of 300 to 700°K

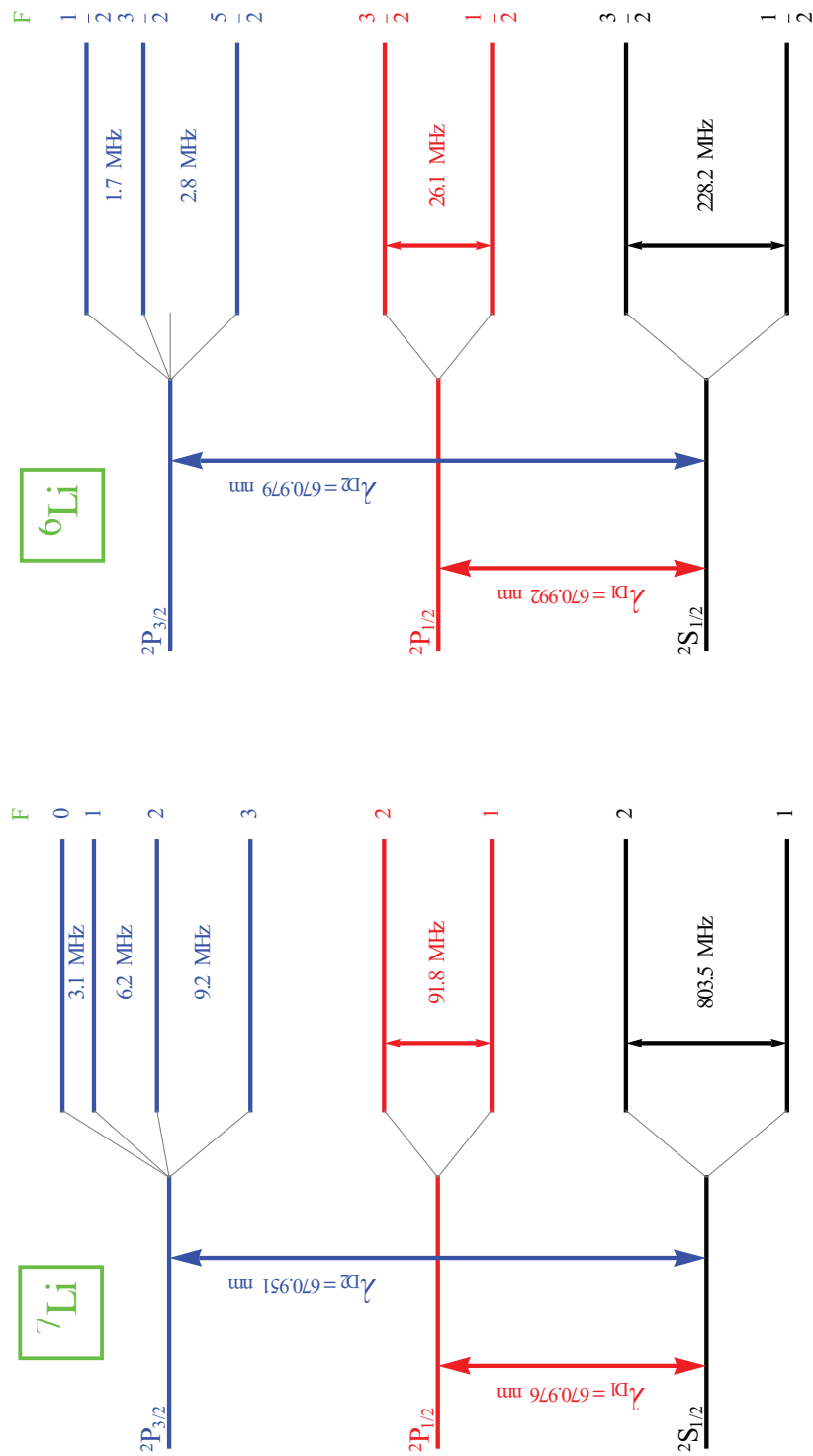


Figure A-1

Li D1 and D2 transitions

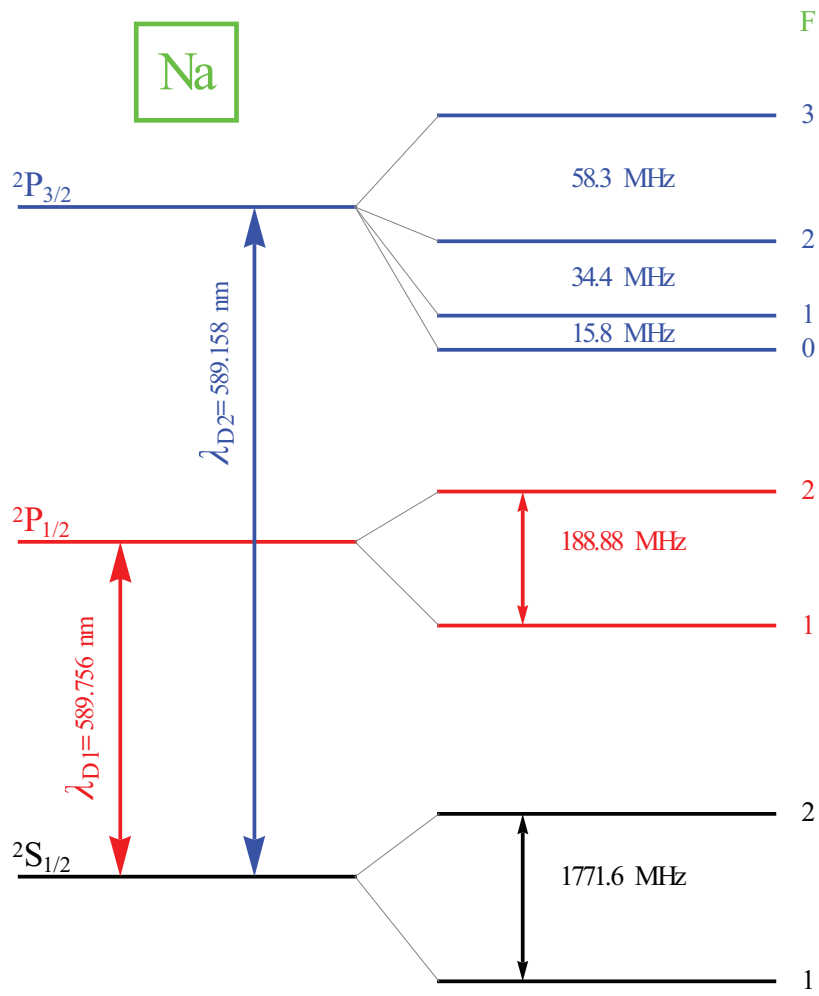


Figure A-2

Na D1 and D2 transitions

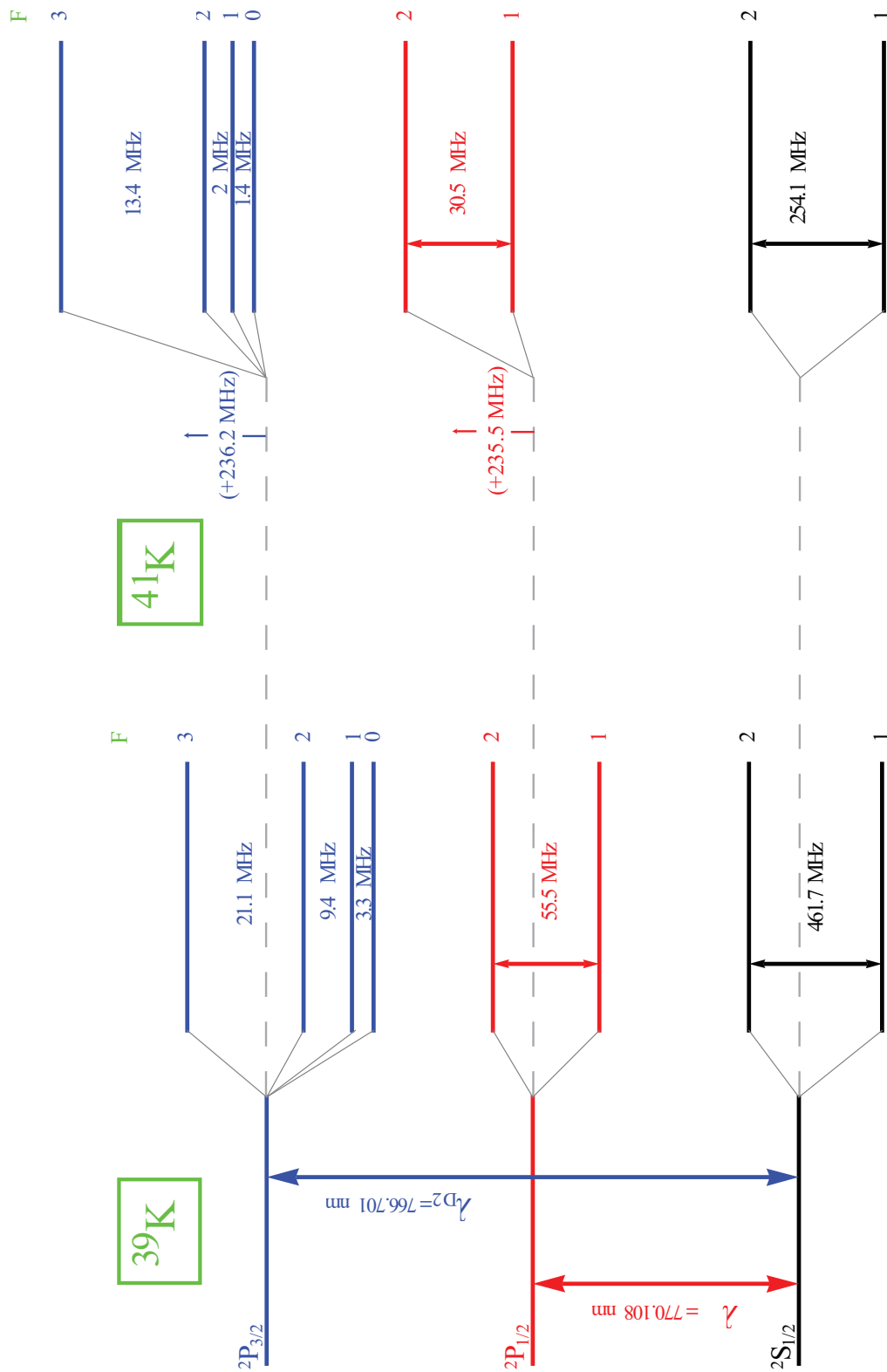


Figure A-3

K D1 and D2 transitions

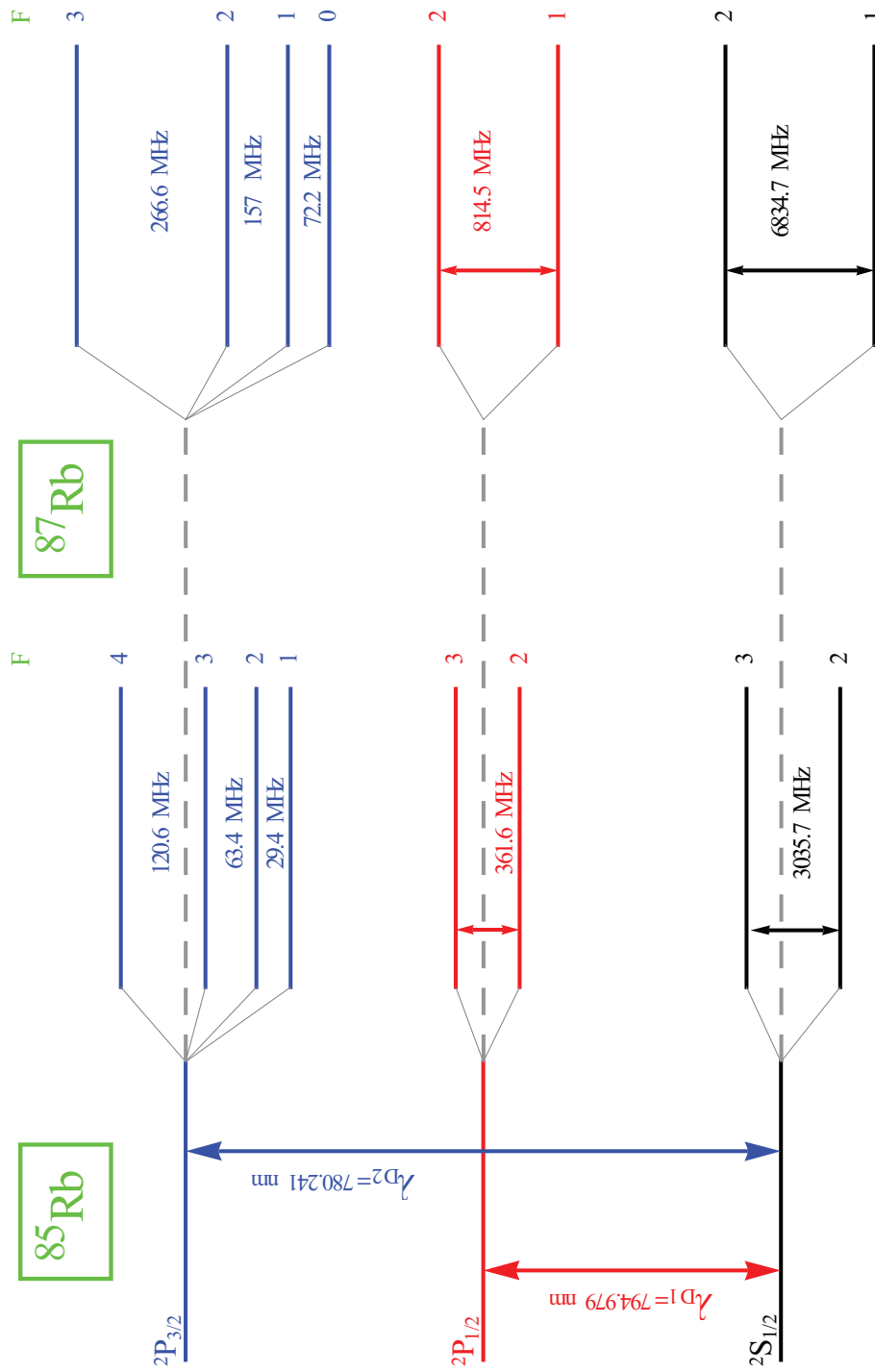


Figure A-4

Rb D1 and D2 transitions

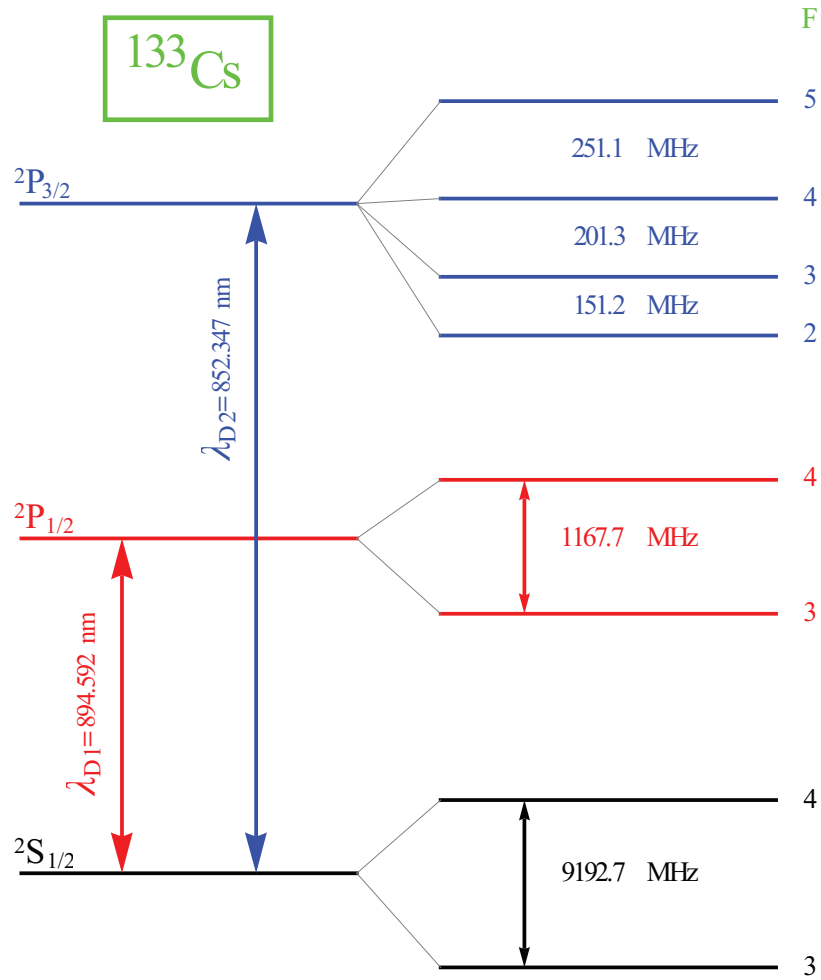


Figure A-5

Cs D1 and D2 transitions

Appendix B

Shot noise and polarimetry

B.1 Photodiode shot noise

The current of the photodiode is proportional to the rate, k , at which electrons are generated times the electron charge:

$$\langle i \rangle = k e \quad (\text{B.1})$$

For a measurement time τ and assuming the generation process is Poissonian*, the mean number and variance of generated electrons is:

$$\langle n_e \rangle = k \tau \quad \text{and} \quad \langle \delta n_e^2 \rangle = \langle (n_e - \langle n_e \rangle)^2 \rangle = \langle n_e \rangle = k \tau \quad (\text{B.2})$$

Thus, the variance in the current, which we identify as the rms noise current, is:

$$\mathbf{i}_{\text{rms}}^2 \equiv \langle \Delta i^2 \rangle = \langle (i - \langle i \rangle)^2 \rangle = \left(\frac{e}{\tau} \right)^2 \langle n_e \rangle = \frac{e}{\tau} \langle i \rangle \quad (\text{B.3})$$

For a measurement time τ , the noise bandwidth is defined by:

$$\Delta f = \frac{1}{2 \tau} \quad (\text{B.4})$$

and the noise current becomes:

$$\mathbf{i}_{\text{rms}} = \sqrt{2e\langle i \rangle} \sqrt{\Delta f} \quad (\text{B.5})$$

The first part in the equation above has units of $\text{A}/\sqrt{\text{Hz}}$ and is the quantity of interest when measuring power spectral densities (PSD).

*The electronic and photon shot noise is, indeed, a Poissonian process. As such, the mean and variance of shot noise created parameters coincide.

If the current i is a photocurrent due to an incident light power P , then we can convert between the two via:

$$i = r P, \quad \text{with } r = \frac{\eta e}{h f} \text{ [units : A/W]} \quad (\text{B.6})$$

where the coefficient r is the *responsivity* of a photodiode with quantum efficiency η at laser frequency f . In the general case the incident light is not strictly monochromatic and the above equation has to be integrated over frequencies. However, the above remains a good approximation for narrow band light and for photodiodes with a relatively flat spectral response around the central frequency of the light spectrum. For our Rb experiments, the above conditions were fulfilled, with our detector (Thorlabs DET210) operating near the peak of its spectral response, with a responsivity $r \simeq 0.45\text{A/W}$.

To measure the photocurrents it usually suffices to convert them into voltages on a load resistor, R . This noise voltage, thus, is:

$$\mathbf{v}_{\text{rms}} = \mathbf{i}_{\text{rms}} R = \sqrt{\Delta f} \sqrt{\frac{2 \eta e^2 R^2}{h f}} \sqrt{P} \quad (\text{B.7})$$

with the rightmost two terms constituting the PSD part of the noise voltage. For example, for the Rb D2 line at $\lambda = 780\text{nm}$ and for a $10\text{k}\Omega$ load resistor, the above relation gives for the PSD noise voltage:

$$\mathbf{v}_{\text{rms}}^{[\text{PSD}]} \text{ [in nV}/\sqrt{\text{Hz}}] \simeq 4 \sqrt{P \text{ [in } \mu\text{W}]} \quad (\text{B.8})$$

B.2 Polarimetry

Polarimetry is a technique used to characterize the polarization state of optical radiation and is a powerful tool in determining optical anisotropies in a medium. Various geometries of the medium-light interaction can be used to infer information about such optical anisotropies; monitoring of transmitted or reflected light at an interface or measurement of secondary emission, such as fluorescence, luminescence or scattering. In any case, the effect of the interaction of the medium is to alter the ratio of the phases and/or amplitudes of two mutually orthogonal polarization components of the beam [Zap82]. Thus, the measurement of the angle of rotation of a linearly polarized light beam passing through an anisotropic medium can be approached in two different ways: one could chose to compensate for the phase alterations by means of a circular phase plate, or he could chose to measure or compensate for the amplitude alterations of the linearly polarized components by means of a linear polarizer. However, since the measurement is

ultimately performed by a photodetector responding to the intensity of the light beam, regardless of the methodological approach used, the main factor determining the sensitivity of polarimetric measurements will be the ratio of the signal magnitude (intensity change of one polarization component or intensity difference between two mutually orthogonal components) to the noise induced by the light flux.

B.2.1 One photodiode: crossed and 45° geometries

Small rotations of the polarization plane of linearly polarized light can be detected by means of a linear polarizer and a photodetector. The basic question is: which position of the linear polarizer relative to the plane of polarization produces the maximum signal-to-noise ratio?

The rotation angle can be connected to the detected light intensity through Malus' law:

$$I = I_o \sin^2 \varphi \quad (\text{B.9})$$

where I_o is the light intensity incident on the polarizer and φ is the angle between the polarization plane and the principal axis of the polarizer, measured from the crossed position[†] There are two main geometries used for the detection:

- The *45° geometry*, where the axis of the polarizer is at 45° relative to the unperturbed plane of polarization. This position corresponds to the maximum slope of the $I(\varphi)$ function, that is to maximum *absolute* change in light intensity per unit angle of rotation of the polarization plane
- The *crossed geometry*, where the axis of the polarizer is at 90° ($\varphi = 0$) relative to the unperturbed plane of polarization. This position corresponds to the maximum *relative* change in light intensity per unit angle of rotation of the polarization plane, as $\frac{\Delta I/I}{\Delta \varphi} \rightarrow \infty$ as $\varphi \rightarrow 0$.

Evaluation of the signal-to-noise ratio in these two geometries requires consideration of three main sources of noise:

- ▷ Quantum shot noise of the photocurrent (usually sets the sensitivity limit)
- ▷ Excess noise due to intensity fluctuations of the light beam
- ▷ Excess intrinsic noise of the photodetector and the recording channel in general

[†]i.e. from the position of maximum extinction.

Assuming only shot noise at first, we evaluate the signal-to-noise ratio. According to Eq. (B.5), the noise current will be:

$$\mathbf{i}_{\text{rms}} = \sqrt{\frac{2 e^2 \eta P_o}{h f} \sin^2 \varphi \Delta f} \quad (\text{B.10})$$

The dependence of the signal on the rotation angle will be ($\Delta\varphi \ll \varphi \ll 1$):

$$\Delta i = r I_o [\sin^2(\varphi + \Delta\varphi) - \sin^2(\varphi)] \simeq \frac{\eta e P_o}{h f} 2 \sin \varphi \cos \varphi \Delta\varphi \quad (\text{B.11})$$

and so, the resulting relation between the signal to photocurrent noise ratio and the angle will be:

$$\frac{\Delta i}{\mathbf{i}_{\text{rms}}} = \sqrt{\frac{2 \eta P_o}{h f \Delta f}} \cos \varphi \Delta\varphi \quad (\text{B.12})$$

Immediately apparent from the equation above, is that sensitivity is mainly determined by the factor $\sqrt{\frac{\eta P_o}{h f}} = \sqrt{\eta \dot{N}}$, where $\dot{N} = P/(hf)$ is the photon flux incident on the analyzer, or, equivalently, the minimum discernible angle will be $\Delta\varphi = 1/\sqrt{2\dot{N}}$. Thus, the most direct way of increasing the sensitivity is by increasing the amount of light interacting with the medium. It is to be understood at this point that the intensity arriving at the photodetector can be low, as it is the case in crossed geometry, and still have high sensitivity, as long as the intensity interacting with the medium is high. Regarding the optimal position of the detector, from Eq. (B.12) we see that, in the case of pure shot noise limited polarimetry, the crossed and 45° geometries are essentially equivalent, since the latter is just a factor of $\sqrt{2}$ less sensitive than the former.

We apply another layer of realism, now, by allowing excess noise due to light intensity fluctuations. For typical conditions, intensity fluctuations are dominant over shot noise, usually by many orders of magnitude. In this case the crossed geometry gains a clear advantage over the 45° geometry, since introducing more crossing maintains the relative value of excess noise, but the relative level of the signal is rapidly increased, as mentioned previously. Ideally, crossing to $\varphi = 0^\circ$ would completely rid the measurement of excess noise, rendering it shot noise limited.

This, however, is not entirely true, since we have to take into account two factors: the first is that, the more crossed the geometry, the more important the intrinsic noise sources of the recording channel become; nevertheless, this type of noise is neglected for the rest of this paragraph. The second are the inevitable imperfections of real-life polarizers and the inhomogeneities of the medium, which collectively lead to formal violation of Malus' law near the crossed position, $\varphi = 0^\circ$. The solution is to characterize the imperfections of the existing polarizers and compensate for the results by modifying Malus' law into:

$$I = I_o (\sin^2 \varphi + \xi \cos^2 \varphi) \quad (\text{B.13})$$

where ξ is the *extinction parameter* defined as the ratio of the light intensity passing through the polarizer when the polarization plane is parallel to the polarizer axis to the corresponding value for mutually perpendicular polarizations. In this description, the light intensity passing through the polarizer at the crossed position is:

$$I = \xi I_o \quad (\text{B.14})$$

and the signal-to-noise ratio, when light intensity fluctuations are dominant, is given by:

$$\frac{S}{N} = (1 - \xi) \frac{\sin(2\varphi)}{\sin^2 \varphi + \xi \cos^2 \varphi} \quad (\text{B.15})$$

where all factors independent of φ are dropped. Assuming a small extinction ratio ($\xi \ll 1$), the optimal value of the angle, φ , yielding the maximum signal to noise ratio is found to be:

$$\varphi_{\text{opt}} = \sqrt{\xi} \quad (\text{B.16})$$

Concluding this paragraph, we note that for almost all light sources in use today, this optimization of the crossed geometry leads to a gain in sensitivity which scales as $1/\sqrt{\xi}$ relative to the 45° geometry. With typical values of ξ in the range of 10^{-4} to record values of 10^{-9} , a gain of sensitivity of many orders of magnitude is possible.

B.2.2 Two photodiodes: balanced polarimetry

As explained in the previous paragraph, noise due to fluctuations of light intensity is usually the dominant type. However, if the light beam is split into two, equally intense parts, then intensity fluctuation noise remains correlated. This means that subsequent subtraction of the photocurrents created by these two sub-beams, after traversing equal distances, results in complete extinction of the light intensity fluctuation noise. Although this may seem trivial, it is not. For example the same is not true for shot noise, which is uncorrelated noise and where the shot noise of the subtracted signal is $\sqrt{2}$ times higher than that of each channel alone. In a, so called, *balanced polarimeter* we take advantage of this property of intensity fluctuation noise.

In a balanced polarimeter, a polarizing beam splitter (PBS) is positioned on the propagation path of the light beam, with its axis in a 45° geometry relative to the polarization plane of the beam. Thus, two equally intense, mutually perpendicularly polarized beams emerge from the PBS and are detected by two

photodetectors, the photocurrents of which are subtracted to create the detected signal.

Ideally, the signal of a balanced polarimeter is completely shot noise limited, with a sensitivity calculated as follows. From Malus' law we get for the two polarization components:

$$I_{[\uparrow]} = I_o \cos^2 \varphi \quad \text{and} \quad I_{[\leftrightarrow]} = I_o \sin^2 \varphi \quad (\text{B.17})$$

thus:

$$\tan^2 \varphi = \frac{I_{[\uparrow]}}{I_{[\leftrightarrow]}} \Rightarrow \delta(\tan^2 \varphi) = \frac{2 \tan \varphi}{\cos^2 \varphi} \delta \varphi \quad (\text{B.18})$$

and from the last relation, after some manipulation similar to the calculations above, we get the shot noise limit:

$$\delta \varphi = \frac{1}{2\sqrt{N}} \quad [N \text{ is the number of detected photons}] \quad (\text{B.19})$$

$$\text{or in PSD units: } \delta \varphi_{\text{PSD}} = \frac{1}{2\sqrt{\dot{N}}} \quad [\dot{N} = P/(hf) \text{ is the photon flux}] \quad (\text{B.20})$$

As this was the polarimetric method of preference in our experiments, further discussion on its application is made in the main text.

Appendix C

Alkali vapor density measurements

Although the Killian formula (1.2.1) for the saturated alkali vapor density is generally applicable, nevertheless the validity of the specific parameters A and B tabulated in Table A#1 for a particular cell is questionable. It is a well known fact that a newly formed glass cell (inside which we have distilled a few alkali metal droplets) undergoes a *curing* process, lasting days, weeks or maybe months, at the end of which the alkali metal - glass cell system arrives at an equilibrium state. The origin of the non-equilibrium initial state of the cell is believed to be in its hot formation process. The heat required to distill the droplets and seal the cell, supposedly deforms the inner cell walls and alkali atoms are trapped in the surface layers. This results in the density of alkali atoms inside the cell to be affected by the release of trapped atoms, while also the cell walls become more absorptive than they should be. The curing process is, essentially, a stress release of the cell walls, during which the relative amount of trapped to free atoms is stabilized [MKJ⁺09].

Since in our experiments, the rubidium cells were used immediately after their seal-off, it was essential to measure the actual density of the vapor, rather than rely on the tabulated values. Usually one goes about this task by means of the *integrated absorption method*: the frequency of the laser is scanned across the absorption line of the alkali and the integrated absorption cross section is given by:

$$\int \sigma(f) df = \frac{\pi e^2 f_{ge}}{m_e c} = \frac{1}{n_d l} \int \ln \left(\frac{I_o}{I(f)} \right) df \quad (\text{c.1})$$

where I_o and I is the incident and transmitted light intensity, respectively. Given the absorption oscillator strength, f_{ge} , and cell length, l , the integrated absorption

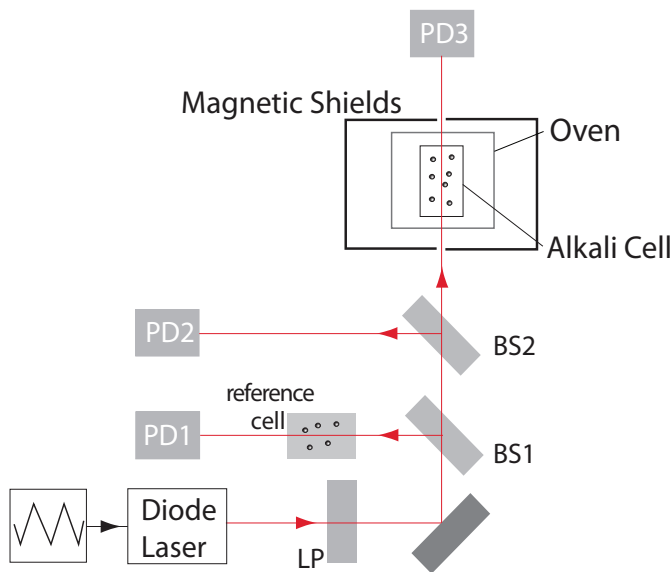


Figure C-1

Experimental setup for the integrated absorption measurement of the alkali number density. See text for details.

cross section yields the number density of the vapor, n_a . This method, although particularly simple, is unsuitable at the high temperatures where our experiments were performed. The reason for this, of course, is that at high temperatures the vapor becomes optically thick and all light is absorbed near the center of the transition. However, it was employed in our measurements at low temperatures and the resulting spectra were used to calibrate the frequencies for the high temperature spectra, the latter taken with a dispersion method described further below.

A simplified diagram of the experimental setup used is shown in Fig. C-1. The light beam is linearly polarized (LP) and its frequency is scanned by applying a triangular oscillating voltage, with a frequency of a few Hz, at the grating of the external diode cavity. This provides us with nearly 60GHz of mode-hop free, frequency scan. A small part of the beam is split apart with a 90:10 beam splitter (BS1) and guided through a cell containing pure rubidium, upon emergence from which, it is detected by a photodiode (PD1). The pure rubidium cell provides us with spectra where the well known hyperfine structure of the ground state is clearly discernible and, thus, serve as frequency calibration. The remaining beam is split anew by a 90:10 beam splitter (BS2), and the weak part is monitored by a photodiode (PD2), thereby providing a measurement of the incident light intensity. The beam then traverses the cell, which is located inside the air-heated oven, and the transmitted intensity is monitored by a third photodiode (PD3). As can be seen from the figure, this rather simple measurement did not require any sophisticated equipment. The photodiode voltages, calibrated by a power meter, were fed to the inputs of the BNC2090, to be recorded by a custom made LabView virtual instrument. From there, data analysis was performed in the statistical package IGOR.

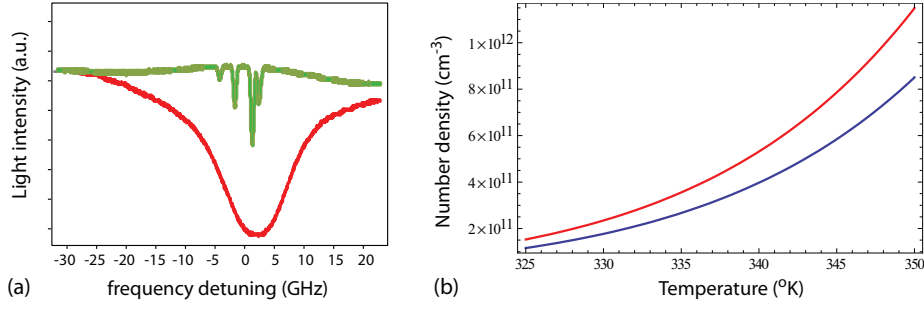


Figure C-2

- (a) Typical reference (green) and absorption (red) signals
 (b) Calculated (blue) and bibliography (red) vapor density according to the Killian.

Typical reference (PD1) and absorption signals (PD3) as functions of the laser frequency detuning from the D2 resonance frequency of rubidium are depicted in Fig.C-2(a). The reference signal clearly shows the D2 absorption peaks of ^{85}Rb (inner peaks) and ^{87}Rb (outer peaks) and the heated, alkali metal - buffer gas absorption signal owes its width to collisional broadening. In Fig.C-2(b) the extracted rubidium number density is compared to the Killian density according to the tabulated A and B parameters for rubidium (c.f. Table A#1). The comparison clearly indicates an uncured cell, with the experimental number densities being significantly lower than expected. The formula arrived at for the alkali number density at low temperatures is:

$$n_d = \frac{10^{26.145-4084.9/T}}{T} \quad \left(\text{cm}^{-3} / \text{Bibliography: } n_d = \frac{10^{26.72-4215/T}}{T} \right) \quad (\text{c.2})$$

or

$$P = 10^{4.279-4084.9/T} \quad \left(\text{Atm} / \text{Bibliography: } P = 10^{4.857-4215/T} \right) \quad (\text{c.3})$$

At higher temperatures, supplementary information on the alkali vapor number density was provided by a Faraday rotation measurement technique; a variation of the procedure proposed in [WKH⁺86]. The experimental setup used is shown in Fig. C-3. An external cavity diode laser is blue or red detuned at $\sim 20\text{GHz}$ and is linearly polarized. Its frequency is scanned across a $\pm 15\text{GHz}$ range, by applying a $2.5\text{V}_{\text{p-p}}$ triangular signal on the piezoelectric actuator of the cavity grating, at a low frequency of about 5.5Hz . Part of the beam power is split apart and used to visually assess the frequency range by comparing to a reference, pure Rb cell at room temperature (BS1/reference cell/PD1) and another part is used to monitor the incident power on the cell (BS2/PD2). Prior to the latter, a Faraday rotator crystal is positioned along the beam propagation path. The crystal is placed along the axis of a $L = 14.2\text{mH}$, $R = 5.4\Omega$, $N = 1500$ turns solenoid, capable of producing a magnetic field of about 150G at its

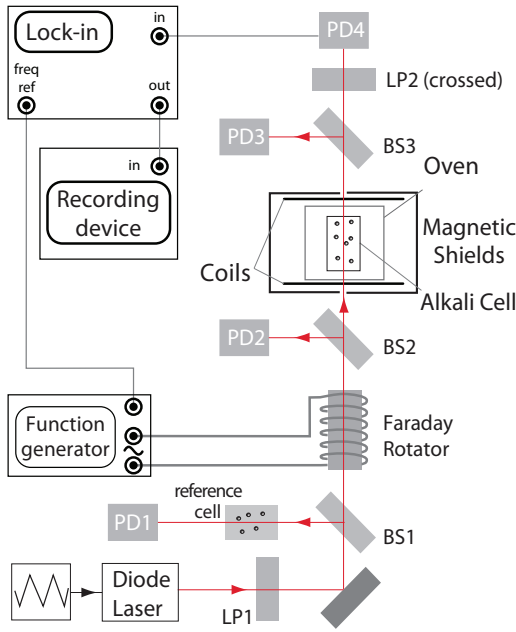


Figure C-3

Faraday rotation measurement setup for the determination of alkali vapor number densities.

core. The current of the solenoid is modulated at a frequency of 5.66kHz and the option to introduce a strong DC offset is also available. The beam traverses the heated cell and a transmitted power reading is obtained by splitting a part of the emerging light and guiding it on a photodiode (BS3/PD3). The main part of the transmitted power is incident on a linear polarizer (LP2) set for maximum extinction relative to the initial polarization (LP1). The light thus received by the photodiode at the end of the beam path (PD4) is fed to a lock-in amplifier, referenced to the frequency of the Faraday rotator modulation. The lock-in signal at the reference frequency is recorded by a digital oscilloscope, as are also the grating voltage (corresponding to laser frequency), the incident (PD2) and transmitted (PD3) power and the reference signal from the pure Rb cell (PD1).

For small rotations of the polarization plane of the beam, the lock-in signal at the reference frequency can be approximated by:

$$S_{\omega} = I_t \left(2 - \frac{1}{R} \right) \theta \varphi_{\omega} \quad (\text{c.4})$$

where I_t the transmitted laser power, R is the LP2 rejection ratio ($R = 65$ in our case), θ is the Faraday rotation angle and φ_{ω} is the angle component due to the Faraday rotator modulation signal. By controlling the DC offset of the voltage applied to the Faraday rotator, we can rotate the polarization plane of the laser light by known angles and, thus, use Eq. (c.4) to calculate φ_{ω} . We do so for $\theta = 2$ and 4° to get:

$$\varphi_{\omega} = (1.21 \pm 0.08) \times 10^{-4} \text{rad} \quad (\text{c.5})$$

We now switch off the DC part of the Faraday rotator voltage and subject the vapor cell to a longitudinal (along the beam path) magnetic field, $B = 50\text{G}$. The induced Faraday rotation angle depends on the field magnitude, on the density of atoms and on the laser detuning. Using the Faraday rotation theory developed in paragraph 1.1.5c/, we arrive at the following expression for the dependence of the rotation angle on the magnetic field:

$$\theta = n_d \frac{l f_{g_e} e^2}{8\pi m_e c} \left(\frac{5}{2} g_e - \frac{1}{2} g_g \right) \frac{\delta^2 - (\gamma/2)^2}{[\delta^2 + (\gamma/2)^2]^2} \frac{\mu_B B}{\hbar} \quad (\text{c.6})$$

where δ is the laser detuning in Hz and the rest of the symbolization has been defined prior to this point. Although the above expression is valid for a mono-isotopic alkali metal vapor and for unresolved ground and excited state hyperfine structure, it is less so for naturally abundant rubidium, which consists of two isotopes and for which the hyperfine structure brings in significant corrections on the expected rotation angle values as the frequency of the laser is shifted close to resonance. Also, the frequency dependence of the absorption has to be taken into account if the formula is to be used to fit experimental data. Therefore, the actual theoretical calculation of Faraday rotation angles was performed via the expression:

$$\Theta = \sum_{\substack{R= \\ {}^{85}\text{Rb}, {}^{87}\text{Rb}}} \sum_{F=I-1/2}^{I+1/2} [\theta_R(\delta_F^{(R)}) \exp(-n_d^{(R)} l \sigma_F^{(R)})] \quad (\text{c.7})$$

where the excited state hyperfine structure is still ignored, the detuning and absorption cross section are transition and isotope dependent and the ratio of number densities of ${}^{85}\text{Rb}$ and ${}^{87}\text{Rb}$ is approximately 2.6:1.

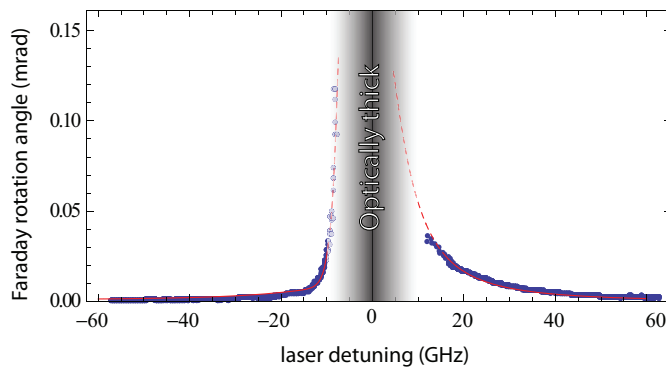
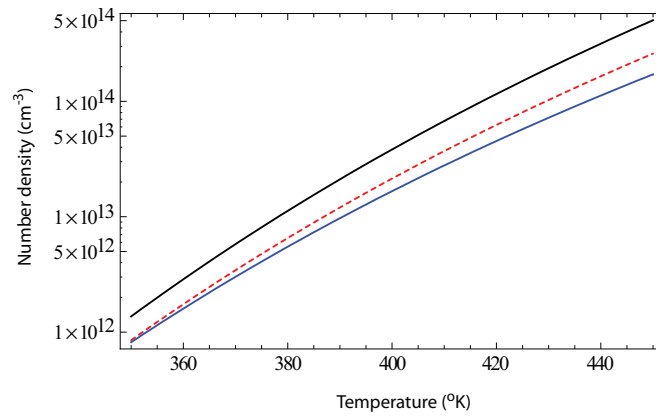


Figure C-4

Experimental Faraday rotation angle and fit at a temperature of 97.7° . The frequency span has been extended in this case, for illustration purposes, by shifting the central frequency.

**Figure C-5**

Experimental (blue) and Killian (black) number densities. Also shown is the low temperature result for the number density formula (red/dashed)

So, with all other quantities known, fitting the experimentally measured Faraday rotation angles with the above expression yields the number density of the atomic vapor. We fit both for red and blue detunings and a typical experimentally obtained set of points is seen in Fig. C-4, along with the fitted curve. Repeating the procedure for various temperatures then yields the temperature dependence of the number density. Taking into account the measured densities for the lower temperatures, obtained through the integrated absorption method, the saturated vapor pressure formula is arrived at:

$$n_d = \frac{10^{25.397-3829.3/T}}{T} \quad \left(\text{cm}^{-3} / \text{Bibliography: } n_d = \frac{10^{26.72-4215/T}}{T} \right) \quad (\text{c.8})$$

or

$$P = 10^{3.531-3829.3/T} \quad \left(\text{Atm} / \text{Bibliography: } P = 10^{4.857-4215/T} \right) \quad (\text{c.9})$$

The comparison of the experimentally obtained density to the Killian formula and to the low temperature density is shown in Fig. C-5. The significantly lower densities clearly indicate an uncured cell, which, as explained in the conclusions of section 1.3.1, was the main source of error in the measurement of the transverse relaxation rate of rubidium.

Appendix D

Vector models in radical pairs

Since the onset of quantum mechanics, physicists have been both very eager and very hesitant to provide classical pictures which would bring the microscopic world into a perspective more relevant to everyday experience. Pictorial representations can, perhaps, reveal important features of the inner structure of quantum phenomena, but can also lead to immensely paradoxical predictions if taken out of proportion. The notion of identical particles, non-classical degrees of freedom such as half-integer spins, non-locality, complementarity, state superpositions and entanglement are some of the microworld-specific characteristics which are routinely found at the heart of quantum paradoxes.

In the context of radical ion pair reactions, at least two different, semi-classical pictures of the entangled spin dynamics have been proposed to assist the explanation of magnetic field effects. The first was given in the late 1970's by K. Schulten and P.G. Wolynes in [SW78] and an account of the second can be found in [BM96], among other works. In this chapter, we briefly describe these two pictures and also present a spin-vector model of our own devise in order to account for Singlet to Triplet and inter-Triplet transformations produced by magnetic fields and hyperfine interactions in a simple radical pair.

▷ a:/ *The semi-classical vector model*

In [SW78] the authors make the observation that in a system with many nuclei, the mean nuclear spin is, on average, much larger than its electronic counterpart. So, the hyperfine precession of the electron and nuclear spin about each other, leaves the latter largely unaffected, thus enabling its description as a classical vector, which, combined with the vector of the external magnetic field, defines the axis about which the electronic spin precesses. Such is the case depicted in Fig.D-1 for a pyrene-dimethylaniline pair, where the phasor-like contributions

from the various nuclei make up the total nuclear spins, I_1 and I_2 , which are then added to \mathbf{B} to define the local precession axis. The hollow-line vectors are the two electronic spins, initially arranged in a simplistic representation of a Singlet state. As should be apparent from the figure, allowed to evolve, the two electronic spins will precess about different axes at different frequencies, thus materializing the transformation of the initial Singlet state into a - coherent - mixture of Singlet and Triplet components. This picture highlights the origins of the magnetic field effect, since the extent of the Singlet-Triplet mixing is clearly influenced by the magnetic field. The authors of the paper proceed to formulate a theoretical treatment of the coherent motion of the electronic spin based on this semi-classical picture, which would later include the phenomenological recombination terms and evolve into the PME.

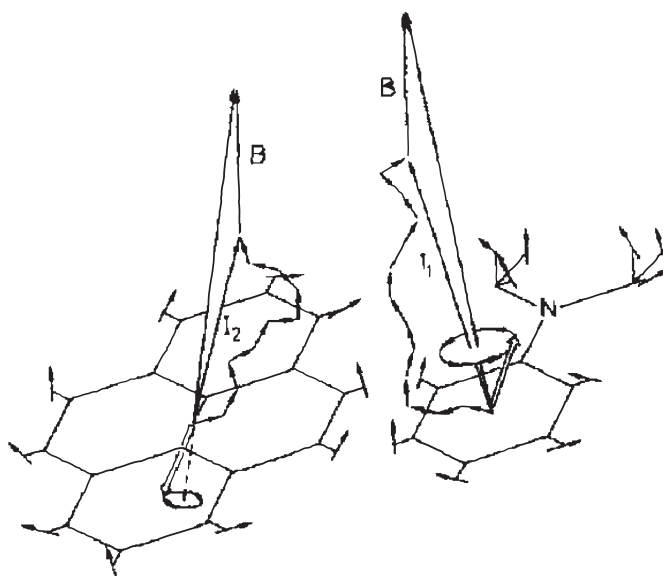


Figure D-1

A vector model in the pyrene - dymethylaniline (${}^2\text{Py}^{\bullet-} + {}^2\text{DMA}^{\bullet+}$) radical pair [SSW+76]

▷ *b:/ The qualitative spin vector model*

The vector model described in [BM96] is depicted in Fig.D-2. The basis states spanning the Hilbert space of the two electrons are shown on the left with the two spins depicted as arrows, the relative phase and orientation of which are both important. On the right, the presence of a single nucleus forces the local electronic and nuclear spin to precess about each other. This precession can transform an initial Singlet state into a Triplet with a zero projection along some axis. However, for the Singlet to transform into an oriented Triplet state ($|T_{\pm}\rangle$),

the combined action of the hyperfine interaction and a local magnetic field is necessary.

This model, albeit simplistic, can provide useful insight to the evolution of a radical pair and is expandable in the sense that it can also account for other, non-coherent, effects such as spin exchange. These can cause random differences in the rates of precession of each spin thereby changing the phase relation between the spins on the different radicals and causing $|S\rangle - |T_0\rangle$ interchange.

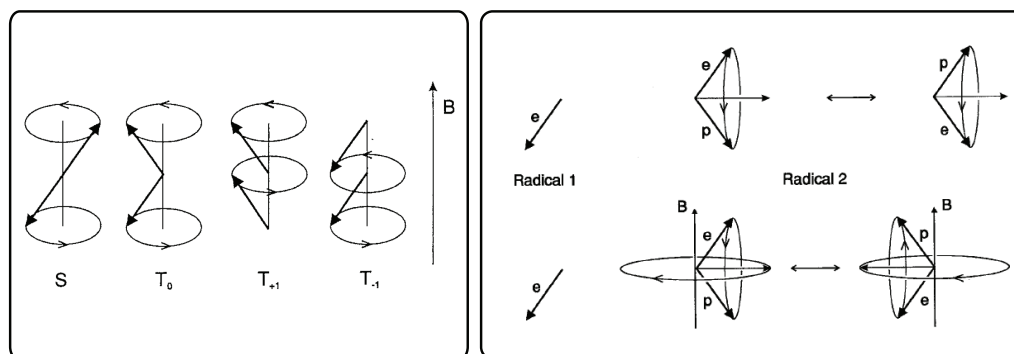


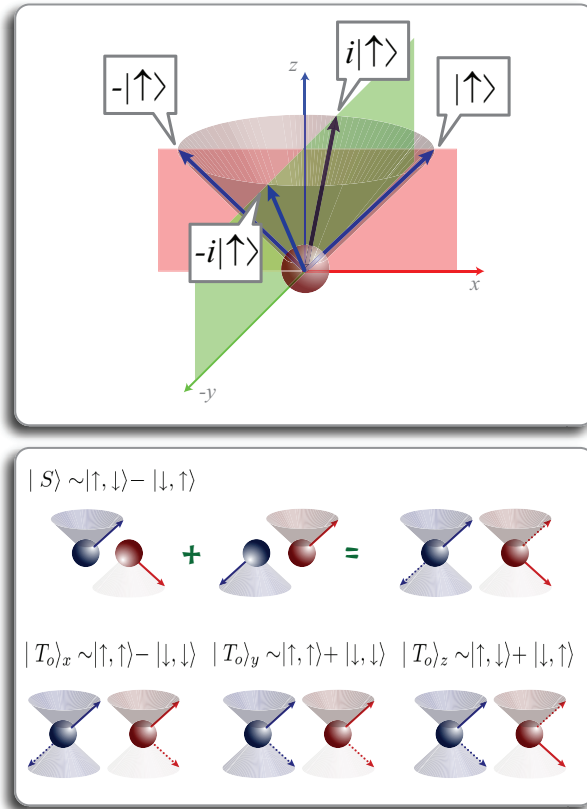
Figure D-2

The vector model described in [BM96]. On the left, the basis states spanning the Triplet manifold and the Singlet are shown. On the right, a single nucleus coupling to one of the two electrons induces a precession of the electronic and nuclear spin about each other. The presence of a magnetic field can complete the Singlet to - oriented - Triplet transformation.

▷ c:/ *The home-bred vector model*

Our model is actually more of a method, rather than a full fledged account of the actual spin evolution. In Fig.D-3 we show how the various states are represented. First of all, assuming that \hat{z} is the quantization axis, the phase of a particular electronic spin state is defined relative to the azimuth of the spin vector; i.e. the angle that its (xy) -plane projection makes with the \hat{x} -axis. Generally, if φ is the azimuthal angle, this phase is given by $e^{i\varphi}$. Using this phase convention, we give a representation of the zero-projection basis states of Eq.11.3.2. Since these states comprise two coherently superposed components, in order to make the representation more compact, we depict the first component with solid arrows and the second with dotted. This also serves to imply and remind that each electron is in a non-classical state, wherein the measurement of its spin projection on the quantization axis can yield more than one value.

We now proceed to examine the influence of a \hat{z} -axis magnetic field on these states. We remind at this point that, since the electronic spin is a non-classical vector corresponding to a half-integer value of angular momentum (namely $\frac{\hbar}{2}$ for the projection or $\frac{\sqrt{3}}{2}\hbar$ for the magnitude of the vector), it rotates half as fast

**Figure D-3**

Top: The phase of a single-electron, spin-up state, $|\uparrow\rangle$, relative to its projection position on the (xy) -plane. The general formula for the phase is, of course, $e^{i\varphi}$, where φ is the angle between the projection on the (xy) -plane and the \hat{x} -axis. Bottom: Pictorial representation of the basis states in Eq. 3.2 following the phase convention described above. The blue and red spheres stand for the two electrons of the pair. The method used to depict their states is quite self-evident.

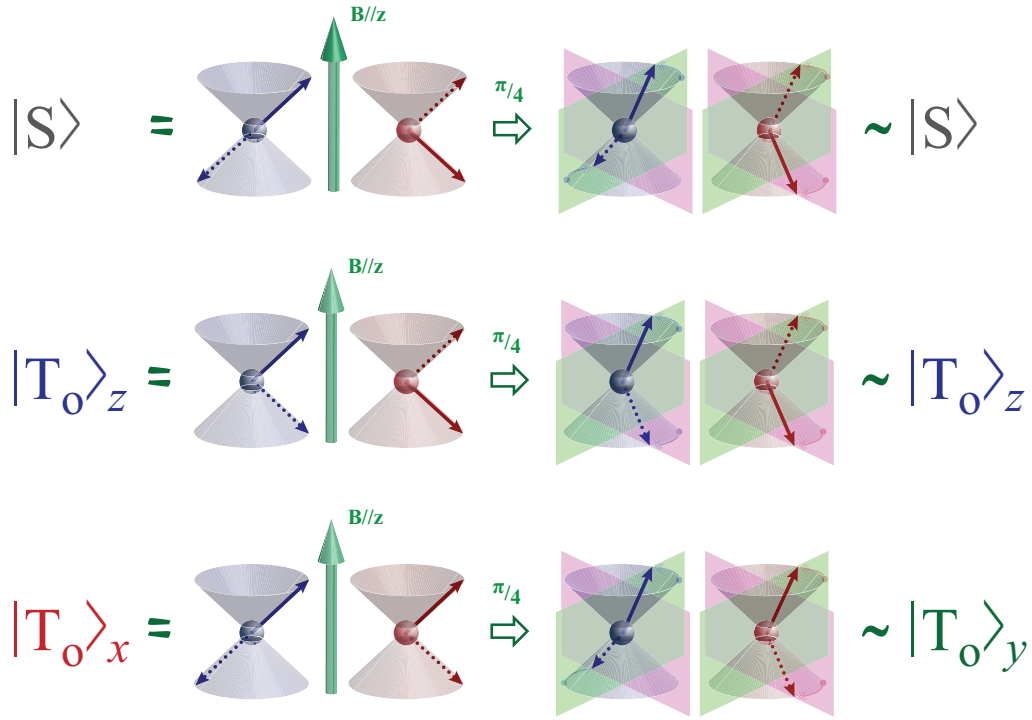
relative to a classical, spin-1 vector. Thus, if a Triplet state is formed from two electronic spins, a $\frac{\pi}{2}$ rotation of this state would correspond to the two electrons having rotated just by $\frac{\pi}{4}$. We also remind that Larmor precession proceeds in different senses for the $|\uparrow\rangle$ and $|\downarrow\rangle$ states; in a top down perspective, the tip of the $|\uparrow\rangle$ rotates counter-clockwise and the tip of $|\downarrow\rangle$ rotates clockwise. At the top of Fig. D-4 we examine the $|S\rangle$ state. As the electronic spins rotate by $\frac{\pi}{4}$, the Singlet state is transformed as follows:

$$|S\rangle \sim |\uparrow\downarrow\rangle - |\downarrow\uparrow\rangle \rightsquigarrow e^{i\frac{\pi}{4}}|\uparrow\rangle e^{-i\frac{\pi}{4}}|\downarrow\rangle + e^{i\frac{3\pi}{4}}|\downarrow\rangle e^{i\frac{\pi}{4}}|\uparrow\rangle = |\uparrow\downarrow\rangle - |\downarrow\uparrow\rangle \sim |S\rangle$$

Similarly, for the $|T_0\rangle_z$ state occupying the middle row of the figure:

$$|T_0\rangle_z \sim |\uparrow\downarrow\rangle + |\downarrow\uparrow\rangle \rightsquigarrow e^{i\frac{\pi}{4}}|\uparrow\rangle e^{-i\frac{\pi}{4}}|\downarrow\rangle + e^{-i\frac{\pi}{4}}|\downarrow\rangle e^{i\frac{\pi}{4}}|\uparrow\rangle = |\uparrow\downarrow\rangle + |\downarrow\uparrow\rangle \sim |T_0\rangle_z$$

and so, the $|S\rangle$ and $|T_0\rangle_z$ states remain unaffected by the \hat{z} -magnetic field. The same is obviously true for the $|T_{\pm}\rangle$ states, since for them the initially aligned spins just co-rotate about the field vector. The only influence of the magnetic


Figure D-4

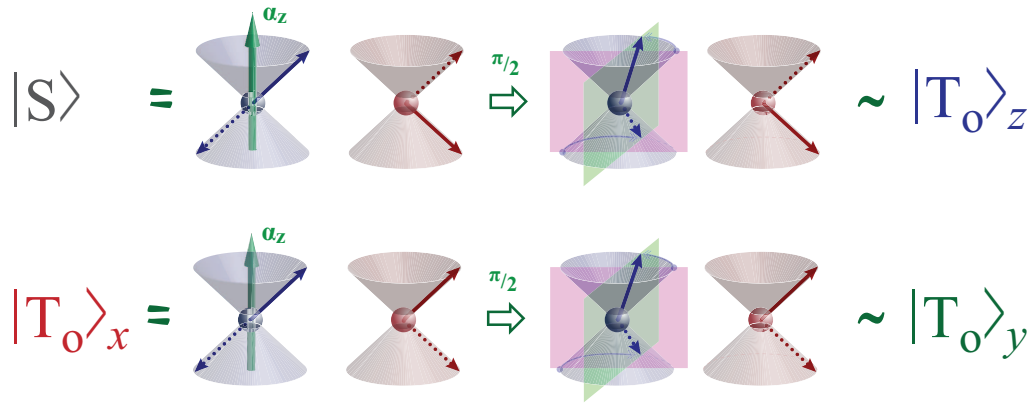
Influence of a \hat{z} -magnetic field on the basis states. As explained in the text, the $|S\rangle$ and $|T_o\rangle_z$ states simply acquire phase but remain otherwise unaffected, while the $|T_o\rangle_x$ and $|T_o\rangle_y$ states transform into one another. The colored, semi-transparent planes shown in the pictures are at $\pm 45^\circ$ relative to the \hat{x} -axis and serve as visual aids.

field thus, lies in the interconversion of the $|T_o\rangle_x$ state into $|T_o\rangle_y$ and vice versa. Starting from the $|T_o\rangle_x$:

$$|T_o\rangle_x \sim |\uparrow\uparrow\rangle - |\downarrow\downarrow\rangle \rightsquigarrow e^{i\frac{\pi}{4}} |\uparrow\rangle e^{i\frac{\pi}{4}} |\uparrow\rangle + e^{i\frac{3\pi}{4}} |\downarrow\rangle e^{-i\frac{\pi}{4}} |\downarrow\rangle = i(|\uparrow\downarrow\rangle + |\downarrow\uparrow\rangle) \sim |T_o\rangle_y$$

Completely analogous results can be obtained for magnetic fields oriented along different axes.

We next examine how the components of the hyperfine interaction affect the same set of states. We focus on the \hat{z} -component of the interaction, since analogous conclusions can be drawn for the rest. The \hat{z} -component of the hyperfine interaction can be thought of as a local \hat{z} -magnetic field coupled to only one of the two electrons. Now however, since only one of the electrons acquires phase, for a transformation to complete, the electron has to span a $\frac{\pi}{2}$ angle, rather than the $\frac{\pi}{4}$ of the previous case where both electrons acquired phase. In the top row of Fig.D-5, we show how the Singlet to Triplet conversion takes place under

**Figure D-5**

Influence of the \hat{z} -hyperfine component on the basis states. Nuclei are assumed to be present only at one site of the radical pair. As explained in the text, the \hat{z} component of the hyperfine interaction induces two types of spin state conversion: Singlet to Triplet, $|S\rangle \rightleftharpoons |T_0\rangle_z$, and inter-Triplet, $|T_0\rangle_x \rightleftharpoons |T_0\rangle_y$. The obvious analogy holds for the rest of the hyperfine components. The semi-transparent planes are now at 0° and 90° relative to the \hat{x} -axis.

the influence of the hyperfine interaction. A rotation of the hyperfine coupled electronic spin by $\frac{\pi}{2}$, transforms the initial Singlet into:

$$|S\rangle \sim |\uparrow\downarrow\rangle - |\downarrow\uparrow\rangle \rightsquigarrow i|\uparrow\rangle|\downarrow\rangle + i|\downarrow\rangle|\uparrow\rangle = i(|\uparrow\downarrow\rangle + |\downarrow\uparrow\rangle) \sim |T_0\rangle_z$$

and thus $|S\rangle$ is converted to $|T_0\rangle_z$. Continuation of the spin precession will transform the $|T_0\rangle_z$ back to $|S\rangle$ and so on. If the initial state is the $|T_0\rangle_x$, then the transformation depicted in the bottom row of the figure yields:

$$|T_0\rangle_x \sim |\uparrow\uparrow\rangle - |\downarrow\downarrow\rangle \rightsquigarrow i|\uparrow\rangle|\uparrow\rangle + i|\downarrow\rangle|\downarrow\rangle = i(|\uparrow\downarrow\rangle + |\downarrow\uparrow\rangle) \sim |T_0\rangle_y$$

and the $|T_0\rangle_x$ transforms into $|T_0\rangle_y$, much as it would under the influence of a \hat{z} -magnetic field experienced by either or both of the electrons.

List of Symbols and Abbreviations

Abbreviation	Description	Definition
RNG	Random Number Generator	page 78
PRNG	Pseudo Random Number Generator	page 78
TRNG	True Random Number Generator	page 79
QRNG	Quantum Random Number Generator	page 79
CRNG	Chaotic Random Number Generator	page 79
DRBG	Deterministic Random Bit Generator	page 78
DFT	Discrete Fourier transform	page 84
RIP	Radical Ion Pair	page 102
RP	Radical Pair	page 102
MFE	Magnetic Field Effect	page 103
LFE	Low Field Effect	page 105
SLE	Stochastic Liouville Equation	page 125
PME	Phenomenological Master Equation	page 125
QMME	Quantum Measurement Master Equation	page 127
EPR	Electron Paramagnetic Resonance	page 130

List of Figures

l:1-1	Multipole expansions in a state multiplet of specific F	18
l:1-2	Ground state eigenobservables for a $\frac{3}{2}$ nuclear spin	19
l:1-3	Binary collisions and van der Waals molecule formation	25
l:1-4	Spin exchange potential curves	31
l:1-5	Spin exchange and spin temperature distribution	35
l:1-6	Effect of rapid spin exchange collisions	37
l:2-1	Vacuum setup for filling pyrex cells	50
l:2-2	Mu-metal magnetic shielding	51
l:2-3	Alkali cell heating oven	53
l:2-4	Melles-Griot optical table	54
l:2-5	New Focus and Sacher diode lasers.	56
l:2-6	Littrow and Littman-Metcalf ECDL configurations	56
l:2-7	Thorlabs SA200-7A Fabry Perot interferometer.	57
l:2-8	Ocean Optics HR4000 fiber optic spectrometer.	58
l:2-9	HighFinesse Ångstrom WS/7 wavelength meter.	59
l:2-10	Stanford Research Systems Lock-In amplifier	60
l:2-11	SRS SR785 Dynamic Signal Analyzer	61
l:2-12	Bartington Mag-03 fluxgate sensor and power supply.	62
l:3-1	Spin noise measurements experimental setup	73
l:3-2	Spin noise spectra	74
l:3-3	Integrated spin noise power vs number density and laser power	76
l:3-4	Measured and calculated transverse relaxation rates.	77

I:3-5	Experimental setup for the QRNG	86
I:3-6	Transient signals and S/N ratio vs probe power in the QRNG . .	87
I:3-7	Illustrative statistical tests performed on random sequences . . .	91
II:1-1		
	Py + DMDMA reaction scheme in methanol [SSW ⁺ 76]	104
II:1-2	MARY curves indicating LFE	105
II:1-3	Hyperfine induced LFE	106
II:1-4	Δg mechanism in photosynthetic centers	107
II:1-5	J-resonances in $\text{Py}^{\bullet+} + \text{DCB}^{\bullet-}$	108
II:1-6	Dipolar interaction in photosynthetic reaction centers	109
II:1-7	Characteristics of Earth's magnetic field; inclination and strength	110
II:1-8	Reorientation of European Robins along a rotated magnetic field	112
II:1-9	The avian compass as an inclination compass	112
II:1-10	Wavelength dependence of the avian compass	113
II:1-11	Disruption of the avian compass by a weak RF field	114
II:1-12	RIP mechanism for magnetoreception	116
II:1-13	The radical pair candidates in cryptochrome	118
II:1-14	Cryptochrome FADH-Trp radical pair chain	119
II:1-15	Magnetic fields may induce visual patterns perceived by birds . .	120
II:1-16	Field dependence of magnetic field induced, visual patterns . . .	121
II:1-17	C-P-F scheme for the proof-of-principle of RIP magnetoreception	122
II:2-1	Recombination scheme in the Jones-Hore theory	126
II:2-2	Zeeman effect with superimposed HF widths	131
II:2-3	RIP Spin Exchange energies and impact of Zeeman effect	133
II:2-4	Combined spin exchange, dipolar and Zeeman interactions	134
II:2-5	Domination magnetic field regions of MFEs	135
II:3-1	QMME reproduction of Oxford data	142
II:3-2	QMME vs PME: Spin relaxation effect	144
II:3-3	QMME δB and $\delta\varphi$	145
II:3-4	Slow down of reaction time in the Zeno regime	146
II:3-5	Population evolution for anisotropic hyperfine coupling ($B = 0$) .	149
II:3-6	$ S\rangle \rightleftharpoons T\rangle$ and $ T\rangle \rightleftharpoons T\rangle$ transitions induced by A and B	150
II:3-7	A coherent Triplet can give anisotropic effects in isotropic media	151
II:3-8	$ T_0\rangle$ state in isotropic material: angular variation of yield and $\delta\varphi$	152
II:3-9	Orientalional sensitivity of $ T_{\pm}\rangle$ states in isotropic media	154
II:3-10	$ T_0\rangle_y$ state in \hat{z} -anisotropic HF coupling. Transition scheme. . .	155
II:3-11	Angular dependence of yield for anisotropic hyperfine coupling .	156
II:3-12	Explanation of $\delta\varphi$ enhancement in the Zeno regime	157
II:3-13	Heading error for anisotropic hyperfine coupling	158

II:3-14	Impact of spin exchange and relaxation on angular precision . . .	159
II:3-15	Impact of non-axial hyperfine coupling on angular precision . . .	159
A-1	Li: D1 and D2 transitions	172
A-2	Na: D1 and D2 transitions	173
A-3	K: D1 and D2 transitions	174
A-4	Rb: D1 and D2 transitions	175
A-5	Cs: D1 and D2 transitions	176
C-1	Absorptive density measurement setup	184
C-2	Absorptive signals and calculated vapor density	185
C-3	Faraday rotation setup for the measurement of alkali number densities	186
C-4	Experimental and fitted Faraday rotation angle	187
C-5	Experimental to Killian number density comparison	188
D-1	Electron spin vector model of [SW78]	190
D-2	Electron spin vector model of [BM96]	191
D-3	Electron spin vector model devised for this work	192
D-4	Influence of \hat{z} -magnetic field on basis states	193
D-5	Influence of \hat{z} -hyperfine component on basis states	194

List of Tables

I:1#1	Alkali metal - buffer gas D_0 diffusion constants in cm^2/sec	29
I:2#1	List of suppliers	64
A#1	Alkali metals properties and parameters	169